

**Experimental and quantum chemical studies on the
extraction of actinides using organophosphorous
compounds: Elucidating structural effects and third
phase formation**

By

ADITI CHANDRASEKAR

(Enrollment No: CHEM02201404002)

Indira Gandhi Centre for Atomic Research, Kalpakkam

A thesis submitted to the

Board of Studies in Chemical Sciences

In partial fulfillment of requirements

For the Degree of

DOCTOR OF PHILOSOPHY

of

HOMI BHABHA NATIONAL INSTITUTE



February 2019

Homi Bhabha National Institute

Recommendations of the Viva Voce Committee

As members of the Viva Voce Committee, we certify that we have read the dissertation prepared by **Aditi Chandrasekar** entitled “**Experimental and quantum chemical studies on the extraction of actinides using organophosphorous compounds: Elucidating structural effects and third phase formation**” and recommend that it may be accepted as fulfilling the thesis requirement for the award of Degree of Doctor of Philosophy.

Chairman – Dr. R. V. Subba Rao



Date: 26/7/19

Guide / Convener – Dr. N. Sivaraman



Date: 26.07.2019

Examiner -



Date: 26.07.2019

G. R. Rajaman

Member 1- Dr. John Philip



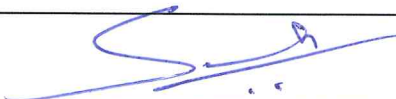
Date: 26.07.2019

Member 2- Dr. V. Sridharan



26/7/19

Member 3- Dr. A. Suresh



Date: 26/7/19

Final approval and acceptance of this thesis is contingent upon the candidate's submission of the final copies of the thesis to HBNI.

I/We hereby certify that I/we have read this thesis prepared under my/our direction and recommend that it may be accepted as fulfilling the thesis requirement.

Date: 26.07.2019

Place: Kalpakom



Dr. N. Sivaraman
Guide

STATEMENT BY AUTHOR

This dissertation has been submitted in partial fulfillment of requirements for an advanced degree at Homi Bhabha National Institute (HBNI) and is deposited in the Library to be made available to borrowers under rules of the HBNI.

Brief quotations from this dissertation are allowable without special permission, provided that accurate acknowledgement of source is made. Requests for permission for extended quotation from or reproduction of this manuscript in whole or in part may be granted by the Competent Authority of HBNI when in his or her judgment the proposed use of the material is in the interests of scholarship. In all other instances, however, permission must be obtained from the author.


Aditi Chandrasekar

DECLARATION

I, hereby declare that the investigation presented in the thesis has been carried out by me. The work is original and has not been submitted earlier as a whole or in part for a degree / diploma at this or any other Institution / University.


Aditi Chandrasekar

LIST OF PUBLICATIONS ARISING FROM THE THESIS

Publications in international journals

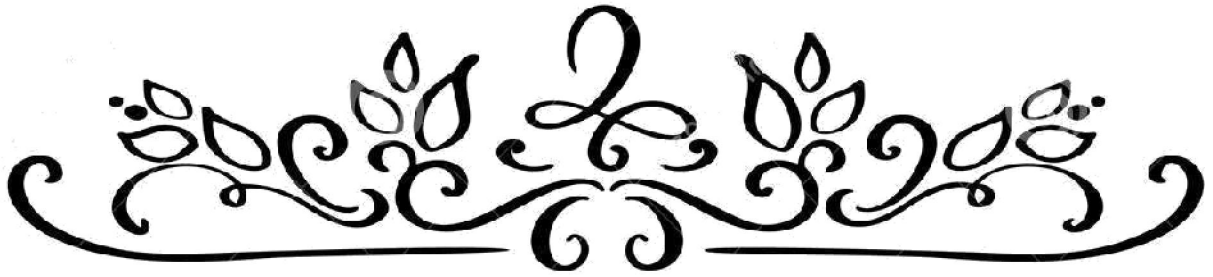
1. **Aditi Chandrasekar**, A. Suresh and N. Sivaraman. Third Phase Formation in the Extraction of Th (NO₃)₄ by Tri-sec-butyl phosphate: a Comparison with Tri-n-butyl phosphate. *Radiochim. Acta* 2017; **105** (4), 321–328.
2. **Aditi Chandrasekar**, A. Suresh, V. K. Aswal and N. Sivaraman. Trends in Small Angle Neutron Scattering of Actinide–trialkyl Phosphate Complexes: a Molecular Insight into Third Phase Formation. *RSC Advances*, 2016, **6** (95), 92905-92916.
3. **Aditi Chandrasekar**, C.V.S. Brahmmananda Rao, Mahesh Sundararajan, Tapan K. Ghanty, and N. Sivaraman. Remarkable Structural Effects on the Complexation of Actinides with H-phosphonates: A Combined Experimental and Quantum Chemical Study. *Dalton Trans.* 2018, **47**, 3841–3850.
4. **Aditi Chandrasekar**, A. Suresh, Meenakshi Joshi, Mahesh Sundararajan, Tapan K. Ghanty, and N. Sivaraman. Highly Selective Separations of U(VI) from a Th(IV) Matrix by Branched Butyl Phosphates: Insights from Solvent Extraction, Chromatography and Quantum Chemical Calculations. *Separation and Purification Technology* 2019, **210**, 182-194
5. **Aditi Chandrasekar**, C.V.S. Brahmmananda Rao, Mahesh Sundararajan, Tapan K. Ghanty, N. Sivaraman. Structure Modulated Complexation of Actinides with Phosphonates: A Combined Experimental and Quantum Chemical Investigation. *Chemistry Select*, 2018, **3**(40), 11309-11315.
6. **Aditi Chandrasekar**, N. Sivaraman, Tapan K. Ghanty and A. Suresh. Experimental evidence and quantum chemical insights into extraction and third phase aggregation trends in Ce(IV) organophosphates. *Separation and Purification Technology*, 2019, **217**, 62-70.
7. **Aditi Chandrasekar** and Tapan K. Ghanty. Uncovering Heavy Actinide Covalency: Implications for Minor Actinide Partitioning. *Inorganic Chemistry*, **58**(6), 3744–3753.
8. **Aditi Chandrasekar**, Tapan K. Ghanty, C.V.S. Brahmmananda Rao, Mahesh Sundararajan, and N. Sivaraman. Strong Influence of Weak Hydrogen Bonding on Actinide-Phosphonate Complexation: Accurate Predictions from DFT Followed by Experimental Validation. *Physical Chemistry Chemical Physics*, 2019,**21**, 5566-5577.

Conferences/Symposia

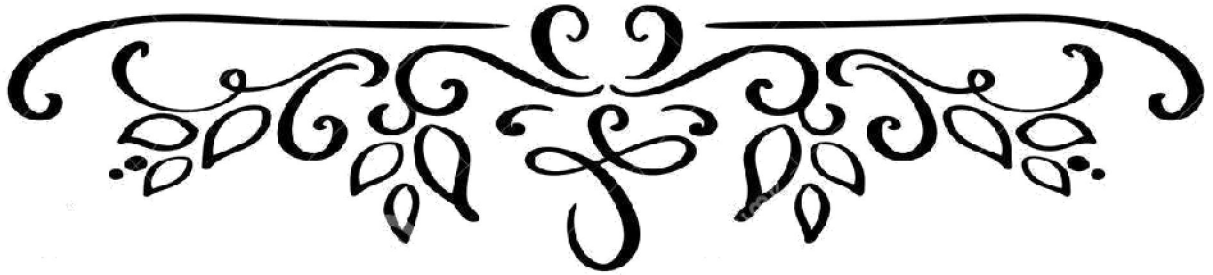
1. **Aditi Chandrasekar**, A. Suresh, N. Sivaraman and V.K Aswal. Small Angle Neutron Scattering of Tri-n-butyl Phosphate and its Isomers loaded with Thorium Nitrate. Proc. of Emerging Trends in Separation Science and Technology (SESTEC-2016), IIT-Guwahati, India, May 17-20 2016. P.207.
2. **Aditi Chandrasekar**, A. Suresh and N. Sivaraman. Third Phase Formation in the extraction of $\text{Th}(\text{NO}_3)_4$ by Tri-n-butyl Phosphate and Tri-sec-butyl Phosphate. Proc. of Emerging Trends in Separation Science and Technology (SESTEC-2016), IIT-Guwahati, India, May 17-20 2016. P.208.
3. A. Suresh, **Aditi Chandrasekar**, N. Sivaraman, M. Joseph and V.K. Aswal. Effects of Temperature on Small Angle Neutron Scattering of Trialkyl Phosphates loaded with Thorium Nitrate Proc. of Emerging Trends in Separation Science and Technology (SESTEC-2016), IIT-Guwahati, India, May 17-20 2016. P.209.
4. **Aditi Chandrasekar**, C.V.S. Brahmmananda Rao and N. Sivaraman. Extraction Studies of Actinides by Dibutyl H phosphonate and its Branched Derivatives. Proc. of Nuclear and Radiochemistry Symposium (NUCAR-2017), KIIT University, Bhubaneswar, India, 6-10th February, 2017. P.258.
5. **Aditi Chandrasekar**, G. Gopakumar, C.V.S B. Rao, P. Velavendan and N. Sivaraman. DFT Studies on Third Phase Formation in 1.1M butyl H Phosphonates in Dodecane during Extraction of Nitric Acid. Proc. of Nuclear and Radiochemistry Symposium (NUCAR-2017), KIIT University, Bhubaneswar, India, 6-10th February, 2017. P.260
6. **Aditi Chandrasekar**, C.V.S. Brahmmananda Rao and N. Sivaraman. Extraction of Actinides by Amyl H Phosphonates, Proc. of Emerging Trends in Separation Science and Technology (SESTEC-2018), BITS-Goa, India, May 23-26, 2018. P. 67
7. **Aditi Chandrasekar**, A. Suresh and N. Sivaraman. Chromatographic Separations of U(VI) from Th(IV). Proc. of Emerging Trends in Separation Science and Technology (SESTEC-2018), BITS-Goa, India, May 23-26, 2018. P.148.
8. **Aditi Chandrasekar** and Tapan K. Ghanty. Increased Covalent Interactions in Heavy Actinides. Proc. of Emerging Trends in Separation Science and Technology (SESTEC-2018), BITS-Goa, India, May 23-26, 2018. P.174
9. **Aditi Chandrasekar**, A. Suresh and N.Sivaraman. Third Phase Formation in the Extraction of Ce(IV) by tri-n-butyl phosphate and tri-sec-butyl phosphate from nitric acid media. Proc. of Nuclear and Radiochemistry Symposium (NUCAR-2019), BARC, Mumbai, India, 15-19th January, 2019. P.57

Additional publications (journal and conference)

1. Meenakshi Joshi, **Aditi Chandrasekar** and Tapan K. Ghanty. Theoretical investigation of $M@Pb_{122}$ - and $M@Sn_{122}$ - Zintl clusters ($M = Ln^{n+}$, Lun^{+} , La^{3+} , Ac^{3+} and $n = 0, 1, 2, 3$). *Phys. Chem. Chem. Phys.*, 2018, 20, 15253.
2. Meenakshi Joshi, Ayan Ghosh, **Aditi Chandrasekar** and Tapan K. Ghanty Counter-Intuitive Stability in Actinide Encapsulated Metalloid Clusters with Broken Aromaticity. *J. Phys. Chem. C*. 2018, 122, 22469.
3. N. Ramanathan, Shubhra Sarkar, K.Sundararajan, **Aditi Chandrasekar**, K. Sankaran. Influence of Branching on the Conformational Space: A Case Study of Tri-secondary-Butyl Phosphate using Matrix Isolation Infrared Spectroscopy and DFT Computations. *J. Phys. Chem. A*, 2018, 122, 8229.
4. Ayan Ghosh, **Aditi Chandrasekar**, Meenakshi Joshi and Tapan K. Ghanty. Van der Waals Complexes of Noble Gas Atom with Coinage Metal Clusters: Effect of Relativistic Interaction. Proc. of the Trombay Symposium on Radiation and Photochemistry (TSRP-2018), BARC, Mumbai, India, Jan 3-7, 2018. P.64
5. Meenakshi Joshi, **Aditi Chandrasekar** and Tapan K. Ghanty. Fluorescent Characteristics of Th and Ce Complexes from the Ground State Electronic Structures. Proc. of Emerging Trends in Separation Science and Technology (SESTEC-2018), BITS-Goa, India, May 23-26, 2018. P. 178



Dedicated to my parents
Nalini Venkatesh Bhat and Chandrasekar
Krishnamurthy



ACKNOWLEDGEMENTS

With deepest gratitude and respect, foremost I acknowledge my parents **Ms. Nalini V. Bhat** and **Mr. K. Chandrasekar** who held my hand when I took my very first step and every other since. My father is the embodiment of my strength and my mother, the embodiment of selfless love. Those priceless hands I will continue to hold for the remainder of my life.

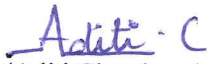
I thank my energetic and experienced guide **Dr. N. Sivaraman** for willingly sharing his knowledge, providing directions to my research and most of all for allowing me freedom to think, express and do almost as I please with respect to our academic study together. His patience and tenacity for radio-active work inspired me. His fantastic ability to revise manuscripts has played an important part in our projects. The times I spent with him working together, executing Swacch Bharath cleaning mission in our lab, in casual arguments on random topics, laughing with him at his jokes/anecdotes and listening to his mock interviews to “permanent” staff has made this learning experience pleasantly memorable.

I am grateful to **Dr. Tapan K. Ghanty**, an Outstanding Scientist from BARC, Mumbai for his crucial help to carry out the computational studies; a significant part of this work. He constantly encouraged me with his positive approach to research, writing and critical reading of our papers. He stood by me through the morally toughest and an ethically disappointing patch in my tenure. Through his support and care the darkness passed, making way for new light on my research spirits and on this study of actinide complexes. This work has marvellously benefited from his contributions and dedicated time that he spent teaching me computational chemistry over BARC-IGCAR telephone calls. The thesis in this form is evidence that we didn't give up.

I thank my co-authors, **Dr. A. Suresh**, **Dr. Brahmananda Rao** and **Dr. S. Mahesh** for the discussions on our work, **Dr. Vinod K. Aswal** for SANS beam-time at Dhruva reactor, BARC, and also for his valuable inputs during the interpretation of neutron scattering profiles. My colleagues **Ms. Jayalakshmi**, **Mr. Amarendran**, **Ms. Ganga**, **Ms. Navamani**, **Dr. Sreenivasulu** and **Dr. Pitchiah** have made our lab atmosphere co-operative and filled with humour. I thank them for making this PhD a harmonious experience with a lot of laughter. I thank **Dr. P.A. Sreeram** and Computer Division, IGCAR for their timely and vital help in facilitating my computational work on the clusters.

I am immensely grateful to my school teachers **Dr. Kamala Mukunda**, **Dr. K. Srinivasan**, **Dr. Yasmin Jaithirtha**, and **Dr. Richard Fernandes** for providing me a concrete foundation in Science and Mathematics and more so for their belief in my potential. I thank **Dr. H.S. Nagaraja** for persuading and then training me to clear IIT-JEE which gave me access to education and research at IISER. I thank **Prof. T. Pradeep** at IIT-Madras through whom I had my very first and unforgettable research exposure and learnt how much the “little things” mattered. He conveys the value of perfection; long, productive, working hours and sustained dedication by being an example himself.

I thank my many jovial and considerate friends at IGCAR for all the fun and frolic that made this whole experience complete.


(Aditi Chandrasekar)

CONTENTS

SL. NO.	TITLE	PAGE NO.
i	Abstract of Thesis	I
ii	Synopsis	III
iii	List of Tables	XIII
iv	List of Figures	XVII
v	List of Abbreviations	XXIII

CHAPTER 1 INTRODUCTION

1.1	Energy for sustenance	1
1.2	Renewable and non-renewable sources of energy	1
1.3	Nuclear power	3
1.4	Solvent extraction—A separation technique for the recovery and purification of metals	6
1.5	Neutrons to predict third phase formation	10
1.6	Density functional theory for actinide complexes	14
1.7	Scope of the present work	19

CHAPTER 2 EXPERIMENTAL

2.1	Materials	27
2.2	Instruments	29
2.3	Experimental methods	29
2.4	Synthesis and characterisation of H-phosphonates	31
2.5	Synthesis and characterisation of dialkylalkyl phosphonates	42
2.6	Measurement of physicochemical properties	52
2.7	Extraction of metal ions	54
2.8	Analytical procedures	56
2.9	Computational methodology	58

CHAPTER 3

EXTRACTION OF THE TETRAVALENT METAL IONS Th(IV) AND Ce(IV): THIRD PHASE FORMATION AND QUANTUM CHEMICAL STUDIES

3.1	Introduction	61
3.2	Extraction of Th(IV) with TBP, TiBP and TsBP	62
3.3	Measurement of extractant concentration in third phase and diluent-rich phase	67
3.4	Extraction of Ce(IV) by TBP and TsBP as a function of aqueous Ce(IV)	70
3.5	Extraction of Ce(IV) by TBP and TsBP as a function of nitric acid	72
3.6	Computational results on Ce(IV) complexes and dimers	74
3.7	Conclusion	84

CHAPTER 4

TRENDS IN SMALL ANGLE NEUTRON SCATTERING OF ACTINIDE-TRIALKYL PHOSPHATE COMPLEXES: A MOLECULAR INSIGHT INTO THIRD PHASE FORMATION

4.1	Introduction	87
4.2	SANS Measurement	88
4.3	Study on metal free HNO ₃ systems	89
4.4	Aggregation behaviour of Th(NO ₃) ₄ systems	90
4.5	Investigations on UO ₂ (NO ₃) ₂ systems	96
4.6	Comparing U(VI) and Th(IV) SANS	100
4.7	Predictions on third phase formation	102
4.8	Conclusion	103

CHAPTER 5

SELECTIVE SEPARATIONS OF U(VI) FROM A Th(IV) MATRIX BY BRANCHED BUTYL PHOSPHATES: INSIGHTS FROM SOLVENT EXTRACTION, CHROMATOGRAPHY AND QUANTUM CHEMICAL CALCULATIONS

5.1	Introduction	105
5.2	Solvent extraction studies on the separation of U(VI) from Th(IV)- Extraction and stripping	106
5.3	Electronic structure calculations on U(VI) and Th(IV) complexes	111
5.4	Demonstration U/Th separation by coated polymer columns	115
5.5	Conclusion	125

CHAPTER 6

STRUCTURAL EFFECTS ON THE COMPLEXATION OF ACTINIDES WITH BRANCHED PHOSPHONATES: A COMBINED EXPERIMENTAL AND QUANTUM CHEMICAL STUDY

(A) H-PHOSPHONATES

6A.1	Introduction	127
6A.2	Physico-chemical properties of butyl H-phosphonates	128
6A.3	Extraction of U(VI)	130
6A.4	Explorations into the acid-dependent mechanism of extraction	132
6A.5	Extraction of Am(III)	137
6A.6	Theoretical predictions	138
6A.7	Conclusion	144

(B) DIALKYLALKYL PHOSPHONATES

6B.1	Introduction	147
6B.2	Physico-chemical properties of dialkyl alkyl phosphonates	148
6B.3	Extraction of U(VI), Th(IV), Pu(IV) and Am(III)	150
6B.4	Computational results	154
6B.5	Conclusion	158

CHAPTER 7

DENSITY FUNCTIONAL THEORY AS A PREDICTIVE TOOL IN ACTINIDE CHEMISTRY

(A) THE INFLUENCE OF WEAK HYDROGEN BONDING ON THE EXTRACTION BEHAVIOUR OF H-PHOSPHONATES TOWARDS ACTINIDES

7A.1	Introduction	161
7A.2	Theoretical insights and predictions	162
7A.3	Physico-chemical properties of amyl H-phosphonates	168
7A.4	Extraction of uranyl nitrate from nitric acid medium	169
7A.5	Extraction of Th(IV) and Pu(IV) from nitric acid medium	172
7A.6	Extraction of Am(III) and theoretical studies	176
7A.7	Keto-enol tautomerisation of amyl H-phosphonates	178
7A.8	Conclusion	181

(B) COMPLEXATION BEHAVIOUR OF TRANSPLUTONIUM ACTINIDES

7B.1	Introduction	183
7B.2	Heavy actinide complexes with cyanex ligands	183
7B.3	Heavy actinide complexes with DPA ligand	185
7B.4	Heavy actinide complexes with TPAEN ligand	188
7B.5	Analysis of energy levels	193
7B.6	Conclusion	194

CHAPTER 8

SUMMARY AND CONCLUSION

8.1	Conclusions	197
8.2	Future directions	200

REFERENCES

ABSTRACT OF THESIS

The quest for actinide specific extractants has been a long and difficult one. However, research on extraction and separation of actinides finds immediate and vital application in the processing of spent nuclear fuels which involves the separation of U and Pu from a large number of fission products, which are produced during nuclear fission. Solvent extraction is one of the most important methods used for reprocessing of spent fuels as well as in the extraction of U and Th from ores. In order to separate fuel material from other elements either in irradiated fuel or from their ores, a ligand with high selectivity towards U, Th and Pu is required. Currently, Tri-n-butyl phosphate (TBP) is being used for this purpose. There are limitations associated with TBP, warranting a search for alternate extractants which eliminate the disadvantages of TBP while retaining its advantageous properties. The experimental work done in this thesis predominantly pertains to the examination of alternate organophosphorous extractants and their application in solvent extraction and extraction chromatography for actinide extraction. Though the alternatives are not intended to replace TBP for spent fuel reprocessing, the new extractants are synthesised and their solvent extraction behaviour with actinides are explored to employ them as potential candidates for various other applications in nuclear fuel cycle, e.g. U/Th separation. The difference in extraction and specific binding for different metal–extractant systems may be correlated to the theoretical binding energetics; the role of complexation energy and its influence on the extraction efficacy and specificity cannot be underestimated. Therefore, apart from experiments, density functional theory (DFT) studies of actinides complexes using these novel extractants have also been carried out.

The complexation behaviour and third phase formation in the extraction of Th(IV) and Ce(IV) by branched organophosphates have been studied. Ce(IV) has been employed as a surrogate for Pu(IV), which is an important fuel material. The work effectively elaborates both experimentally as well quantum chemically, the effects of structural isomerism on the complexation of both tetravalent and trivalent cerium. For the first time, the drastic effect of solely changing the oxidation state on the metal extraction energetics is clearly derived from the calculations and corroborates well with experimental findings. Further, aggregation tendencies are rightly predicted by careful interpretation of single-molecule parameters. This study though pertaining to one kind of metal-ligand system, in its essence emphasises a consensus between theory and experiments, forming a basis for theoretically predicting properties of many atom complexes.

Historically, third phase has been studied after its formation; however, it has not been predicted before its onset. Small angle neutron scattering (SANS) has been used as a probe to study the organic phase prior to third phase formation in Th(IV) and U(IV) systems. The effect of changing the extractant, temperature and metal concentration have been extensively investigated and the attraction potential energy has been obtained by fitting the SANS profiles. For the first time, the third phase has been predicted before its onset and moreover, numbers have been assigned to third phase thresholds which have never been envisaged in the literature earlier.

Apart from third phase formation, studies on the separation of U(VI) from a Th(IV) matrix have been carried out using solvent extraction as well as extraction chromatographic technique. This study has been carried out in the light of processing both naturally occurring thorium ore as well as for the processing of the thorium blanket in the fast reactor in which ^{232}Th is transmuted to the

fissile ^{233}U . In both these cases the U:Th ratio is typically in the order 1:800. For the first time it has been demonstrated that U(VI) can be separated from Th(IV) in U/Th ratios as high as 1:10000 using a branched organophosphate, namely, Tri-sec-butyl phosphate (TsBP). Further, quantum chemical calculations of the binding energy and ligand deformation energy showed the preferential binding of TsBP over the conventional TBP extractant.

Among the organophosphorous compounds, phosphonates have shown greater promise than phosphates towards actinide extraction. In addition to the phosphate extractants, both H-phosphonates and dialkyl alkyl phosphonates have been examined in actinide extraction *viz.* U, Th, Am and Pu. It is also possible to tailor the carbon chain structure in phosphonate ligands. For the first time, structural effects of carbon chain length and branching have been systematically investigated. ESI-MS of this class of complexes has been obtained for the first time. The study on phosphonate demonstrates the variation in metal complexation behaviour and its sensitivity to extractant structure. Changes in the extractant structure as far as five or six atoms away from the complexing site affect complexation affinities significantly. The implication of structural changes on the behaviour of ligands towards metal ions remains a valid question to this day and our results provide avenues for fine tuning metal specific complexation in the microgram regime.

Apart from experiments, DFT calculations elucidate the binding energetics as well as the pH dependent keto-enol tautomeric extractions that occur in H-phosphonates. For the first time, DFT predicts the preferential stabilisation of a U(VI)-phosphonate complex stabilised by weak hydrogen binding. This stabilisation leading to anomalous extraction behaviour has been verified by experiments. DFT studies also examined the increased covalency in heavy actinide complexes (Am, Cm, Bk and Cf). For the first time, the metal-ligand bond, has been explicitly decomposed into electrostatic, Pauli and orbital interaction components and showed a counter-intuitive increase in covalency along the actinide period. These study opens-up windows through which the predictive powers of DFT can be applied in the realm of actinide-organophosphorous complexes as well as towards screening ligands for minor actinide partitioning. These complexes are of immediate interest in the processing of nuclear fuels where a plethora of extractants are still screened by involved experimental procedures posing radioactive hazards. The ideas presented in this work can potentially be extended, thereby weaving a predictive future for actinide specific extractions and separations.



Homi Bhabha National Institute

SYNOPSIS OF Ph. D. THESIS

Chapter 1: Introduction

The quest for actinide specific extractants has been a long and difficult one. Particularly among these, discovering new extractants that bind specifically to certain actinide elements over others is an even greater challenge due to the chemical similarity of actinides¹. However, research on both these aspects finds immediate and vital application in the processing of spent nuclear fuels which involves the separation of U and Pu from a large number of fission and activation products produced during nuclear fission². Solvent extraction is one of the most important methods used for reprocessing of nuclear fuels as well as in the extraction of U and Th from ores. In order to separate fuel material from other elements either in irradiated fuel or from their ores, a ligand with high selectivity towards U, Th and Pu is required. Currently, Tri-n-butyl phosphate (TBP) is being used for this purpose and has stood the test of time for the past 60 years³. However, there are some limitations associated with TBP which pose problems during the reprocessing of fast reactor fuels. Hence there is a need to find alternate extractants which eliminate the disadvantages of TBP while retaining its advantageous properties^{4, 5}. The experimental work done in this thesis predominantly pertains to the examination of alternate organophosphorous extractants and their application in solvent extraction and extraction chromatography for actinide extraction. Though the alternatives are not intended to replace TBP for spent fuel reprocessing, the new extractants are synthesised and their solvent extraction behaviour with actinides are explored to employ them as potential candidates for various other applications in nuclear fuel cycle, e.g. U/Th separation. The difference in extraction and specific binding for different metal–extractant systems may be correlated to the theoretical binding energetics; the role of complexation energy and its influence on the extraction efficacy and specificity cannot be underestimated^{6, 7}. Therefore, apart from experiments, density functional theory (DFT) studies of actinides

complexes using these novel extractants have also been carried out. Geometries of extractant-actinide complexes have been optimized using electronic structure calculations. Theoretical binding energies of complex formation have been computed. The significant influences of electronic structure of the extractants on the tautomeric mechanisms, deformation energies, intramolecular interactions and complexation trends have been elucidated using the quantum chemical calculations. The power of prediction, however challenging, is one of the greatest merits of DFT⁸. In the final chapter, the essence of this predictive element has been brought out to understand actinide-extractant complexes in their extraction and separations.

Chapter 2: Experimental

Experimental procedures used in the entire thesis work will be elaborated. This includes the preparation of stock solutions, indicators etc. Methods used for the estimation of various actinide ions by techniques such as radiometry is explained. Instruments and reagents used are specified.

Chapter 3: Extraction of tetravalent metal ions Th(IV) and Ce(IV): Third phase formation and quantum chemical studies

“Third phase” formation is an aggregation phenomenon that arises due to the mutual attraction of the polar cores of reverse micelles in a non-polar medium. A major concern that can potentially arise during solvent extraction of actinides e.g. Pu(IV) is third phase formation at the aqueous-organic interface. This phenomenon takes place when the metal loaded in the organic phase exceeds a threshold known as the limiting organic concentration (LOC) beyond which the organic phase splits into a metal-extractant rich third phase and a metal poor diluent rich phase, leading to difficulties in metal ion extraction. Earlier studies carried out in our laboratory indicated that tri-sec-butyl phosphate (TsBP) is a potential extractant for U/Th separation. The extraction and third phase formation behaviour of 1.1 M solutions of tri-iso-butyl phosphate (TiBP) and TsBP in *n*-dodecane in the extraction of Th(IV) from 1M HNO₃ at 303 K over a wide range of Th concentrations were investigated and the results are compared with the literature data on TBP system. Concentrations of Th(IV) and HNO₃ loaded in the organic phase before third phase formation (biphasic region) as well as in third phase and diluent-rich phase after third phase formation (triphasic region) were measured as a function of equilibrium aqueous phase Th(IV) concentration. The density of loaded organic phase was also measured at various Th(IV)

concentrations. The extraction profiles in the biphasic region indicated that extraction of Th(IV) by TBP is higher than that of TiBP which in turn is higher than that of TsBP. Extractant concentration in the diluent-rich phase and third phase was measured for the triphasic region.

This study revealed that TsBP has higher third phase formation limits compared to TBP in the extraction of tetravalent thorium from nitric acid media. Furthermore, the data on Pu(IV) third phase formation is crucial for designing solvent extraction processes. In this light, in a preliminary study on the third phase behaviour of Ce(IV), which is a chemical analogue of Pu(IV) has been carried out in the present work⁹. The aqueous Ce(IV) concentration was varied over a wide range (1–280 mg/mL) and the Ce(IV) extracted into the organic phase was measured both before LOC as well as beyond LOC in the third and diluent-rich phases after the phase splitting. The acid extracted into the organic phase and densities of organic phases were also estimated. Apart from experimental studies, quantum chemical calculations using density functional theory were also carried out. Energetics of complex formation for these extraction systems with Ce(IV) as well as the Ce(III)-TBP system have been obtained. Apart from complexation energies, third phase formation tendencies have been predicted by DFT for the Ce(IV) systems. All the computational results were in good match with the experimental observations.

Chapter 4: Trends in Small Angle Neutron Scattering of Actinide–Trialkyl Phosphate

Complexes: A Molecular Insight into Third phase formation

Third phase formation has been studied after its occurrence; however, it has not been anticipated before its onset. As Small Angle Neutron Scattering (SANS) is a powerful tool to probe colloidal particles, it is considered as an important technique to study the aggregation behaviour of actinide complexes in solvent extraction systems¹⁰. The structurally different trialkyl phosphate (TalP) based extractants, namely, tri-*n*-butyl phosphate (TBP), tri-*iso*-butyl phosphate (TiBP) and tri-*sec*-butyl phosphate (TsBP) have been examined for the first time using SANS technique to investigate third phase formation phenomena with some of the actinides. A higher homologue tri-*sec*-amyl phosphate (TsAP) has also been considered. SANS was employed to get insights into third phase formation behaviour in the extraction of Th(IV) and U(VI) from 1M HNO₃ by 1.1M solutions of TalP in deuterated dodecane (*n*-C₁₂D₂₆, 98 atom %D). Deuterated diluent was used in order to provide contrast during the neutron scattering measurements. The stickiness

parameter (τ^{-1}), a measure of the attractive interaction between the micelles as well as attractive potential energy (U_0) has been quantified as a function of metal in the organic phase. The data are fitted using Baxter's sticky-sphere model. A clear correlation has been established between the stickiness parameter and the tendency for third phase formation with TalP systems. As U(VI) does not form third phase with these extractants at 1M HNO₃, comparative studies were carried out with U(VI) – TalP complexes. These studies established lower stickiness and attraction between the micelles with U(VI) system. The correlation between SANS parameters and third phase formation tendency was extended to a temperature dependent study and these studies established higher third phase limits when temperature was enhanced, corroborating well with our experimental results. This study is the first of its kind to “quantitatively predict third phase” before its formation for a range of actinide – extractant systems.

Chapter 5: Selective Separations of U(VI) from a Th(IV) Matrix by Branched Butyl Phosphates: Insights from Solvent Extraction, Chromatography and Quantum Chemical Calculations

Apart from the extraction of an individual actinide and the associated phenomena such as third phase formation, the separation of actinides is a daunting task due to their similar chemical behaviour. Among these, the separation of uranium from a thorium matrix is one of the persisting challenges, which finds application in the processing of thorium ores as well as of thorium irradiated in a nuclear reactor, where some fertile ²³²Th is transmuted to the fissile ²³³U. U/Th separation has been conventionally achieved by solvent extraction using tri-n-butyl phosphate (TBP). In this work, a significantly better separation factor has been observed using tri-sec-butyl phosphate (TsBP) with a high selectivity for U(VI) over Th(IV) due to its combined structural and electronic effects close to the binding site. Systematic and comprehensive studies at both liquid-liquid as well as solid-liquid interfaces have been carried out under a wide range of experimental conditions. The balance between specificity towards U(VI) and process throughput as a function of ligand concentration has been examined at the liquid interface. In addition, TBP and TsBP were impregnated on to a polymer support and the separation of U(VI) from Th(IV) feed solutions with various U/Th ratios has been achieved using extraction chromatography. Strategically optimized conditions of loading and elution stages for varying U/Th feed ratio were found and employed to demonstrate the feasibility of a specific ligand coated column for the tail-

end purification of aqueous product containing U(VI) and Th(IV). Additionally, electronic structure calculations using density functional theory (DFT) were carried out to shed light on the energetics and specificity of complexation for U(VI) over Th(IV) with TsBP and compared with equivalent complexes with TBP. Theoretically calculated, solvent corrected complexation energies for the formation of U(VI) and Th(IV) complexes with TBP and TsBP were in good agreement with the experimental observations. These studies have established that uranium can be effectively separated from a thorium matrix (1:10000).

Chapter 6: Structural Effects on the Complexation of Actinides with Branched Phosphonates: A Combined Experimental and Quantum Chemical Study

(A) H-Phosphonates

The basicity of the phosphoryl group is enhanced when the C-O-P group is replaced by a C-P group¹¹. Neutral organophosphorus extractants show the variation in the basicity of the phosphoryl oxygen as follows: phosphine oxides > phosphinates > phosphonates > phosphates. Phosphonates, being more basic, prove to be stronger extractants than the corresponding phosphates. Phosphonates have shown promising specificity and extractability towards actinide elements^{12, 13}. Structural effects of the carbon chain in the extraction of actinides by organophosphorous extractants have been examined experimentally and by computation. Branched butyl H-phosphonates and their linear chain isomer, *n*-butyl H-phosphonate (DBHP), were synthesised and characterised using IR, NMR and GC-MS techniques. Their physical properties *viz.* viscosity, density and aqueous solubility have been determined. DBHP, Di-*iso*-butyl H phosphonate (DiBHP) and Di-*sec*-butyl H phosphonate (DsBHP) were employed for the extraction of U(VI) and Am(III) ions from nitric acid. ²³³U (-tracer) and ²⁴¹Am (-tracer) were employed as representative isotopes for the extraction of U and Am, respectively, and their distribution ratio (D) was measured as a function of nitric acid concentration (0.01–8M). Branching of the alkyl chain at the secondary carbon atom showed unexpected neutral extractant behaviour for DsBHP which is generally classified as an acidic extractant. The acid-dependent dual extraction mechanisms for the H-phosphonates have been examined both experimentally and through quantum chemical calculations. This dramatic effect can be partly attributed to the hindrance in the formation of the *enol* tautomer through the strengthening of the P=O---H hydrogen bonding in the DsBHP extractant. Density functional theory (DFT) based calculations

were carried out to understand the complexation behaviour of actinides with the extractants DBHP and DsBHP. Possible structures and binding affinities of actinides with H-phosphonates have been deduced from electronic structure calculations. Finally, the trends in distribution ratios were additionally explored and correlated with experimental observations for both U(VI) and Am(III).

(B) Dialkylalkyl phosphonates

The H-phosphonates were then strategically coupled with alkyl chains to form dialkylalkyl phosphonates with varying branching and carbon chain length. Among all the organophosphorous compounds, phosphonates have the dual advantage of simplicity in preparation coupled with the flexibility to tailor-make their carbon chain structure. Symmetrical Diisobutylisobutyl, Diisoamylisoamyl and unsymmetrical Diisoamylhexyl and Diisoamylbutyl branched phosphonates were synthesised and characterised by NMR and GC-MS. These ligands were used to bind Th(IV), U(VI), Pu(IV) and Am(III) at the liquid-liquid interface. The extractants were examined for their physicochemical properties such as density, viscosity, aqueous solubility and dielectric constant, which are significantly affected by changes in the alkyl chain structure. A combination of physico-chemical parameters, as well as the structure modulated chemical nature of the extractants, cause variations in the distribution ratio towards metal ions. These effects have been probed in detail using Th(IV), U(VI), Pu(IV) and Am(III) extractions and found to correlate with the carbon chain length of the organic groups on the phosphoryl centre. Further, density functional theory was employed to understand the electronic structure of the extractants and their metal complexes with U(VI) and Th(IV). The computed complexation energies in the formation of metal-ligand complexes compared well with the trends observed in the experiments. Both experiment and quantum chemistry emphasizes the importance of the carbon chain structure on the actinide binding ability of phosphonate ligands.

Chapter 7: Density functional theory as a predictive tool in actinide chemistry

(A) The influence of weak hydrogen bonding on the extraction behaviour of H-phosphonates towards actinides

Among the varied classes of weak hydrogen bond, the $\text{CH}\cdots\text{O}$ type is one of immense interest as it governs the finer structure of biological and chemical molecules, hence determining their functionality¹⁴. In the present work, this particular weak hydrogen bond has been shown to influence the complexation behaviour of uranyl nitrate $[\text{UO}_2(\text{NO}_3)_2]$ with Diamyl H-phosphonate (DAHP) and Disecamyl H-phosphonate (DsAHP) strongly. The structures of the bare ligands and complexes have been optimised in the framework of DFT. Surprisingly, despite having the same chemical composition, the $\text{UO}_2(\text{NO}_3)_2\cdot 2\text{DsAHP}$ complex shows a remarkable stability ($\sim 14\text{kcal/mol}$) compared to the $\text{UO}_2(\text{NO}_3)_2\cdot 2\text{DAHP}$ complex. Keener observation of the optimized structures attributes this stability to weak hydrogen bonding interactions between the nitrate oxygens and the -H -hydrogens in the alkyl chains of the complexing ligands. The binding free energies associated with the formation of these complexes are tested by carrying out extraction of U(VI) from nitric acid media using these ligands. It was discovered that indeed the DsAHP complexation is more favoured and the ligand DsAHP shows higher extraction towards U(VI). H-phosphonates are generically classified as acidic extractants owing to the formation of an enol tautomer at lower acidities, and hence complexes the metal ion by proton exchange. Our experiments interestingly reveal an unexpected neutral extractant characteristic for DsAHP. Furthermore, the keto-enol tautomerisation of H-phosphonates that govern their extraction profiles at lower acidities is also explored by DFT and the anomalous extraction behaviour of DsAHP could be successfully explained.

(B) Complexation behaviour of transplutonium actinides

It is desirable to remove the minor actinides from the high level nuclear waste as this will greatly reduce the amount of time the bulk of the waste is stored. Across the actinide period, the stability of the trivalent oxidation state predominates in the heavy actinides, making their chemical nature close to that of rare earth elements. The resemblance in their chemistry poses difficulties in separating heavy actinides from lanthanides, which is a vital separation in the minor actinide partitioning process. Actinide contraction has conventionally implied electrostatic actinide-ligand interactions among the heavy actinides. The present study challenges this conventional

understanding and reveals increasing covalency in the actinide-ligand bond across Am to Cf. Complexes of Am, Cm, Bk and Cf have been examined for their electronic structure with focus on the nature of their interactions with different minor actinide specific ligands. The choice of ligands selected for this study facilitates the effect of donor atom as well as denticity to be accounted for. Hence, heavy actinide complexes of the N and O-donor ligand dipicolinic acid, S and O mixed donor ligands of the cyanex type and an octadentate ligand N,N,N',N'-tetrakis[(6-carboxypyridin-2-yl)methyl]ethylenediamine have been optimised and evaluated. In each case the metal-ligand interaction energy has been explicitly decomposed into components which have then been analysed. Irrespective of the hard-soft characteristics of donor atoms or the denticity of the ligands, steadily increased covalency has been observed across Am to Cf. Inspection of the ligand HOMOs and metal orbitals shed light on the origin of the unexpected covalency.

Chapter 8: Conclusions

This work elucidates the effect of the complexing ligands' structure on the separation of elements which are very similar in their chemical behaviour. The separation of the f-block elements has been a constant challenge due to their closely related chemistry. The work presented in this study achieved this by controlled parameters implemented at both liquid-liquid as well as solid-liquid interfaces and elucidated the importance of geometrical structures and the energetics through DFT. This work naturally widens arenas towards different extractants which can be tailor-made in a single step reaction, resulting in ligands with a desired level of selectivity. This thesis is a classic example of the correlation between "structure and binding", a deeply investigated concept in the important field of separation science.

In its finale, the study carried out here opens exciting windows through which the predictive powers of DFT can be applied in the realm of actinide-organophosphorous complexes. These complexes especially are of immediate interest in the processing of nuclear fuels, where a plethora of organophosphorous extractants are still screened by involved experimental procedures posing radioactive hazards. Experimental work in ligand synthesis for the extraction of actinide ions can also be minimised. Though this particular study pertains to uranyl complexes, the ideas presented here can potentially be extended to other actinides, weaving a predictive future for actinide specific extractions and separations.

References

1. P.-W. Huang, C.-Z. Wang, Q.-Y. Wu, J.-H. Lan, G. Song, Z.-F. Chai and W.-Q. Shi, *Dalton Transactions*, 2018, **47**, 5474-5482.
2. A. Suresh, T. G. Srinivasan and P. R. V. Rao, *Solvent Extraction and Ion Exchange*, 1994, **12**, 727-744.
3. W. W. Schulz, Berger, L. L., and Navratil, J. D, *RC Press*, 1990, **3**.
4. K. B. Rakesh, A. Suresh, N. Sivaraman, V. K. Aswal and P. R. V. Rao, *Journal of Radioanalytical and Nuclear Chemistry*, 2016, **309**, 1037–1048.
5. C. V. S. Brahmmananda Rao, Chirag K. Vyas, S. Jayalakshmi, P. M. Joshirao, and V. K. Manchanda, *Radiochim. Acta*, 2015, **103**, 277–285.
6. A. Bhattacharyya, T. K. Ghanty, P. K. Mohapatra and V. K. Manchanda, *Inorganic Chemistry*, 2011, **50**, 3913-3921.
7. D. Manna and T. K. Ghanty, *Physical Chemistry Chemical Physics*, 2012, **14**, 11060-11069.
8. D. Manna, S. Mula, A. Bhattacharyya, S. Chattopadhyay and T. K. Ghanty, *Dalton Transactions*, 2015, **44**, 1332-1340.
9. R. Marsac, F. Real, N. L. Banik, M. Pedrot, O. Pourret and V. Vallet, *Dalton Transactions*, 2017, **46**, 13553-13561.
10. T. A. Wagay, J. Dey, S. Kumar, V. K. Aswal and K. Ismail, *RSC Advances*, 2016, **6**, 66900-66910.
11. L. Burger, *The Journal of Physical Chemistry*, 1958, **62**, 590-593.
12. K. D. Troev, *Chemistry and application of H-phosphonates*, Elsevier, 2006.
13. C. V. S. Brahmmananda Rao, S. Jayalakshmi, S. Subramaniam, N. Sivaraman and P. R. V. Rao, *Radiochimica Acta*, 2015, **103**, 345-358.
14. G. R. Desiraju, *Nature*, 2001, **412**, 397.

LIST OF TABLES

TABLE	TITLE	PAGE
3.1	Extractant concentrations in the diluent-rich phase and third phase obtained by density and nitric acid equilibration methods	68
3.2	Solvent corrected binding free energies (kcal mol ⁻¹) using M06-2X functional and computed structural parameters (Å) of actinide extractant complexes	76
3.3	Hirshfeld charges on phosphorous and phosphoryl oxygen atoms in the bare ligand and after complexation calculated using M06-2X. Charges on the metal centre as well as nitrate oxygen atoms bound to the metal are also shown	76
4.1	Concentration of metal ions/acid in the samples used for SANS experiments	92
4.2	The fitted parameters of SANS data for (a) 1.1 M TalP/n-C ₁₂ D ₂₆ - Th(NO ₃) ₄ /1M HNO ₃ systems, loaded with 30 g/L of Th(IV) at 303K. (b) 20g/L and 40g/L Th(IV) loaded TalP/ n-C ₁₂ D ₂₆ systems at 303K. (c) 1.1 M TalP/n-C ₁₂ D ₂₆ - Th(NO ₃) ₄ /1M HNO ₃ systems, loaded with 40 g Th/L as a function of temperature	98
4.3	The fitted parameters of SANS data for (a) 1.1 M TalP/n-C ₁₂ D ₂₆ -UO ₂ (NO ₃) ₄ /1M HNO ₃ systems at 303K. (b) 1.1M TalP/n-C ₁₂ D ₂₆ -UO ₂ (NO ₃) ₂ /1M HNO ₃ systems loaded with 120 g U/L at 303K. (c) 1.1 M TalP/n-C ₁₂ D ₂₆ /1M HNO ₃ systems with U(VI): 40g/L in TBP and TiBP and 20g/L in TsBP as a function of temperature. (d) 1.1 M TBP and TiBP in C ₁₂ D ₂₆ loaded with 40g/L Th(IV) and U(VI)/1M HNO ₃ at 308K	85
5.1	Extraction of U(VI) and Th(IV) as a function of extractants concentration (M) in dodecane. The aqueous phase contained initially a mixture of 180 µg/mL U(VI) and 160 mg/mL Th(IV) in 3M nitric acid	107
5.2	Extraction of U(VI) and Th(IV) as a function of extractants concentration (M) in dodecane. The aqueous phase contained initially a mixture of 180 µg/mL U(VI) and 160 mg/mL Th(IV) in 5M nitric acid	108
5.3	Recovery of U(VI) from the organic phase 0.11 M (3%) TBP and TsBP solutions in dodecane after extraction from a feed solution containing 180 µg/mL U(VI) and 160 mg/mL Th(IV) in 3M nitric acid. The organic phase was then equilibrated with 3M HNO ₃ followed by two stages of equilibration with 0.01 M HNO ₃	110
5.4	Solvent corrected binding free energies (kcal mol ⁻¹) using M06-2X functional and computed structural parameters (Å) of actinide extractant complexes	112

5.5	Mulliken charges on phosphorous and phosphoryl oxygen atoms in the bare ligand and after complexation calculated using M06-2X. Charges on the metal centre, as well as uranyl and thorium nitrate oxygen atoms bound to the metal are also shown	113
5.6	Deformation energy (kcal mol^{-1}) per ligand for TBP/TsBP ligands in U(VI) and Th(IV) complexes calculated using M06-2X	114
5.7	Summarised results for the separation of U(VI) from Th(IV) from TsBP coated columns. (b) Comparative study for TBP and TsBP column for isolation of U(VI) from 1:10000 U:Th ratio	124
6A.1	Density, viscosity at 31°C , activation energy and aqueous solubility of various H-phosphonates	129
6A.2	The percentage of <i>enol</i> tautomer formed for the three extractants based on titration of NaOH before and after extraction	134
6A.3	IR stretching and shifts: Theoretical and experimental P=O and U=O stretching frequencies in cm^{-1} . Corresponding experimental values are in parenthesis	141
6A.4	Computed binding free energies for uranyl nitrate complexes (kcal mol^{-1})	142
6B.1	Density (g/mL), viscosity (cp) at 304K, activation energy (kJ/mol), aqueous solubility (g/L) and dielectric constant of DiBiBP, DiAiAP, DiAButylP and DiAHexylP	150
6B.2	Structural parameters of actinide extractant complexes calculated using BP86 functional and SVP basis set	156
6B.3	Mulliken charges on phosphorous and phosphoryl oxygen atoms in the bare ligand and after complexation calculated using M06-2X. Charges on the metal centre, as well as uranyl and thorium nitrate oxygen atoms bound to the metal are also shown	156
6B.4	Computed binding affinities (G , kcal mol^{-1}) for uranium and thorium complexes with DiBiBP and DiAHexylP using M06-2X	157
7A.1	Solvent corrected relative energies of the uranyl nitrate complexes with DsAHP and DiAHP with respect to the energy of the $\text{UO}_2(\text{NO}_3)_2 \cdot 2\text{DAHP}$ complex by using different functionals	162
7A.2	Solvent corrected binding free energies (kcal mol^{-1}) using M06-2X functional and computed structural parameters (\AA) of uranyl nitrate complexes with the keto tautomer of DAHP, DsAHP and DiAHP	165
7A.3	Solvent corrected binding free energies (kcal mol^{-1}) using M06-2X and DFT-D3 functionals BP86 and the hybrid PBE0 functional of uranyl nitrate complexes with DAHP and DsAHP.	166
7A.4	CH...O Hydrogen-Bond Distance (R) and the Corresponding Electron density and Laplacian of the Electron Density Values in Uranyl Nitrate Complexes with DAHP and DsAHP	167
7A.5	Density (g/mL), viscosity (cP) at 31°C , activation energy (kJ/mol) and aqueous solubility (g/L) at 298K of the H-phosphonates	168
7A.6	The percentage of <i>enol</i> tautomer formed for DAHP, DiAHP and DsAHP based on titration of NaOH before and after extraction	172

7A.7	Solvent corrected binding free energies (kcal mol^{-1}) using M06-2X functional and computed structural parameters (\AA) of uranyl nitrate complexes with the enol tautomers of DAHP and DsAHP	180
7B.1	Computed structural parameters (\AA) of actinide cyanex complexes using PBE/TZ2P method	184
7B.2	Computed structural parameters (\AA) of actinide-DPA complexes using PBE/TZ2P method	187
7B.3	Computed bond lengths (\AA) of actinide-TPAEN complexes obtained using PBE/TZ2P method	190

LIST OF FIGURES

FIGURE	TITLE	PAGE
2.1	^1H NMR spectrum of Dibutyl H phosphonate (DBHP)	32
2.2	^{31}P NMR spectrum of Dibutyl H phosphonate (DBHP)	32
2.3	^1H NMR spectrum of Diisobutyl H phosphonate (DiBHP)	33
2.4	^{31}P NMR spectrum of Diisobutyl H phosphonate (DiBHP)	33
2.5	^1H NMR spectrum of Disecbutyl H phosphonate (DsBHP)	34
2.6	^{31}P NMR spectrum of Disecbutyl H phosphonate (DsBHP)	34
2.7	GC – MS spectrum for DBHP	36
2.8	GC – MS spectrum for DiBHP	37
2.9	GC – MS spectrum for DsBHP	38
2.10	^1H NMR spectrum of Diamyl H phosphonate (DAHP)	39
2.11	^{31}P NMR spectrum of Diamyl H phosphonate (DAHP)	39
2.12	^1H NMR spectrum of Diisoamyl H phosphonate (DiAHP)	40
2.13	^{31}P NMR spectrum of Diisoamyl H phosphonate (DiAHP)	40
2.14	^1H NMR spectrum of Disecamyl H phosphonate (DsAHP)	41
2.15	^{31}P NMR spectrum of Disecamyl H phosphonate (DsAHP)	41
2.16	^1H NMR spectrum of DiBiBP	44
2.17	^{31}P NMR spectrum of DiBiBP	44
2.18	^1H NMR spectrum of DiAiAP	45
2.19	^{31}P NMR spectrum of DiAiAP	45
2.20	^1H NMR spectrum of DiAButylP	46
2.21	^{31}P NMR spectrum of DiAButylP	46
2.22	^1H NMR spectrum of DiAHexylP	47
2.23	^{31}P NMR spectrum of DiAHexylP	47
2.24	GC – MS spectrum for DiBiBP	49
2.25	GC – MS spectrum for DiAiAP	50
2.26	GC – MS spectrum for DiAButylP	51
2.27	GC – MS spectrum for DiAHexylP	52

3.1	Variation of (A) organic phase Th(IV) concentration (B) density of the organic phase (C) organic phase nitric acid concentration as a function of equilibrium aqueous phase Th(IV) concentration in the extraction of Th(IV) for 1.1M TBP/DD, TiBP/DD and TsBP/DD systems in biphasic regions	63
3.2	Variation of (A) organic phase Th(IV) concentration (B) density of the organic phase, third phase and diluent-rich phase as a function of equilibrium aqueous phase Th(IV) concentration in the extraction of Th(IV) for 1.1M TBP/DD and TsBP/DD systems in biphasic and triphasic regions	64
3.3	A fit of the organic phase thorium concentration against the organic phase density for the biphasic and third phase regions for 1.1M TsBP/DD system	66
3.4	(A) The change in concentration of acid in the organic phase, third phase and diluent-rich phase with increase in the aqueous thorium concentration (B) The variation of V_{DP}/V_{TP} ratio as a function of function of equilibrium aqueous phase Th(IV) concentration	67
3.5	(A) Variation of Ce(IV) concentration in organic phase, third and diluent phases as a function of $[Ce(IV)]_{aq}$. The (CAC, LOC) points are marked in the inset for both the extractants. (B) Variation of the density in the organic phase, third and diluent phases as a function of $[Ce(IV)]_{aq}$.	71
3.6	(A) Graph of the density of the phase vs. biphasic and third phase concentration of cerium (B) Concentration of acid in the organic phase, third and diluent phases as a function of $[Ce(IV)]_{aq}$.	72
3.7	Distribution ratio of Ce(IV) as a function of nitric acid concentration. The insets indicate the initial aqueous concentration of Ce(IV).	73
3.8	IR spectra for the cerium nitrate complex with TBP compared with 1.1M TBP/DD system. The peak corresponding to the Ce-O-Ce bridged bond is marked. The spectra for 1.1M TsBP/DD system and the corresponding Ce-complex are also shown. The bare TsBP extractant itself has a peak at 592 cm^{-1}	73
3.9	Optimized geometries of $Ce(NO_3)_4 \cdot 2TBP$ and $Ce(NO_3)_4 \cdot 2TsBP$ complexes	76
3.10	Optimized geometry of $Ce(NO_3)_3 \cdot 3TBP$ complex	77
3.11	(A) Distribution of the number of $CH \cdots O$ interaction distances in each length range and (B) Energy decomposition components of the total interaction energy for complexes of Ce(IV) with TBP and TsBP	79
3.12	Representation of the relative energies of $Ce(NO_3)_4 \cdot 2TsBP$ and $Ce(NO_3)_4 \cdot 2TBP$ complexes. A few of the $CH \cdots O$ interaction distances are marked on the structures	80
3.13	Representation of the relative energies of Ce nitrate–TBP and Ce nitrate–TsBP dimers. The energy scheme in the inset indicates the relative stabilisation of the Ce nitrate–TsBP dimer	81
3.14	Distribution of the number of $CH \cdots O$ interaction distances in each length range for Ce–TsBP and Ce–TBP dimers	83

3.15	Experimentally observed and calculated IR spectra for the cerium nitrate complex dimer with TBP and TsBP. The peak corresponding to the Ce-O-Ce bridged bond is marked along with the P=O stretching peak. The experimental and calculated spectra for and the bare ligands TBP and TsBP are also shown. The frequencies shown mark the P=O stretch for the bare ligands	84
4.1	SANS data of metal free 1.1 M TalP/n-C ₁₂ D ₂₆ -1M HNO ₃ systems at 303K	90
4.2	SANS data obtained for the 1.1 M TalP/n-C ₁₂ D ₂₆ -Th(NO ₃) ₄ /1M HNO ₃ systems loaded with 30 g Th/L at 303K	91
4.3	SANS plots of 1.1 M TalP/n-C ₁₂ D ₂₆ -Th(NO ₃) ₄ /1M HNO ₃ systems with organic Th(IV) loading of 20 g/L and 40 g/L at 303K (A) TiBP (B) TsAP (C) TBP and (D) TsBP	93
4.4	Variation in the scattering pattern as a function of temperature for 1.1 M TalP/n-C ₁₂ D ₂₆ -Th(NO ₃) ₄ /1M HNO ₃ systems with a Th(IV) loading of 40g/L in the organic phase. (A) TBP (B) TiBP (C) TsBP systems are shown in the panels	95
4.5	Variation of SANS curves as a function of metal loading obtained from 1.1 M TalP/n-C ₁₂ D ₂₆ -UO ₂ (NO ₃) ₂ /1M HNO ₃ systems at 303K (A) TiBP (B) TBP and (C) TsAP	97
4.6	SANS data obtained for 1.1M TalP/n-C ₁₂ D ₂₆ -UO ₂ (NO ₃) ₂ /1M HNO ₃ systems loaded with 120 g U/L at 303K	99
4.7	Temperature variants in SANS obtained from 1.1 M TalP/n-C ₁₂ D ₂₆ -UO ₂ (NO ₃) ₂ /1M HNO ₃ systems with U(VI): (A) 40g/L U(VI) in TBP (B) 40g/L U(VI) in TiBP and (C) 20g/L U(VI) in TsBP	100
4.8	SANS patterns obtained at 35°C from 1.1 M TalP/C ₁₂ D ₂₆ (A) TBP and (B) TiBP loaded with 40g/L Th(IV) and U(VI)/1M HNO ₃ .	101
5.1	Plot of logarithm of D (distribution ratio) vs. logarithm of extractant concentration. The slope of the graph can be used to find the metal solvate composition in (A) Th(IV) extraction (B) for U(VI) extraction	110
5.2	Optimized geometries of (A) UO ₂ (NO ₃) ₂ ·2TBP (B) UO ₂ (NO ₃) ₂ ·2TsBP (C) Th(NO ₃) ₄ ·3TBP and (D) Th(NO ₃) ₄ ·3TsBP complexes	111
5.3	Comparison of experimental and calculated spectra for the complexes of U(VI) and Th(IV) with TBP and TsBP	115
5.4	Kinetics of metal ion uptake from 4M HNO ₃ solutions by TBP and TsBP coated XAD - 7 resins (A) Individual metal ions (B) From a 1:1 mixture	117
5.5	(A) Loading of U(VI) and Th(IV) from 4M HNO ₃ medium on 40% TsBP coated resin columns followed by (B) Elution with 0.01M HNO ₃ and (C) Total elution curve	118

5.6	Eluent from two different column runs for the separation of U(VI) from Th(IV) from a feed solution containing (A) ~10µg/mL of U(VI) and 1mg/mL of Th(IV) (B) 10µg/mL of U(VI) and 10mg/mL of Th(IV) (C) 10µg/mL of U(VI) and 100mg/mL of Th(IV). (D) U(VI) and Th(IV) concentrations in the eluate collected in the second column run carried for the 1:10000 mixture after the first step of separation. The feed used for this further purification is indicated. The acids used for washing and their volumes are provided in the insets. Uranium sorbed in the column runs have been eluted with 20mL of 0.01M HNO ₃ (5.7A–D)	122
5.7	Comparison of the separation of U(VI) from Th(IV) by TBP and TsBP coated columns from a feed solution containing 10µg/mL of U(VI) and 100mg/mL of Th(IV)	125
6A.1	Logarithm of viscosity against 1/T for the three H–phosphonates, DBHP, DiBHP and DsBHP. The activation energies are calculated from the slopes	130
6A.2	Variation in D values as a function of HNO ₃ concentration in the extraction of U(VI) by butyl H-phosphonates	132
6A.3	(A) IR spectrum of DBHP, (B) DsBHP and (C) DiBHP before and after extraction of U(VI) from 0.001M nitric acid	133
6A.4	(A) IR spectrum of 1.1M DBHP/toluene (B) 1.1M DiBHP/toluene and (C) 1.1M DsBHP/toluene before and after extraction of U(VI) from 4M nitric acid	136
6A.5	ESI mass spectra for the bare ligand DiBHP compared with the organic phase uranyl complexes extracted from 0.01M and 4M nitric acid	137
6A.6	Variation in D values as a function of HNO ₃ concentration for the extraction of Am (III) by butyl H-phosphonates	138
6A.7	Optimized structures of DBHP and DsBHP bound with uranyl nitrate (keto form)	139
6A.8	Optimized structures of DBHP and DsBHP bound with uranyl nitrate (enol form)	139
6A.9	Comparison of experimental and calculated IR spectra for uranyl nitrate complexes of DBHP and DsBHP both in the keto and enol forms	141
6A.10	Optimized structures of bare DBHP and DsBHP ligands indicating the P=O---H hydrogen bonding	143
6A.11	Optimized structures of DBHP bound with Am(III)nitrate in keto form	144
6B.1	Logarithm of viscosity 1/T for the dialkylalkyl phosphonates DiBiBP, DiAiAP, DiAButylP and DiAHexylP. The activation energy is calculated from the slopes	149
6B.2	Variation in D values as a function of HNO ₃ concentration in the extraction of U(VI) by unsymmetrical and symmetrical branched dialkylalkyl phosphonates	151
6B.3	Variation in D values as a function of HNO ₃ concentration in the	152

	extraction of Th(IV) by unsymmetrical and symmetrical branched dialkylalkyl phosphonates	
6B.4	Variation in D values as a function of HNO ₃ concentration in the extraction of Pu(IV) by unsymmetrical and symmetrical branched dialkylalkyl phosphonates	153
6B.5	Variation in D values as a function of HNO ₃ concentration in the extraction of Am(III) by unsymmetrical and symmetrical branched dialkylalkyl phosphonates	153
6B.6	Extraction of nitric acid by the four dialkylalkyl phosphonates as a function equilibrium HNO ₃ concentration in the aqueous phase	154
6B.7	Optimized geometries of the UO ₂ (NO ₃) ₂ ·2DiBiBP and UO ₂ (NO ₃) ₂ ·2DiAHexylP complexes	155
6B.8	Optimized geometries of the Th(NO ₃) ₄ ·3DiBiBP and Th(NO ₃) ₄ ·3DiAHexylP complexes	155
6B.9	Comparison of experimental and calculated spectra for the extractants DiBiBP, DiAHexylP and their complexes with U(VI)	158
7A.1	Optimized structures of DAHP and DsAHP bound with uranyl nitrate. The energy schematic represents the stability of the UO ₂ (NO ₃) ₂ ·2DsAHP and UO ₂ (NO ₃) ₂ ·2DiAHP complex compared with the uranyl nitrate complex formed by the linear chain isomer DAHP	165
7A.2	Logarithm of viscosity against 1/T for the three H-phosphonates, DAHP, DiAHP and DsAHP. The activation energies are calculated from the slopes	169
7A.3	Variation in D values as a function of HNO ₃ concentration in the extraction of U(VI) by 1.1M solutions of amyl H-phosphonates in n-dodecane. The extraction of U(VI) by 1.1M TBP/DD is also shown	170
7A.4	Calculated IR spectra for the uranyl nitrate complexes of DAHP and DsAHP and the bare ligands. The calculated spectra are compared with those experimentally measured for each compound. The frequencies marked are the U=O asymmetric stretch, P=O stretch and P-H stretch	171
7A.5	Variation in D values as a function of HNO ₃ concentration in the extraction of (A) Th(IV) by 0.1M solutions of amyl H-phosphonates in n-dodecane and (B) Pu(IV) by 1.1M solutions of amyl H-phosphonates in n-dodecane	174
7A.6	ESI-MS spectra for the DsAHP bare ligand denoted as (L). The peaks corresponding to the relevant m/z are assigned	175
7A.7	ESI-MS spectra for the DsAHP bound uranyl nitrate complex denoted as (M). The peaks corresponding to the relevant m/z are assigned	175
7A.8	ESI-MS spectra for the DsAHP bound thorium nitrate complex denoted as (M). The peaks corresponding to the relevant m/z are assigned	176
7A.9	Variation in D values as a function of HNO ₃ concentration in the extraction of (A)Am(III) by 1.1M solutions of amyl H-phosphonates in n-dodecane	177

7A.10	The optimized structure for the Am(NO ₃) ₃ ·3DAHP complex	177
7A.11	Optimized structures of DAHP and DsAHP bare ligands. The marked interaction distances between the phosphoryl oxygen and the -hydrogen atoms are indicated	179
7A.12	Optimized structures of UO ₂ ·2EnolDAHP and UO ₂ ·2EnolDsAHP complexes	180
7B.1	Optimised geometries of Cf complexes with cyanex 272, cyanex 302 and cyanex 301 ligands	184
7B.2	EDA of heavy actinide complexes with cyanex 272, cyanex 302 and cyanex 301 ligands. The different interaction components are plotted from Am-Cf	185
7B.3	The optimized geometries of 1:0, 1:1, 1:2 and 1:3 complexes of Am(III) with DPA	186
7B.4	Gas phase EDA of actinide–DPA complexes for Am, Cm, Bk and Cf	187
7B.5	Solvent corrected EDA of actinide–DPA complexes for Am, Cm, Bk and Cf	188
7B.6	Optimised geometries of Am ³⁺ , Cm ³⁺ , Bk ³⁺ and Cf ³⁺) complexes with the octa-coordinate TPAEN ligand	189
7B.7	Complexation energy for the heavy actinides with the Cyanex 301 Cyanex 302, Cyanex 272 and TPAEN ligands	190
7B.8	EDA of actinide–TPAEN complexes for Am, Cm, Bk and Cf in gas phase and solvent phase	191
7B.9	EDA of heavy actinide complexes with cyanex 272, cyanex 302 and cyanex 301 ligands on incorporating spin-orbit coupling. The different interaction components are plotted from Am-Cf	192
7B.10	EDA of Am-Cf complexes with 3DPA ligands on incorporating spin-orbit coupling. The different interaction components are plotted from Am-Cf	192
7B.11	EDA of heavy complexes with TPAEN ligand on incorporating spin-orbit coupling. The different interaction components are plotted from Am-Cf	193
7B.12	Energy level diagram for the heavy actinides, DPA and TPAEN ligands in solvent phase. The energy difference between the Cf 5f energy level and the HOMO of DPA and TPAEN are schematically indicated	194

LIST OF ABBREVIATIONS

Sl. No.	FULL NAME	ABBREVIATION
1	Critical aqueous concentration	CAC
2	Limiting organic concentration	LOC
3	Tri-n-butyl phosphate	TBP
4	Tri-iso-butyl phosphate	TiBP
5	Tri-sec-butyl phosphate	TsBP
6	Tri-sec-amyl phosphate	TsAP
7	Dibutyl H-phosphonate	DBHP
8	Di-iso-butyl H-phosphonate	DiBHP
9	Di-sec-butyl H-phosphonate	DsBHP
10	Diamyl H-phosphonate	DAHP
11	Di-iso-amyl H-phosphonate	DiAHP
12	Di-sec-amyl H-phosphonate	DsAHP
13	Diisobutylisobutyl phosphonate	DiBiBP
14	Diisoamylisoamyl phosphonate	DiAiAP
15	Diisoamylbutyl phosphonate	DiAButylIP
16	Diisoamylhexyl phosphonate	DiAHexylIP
17	Small Angle Neutron Scattering	SANS
18	Density Functional Theory	DFT
19	Energy Decomposition Analysis	EDA
20	Atoms-in-molecule	AIM
21	Dipicolinic acid	DPA
22	N,N,N',N'-tetrakis[(6-carboxypyridin-2-yl) methyl] ethylenediamine	TPAEN
23	Bis(2,4,4-trimethylpentyl) dithiophosphinic acid	Cyanex 301
24	Bis(2,4,4-trimethylpentyl) thiophosphinic acid	Cyanex 302
25	Bis (2,4,4-trimethylpentyl) phosphinic acid	Cyanex 272
26	Trialkyl phosphate	TalP

27	Infrared	IR
28	Electrospray ionisation mass spectrometry	ESI-MS
29	Molecular weight	M.W.
30	Bond critical point	BCP



Chapter 1



“There are only two ways to live your life. One is as though nothing is a miracle. The other is as though everything is a miracle”

~ Albert Einstein

INTRODUCTION

1.1 Energy for sustenance

The sustainable development and security of a nation is strongly correlated to its energy demands being met in a self-sufficient manner. In developing countries like India, the demands on energy increase, as electricity is a mark of empowerment for the large expanses of the developing rural landscape^{1, 2}. The economics of energy production depend on the availability of energy reserves, the technology to utilise these and cost incurred during the entire process of producing energy from the reserve³. Cost is not only monetary, but also the cost to the environment is justifiably a major consideration. The nature of the energy reserve, the methods of its conversion to energy in a usable form and its long-term sustainability are among the important parameters that are considered while evaluating energy sources.

In this light, the distinction between renewable and non-renewable energy sources arises. Although it might be available in abundance, a non-renewable energy source cannot sustain itself in the long run. An energy source which produces little energy on burning large masses of the reserve is considered as one with low energy density. This coupled with non-renewable nature of the fuel implies the short-term nature of the energy source. On the other hand, renewable energy is derived from sources such as wind, hydrothermal, solar etc. which do not deplete. A larger focus on renewable energy sources is gaining importance globally as these could well be the gateway towards sustainable energy.

1.2 Renewable and non-renewable sources of energy

The major non-renewable energy sources powering energy needs world-wide are fossil fuels viz. coal and oil. Apart from their non-availability on the long run, there are other disadvantages associated with fossil fuels as an energy source. Among these is the climate change caused by the emission of green house gases into the atmosphere⁴. Carbon monoxide, carbon dioxide and sulphur dioxide contribute to the green house effect. Among these,

particularly carbon dioxide absorbs infra-red radiation emitted from the earth, preventing the heat energy from leaving the earth's atmosphere. This causes global warming which is destroying several habitats in almost all countries. The demand for oil in both developing and developed countries is large. However, there is uncertainty associated with oil prices in the global market, as it is among the most precious commodities in today's economic scenario. Combustion of oil leads to the emission of toxic gases viz. CO and oxides of nitrogen and sulphur, which pollute the surrounding air⁵⁻⁷. This combined with the risks of oil spillage into oceans take a toll on aquatic as well as other life forms⁸. An alternate fuel could hence be a welcome alternative.

The quest for alternative fuels engages many researchers around the world⁹. Renewable fuels such as hydroelectric, solar, wind energy etc. are some alternatives that have been explored. In contrast to non-renewable energy sources, the negative impact of renewable energy on the planet is negligible¹⁰. Nevertheless, there are other difficulties associated with producing power from the non-renewable sources. The extent of rainfall is a key factor that decides the amount of power generated from hydroelectric projects making them inherently unreliable^{11, 12}. Countries receiving large amounts of solar radiation can potentially use solar energy, but often the limited technological advances coupled with high initial costs are constraining factors. Wind energy is a very good source with relatively low capital investments and is being used in regions that witness strong and consistent wind currents^{13, 14}. Unfortunately the amount of energy generated by windmills is very small, and hence this source cannot solely meet the current energy demands¹⁵. Likewise there are other sources such as geothermal and tidal energy that can potentially produce small percentages of the total energy requirements, however, the technology development towards these is in its rudimentary stage.

1.3 Nuclear power

Among all the alternatives to fossil fuels explored till date, nuclear energy has emerged as a prime alternative for several reasons^{16, 17}. The technology required in operating nuclear power plants are well in place and research to improve power production is also actively underway in several countries. The energy obtained per unit mass of the fuel material is known as the energy density. The energy density of nuclear fuels is in the order of a million times higher than that of fossil fuels due to Einstein's mass-energy relation. The fission or fusion of nuclei produce a mass defect (m) or "missing mass" which is converted to energy (E) and is given by the relationship $E=mc^2$ where ' c ' is the velocity of light in vacuum (3×10^8 m/s). As the mass-energy proportionality constant is in the order of 10^{16} , small mass defects produce astronomical quantities of energy. As a consequence, the fuel requirement for a nuclear reactor is very small and so is the waste volume generated at the end.

There are further merits to the use of nuclear power that can be understood by getting into some detail. One of these is that the fuel used in fast breeder reactors can be regenerated by breeding. Fast breeder reactors use uranium and plutonium mixed oxides or carbides as the fuel. As the isotopes ^{239}Pu and ^{235}U undergo fission, energy, fission products and neutrons are produced. Isotopes that undergo fission are known as fissile and those that can potentially be converted to a fissile isotope by nuclear processes are known as fertile. The generated neutrons are captured by ^{238}U , which is $\sim 99.3\%$ isotopic ratio of the total uranium. After neutron capture, the ^{238}U isotope undergoes double beta decay and forms ^{239}Pu which is a fissile material fuelling the reactor. This process is known as breeding. Nuclear fuel is the only kind that produces new fuel while burning the existing fuel. In fact, in about 15 years period reactors employing metallic fuel can generate enough ^{239}Pu to power another reactor. This duration is conventionally known as "doubling time". In reactors with carbide/nitride

and oxide fuels also this is certainly possible and it takes about 20 years and 25 years, respectively. This is a unique and one of the most remarkable features of nuclear power.

In addition to generating electricity, a plethora of radioisotopes such as ^{60}Co , ^{137}Cs , ^{131}I , ^{90}Sr and ^{32}P produced in nuclear reactors find immense application in a range of fields. A few of these are: the treatment of cancer, increasing storage life of perishable foods such as fruits, sterilization of equipment, waste or sewage treatment and monitoring nutrient uptake by plants. Radioisotopes are replacing several cumbersome and long procedures in the medical field. Apart from therapy, radio-isotopes in medical diagnosis and imaging are elevating modern medicine by leaps and bounds.

Among the alternatives to fossil fuel, nuclear power is the second largest global producer of electricity, powering 10.6% of the world's consumption. The potential of nuclear power to increase its power production is immense, due to large reserves of uranium as well as thorium in several parts of the world coupled with the huge amounts of energy that can be obtained from each gram of these reserves. Natural uranium consists mainly of ^{238}U (~99.3 atom%), ^{235}U (~0.7 atom%) and a very small amount of ^{234}U . Naturally occurring thorium occurs as a single isotope of ^{232}Th . Though the ^{235}U isotope of uranium is fissile, energy can be harnessed from ^{232}Th as well as ^{238}U by converting them into fissile isotopes, namely U^{233} and ^{239}Pu , respectively.

India has abundant thorium reserves and has developed an ingenious three stage nuclear programme in which thorium can be effectively used¹⁸⁻²⁰. In the first stage, natural uranium is used as the fuel. Thermal neutrons with kinetic energy in the 0.025-1eV range bombard the uranium nuclei and ^{235}U fissions to produce energy, fission products and additional neutrons. Heavy water is used as the coolant to transfer away the heat from the core which is required to produce steam for the turbines to generate electricity. The coolant in a thermal reactor is chosen so as to also moderate (slow down) the neutrons produced in fission to the thermal

range by elastic collisions. Meanwhile, the ^{238}U isotope captures neutron and eventually beta decays twice to form ^{239}Pu , a fuel for the second stage.

In the second stage, uranium and plutonium mixed fuel in its oxide, carbide nitride or metallic form is employed. Sodium cooled fast breeder reactors fission ^{239}Pu producing energy, fission products and neutrons which will not be moderated by the sodium coolant. The neutrons produced in the fission are fast neutrons with typical energies in the range of 1-2 MeV. Due to the operation with fast neutrons and 'breeding' new fuel, these reactors get their name. Apart from the fission, there are two more important nuclear reactions that occur in the fast breeder reactor. One is the conversion of ^{238}U to fissile ^{239}Pu which can be used to fuel another reactor as described above. The other is the conversion of ^{232}Th to the fissile ^{233}U isotope by neutron capture followed by two β -decays. The ^{232}Th is used as either a blanket material or placed as one of the fuel rods in the reactor core. The ^{233}U thus produced in the second stage is employed as fuel in the third stage.

The third stage nuclear reactors use a thorium blanket surrounding the fuel core and operate with neutrons in the thermal range. These thorium breeder reactors can produce electricity as well as breed ^{233}U from ^{232}Th thus enabling the third stage to be sustained for several centuries. This nuclear power programme ensures that the long term energy needs of the nation are fulfilled so that the dependence on fossil fuels eventually reduces.

The chemistry involved in implementing this nuclear power programme is rather intricate and cannot be ignored at any cost. The reason for this intricacy is the requirement to separate complex elemental mixtures at every stage. Actinides *viz.* U, and Th have to be extracted from their ores after they are mined, un-burnt fuel has to be separated from fission products once it is removed from the reactor and finally the nuclear waste consisting of almost a third of the elements in the periodic table has to be managed effectively and safely before it is disposed. Each stage of the 'nuclear fuel cycle' requires that attention is paid to the

complexation chemistry of various elements and particularly the actinide elements. Not only do actinides need to be specifically extracted from a mixture of elements, they also need to be separated from each other at certain stages of the cycle. The main methodology used to achieve actinide separation, is their specific complexation from aqueous mixtures consisting of several elements. As a consequence, solvent extraction is one of the most important methods used for the processing of nuclear materials.

1.4 Solvent extraction – A separation technique for the recovery and purification of metals

In the first stage employing thermal neutron reactors, only 1% of the total fissile ^{235}U undergoes fission and this number is ~10-20% in a fast reactor. The major part of the fuel remains un-burnt and can be re-used as fuel if it is separated from the fission products. It has been proposed that metallic fuels are mainly suitable for pyro-processing, which essentially exploits the difference in reduction potentials to electrochemically separate a mixture of elements from a metallic melt²¹. Nevertheless, this technology is still in its developmental stage and not used in the nuclear plant scale²². Aqueous methods using specific organic extractants are well established and are employed to this day for the processes in the nuclear fuel cycle and among these, solvent extraction is the prominent technique used for reprocessing of nuclear fuels as well as in the extraction of U and Th from their ores.

Solvent extraction is a liquid-liquid extraction technique in which a solute distributes itself between two immiscible phases. Generally in the nuclear industry, the specific extractant is solubilized in a hydrocarbon solvent known as the diluent. The diluent does not participate in the complexation reaction; however, it improves the specificity of extraction as well as provides the right viscosity and density to the organic phase in order to achieve good mass transfer between phases. The type of diluents employed for solvent extraction is of three broad categories: hydrocarbon diluents, halogenated diluents and polar diluents. The effect of

the diluent is more apparent when there is large amount of diluent compared to the extractant in the organic phase. When polar diluents such as chloroform or *o*-dichlorobenzene are employed, the extraction of the metal ion by polar extractants drops almost ten-fold. The reason for this decrease that polar diluents associate with a polar extractant and make the extractant less available to interact with the metal ion.

The extraction ability of an extractant for a given metal ion is measured by its distribution ratio (D) which is the ratio of the concentration [X] of the metal in the organic phase to that in the aqueous phase at equilibrium²³.

$$D = \frac{[X_{org}]}{[X_{aq}]}$$

The specificity of the extractant for one metal over the other is given by the separation factor β , which is a ratio of D values of the two metals. Higher β values are indicative of better separation.

$$\beta = \frac{D_{U(VI)}}{D_{Th(IV)}}$$

In order to separate fuel material from other elements either in irradiated fuel or from their ores, a ligand with high selectivity towards U, Th and Pu is required. The separation and recovery of elements with closely related chemistry has been a long-lasting challenge for scientists. Particularly the separation of elements belonging to the f-block is more challenging due the large size of the atoms coupled with poor shielding of the f-orbitals making these elements all the more similar in their chemical nature and reactivity²⁴⁻²⁷. In aqueous solution, early actinides up to Am exist in multiple oxidations states (e.g. Pu(III) to Pu(VI) exist with small potential barriers between the oxidation states), however, for transplutonium actinides the dominant oxidation state is +3. In the case of lanthanides across all the elements the most stable oxidation state is the trivalent one. The challenge in lanthanide-transplutonium actinide separation (minor actinide partitioning) is precisely that the chemistry of the transplutonium

actinides becomes very similar to the actinides. The covalency offered by the 5f orbitals is being made the best use of in designing extractants for minor actinide partitioning.

The quest for actinide specific extractants has been a long and difficult one. Particularly among these, discovering new extractants that bind specifically to certain actinides over others is an even greater challenge due to the chemical similarity of actinides²⁸. Currently, Tri-n-butyl phosphate (TBP) is being used for this purpose and has stood the test of time for the past 60 years²⁹. However, there are limitations associated with TBP *viz.* third phase formation³⁰, chemical and radiation degradation, low U/Th separation factors and red-oil formation³¹. These limitations pose problems, especially during the reprocessing of fast reactor fuels and there is a need to find alternate extractants which eliminate the disadvantages of TBP while retaining its advantageous properties^{32, 33}.

Pioneering work on the potential of alternate extractants for the separation of U(VI) and Th(IV) was done by Siddall³⁴, followed by Griffin³⁵. Investigations into the extraction of U(VI) and Pu(IV) by organophosphorous compounds, was carried out by Burger³⁶ who showed that the extraction of actinides by extractants with electronegative substituents caused a decrease in their extraction potential³⁷. According to Siddall³⁸ and Catrall³⁹, the phosphonates proved to be superior to phosphates as they extract uranium and thorium better than the corresponding phosphates. Nevertheless, the extraction as well as third phase formation tendency of tricyclohexyl phosphate with U(VI) and Th(IV) in nitric acid media has been investigated by Rao *et. al.*⁴⁰ in the recent past. In literature, reports on the extraction of actinides by phosphonates are few^{38, 39} and for the first time, extraction of actinides by unsymmetrical phosphates was carried out in which Dibutylhexyl phosphonate and Dibutyloctyl phosphonate were studied⁴¹.

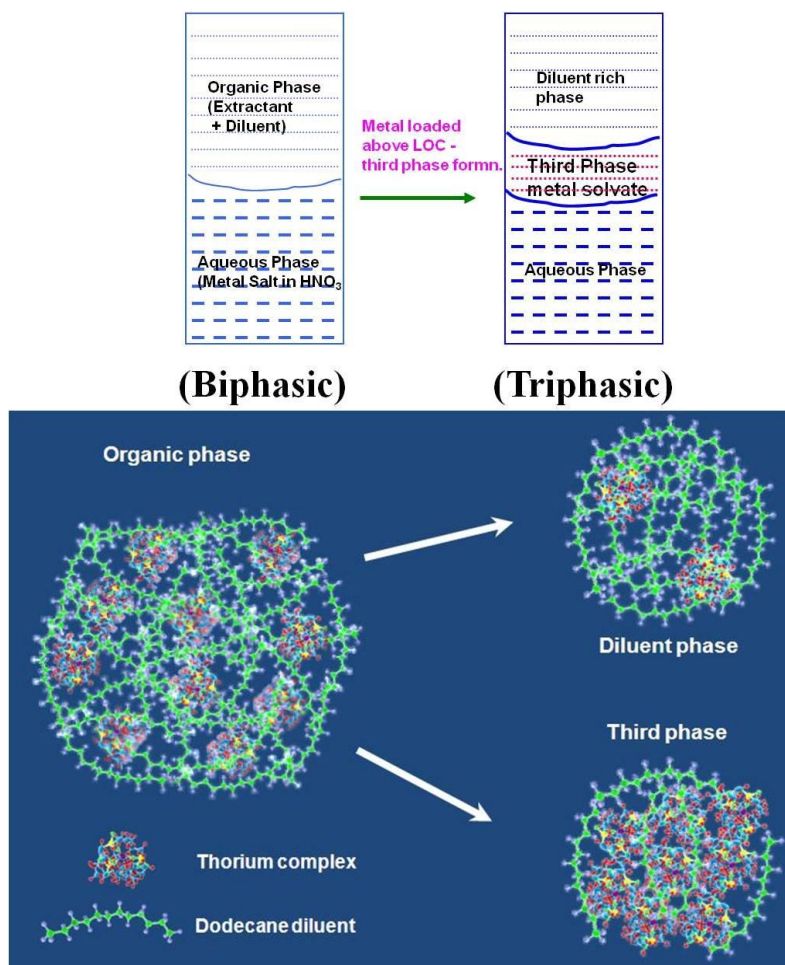
The extraction ability of organophosphorus extractants depends on the basicity of the phosphoryl oxygen as well as the nature of substituents attached to the P atom⁴². The basicity

of the phosphoryl group is enhanced when the C-O-P group is replaced by a C-P group⁴³. Neutral organophosphorus extractants show the variation in the basicity of the phosphoryl oxygen as follows: phosphine oxides $[R_3P=O] > \text{phosphinates } [R_2(RO)P=O] > \text{phosphonates } [R(RO)_2P=O] > \text{phosphates } [(RO)_3P=O]$ ⁴³. Dialkylalkyl phosphonates, being more basic, prove to be stronger extractants than the corresponding phosphates. Studies in the past have found phosphonates to be superior to the corresponding phosphates in the extraction of uranium and thorium^{44,45}. Further, phosphonates do not have very high D values with metal ions, unlike phosphinates and phosphine oxides, thereby ensuring easier recovery of metal ion from the loaded organic phase during the stripping stage⁴⁴. Phosphonates have been used for a wide range of applications including the treatment of osteoporosis^{46, 47}, water treatment^{48,49} and in solvent extraction studies, particularly as actinide binders^{33,41,43,45,50,51}. Complexes of actinide ions with organophosphorous extractants⁵²⁻⁵⁴ have been explored, especially in reference to the nuclear fuel cycle^{42,55-57}. One of the potential applications of phosphonates in which their specificity towards actinides can be exploited is the processing of spent nuclear fuels. However, we also need molecules which can recover actinides from various waste streams, which can extract uranium and plutonium better than TBP.

In the process of searching for alternative extractants to TBP for nuclear fuel reprocessing, it has been found that the structural effects of the alkyl chain considerably affected extraction parameters⁵⁸⁻⁶⁰. The methyl branching in the secondary position in the tri-*sec*-butyl phosphate (TsBP) enhances its extractability of U(VI) compared to TBP⁶¹. Increasing the alkyl chain length reduces the tendency to form the third phase as shown by Rakesh *et. al.* who used tri-*iso*-*amyl*-phosphate as an alternative to TBP for the extraction of actinides^{62,63}. As the carbon chain structure of organophosphorus extractants plays a vital role in its extraction behaviour, extensive studies are needed to understand the influences of the alkyl chain.

1.5 Neutrons to predict third phase formation

One of the effects of the alkyl chain structure is the change in the third phase formation tendency of the metal-extractant complexes. Third phase formation is a potential issue in solvent extraction. When the metal ion concentration in the organic phase exceeds a threshold concentration, the organic phase splits into a metal–extractant rich third phase and a diluent-rich phase that is left with the bulk of the diluent^{30, 64}. The aqueous concentration at the point where the phase splits is known as the critical aqueous concentration (CAC), and the corresponding organic metal concentration is known as the limiting organic concentration (LOC). The third phase is significantly viscous, and prevents efficient mixing of organic and aqueous phases as well as mass transfer between these phases. Formation of the third phase with tetravalent metal ions such as Pu(IV) and Th(IV), is undesirable during the large scale processing of spent fuels, and is one of the drawbacks of TBP when it is used as an extractant^{65, 66}. The parameters that affect third phase formation investigated in the past, found that the nature of extractant, the metal being extracted, diluent, and temperature, all have a role to play⁶³. Tetravalent metal ions such as Zr(IV), Th(IV), and Pu(IV) are more likely to induce third phase with trialkyl phosphates compared to UO_2^{2+} ⁶⁵. Extractants with longer carbon chains have higher third phase formation limits. For, example, tri-iso-amyl phosphate has a higher limiting organic concentration than tri-n-butyl phosphate (TBP). With respect to the diluent, this trend is reversed; diluents with longer carbon chain length are more likely to form third phase than diluents with shorter carbon chain under the same experimental conditions. In the extraction of Th(IV) using TBP, tetradecane with 14 carbon number forms third phase at lower concentrations of Th(IV) than dodecane which contains 12 carbon atom(6). A schematic of third phase formation is shown in Scheme 1.1.



Scheme 1.1: A schematic of third phase formation showing the concentration of metal complexes in the third phase.

Third phase formation is in essence an aggregation phenomenon. This implies its dependence on the nature of interaction or specifically attraction between the metal complexes in the diluent medium. Probing interaction parameters between complexes could show much promise in understanding the occurrence of the third phase.

Molecular level studies related to third phase formation have been carried out using techniques including UV – Vis absorption and EXAFS (Extended X-ray absorption fine structure) to understand third phase formation mechanisms^{67, 68}. SAXS (Small angle X-ray scattering) and SANS (Small angle neutron scattering) measurements have been employed to probe aggregation behaviour of metal complexes which leads to third phase formation^{32, 69-71}.

Conductometric technique has also been used to detect the formation of third phase⁷². NMR studies have been carried out to understand how association and protonation behaviour in malonamide complexes influences third phase formation⁷³. Scattering techniques are effective in the study of matter and their interactions. The probe can be light, neutrons or X-rays and the techniques viz. light scattering, small-angle neutron scattering (SANS) and small-angle X-ray scattering (SAXS) derive their name from which kind of probe is used. The feature common to all these techniques is that the radiation (light, neutrons or X-rays) is elastically scattered by the sample and the results in a scattering pattern. This pattern when correctly interpreted gives information about the size, shape, ordering as well as interactions in the sample. SANS and SAXS techniques can provide structural information in the nanoscale. X-rays with wavelength in the order of a few Angstroms and neutrons possessing De Broglie wavelengths of a similar length scale are employed for such measurements. Light scattering requires transparent media to provide any useful information, however, SAXS and SANS can penetrate optically opaque samples, widening their application potential. Moreover, SANS is more suitable in comparison with SAXS for samples containing elements with low atomic numbers. X-rays are scattered by electron density, whereas neutrons are scattered by the nucleons in the atom making them very sensitive to lighter nuclei e.g. hydrogen, deuterium. Apart from this, neutrons are sensitive enough to distinguish between isotopes of the same element as they have very different scattering length densities for each isotope.

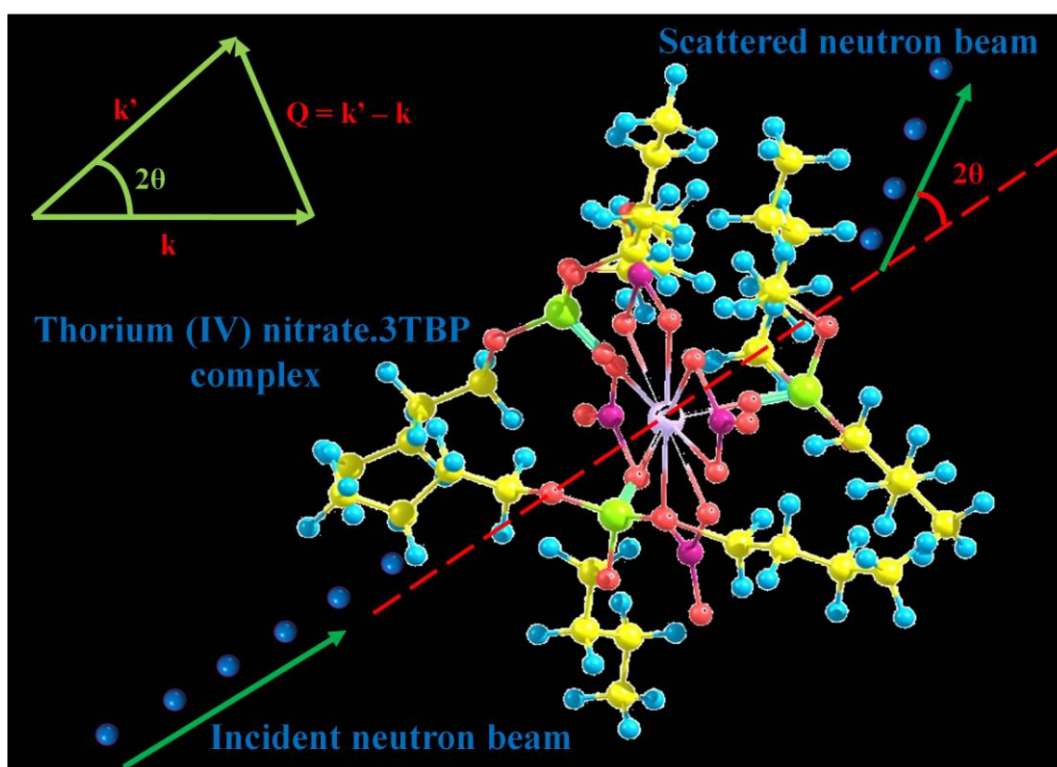
A schematic representation of the neutron beam scattered by a sample containing the metal complex is shown in Scheme 1.2. An incident neutron beam interacts with the sample and is elastically (with change in momentum, but no loss of energy) scattered through an angle 2θ with respect to its initial direction. The incident and outgoing scattered beams are associated

with wave vectors \mathbf{k} and \mathbf{k}' , respectively. The vector difference $\mathbf{k}' - \mathbf{k}$ is the scattering vector \mathbf{Q} which is a measure of the momentum transfer. \mathbf{Q} is given by the equation:

$$Q = \frac{4\pi \sin\theta}{\lambda}$$

In the above equation θ is the half-scattering angle and λ is the mean wavelength of the incident neutrons used. The differential scattering cross-section per unit volume ($d\Sigma/d\Omega$) is measured as a function of scattering vector \mathbf{Q} . Theoretically, the scattering intensity from a collection of particles depends on the form factor $P(Q)$, structure factor $S(Q)$, number density of particles (N_P), square of volume of particles (V_P), and scattering contrast ($\rho_P - \rho_S$). The net intensity, expressed as a product of these, is given by the equation:

$$\frac{d\Sigma}{d\Omega(Q)} = N_P V_P^2 (\rho_P - \rho_S)^2 P(Q) S(Q)$$



Scheme 1.2: Representation of the neutron beam scattered by the sample containing the metal complex. The inset depicts the scattering vector \mathbf{Q} .

For particles experiencing an attractive force between each other, the value of $S(Q)$ can be calculated using Baxter's sticky hard-sphere model⁷⁴. The stickiness parameter (τ^{-1}) is calculated from τ , which is obtained by fitting the data using the Baxter's sticky hard-sphere model. Further, the potential energy of the interaction (U_0) can be obtained from the expression:

$$\tau = \frac{\sigma + \Delta}{12\Delta} \exp\left(\frac{U_0}{k_B T}\right)$$

The diameter of the aggregate (σ), is calculated mathematically assuming the particles to be spherical and Δ is the width of the square-well potential. Data are fitted with the two independent fitting parameters as stickiness ($1/\tau$) and size of the aggregate. The stickiness is mostly sensitive to low Q region, whereas size is determined from the high Q region. As third phase formation is inherently an aggregation phenomenon, sticky hard sphere model is ideal for fitting of the SANS data.

In the present work, for the first time SANS technique has been examined as a probe to predict third phase before its formation. The numerical value of the stickiness parameter and attraction potential energy assigned quantifiable thresholds for the third phase. When these thresholds are crossed, there is a likelihood of the third phase occurring. The structure of the alkyl chain has striking influences on the third phase formation tendencies. Apart from the third phase formation, other extraction parameters e.g. extraction efficacy, specificity and ease of synthesis etc. are also influenced by the carbon chain. Changing the family of the extractant from phosphate to phosphonate also brings its own influences. Extractants that qualify to combine the best of these parameters are the order of the day.

1.6 Density functional theory for actinide complexes

The search for an alternate actinide-specific extractant is a long and tedious one. Not only in terms of the conditions of specificity, but also screening a number of extractants demands involved experimental procedures that pose radioactive hazards. In the case of certain

actinides e.g. Bk and Cf, their availability for an experimental investigation becomes a limitation. However, alternate extractants and their actinide complexes are of immediate interest in the processing of nuclear fuels. An ideal situation would be if new ligands and their behaviour towards actinides could be predicted by some means. With such a predictive framework in place, the experimental load can be drastically reduced as the sheer number of possible alternatives can be narrowed down. Computational chemistry has the power to interpret as well as predict the chemical behaviour of several reacting systems; making it a marvellous platform for the study of actinide complexation. In the recent past, computational chemistry has been a versatile tool in providing insights into the molecular structure, dynamics and behaviour of interacting systems. The preference of a certain metal ion towards a particular ligand or even weak interactions *viz.* hydrogen bonding that stabilise certain conformers over others can be comprehended through interactions at the molecular scale.

Computational chemistry has its origins way back in 1928 when attempts to solve the Schrödinger equation were made by theoretical physicists of that era with hand-cranked calculating machines. In quantum mechanics, a wavefunction provides a complete description of a system. The beauty of the quantum mechanical construct is such, that depending on the information required of the system, the quantum mechanical operator that operates on the wavefunction can be suitably chosen. For every observable in classical mechanics a quantum mechanical operator exists. By means of an eigenvalue equation, the properties of the system can be obtained as eigenvalues. The time-independent Schrödinger equation is an eigenvalue equation in which a quantum mechanical energy operator \hat{H} , operates on a wavefunction Ψ yielding the energy of the system as an eigenvalue.

$$\hat{H}\Psi = E\Psi$$

In general an electron distribution is represented by a wavefunction and the operator \hat{H} , also known as the Hamiltonian is expanded as follows: where i runs over all the electrons and k runs over the nuclei (z) in the system.

$$\hat{H} = - \sum_i \frac{\hbar^2}{2m_i} \nabla_i^2 - \sum_k \frac{\hbar^2}{2m_k} \nabla_k^2 - \sum_i \sum_k \frac{e^2 z_k}{r_{ik}} + \sum_{i < j} \frac{e^2}{r_{ij}} + \sum_{k < l} \frac{e^2 z_l z_k}{r_{kl}}$$

The first two terms represent the kinetic energy of the electrons and nuclei, respectively. The third term is the electron nuclear attraction and the last two terms are the electron-electron and nuclear-nuclear repulsion, respectively. As the mass of the nuclei or electrons are in the denominator of the kinetic energy terms and taking into account the fact that a nucleon is ~1800 more massive than an electron, this Hamiltonian can be further simplified. In what is known as the Born-Oppenheimer approximation, the motion of nuclei is neglected in comparison with the electronic motion which is far more rapid. Not only does this approximation do away with the nuclear kinetic energy term, it additionally fixes the positions of the nuclei, thereby reducing the nuclear-nuclear interaction term to a constant for a given nuclear configuration. Thus the Hamiltonian reduces to:

$$\hat{H} = - \sum_i \frac{\hbar^2}{2m_i} \nabla_i^2 - \sum_i \sum_k \frac{e^2 z_k}{r_{ik}} + \sum_{i < j} \frac{e^2}{r_{ij}}$$

However simplified this operator appears to be, exact solutions to the Schrödinger equation exist only for the hydrogen atom or hydrogen-like atoms which contain a single electron. The introduction of more electrons introduces both mathematical and conceptual complexity in finding exact solutions to such an equation. The maximum complexity arises from the question of how one electron's motions are correlated to the motion of each of the other electrons. Numerous ways to approximately represent electron correlation have been made for multi-electron systems and each has its own associated merits and de-merits. At this juncture, it is worth noting that the merit of a computational method not only lies in how

accurately it describes the real system, but also in the computational feasibility of the calculations required to obtain this accurate description.

Wavefunctions for the electronic orbitals are in the general form $\exp(-r/a)$ where 'r' is the radial distance from the nucleus and 'a' is the first Bohr radius. However for many electron systems overlapping wavefunctions of this form are not analytically integrable and numerical integration is an impractical alternative. However, functions of the Gaussian form: $\exp(-r^2)$ do have analytical solutions for their overlap integrals and are used to approximate the electronic orbitals. To improve the accuracy of such a representation, a linear expansion of normalised, linearly independent Gaussian functions (ϕ_i), with weighted coefficients (c_i) are used to represent the actual wavefunctions via a summation.

$$\Psi = \sum_{i=1}^n c_i \phi_i$$

Each wavefunction is a function of three space variables. Hence, if each wavefunction represented an electron, a system with N electrons would be a function of 3N coordinates; apart from the space variables, the spin of each electron needs to be included. Moreover, a greater number of Gaussian basis functions (ϕ_i) in the expansion provide a more accurate description of the wavefunction Ψ . As a consequence, the computational demand for systems containing many atoms and therefore electrons becomes larger and larger if accurate solutions are to be derived for the ground state properties of the system. This limitation coupled with the question of how to deal with electron correlation was largely responsible for the birth of a totally different and intuitive way to study the electronic structure of matter: Density Functional Theory (DFT).

DFT was founded in 1964 by Hohenberg and Kohn who ingeniously proved that the total electron density $\rho(r)$ was a meaningful and comprehensive variable to work with in order to obtain all the necessary information and properties of a system. Hence, instead of operating

on the wavefunction which is neither a physical observable nor intuitively simple to picture, the Hamiltonian operator operates on $\rho(\mathbf{r})$. Moreover, the integral of $\rho(\mathbf{r})$ over all space provides the total number of electrons in the system. The entire construct was based on two fundamental theorems. The first theorem states that the ground state energy obtained from the Schrodinger equation is a functional of a unique electron density $\rho(\mathbf{r})$. This theorem established a one-to-one mapping between the external potential and the electron density. The second theorem focuses on the minimisation of this energy and states that the true electron density is the one that corresponds to the minimum energy for the given external potential.

However simple this might sound, visualising the energetics of complex systems and geometries through the electron density revolutionised computational chemistry. Not only did density functional theory make way for lower computational cost to the calculations for large systems, it also provided excellent approximations to the elusive electron correlation term. A classic example of a many electron system lacking any symmetry is an actinide complex with organic extractants. On these occasions DFT provides an excellent compromise between accuracy, computational cost and ease of interpretation.

Metal-ligand affinity and binding is a complex phenomenon in the sense that there are combinations of factors which govern these interactions. Electronic factors like the nature of bond, and steric factors like structure of ligand close to the binding site and solvation number are some of the parameters that influence the complexation energetics. However, the role of complexation energy and its influence on the extraction efficacy and specificity cannot be underestimated⁷⁵⁻⁸⁰. The steric and electronic factors that operate during the complexation can be understood clearly by electronic structure calculations within the framework of DFT. Various research groups have explored actinide complexation both theoretically⁸¹⁻⁸⁴ and experimentally with organic ligands⁸⁵⁻⁸⁸ including phosphorous containing extractants⁸⁹⁻⁹². Particularly complexes of uranium with thiophosphinates⁹³, phosphonates^{94,95}, phosphinates

⁹⁶ and phosphonic acid ⁹⁷ have been explored to a greater extent. Interactions of uranium with organophosphorus ligands have also been explored quantum mechanically to understand its structure and binding affinities^{90,91}. The present work employs DFT to interpret experimental findings and goes further to predict extraction trends and mechanisms in some of the systems. The work done in this thesis predominantly pertains to the examination of alternate organophosphorous extractants and their application in solvent extraction and extraction chromatography for actinide extraction. Though the alternatives are not intended to replace TBP for spent fuel reprocessing, the new extractants are synthesised and their solvent extraction behaviour with actinides are explored to employ them as potential candidates for various other applications in nuclear fuel cycle, e.g. U/Th separation. The difference in extraction and specific binding for different metal–extractant systems may be correlated to the theoretical binding energetics. Therefore, apart from experiments, density functional theory (DFT) studies of actinides complexes using these novel extractants have also been carried out. The significant influences of electronic structure of extractants on the tautomeric mechanisms, deformation energies, intra-molecular interactions and complexation trends have been elucidated using the quantum chemical calculations.

1.7 Scope of the present work

Currently, nuclear energy almost solely relies on the fission of uranium, of which 42% is mined from secondary reserves⁹⁸. Owing to the abundance of thorium ores in countries like Canada, India, and Germany among other nations, researchers have envisioned thorium powered nuclear programmes and are making it a fast realizable dream^{2,99,100}. Thorium used for fuel, demands that it be of high purity, and made available in sufficient quantity which is required by its fuel cycle. These demands are achievable by solvent extraction process where TBP is currently used as an extractant in its separation from monazite¹⁰¹. The processing of thorium based spent nuclear fuels by THOREX/Interim-23 process also employs TBP as an

extractant¹⁰². The uranium obtained after separation in the THOREX and Interim-23 processes is invariably contaminated with thorium, which gets co-extracted and needs several stages of scrub for its removal. Further, uranium obtained requires additional purification by ion exchange or precipitation¹⁰³⁻¹⁰⁵. Tri-sec-butyl phosphate (TsBP) shows higher U/Th separation factor compared to TBP owing to its higher extraction of U(VI) due to the increased basicity of the phosphoryl oxygen. To employ TsBP for U/Th separation, it is essential to understand its extraction behaviour with respect to Th(IV). In the processing of irradiated thorium fuel / thorium blanket of FBRs / extraction of Th from monazite, the concentration of Th(IV) is always much higher than U(VI). In this thesis, the extraction behaviour of Th(IV) has been examined using TsBP, a branched isomer of TBP. The properties of the organic phase *viz.* Th(IV) concentration, acidity and density have been measured as a function of aqueous Th(IV) concentration over a large range. U/Th separation has been conventionally achieved by solvent extraction using TBP.

The success of a thorium based fuel cycle rests on the processing of thorium ores as well as the separation of uranium from thorium in the processing of the ²³³U-²³²Th mixtures formed in the nuclear reactor. Monazite, a major ore of thorium also contains small amounts of uranium¹⁰¹. Separation of uranium from a thorium matrix is essential for the utilization of thorium for the nuclear fuel cycle. Typically the amount of Th is about 800 times higher than that of uranium both in monazite as well as in the ²³³U-²³²Th mixture, where ²³³U is formed by neutron capture in a nuclear reactor. In this work selectivity for U(VI) over Th(IV) with TsBP has been investigated due to its combined structural and electronic effects close to the binding site. Systematic and comprehensive studies at both liquid-liquid as well as solid-liquid interfaces have been carried out under a wide range of experimental conditions.

In addition to solvent extraction, chromatography is a versatile separation method extensively employed by analytical chemists¹⁰⁶. Remarkable separation of elements from aqueous media

with higher acid concentrations have been achieved by extraction chromatography¹⁰⁷. A number of extractants such as TBP¹⁰⁸, di-(2-ethylhexyl)phosphoric acid¹⁰⁹, di-(2-ethylhexyl) dithiophosphoric acid¹¹⁰, diamylamyl phosphonate¹¹¹, have been used in the past for the recovery of metal ions from aqueous solutions. Different parameters such as surface area, pore size and the chemical nature of the support material can influence the behavior of extractants coated on to an inert support. The extraction of metal ions by extractants physically impregnated on to a solid support, are achieved by this technique. Extractant molecules are adsorbed by van der Waals interactions on the resin surface. This weak interaction enables the capacity of extraction chromatographic resins to be fine tuned by varying the percentage of the extractant. Both inorganic and organic materials *viz.* silica gel¹¹²⁻¹¹⁵, cryptomelane-type hydrous manganese dioxide¹¹⁶, styrene-DVB copolymer¹¹⁷, poly(4-vinyl pyridine)¹¹⁸, etc. have been employed as supports depending on the requirement. Warshawsky *et. al.* have demonstrated the excellent capacities of the polymeric adsorbent, Amberlite XAD series resins for various extractants¹¹⁸ and this has been chosen in the present study. For the first time, TsBP modified chromatographic columns have been employed for this purpose. Strategically optimized conditions of loading and elution stages for varying U/Th feed ratio were examined and employed to demonstrate the feasibility of a specific ligand coated column for the tail-end purification of aqueous product containing U(VI) and Th(IV).

Third phase studies on the Th(IV) using SANS have been carried out and also compared with the U(VI) system. The variation in the SANS profiles, stickiness parameter and attraction potential energy have been examined as a function of three parameters influencing third phase formation phenomena. The effects of extractant, metal ion concentration and temperature have been systematically investigated. Our studies using SANS indicate prediction of third phase formation behaviour and these results are discussed.

The extraction of tetravalent cerium by TBP from nitric acid is important historically for rare-earth-element refining and also finds immediate application in nuclear fuel reprocessing¹¹⁹,¹²⁰. The tetravalent oxidation state of cerium is particularly of interest in the context of the nuclear fuel cycle due to its chemical similarity with Pu(IV), as observed in aqueous solutions¹²¹, solid state¹²² as well as quantum mechanically¹²³. Extraction isotherms of Ce(IV), however, are challenging to obtain, mainly because of the strong oxidizing power of tetravalent cerium which gets converted to Ce(III) readily. The extraction system is further complicated by the formation of third phase, whose composition is not fully understood¹²⁴. In this light, in a preliminary study, third phase formation behaviour of Ce(IV), which is chemically very similar to Pu(IV) and often used as surrogate for Pu(IV) has been examined in this work.

Studies in the past have mainly been on phosphate ligands, and little has been explored on phosphonates, and particularly H-phosphonates. In general, higher homologues within a given class of compounds have been examined, but not the effects of branching at different positions in the alkyl chain in phosphonates. In this context, members of the organophosphorous family, namely phosphonates have been examined for the structural effects of carbon chains on the extraction behaviour towards actinide ions. Changes in the carbon chain structure and length in dialkylalkyl phosphonates have been systematically examined during the extraction of U(VI), Th(IV), Pu(IV) and Am(III). The dual, pH dependent *keto-enol* extraction mechanisms shown by H-phosphonates have also been investigated.

Electronic structure calculations in the framework of DFT have been carried out to elucidate the steric and electronic factors that operate during metal-ligand complexation. The preferential complexation of U(VI) over Th(IV) with TsBP compared to TBP has been addressed. Calculations on dialkylalkyl phosphonates validated the experimental effects of

the carbon chain length on the extraction ability towards actinides which is modulated by the varying basicity of the phosphoryl group. Binding energy of branched H-phosphonates with U(VI) and Am(III) has been explored. Further the keto and enol mechanisms of extraction have been considered for the complexation studies with U(VI). Ce(IV) complexes with TBP and TsBP and Ce(III) complex with TBP has been optimised and employed for complexation energy calculations. The change in the oxidation state of the metal ion reverses the experimental extraction trends and this has also been corroborated by the theoretical study. Beyond binding energy calculations, for the first time, the difference in third phase formation tendency has been rightly indicated by theoretical calculations and Ce(IV) system with TBP and TsBP has been used as an example.

The success of the theoretical calculations in validating experimental trends motivated a further step to use DFT in a predictive form. Quite often quantum chemistry has been highly successful in predicting new molecules or phenomena, which subsequently have been validated experimentally not only for usual chemical systems¹²⁵ but also for various actinide-lanthanide complexes^{126, 127}. One of the factors that determine the stable geometries and energetics of reacting systems is hydrogen-bonding stabilisation. Among different types of weak hydrogen bonds, the CH \cdots O variant has received significant attention over the past several decades¹²⁸⁻¹³². Apart from conventional molecules and biological macromolecules, hydrogen bonding has been shown to play an important role in the adsorption and separation processes involving metal-organic frameworks¹³³⁻¹³⁵. Recently, the strong effect of non-covalent interactions and particularly synergistic role of hydrogen-bonding in various coordination compounds have been reviewed comprehensively^{136, 137}. These have elaborated on the hydrogen bonding mediated stabilisation of unusual geometries, including intermediates and the selective activation of normally inactive ligands. Hydrogen bonding in the stabilisation of transition metal complexes^{138, 139} and also in the bridging of

organophosphorous compounds of the phosphine family¹⁴⁰ have been reported. However, reports on the role of hydrogen bonding in the complexation of actinides or stabilization of actinide complexes are not many in the literature^{88, 141-144}. In this context, Raymond and co-workers¹⁴⁴ proposed that tailor-made ligands can be designed by exploiting the functional groups present in the ligand in order that a desired metal-ligand complex can be preferentially stabilized through hydrogen-bonding interactions thereby leading to selective extraction of a particular metal ion from a mixture. This aspect is very important especially in the nuclear industry where valuable metal ions need to be extracted and long-lived radioisotopes are to be separated for efficient management of nuclear wastes. In this light, uranyl complexes with branched H phosphonates with the amyl carbon chain have been used as a model system for binding energy predictions. Theoretical calculations are taken-up on the stability for a uranyl nitrate complex with a branched ligand, as compared to the compositionally analogous uranyl nitrate complex with the linear chain ligand. The weak hydrogen-bonding interactions leading to the stabilisation of the uranyl complex with the branched isomer have been examined. The theoretical predictions are experimentally verified by carrying out solvent extraction studies. In addition to predictions founded on weak interactions such as hydrogen bonding, the bond between the actinide and ligand can be theoretically analysed to shed light on the actinide specificity of ligands. A potential application of such an analysis lies in the quest for ligands towards minor actinide partitioning. Minor actinides *viz.* Am, Cm and Np are very similar to lanthanides (occur as fission products) in their chemical behaviour. The metal-ligand interaction at the molecular scale is important to select suitable ligands to partition minor actinides from fission products. Spent nuclear fuel contains a variety of isotopes, of which the un-burnt fuel materials uranium and plutonium are recovered and recycled¹⁴⁵⁻¹⁴⁷. In the remaining elemental mixture which is disposed as nuclear waste, lanthanides form the largest proportion¹⁴⁸. Neutron capture by uranium and plutonium in the reactor, produce minor

actinides such as Am, and Cm. These actinides along with some of their daughter products are long-lived alpha emitters, making the nuclear waste more hazardous as well as increasing the waste storage time. Partitioning of minor actinides from lanthanides is vital both in terms of the safe storage of nuclear waste, as well as for the transmutation of minor actinides to reduce their radio-toxicity¹⁴⁹⁻¹⁵¹. Some lanthanides are neutron poisons (Sm and Gd) and their presence does not allow effective transmutation of the actinide element by neutron bombardment^{152, 153}.

The early actinides can be separated from trivalent lanthanide elements by exploiting their characteristic to exist in multiple oxidation states¹⁵⁴⁻¹⁵⁶. However, along the actinide period the 5f orbital tends to become increasingly localised making the trans-plutonium actinides very lanthanide-like in their chemistry¹⁵⁷. The predominant trivalent oxidation state of heavier actinides, coupled with the similarity in ionic radii with lanthanides places higher demands on ligand specificity for their separation¹⁵⁸⁻¹⁶⁰. Nevertheless, a saving grace is the relative diffusivity of the 5f orbitals compared to 4f, which in turn enables more covalent interactions of actinides with soft donor ligands compared to those seen in the equivalent lanthanide complexes. It has been found that the cyanex class of compounds have displayed good separation factors for Am(III) and Cm(III) over the lanthanide elements⁷⁷. Cyanex 301^{152, 161, 162} with two S donor sites, cyanex 272^{163, 164} with two oxygen donor sites and cyanex 302^{164, 165} with mixed S and O donor sites have been investigated and proved successful for the separation of the minor actinides¹⁶². Energy decomposition analysis (EDA) of complexes of cyanex 301 with trivalent Am, Eu, La and Lu have been carried out by Bhattacharya *et. al.* and showed that there is greater covalency in the Am complexes compared to the three lanthanides⁷⁷. The ability of cyanex 301 to separate Am³⁺ from lanthanides has been attributed to the increased covalency shown by Am. Recently, Batista

and co-workers tested complexes of Am, Cm, Bk and Cf with dipicolinic acid (DPA) for their thermodynamic property of binding energy ¹⁶⁶.

Furthermore, an octadentate ligand N,N,N',N'-tetrakis[(6-carboxypyridin-2-yl)methyl]ethylenediamine (TPAEN) has been investigated experimentally and found to complex Am(III) and Cm(III) with higher stability constants compared to the lanthanides^{167, 168}. From previous experimental and theoretical reports, it is likely that covalency driven preferential bonding to actinides over lanthanides by certain ligands is a key marker in choosing extractants for minor actinide partitioning. Moreover, elucidation of the nature of chemical bonding in heavy actinide complexes through EDA¹⁶⁹ has never been reported in the literature. It is worth mentioning that EDA has been highly successful in the elucidation of nature of bonding in various chemical systems including metal-ligand complexes¹⁷⁰⁻¹⁷⁵. In this thesis, the actinide-ligand interaction energy is explicitly decomposed into Pauli repulsion, electrostatic interaction and orbital interaction which are related to covalency of the bond. Through this the covalency in heavy actinide (Am, Cm, Bk and Cf) complexes has been investigated for the DPA, TPAEN and Cyanex class of extractants.



Chapter 2



“Attitude is a little thing that makes a big difference”

~ Winston Churchill

EXPERIMENTAL

2.1 Materials

Extractants: Tri-*n*-butyl phosphate (TBP) was obtained from Sigma Aldrich and used after washing with dilute sodium carbonate solution (0.2 M) after which the impurities and the residual base were removed by washing with distilled water. The extractants, TsBP, TiBP and TsAP have been synthesized by condensation reaction between POCl₃ with stoichiometric equivalent of corresponding alcohol in the presence of pyridine^{60, 63}. After synthesis, the product was washed with 0.2M sodium carbonate solution and water. It was further purified by distillation under reduced pressure. The absence of acidic impurities, such as dialkyl and monoalkyl phosphoric acids, in TBP and TsBP, was ascertained by measuring the D values for the extraction of U(VI) from 0.01M HNO₃ medium into a 0.183M solution of trialkyl phosphate in *n*-DD. Phosphorus trichloride (Fluka), 1-butanol, iso-butanol, sec-butanol (Merck), toluene, iso-amyl alcohol (Merck), iso-butyl bromide, iso-amyl bromide, bromohexane, bromobutane were obtained from Lancaster.

Solvents: Diluents dodecane (DD) and deuterated dodecane (C₁₂D₂₆) (Lancaster synthesis Ltd., England) were used as such without further purification

Resin: XAD -7 resin (Dow Chemicals, USA) was washed with dilute nitric acid to remove metal ion impurities, followed by water and acetone to remove monomer impurities and then dried. 40 wt% TBP/TsBP impregnated resins with XAD-7 were prepared by dissolving the neat extractant in ethanol: water (60:40) mixture, followed by equilibration with XAD-7 resin for 24 hours. Subsequently, the solution was filtered and the resin was dried under vacuum.

Complexing agents: Diethylenetriaminepentaacetic acid (DTPA) and 2,6-Pyridinedicarboxylic acid (PDCA) (Lancaster Synthesis Ltd., England) have been used for

the complexometric analysis of Th(VI) and U(VI), respectively. Ferrous ammonium sulphate and potassium dichromate (Ranbaxy) were used as received.

Indicators: Xylenol orange indicator (TCI, Tokyo, Japan) was used as received. Barium diphenylamine sulphonate (Merck) was used as received.

Metal nitrates: Nuclear grade thorium nitrate (Indian Rare Earths Ltd., Mumbai, India) was used as received without further purification. Nuclear grade uranyl nitrate $\text{UO}_2(\text{NO}_3)_2 \cdot 6\text{H}_2\text{O}$ obtained from Nuclear Fuel Complex, Hyderabad, India, was used as received. Ce(IV) nitrate was prepared by dissolving ceric oxide in hot concentrated nitric acid (16N HNO_3) with the addition of micromole quantities of hydrofluoric acid. The hydrofluoric acid was removed by evaporation and the acidity of the ceric nitrate solution was adjusted to 4M by dilution with 0.5M nitric acid. ^{233}U was purified by extraction in the form of uranyl nitrate from 4M nitric acid with 5% TBP/*n*-dodecane; this was followed by scrubbing with 4M nitric acid and stripping with dilute nitric acid. This procedure was adopted for separation of ^{233}U from impurities and was used as tracer for uranium extraction studies. Am(III) solution was prepared by dissolving Am_2O_3 in concentrated HNO_3 (~16N) and diluting to the desired concentration. The plutonium solution in IV oxidation state was prepared by taking an appropriate quantity of Pu stock in 1M nitric acid. The oxidation state of Pu was maintained as Pu(IV) by the addition of 0.1mL of 2.5M NaNO_2 and Pu(IV) was extracted with 0.5M TTA/xylene. The organic phase containing Pu(IV) was scrubbed with 1M HNO_3 and stripped with 8M HNO_3 . The aqueous phase (strip solution) was washed twice with equal volume of *n*-hexane to remove the entrained organic phase. The stock solution was used for preparing aqueous Pu(IV) solutions for solvent extraction experiments.

Feed solutions: The feed solutions used for the solvent extraction and extraction chromatography studies were prepared by carefully mixing the required quantities of U(VI)

and Th(IV) stock solutions and then adjusting the acidity by adding calculated amounts of 16M HNO₃.

2.2 Instruments

A Shimadzu model UV-3600 spectrophotometer with a wavelength range of 200-800 nm and a quartz cuvette with a path length of 1 cm were used for measuring the absorbance of various metal complexes.

Infrared spectra were recorded in the range 4000 to 600 cm⁻¹, using a Bruker Alpha table top FTIR spectrometer, operated in ATR mode with a resolution of 2 cm⁻¹. ¹H and ³¹P [¹H]-NMR spectra were recorded by BRUKER DMX-400 and all ¹H chemical shifts were reported relative to the residual proton resonance in deuterated solvents (all at 25°C, CDCl₃). H₃PO₄ was used as an external standard for ³¹P [¹H]-NMR.

The H-phosphonates were analysed for their molecular weight using a Perkin Elmer GC-MS instrument. Infrared spectra of the samples were recorded in the range 4000 to 500 cm⁻¹, using a Vertex 70 FTIR spectrometer, operated at a resolution of 0.5 cm⁻¹ using liquid N₂ cooled mercury cadmium telluride (MCT) detector.

ESI MS analysis was carried out using an Applied Biosystems 3200 QTRAP LC/MS/MS system in the mass range of m/z 80 to 1700. Optimized conditions were as follows: Ion spray Voltage 3.2 kV; Declustering Potential (DP) 50 V, Entrance Potential (EP) 10 V.

2.3 Experimental methods

Preparation of extractant solutions in dodecane

The required molarity of extractant solutions in dodecane were prepared by taking an appropriate quantity of extractant (on weight basis) in a standard flask, and making up the volume with dodecane. Prior to solvent extraction experiments, the extractant solutions were washed by equilibrating with 5M NaOH for two hours to remove any acidic impurities present in the extractant. The NaOH traces were removed from the organic phase by washing

it several times with water until the wash water was nearly neutral. The purity of the extractants was established using gas chromatographic technique (> 98%).

Extraction of metal nitrates

A solution of metal nitrate in HNO₃ medium was equilibrated with an organic phase (required molarity of extractants in *n*-DD). Equal volumes of aqueous and organic phases along with a magnetic stirring bar were taken in an equilibration tube. During these experiments, temperature was maintained at 303K by placing the flask in a water bath contained in a double walled jacket. The two phases were equilibrated for 30 minutes by stirring at a speed enough to mix the two phases. During equilibration, some of the acid gets extracted to the organic phase and aqueous acidity decreases. Acidity of the aqueous phase was maintained at the required concentration by adding few drops of conc. nitric acid (16M) and equilibrating again such that the final equilibrium aqueous concentration of acid was as required. The aqueous and organic phases were allowed to separate and settle before the aliquots were pipetted out. Microlitre glass pipettes of the required capacities ranging from 25 – 500 μ L were used to pipette the aliquots of desired volume required for the analysis of U(VI), Th(IV) and H⁺ in the organic and aqueous phases. The third phase and diluent phase volumes at equilibrium were measured by dividing the total mass of the organic phase by its density to find out V_{DP}/V_{TP} ratio.

For the SANS studies, concentrations of thorium and nitric acid were adjusted such that the equilibrium aqueous acidity was 1M and the organic phase thorium loading was 20, 30 and 40g/L for each extractant system. These concentrations were chosen such that the organic phase loading does not exceed the LOC, after which the organic phase splits into a third phase and a diluent rich phase⁶³.

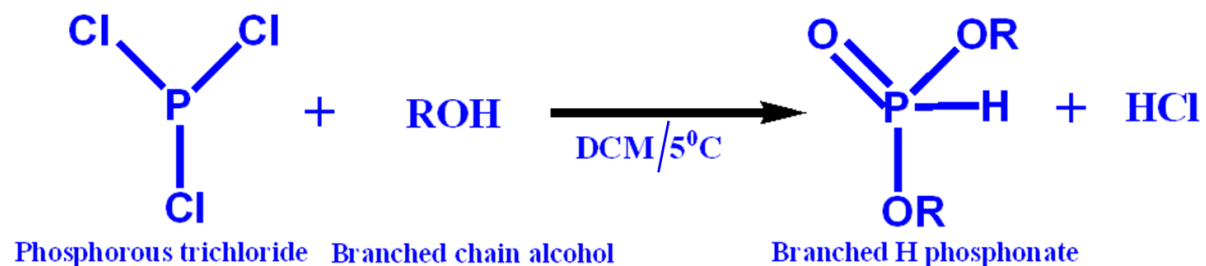
Kinetics of U(VI)/Th(IV) sorption on resin

For the kinetics experiments using coated resins, 2 mL of feed solutions at 4M acidity containing 100ppm of Th(IV) or U(VI) were equilibrated with 100mg of the coated resins and the aqueous metal concentrations were estimated as a function of time. For U(VI) – TsBP kinetic study, a 200ppm U(VI) feed at 4M acid was used as the distribution ratio, “D” values were in general higher in this case.

2.4 Synthesis and characterisation of H–phosphonates

One equivalent of phosphorous trichloride (PCl_3) was dissolved in twice the volume of dichloromethane and stirred in a round bottom flask kept in an ice bath. Three equivalents of the appropriate alcohol (eg. 1-butanol, iso-butanol, sec-butanol) diluted in two volumes of dichloromethane were added drop-wise to the cooled reaction flask. After the addition, the reaction was stirred over-night and then quenched with an ice water mixture. Hydrochloric acid was a by-product, which was removed by washing with sodium carbonate until the wash water was basic. The aqueous and organic phases were subsequently separated using a separating funnel and the organic phase was thoroughly washed with water to remove excess carbonate and any other water soluble impurities. Sodium sulphate was added to the separated organic phase and left to stand in order to remove any moisture present in the organic phase. Finally, organic phase containing the product was placed in a rotary evaporator for 3 hours to remove the volatile solvent (dichloromethane) and other impurities.

The reaction scheme is represented in Scheme 2.1.



Scheme 2.1: Preparation route for H–phosphonates from the starting materials phosphorous trichloride and branched alcohol.

The ^1H and ^{31}P NMR spectra of Dibutyl H-phosphonate (DBHP), Di-iso-butyl H-phosphonate (DiBHP), and Di-sec-butyl H-phosphonate (DsBHP) are furnished (Figures 2.1-2.6 and the structure of the corresponding phosphonates is provided in the insets).

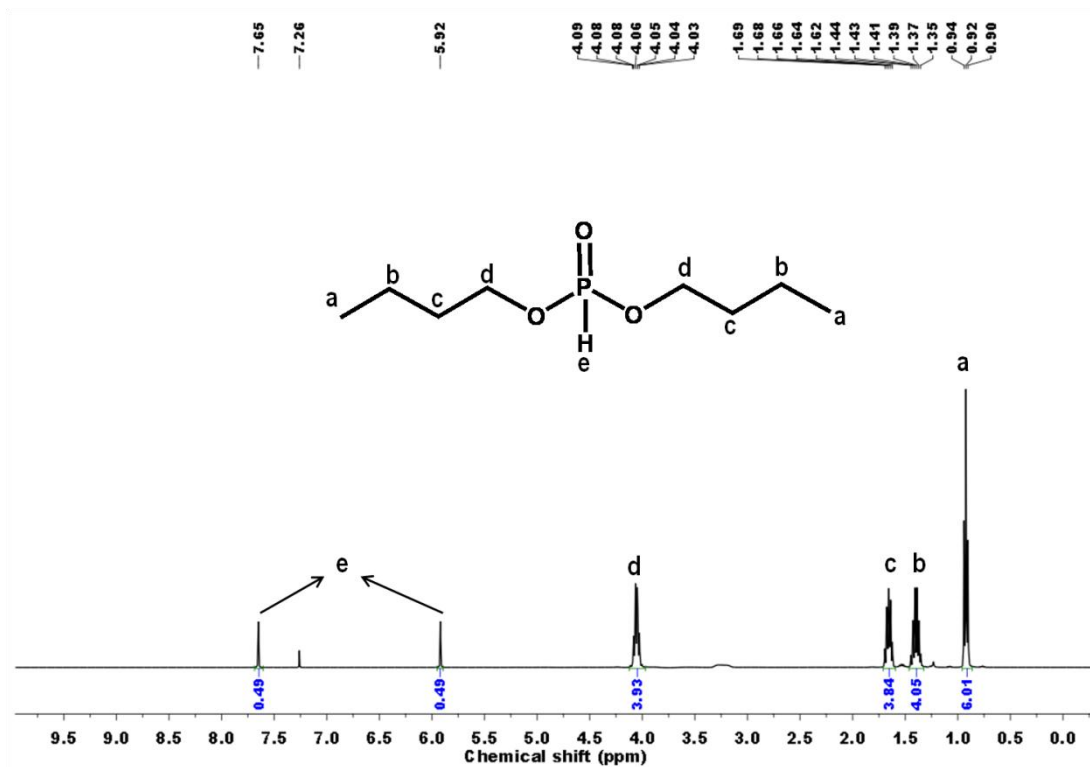


Figure 2.1: ^1H NMR spectrum of Dibutyl H phosphonate (DBHP)

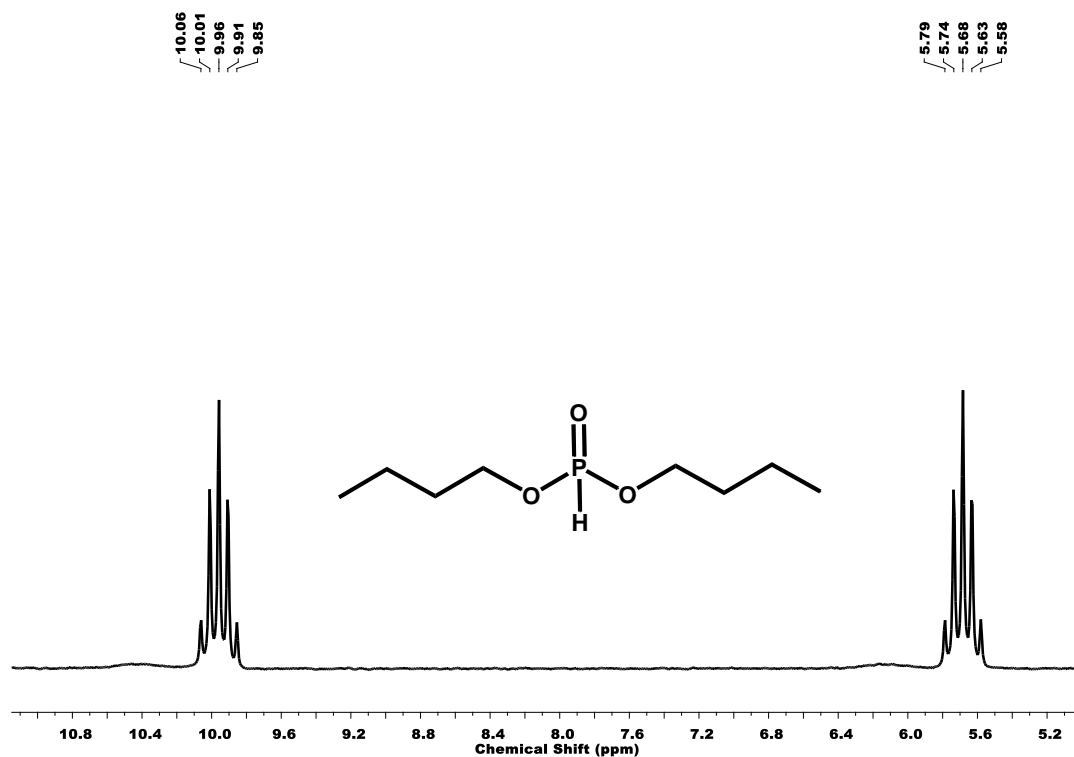
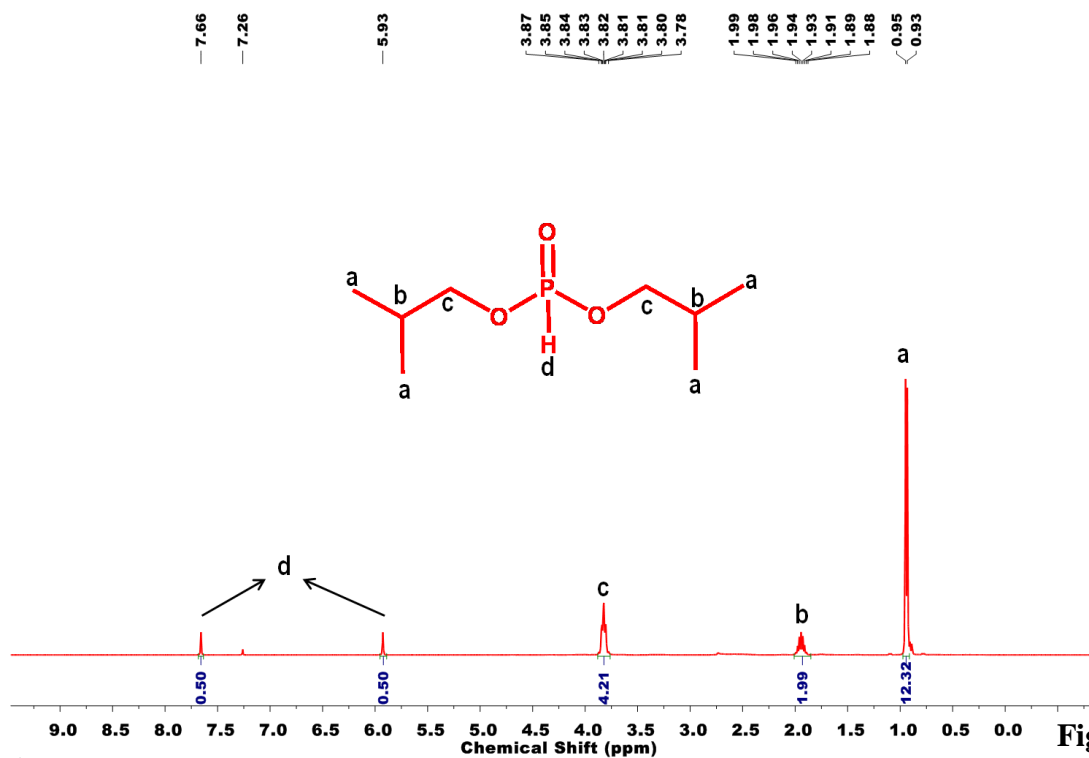


Figure 2.2: ^{31}P NMR spectrum of Dibutyl H phosphonate (DBHP)



2.3: ¹H NMR spectrum of Di-iso-butyl H phosphonate (DiBHP)

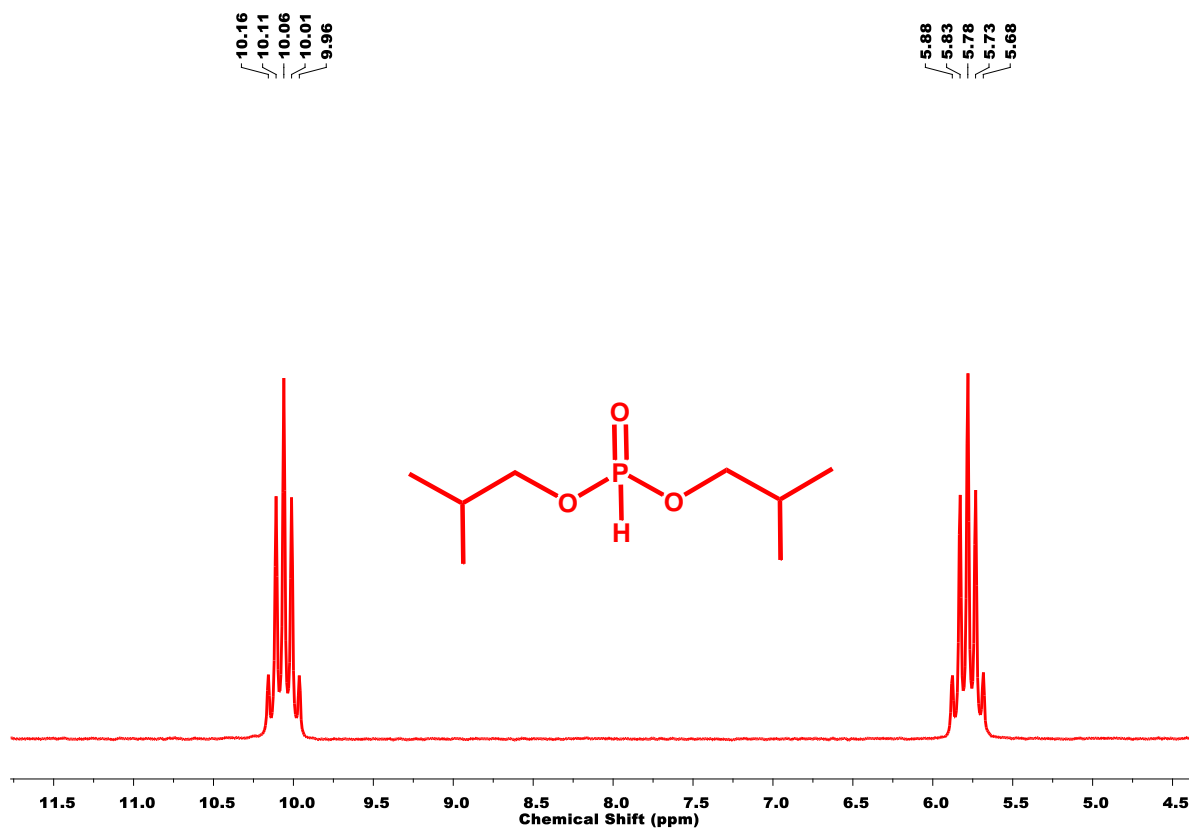


Figure 2.4: ³¹P NMR spectrum of Di-iso-butyl H phosphonate (DiBHP).

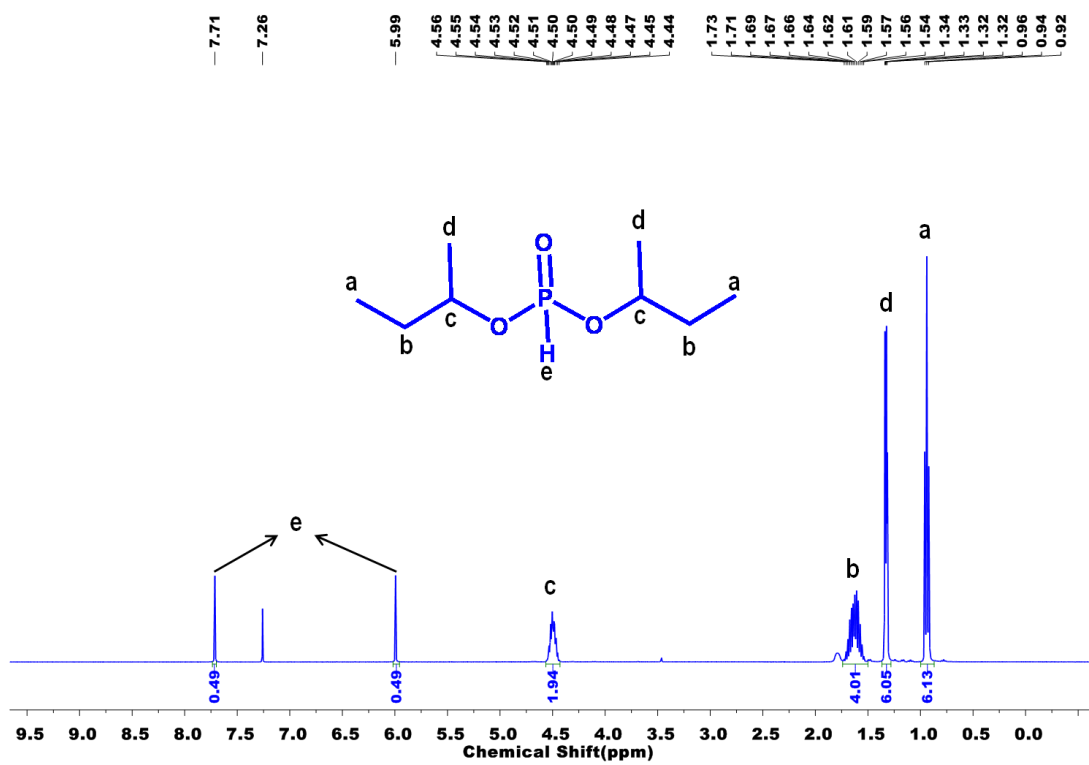


Figure 2.5: ¹H NMR spectrum of Di-sec-butyl H phosphonate (DsBHP)

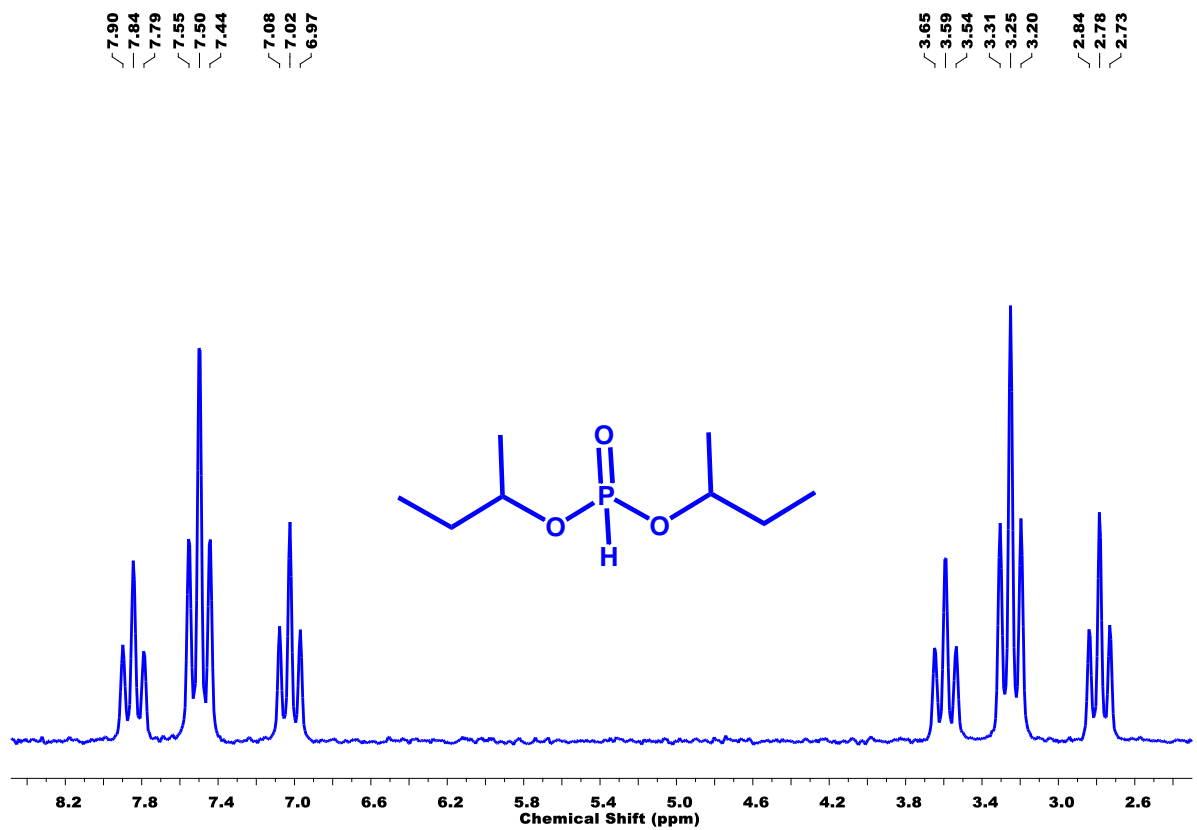


Figure 2.6: ³¹P NMR spectrum of Di-sec-butyl H phosphonate (DsBHP).

DBHP: DBHP was obtained by the reaction of 0.3 moles of PCl_3 and 0.9 moles of 1-butanol yielding DBHP as a colourless liquid (yield ~ 90%). ^1H NMR (400MHz, CDCl_3) $\delta=7.65$ and 5.92 (1H, P-H), 4.09–4.03 (4H, P-O-CH₂), 1.69–1.62 (4H, P-O-CH₂-CH₂), 1.44–1.35 (4H, P-O-CH₂-CH₂-CH₂), 0.94–0.90 (6H, P-O-CH₂-CH₂-CH₂-CH₃). ^{31}P NMR(162.01 MHz, CDCl_3) $\delta = 9.96, 5.68$.

DiBHP: DiBHP was obtained by the reaction of 0.3 moles of PCl_3 and 0.9 moles of 2-methyl propan-1-ol yielding DiBHP as a light yellow liquid (yield~90%). ^1H NMR(400MHz, CDCl_3) $\delta=7.66$ and 5.93 (1H, P-H), 3.87–3.78 (4H, P-O-CH₂), 1.99–1.88 (2H, P-O-CH₂-CH), 0.95–0.93 (12H, P-O-CH₂-CH-CH₃). ^{31}P NMR(162.01 MHz, CDCl_3) $\delta=9.96, 5.68$. ^{31}P NMR(162.01 MHz, CDCl_3) $\delta=10.06, 5.78$.

DsBHP: DsBHP was obtained by the reaction of 0.3 moles of PCl_3 and 0.9 moles of 2-butanol yielding DsBHP as a colourless liquid (yield~85%). The ^1H NMR spectra of DsBHP (Fig. 5S in the SI) shows, δ 7.71 and 5.99 (1H, P-H), 4.56–4.44 (2H, P-O-CH), 1.73–1.54 (4H, P-O-CH-CH₂), 1.34–1.32 (6H, P-O-CH-CH₃), 0.96 – 0.92 (6H, P-O-CH-CH₂-CH₃). ^{31}P NMR (162.01 MHz, CDCl_3) $\delta = 9.96, 5.68$.

The proton-coupled ^{31}P NMR spectra of DBHP, DiBHP and DsBHP (Figures 2S, 4S and 6S in the SI) show two signals at $\delta=5.68, 9.96$ (DBHP), 5.78, 10.06 (DiBHP) and 3.25, 7.50 (DsBHP). The P=O group couples with P-H and the corresponding coupling constants are $^1J_{\text{PH}}=693.4$ for DBHP and DiBHP and $^1J_{\text{PH}}=688.5$ for DsBHP. The coupling constant is reduced by 5 units in the case of DsBHP, which indicates that branching near the P=O group has an effect on the P-H coupling.

The GC–MS spectra of DBHP, DiBHP and DsBHP (Figure.2.7–2.9, respectively) are shown. Protonated molecular mass peaks are seen at $m/z = 195$ in the case of all the three extractants DBHP, DiBHP, DsBHP (M. W. = 194).

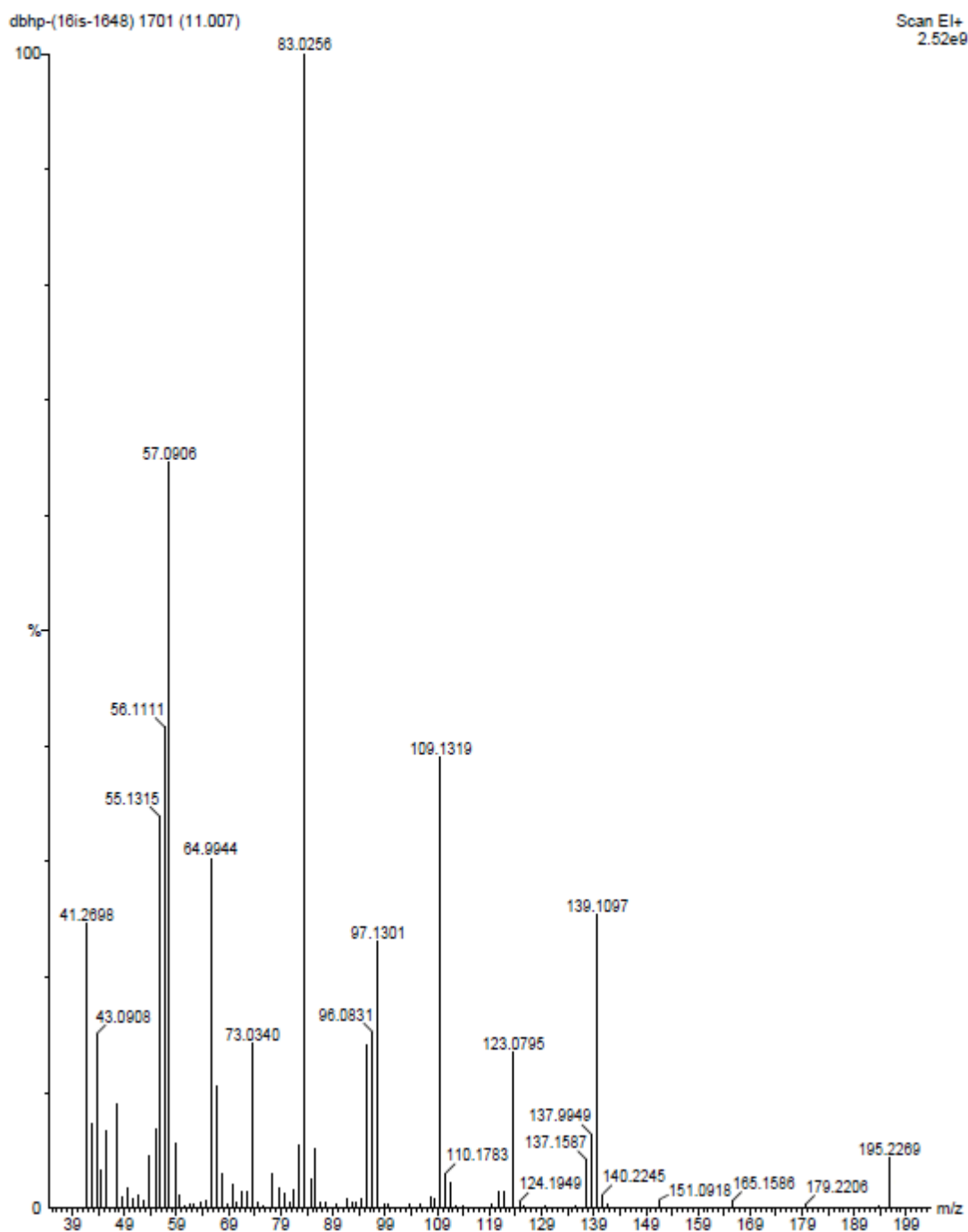


Figure 2.7: GC – MS spectrum for DBHP

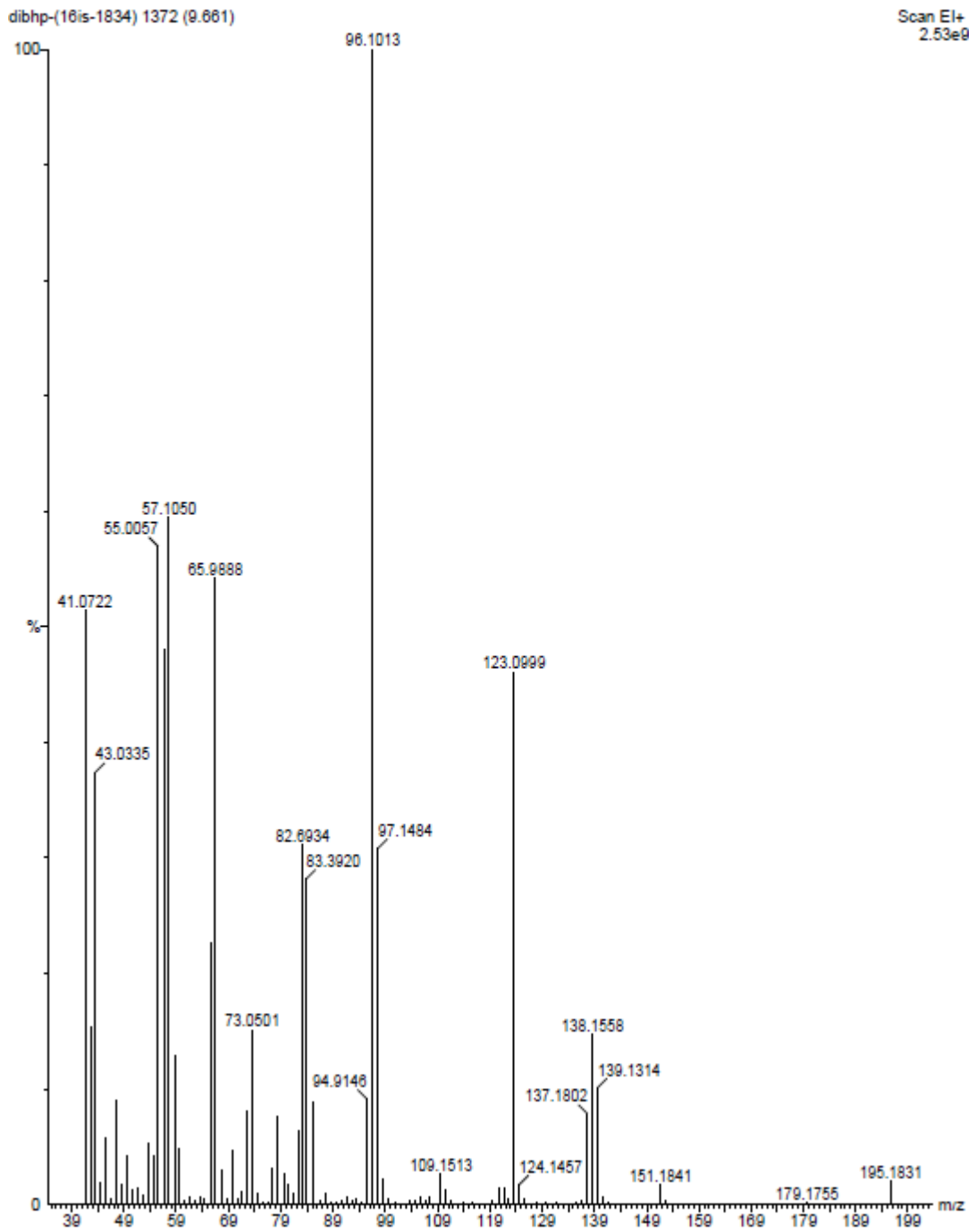


Figure 2.8: GC – MS spectrum for DiBHP

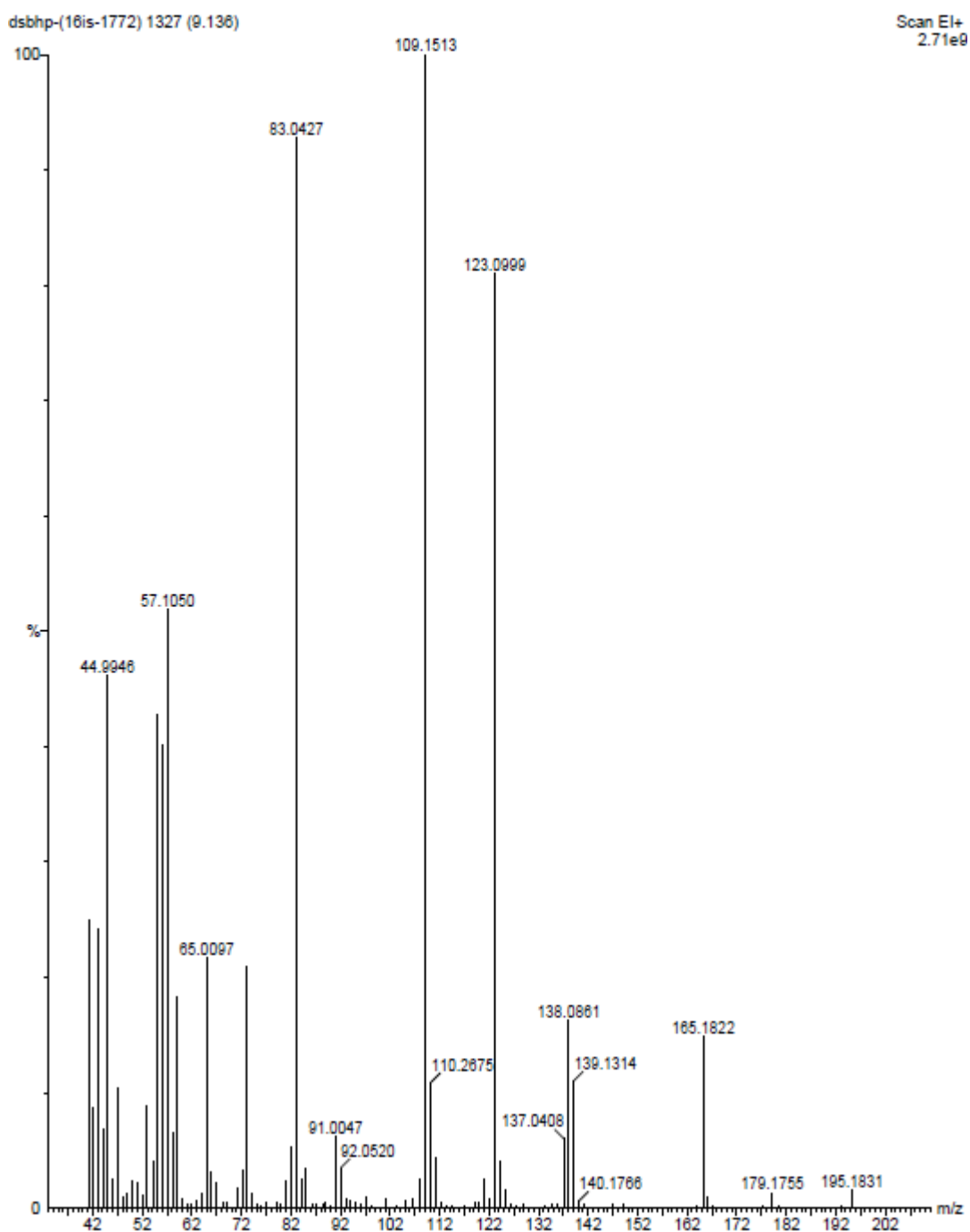


Figure 2.9: GC – MS spectrum for DsBHP

The ^1H and ^{31}P NMR spectra of Diamyl H-phosphonate (DAHP), Di-iso-amyl H-phosphonate (DiAHP), and Di-sec-amyl H-phosphonate (DsAHP) are given (Figures 2.10-2.15) and the structure of corresponding phosphonates is provided in the insets.



Figure 2.10: ^1H NMR spectrum of Diamyl H phosphonate (DAHP)

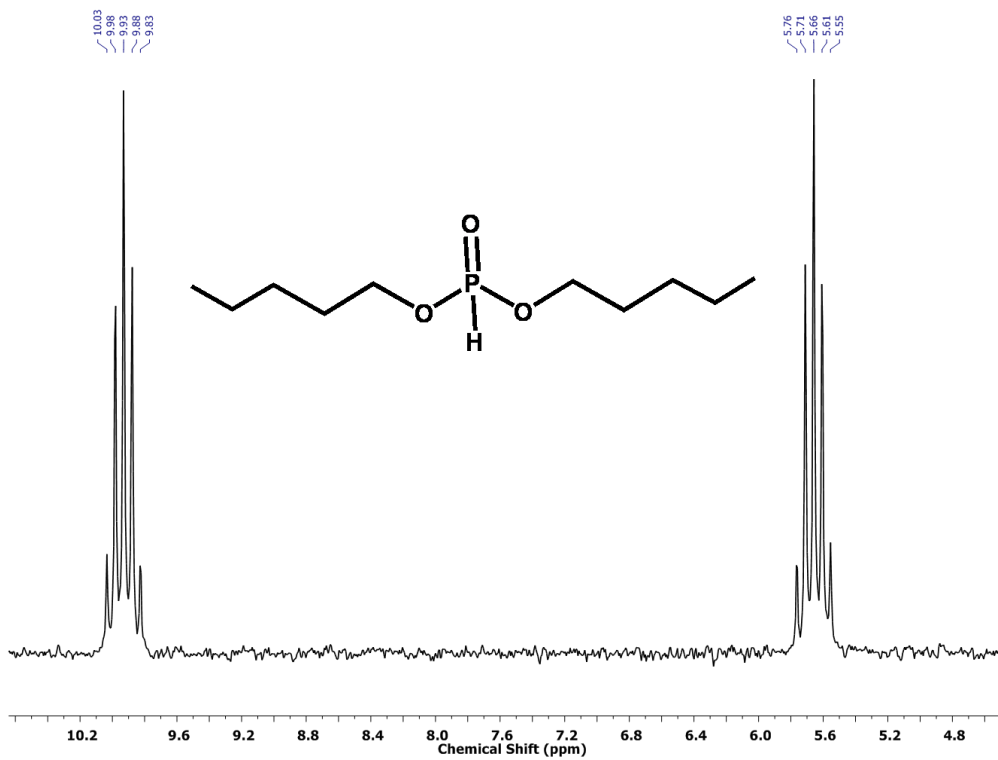


Figure 2.11: ^{31}P NMR spectrum of Diamyl H phosphonate (DAHP)

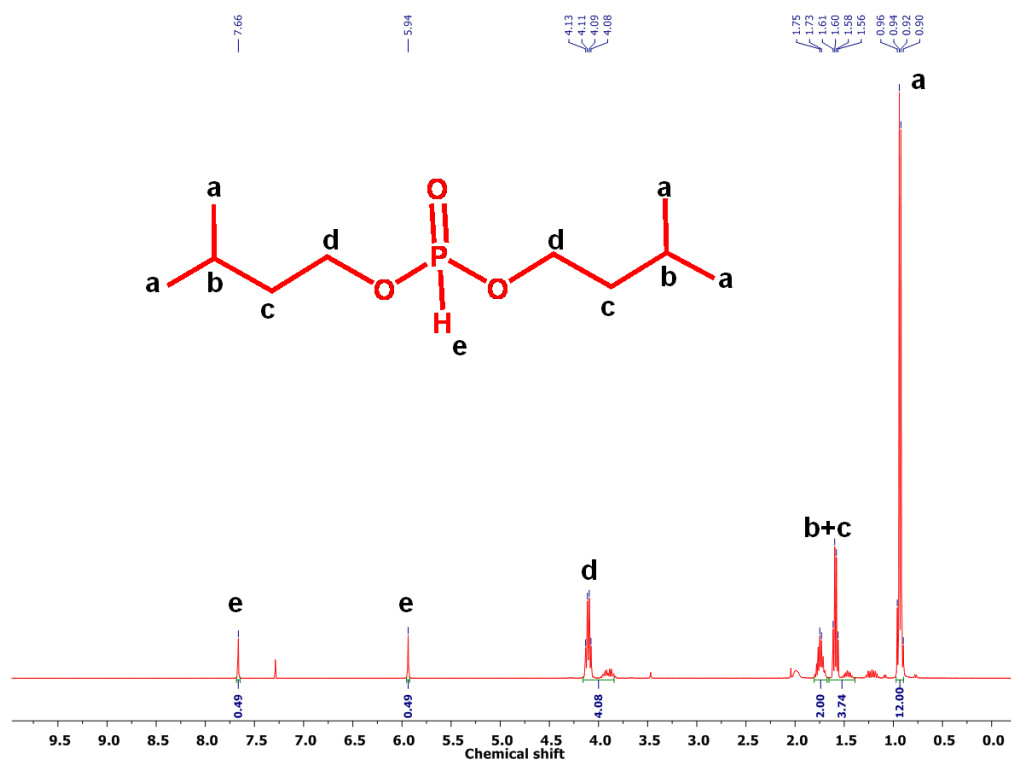


Figure 2.12: ^1H NMR spectrum of Diisooamyl H phosphonate (DiAHP)

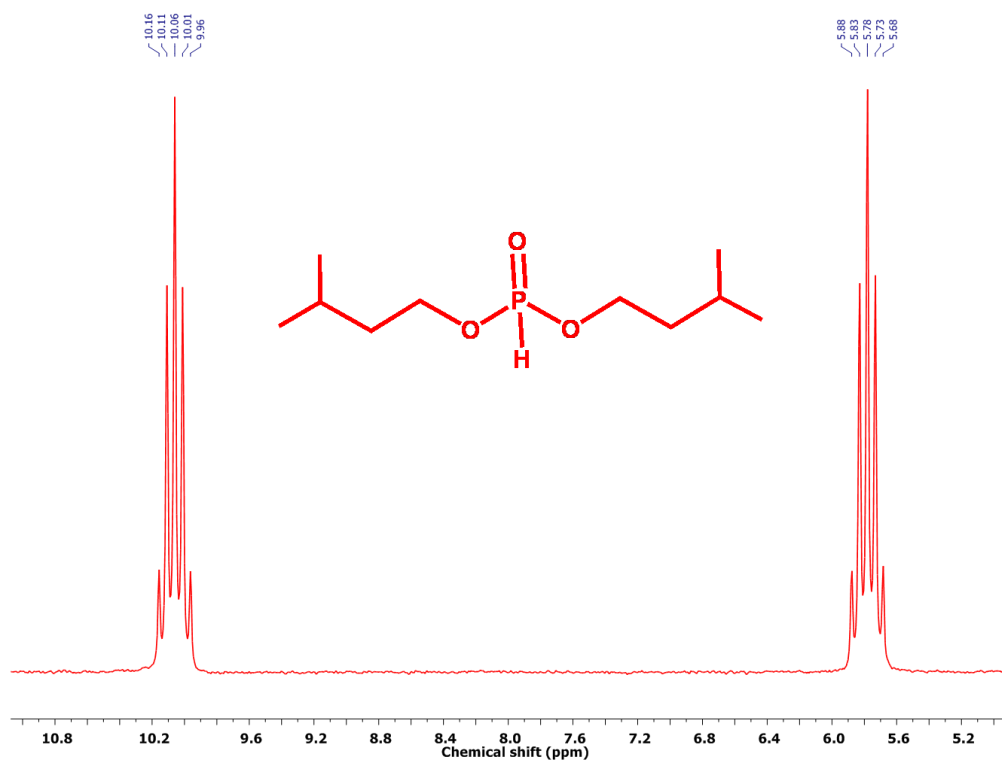


Figure 2.13: ^{31}P NMR spectrum of Diisooamyl H phosphonate (DiAHP).

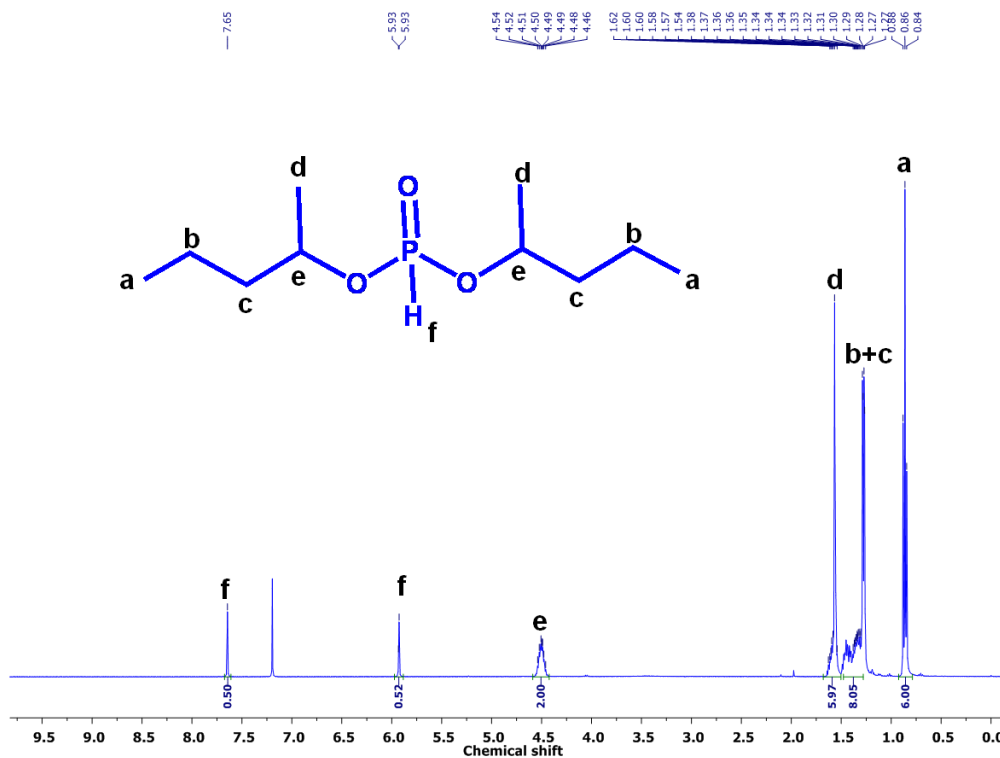


Figure 2.14: ^1H NMR spectrum of Disecamyl H phosphonate (DsAHP)

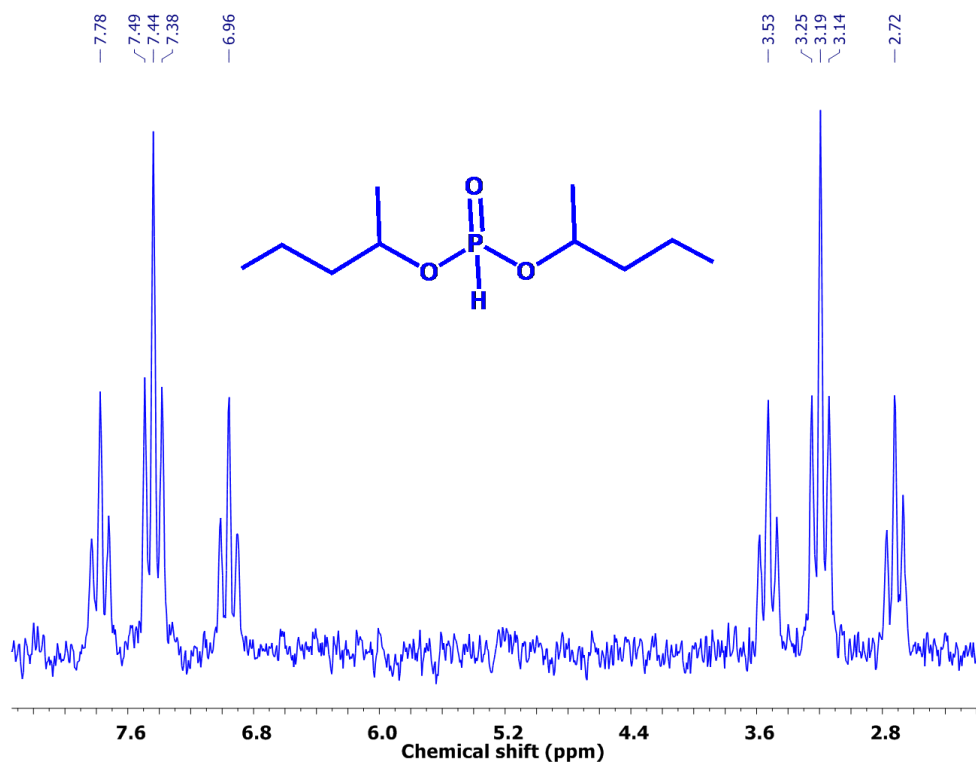


Figure 2.15: ^{31}P NMR spectrum of Disecamyl H phosphonate (DsAHP).

DAHP: DAHP was obtained by the reaction of 0.3 moles of PCl_3 and 0.9 moles of amyl alcohol (1-pentanol) yielding DAHP as a colourless liquid (yield $\sim 70\%$). ^1H NMR (400MHz, CDCl_3) $\delta=7.69$ and 5.96 (1H, P-H), $4.15\text{--}4.02$ (4H, P-O-CH₂), $1.76\text{--}1.66$ (4H, P-

O-CH₂-CH₂), 1.44–1.31 (8H, P-O-CH₂-CH₂-CH₂ and P-O-CH₂-CH₂-CH₂-CH₂), 0.98–0.86 (6H, P-O-CH₂-CH₂-CH₂-CH₂-CH₃). ³¹P NMR(162.01 MHz, CDCl₃) δ = 9.93, 5.66.

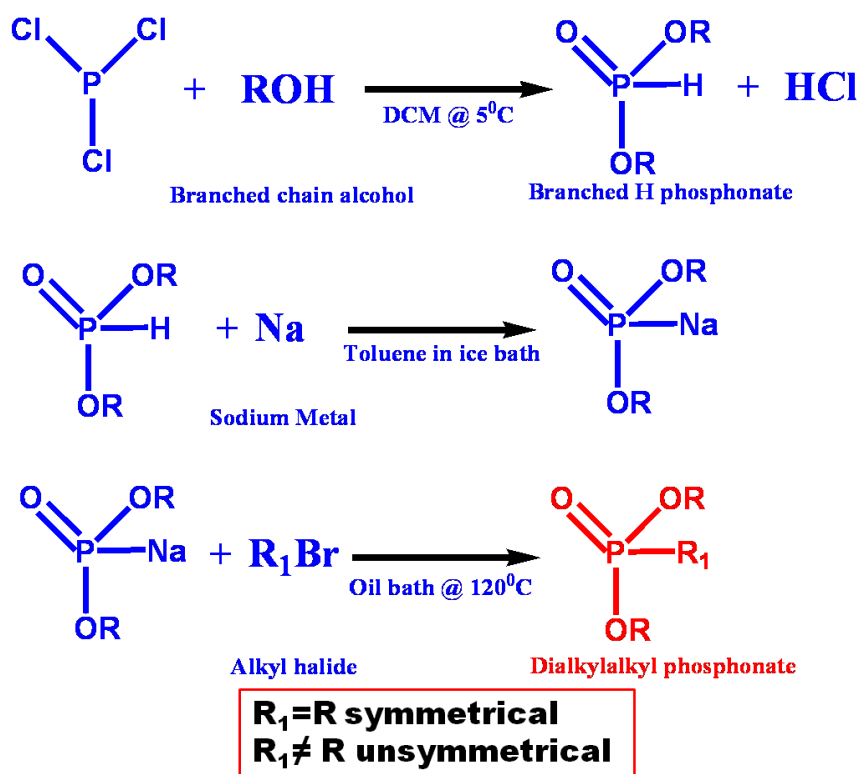
DiAHP: DiAHP was obtained by the reaction of 0.3 moles of PCl₃ and 0.9 moles of isoamyl alcohol (3-methyl butan-1-ol) yielding DiAHP as a light yellow liquid (yield~70%). ¹H NMR(400MHz, CDCl₃) δ=7.66 and 5.94 (1H, P-H), 4.16–3.84 (4H, P-O-CH₂), 1.81–1.67 (2H, P-O-CH₂-CH₂-CH), 1.66–1.39 (4H, P-O-CH₂-CH₂), 0.97–0.90 (12H, P-O-CH₂-CH₂-CH-CH₃). ³¹P NMR(162.01 MHz, CDCl₃) δ=9.96, 5.68. ³¹P NMR(162.01 MHz, CDCl₃) δ=10.06, 5.78.

DsAHP: DsAHP was obtained by the reaction of 0.3 moles of PCl₃ and 0.9 moles of 2-butanol yielding DsAHP as a colourless liquid (yield~65%). The ¹H NMR spectra of DsAHP shows, δ 7.65 and 5.93 (1H, P-H), 4.59–4.42 (2H, P-O-CH), 1.68–1.50 (6H, P-O-CH-CH₃), 1.48–1.28 (8H, P-O-CH-CH₂ and P-O-CH-CH₂-CH₂), 0.93–0.79 (6H, P-O-CH-CH₂-CH₂-CH₃). ³¹P NMR (162.01 MHz, CDCl₃) δ = 7.44, 3.19.

2.5 Synthesis and characterisation of dialkylalkyl phosphonates

Branched dialkylalkyl phosphonates were synthesised from the H-phosphonates obtained by the reaction between PCl₃ and the required branched alcohol (iso-butanol, iso-amyl alcohol). One equivalent of branched dialkyl H-phosphonate was reacted with one equivalent of sodium metal in an inert atmosphere (Ar). 2 to 3 volumes of toluene were used as a solvent medium. The mixture was stirred in an ice bath until the sodium dissolved. Alkyl bromide diluted in toluene was then added drop wise. The mixture was then transferred to an oil bath at 120°C and stirred for an additional 5 hours under an inert atmosphere. The reaction was quenched with ice cold water and the phases separated. Toluene from the organic phase was removed by the rotary evaporator. Dichloromethane was added to the organic phase which was stirred with an equal volume of 4M NaOH for 2 hrs. The product was again placed in a

rotary evaporator until all the solvents were removed. The reaction scheme is shown in Scheme 2.2.



Scheme 2.2: Preparation route for dialkylalkyl phosphonates by a two step reaction between branched H – phosphonate and bromoalkane.

If the alkyl group attached to phosphorous has same carbon chain as in the phospho–ester group, phosphonate is termed as symmetrical. If not, dialkylalkyl phosphonate is termed as unsymmetrical. Hence, DiBiBP and DiAiAP are symmetrical, whereas DiAButylP and DiAHexylP are unsymmetrical.

The ^1H and ^{31}P NMR spectra of Diisobutylisobutyl phosphonate (DiBiBP), Diisoamylisoamyl phosphonate (DiAiAP) and unsymmetrical Diisoamylbutyl phosphonate (DiAButylP) and Diisoamylhexyl phosphonate (DiAHexylP) (Figures 2.16-2.23) and the structure of the corresponding phosphonates is provided in the insets.

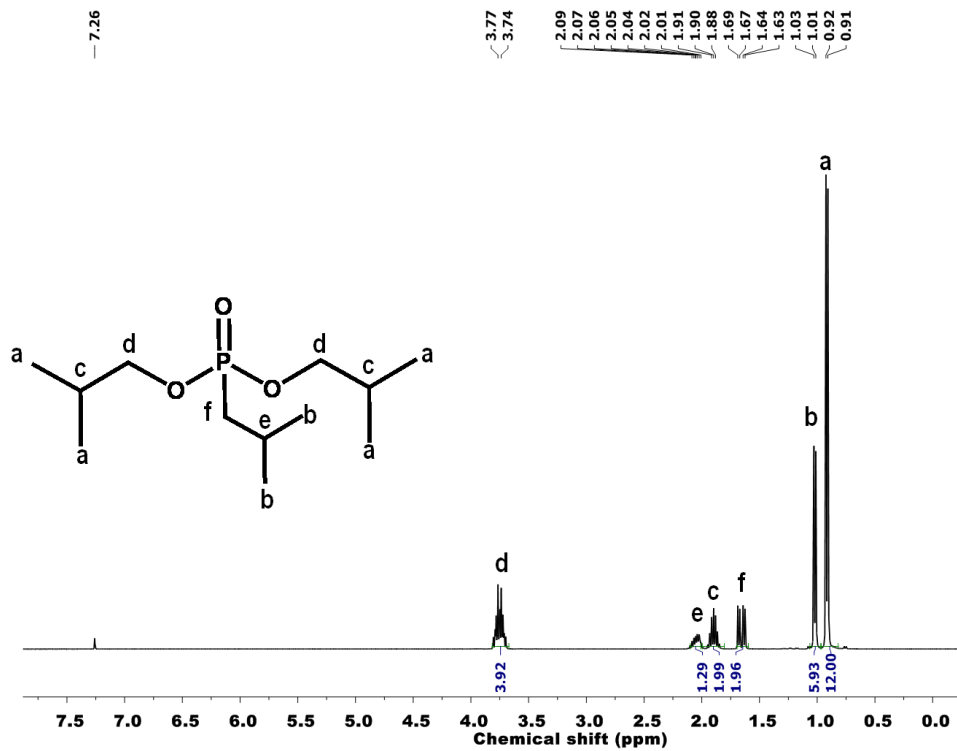


Figure 2.16: ^1H NMR spectrum of DiBiBP

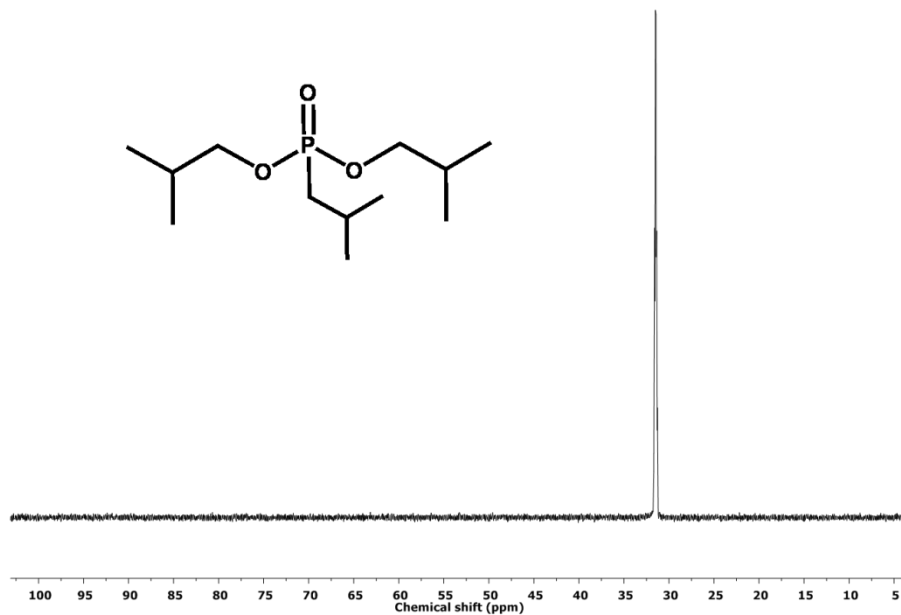


Figure 2.17: ^{31}P NMR spectrum of DiBiBP

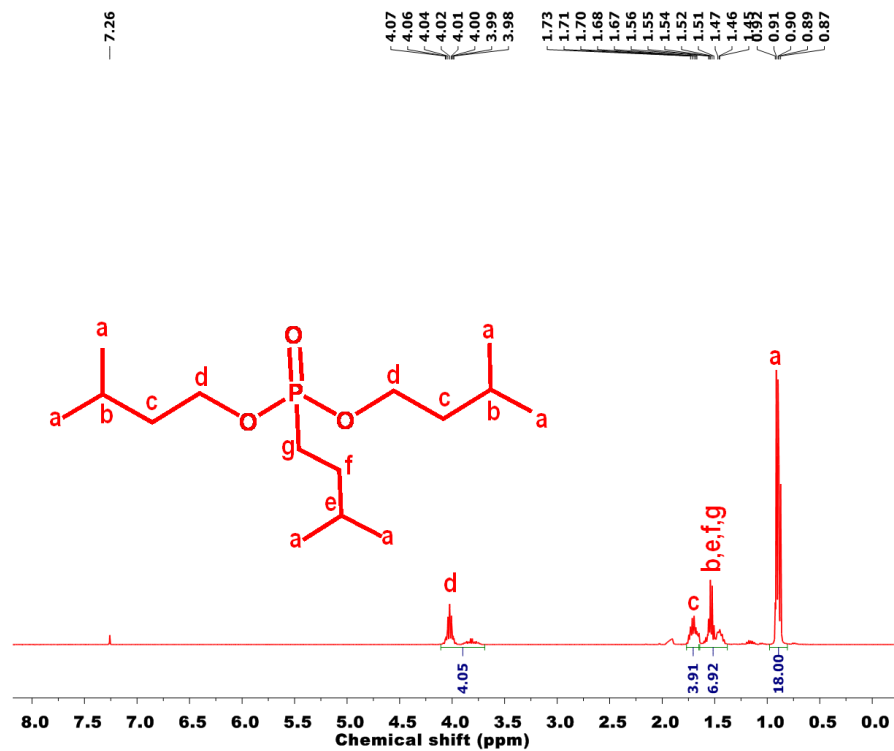


Figure 2.18: ^1H NMR spectrum of DiAiAP

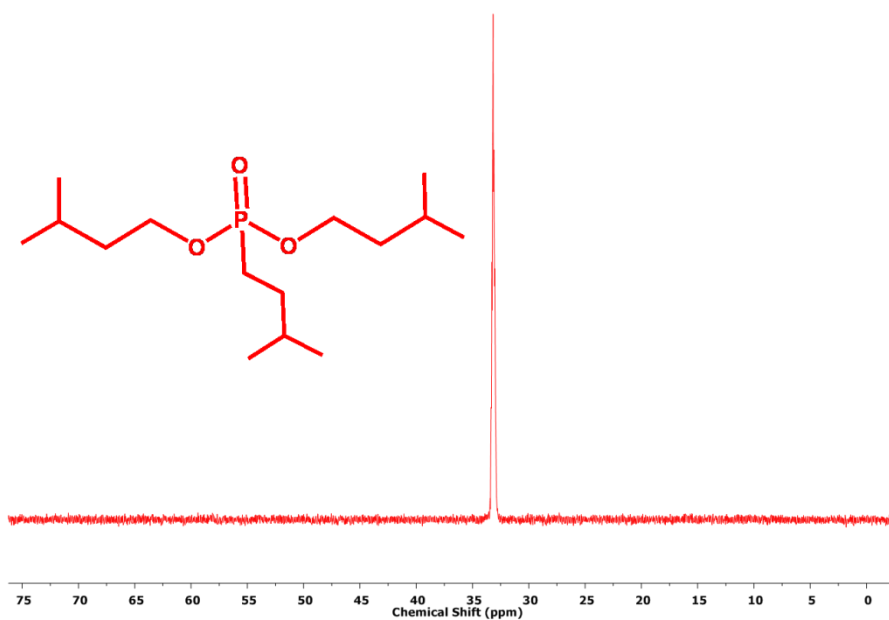


Figure 2.19: ^{31}P NMR spectrum of DiAiAP

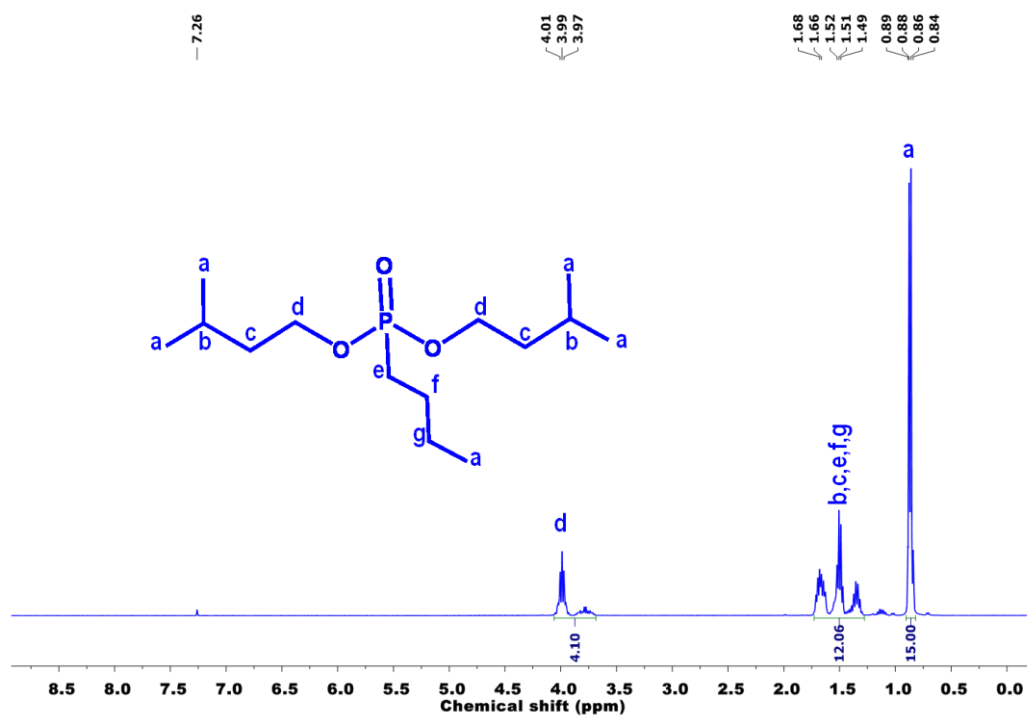


Figure 2.20: ¹H NMR spectrum of DiAButylP

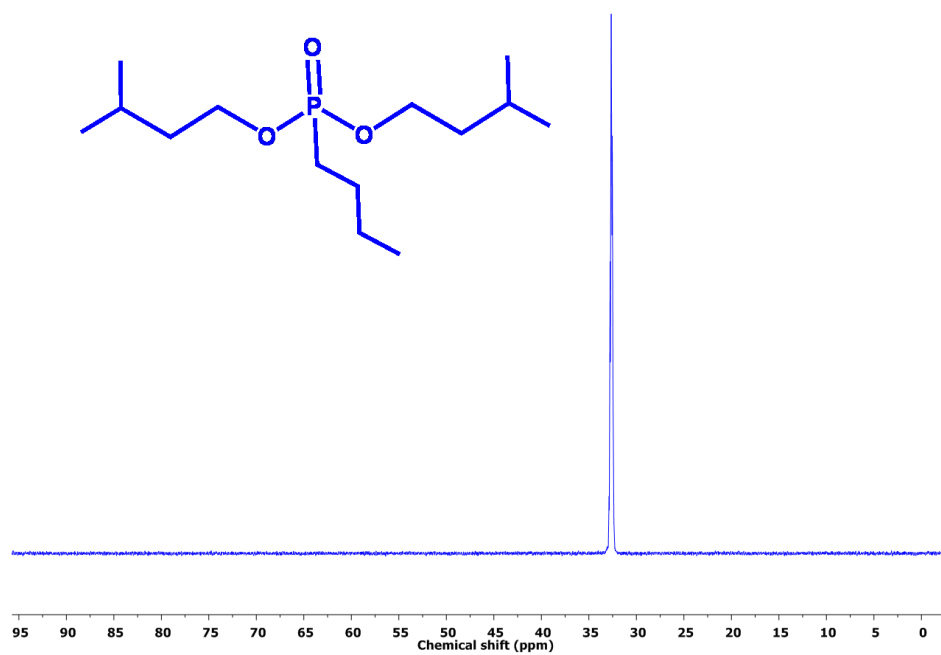


Figure 2.21: ³¹P NMR spectrum of DiAButylP

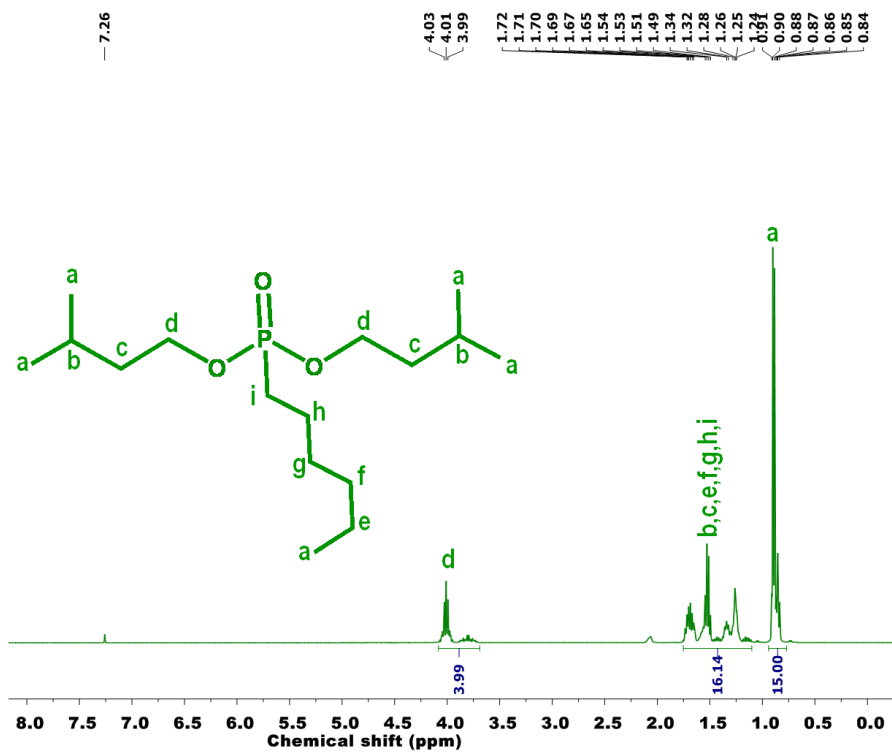


Figure 2.22: ^1H NMR spectrum of DiAHexylP

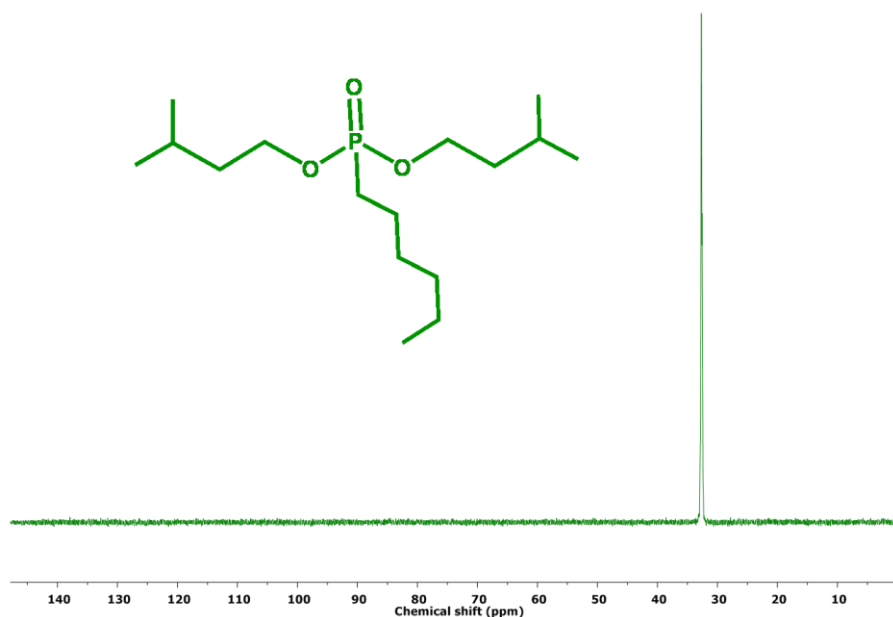


Figure 2.23: ^{31}P NMR spectrum of DiAHexylP

DiBiBP: DiBiBP was obtained by the procedure outlined above using diisobutylisobutyl H – phosphonate as the starting material and coupling with isobutyl bromide. A light yellow liquid was obtained with a yield of ~30%. ^1H NMR of DiBiBP (Figure 2.16) (400MHz, CDCl_3) $\delta=7.65$ shows 3.77 – 3.74 (4H, P–O–CH₂), 2.13 – 2.04 (1H, P–CH₂–CH), 2.02 – 1.83

(2H, P–O–CH₂–CH), 1.72–1.62 (2H, P–CH₂), 1.09–1.00 (6H, P–CH₂–CH–CH₂), 0.99 – 0.85 (12H, P–O–CH₂–CH–CH₃). ³¹P NMR (162.01 MHz, CDCl₃) δ = 31.48 (Figure 2.17).

DiAiAP: DiAiAP was obtained by a similar procedure outlined above. Diisoamyl H – phosphonate was used in the reaction with sodium and subsequently isoamyl bromide was used in the coupling reaction. A colourless liquid was obtained with a yield of ~30%. ¹H NMR of DiAiAP (Figure 2.18), (400MHz, CDCl₃) δ=7.66 shows 4.14 – 3.72 (4H, P–O–CH₂), 1.80 – 1.67 (4H, P–O–CH₂–CH₂), 1.01 – 0.84 (18H, P–O–CH₂–CH₂–CH–CH₃) and 1.66 – 1.41 are assigned to the remaining 6 intermediate hydrogen atoms in the carbon chains and marked in the inset. ³¹P NMR (162.01 MHz, CDCl₃) δ= 33.72 (Figure 2.19).

DiAButylP: DiAButylP was obtained by using diisoamyl H-phosphonate as the starting material and butyl bromide in the coupling reaction. A colourless liquid was obtained with a yield of ~50%. The ¹H NMR spectra of DiAButylP (Figure 2.20) shows 4.09 – 3.71 (4H, P–O–CH₂), 0.93 – 0.85 (15H, P–O–CH₂–CH₂–CH–CH₃) and 1.76 – 1.31 are assigned to the remaining 12 intermediate hydrogen atoms in the carbon chains and marked in the inset. ³¹P NMR (162.01 MHz, CDCl₃) δ = 32.65 (Figure 2.21).

DiAHexylP: DiAHexylP was obtained by using diisoamyl H – phosphonate as the starting material and hexyl bromide in the coupling reaction. A colourless liquid was obtained with a yield of ~50%. The ¹H NMR spectra of DiAHexylP (Figure 2.22) δ 7.71 shows 4.11 – 3.72 (4H, P–O–CH₂), 0.97 – 0.80 (15H, P–O–CH₂–CH₂–CH–CH₃) and 1.78 – 1.13 are assigned to the remaining 16 intermediate hydrogen atoms in the carbon chains and marked in the inset. ³¹P NMR (162.01 MHz, CDCl₃) δ = 32.70 (Figure 2.23).

The GC–MS of DiBiBP, DiAiAP, DiAButylP and DiAHexylP are shown in Figures 2.24–2.27, respectively. Protonated molecular mass peaks are seen at m/z = 251 in the case of DiBiBP (M.W = 250g/mol), m/z = 293 for DiAiAP (M.W = 292g/mol), m/z = 279 for DiAButylP (M. W. = 278g/mol) and m/z = 307 for DiAHexylP (M.W = 306g/mol).

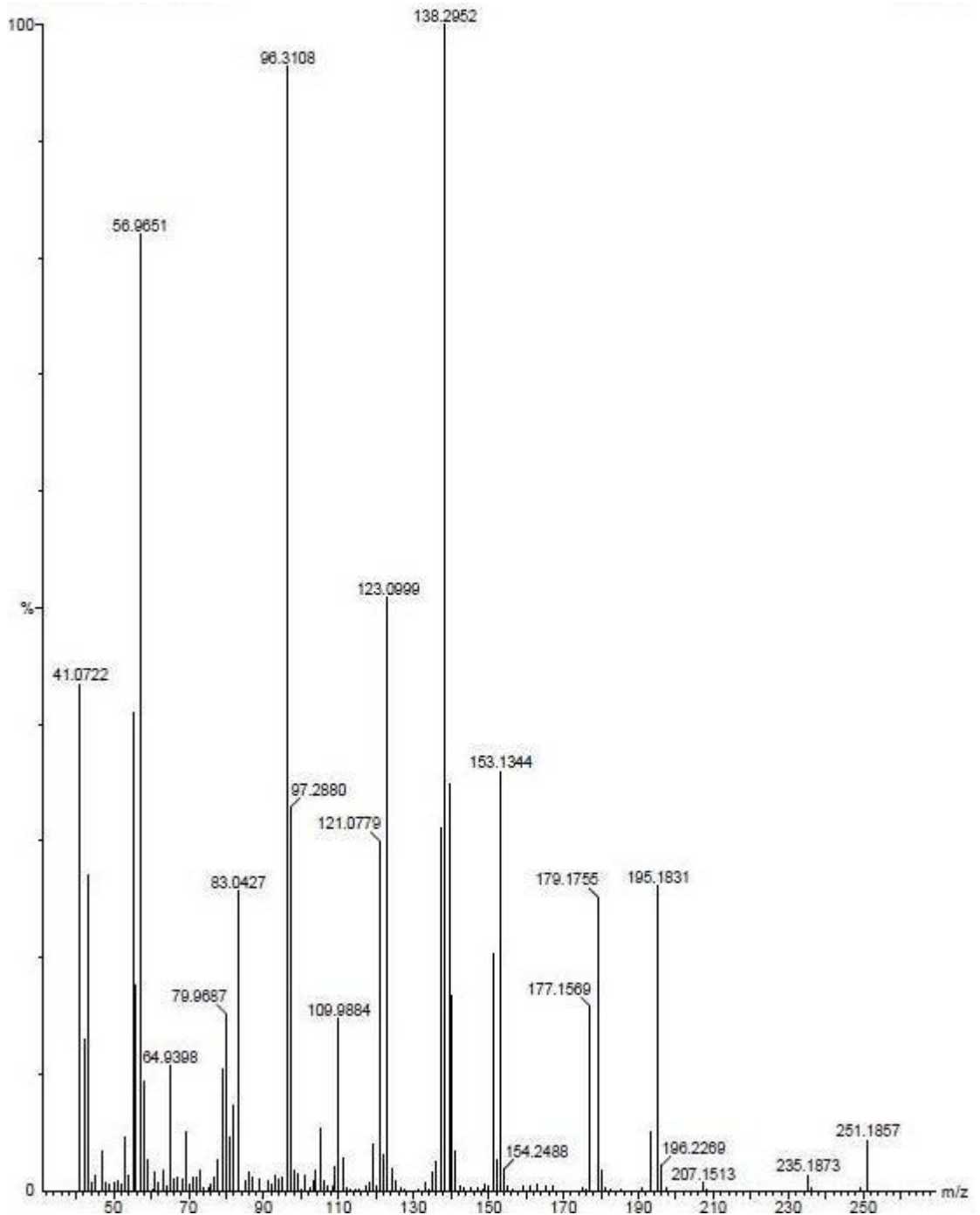


Figure 2.24: GC – MS spectrum for DiBiBP

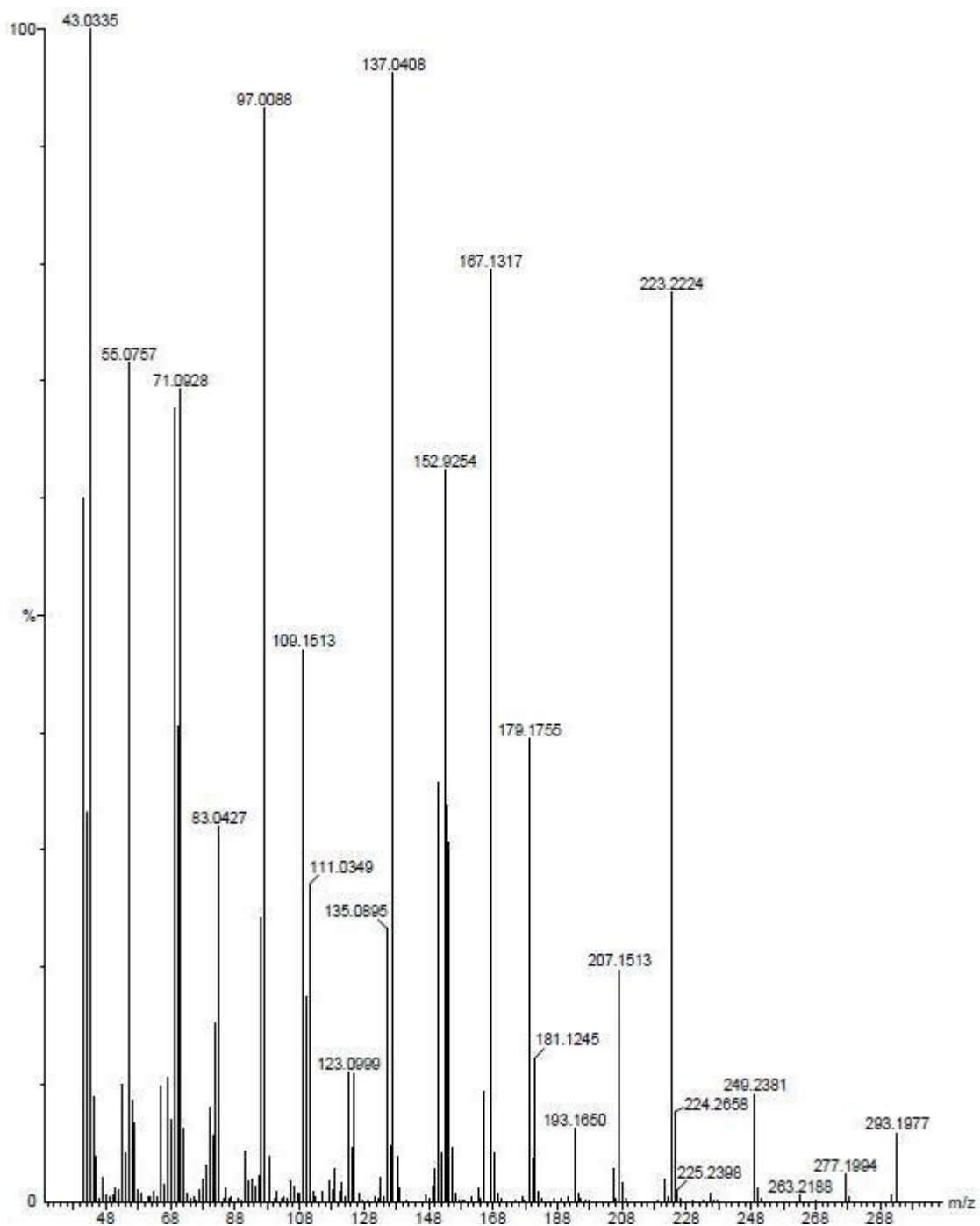


Figure 2.25: GC – MS spectrum for DiAiAP

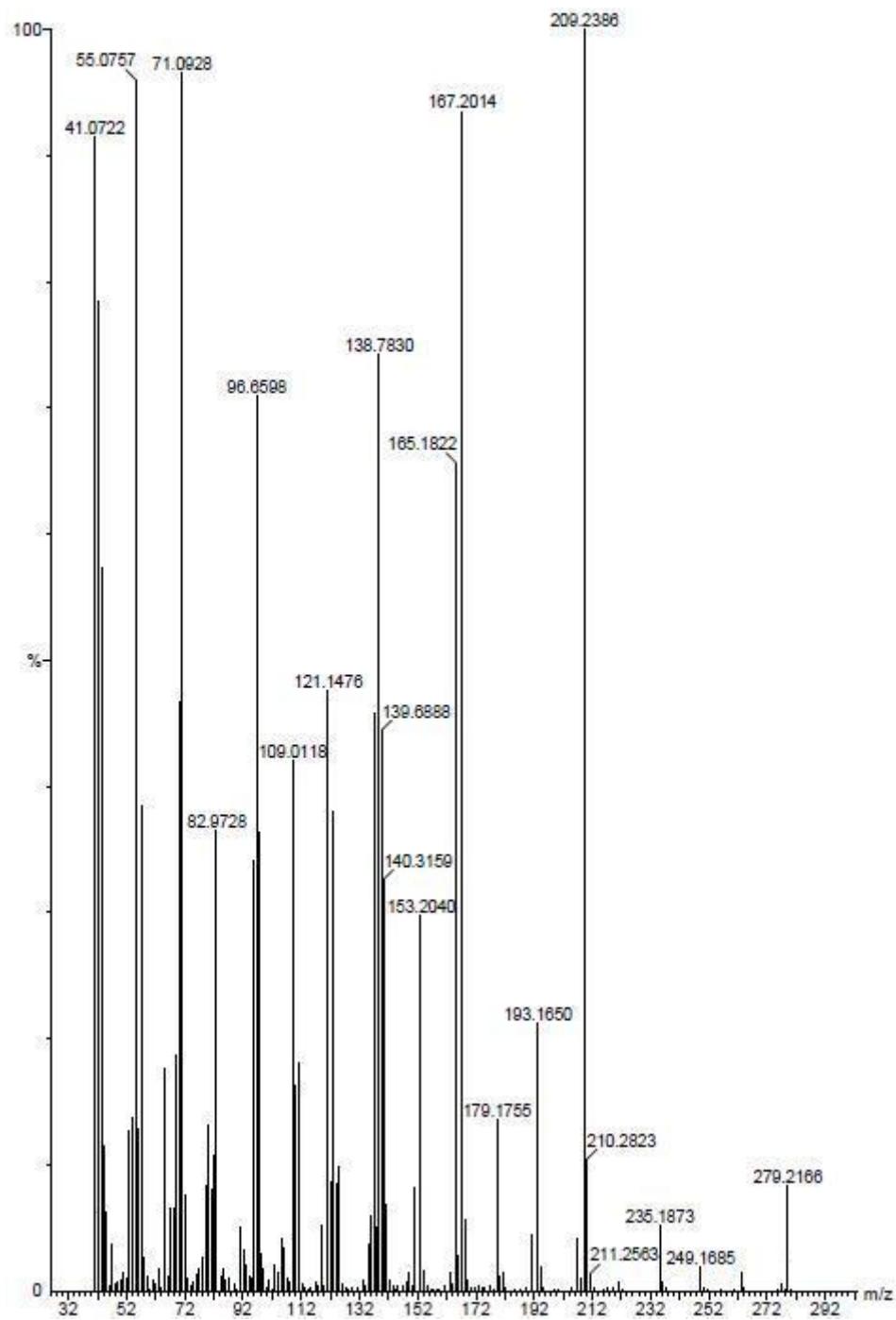


Figure 2.26: GC – MS spectrum for DiAButylP

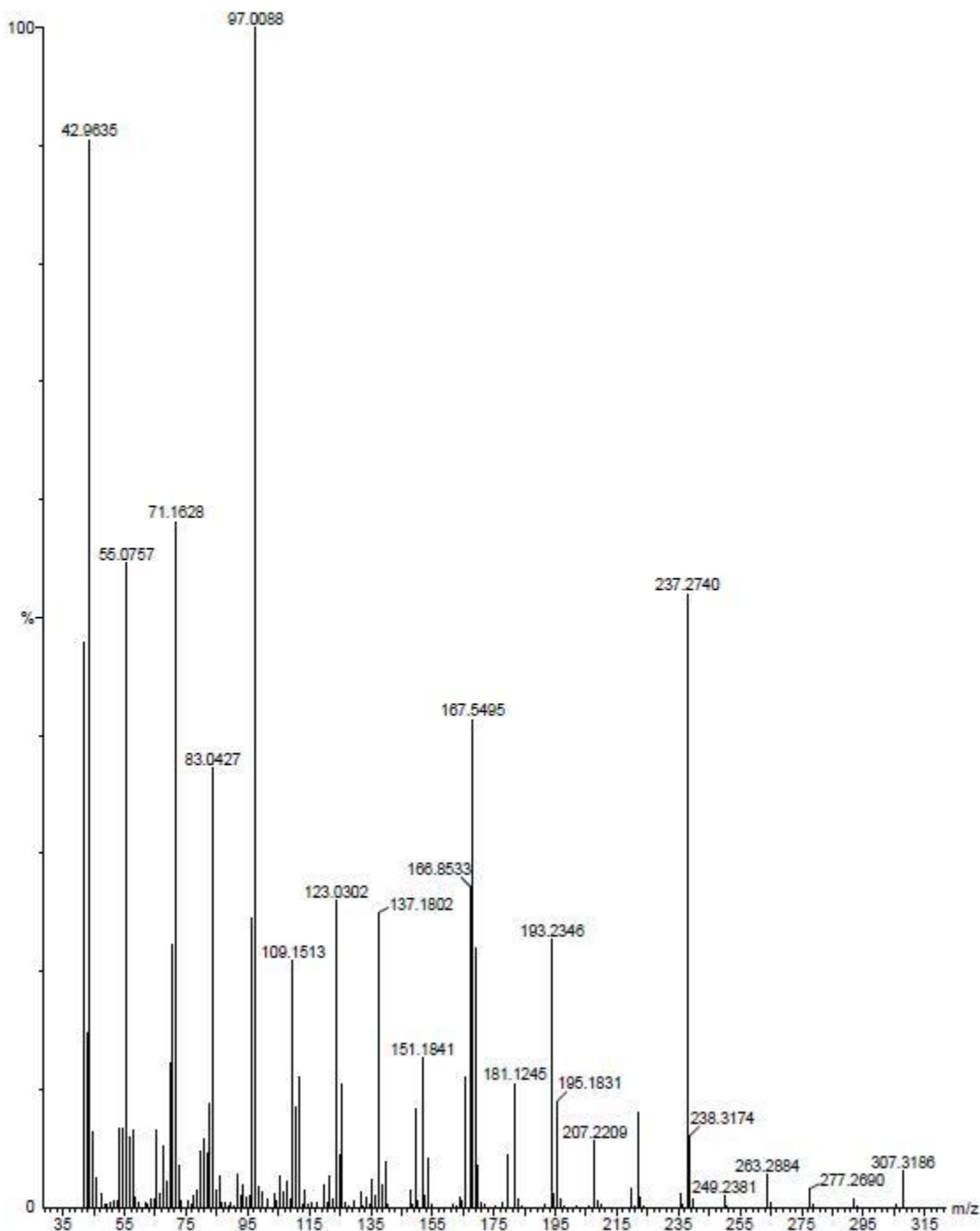


Figure 2.27: GC – MS spectrum for DiAHexylP

2.6 Measurement of physicochemical properties

Measurement of density

Density is an important parameter for a system to qualify as a suitable extractant for the solvent extraction process. The density difference between aqueous and organic phases must be large enough in order to minimise phase separation time. Density of the synthesised

extractants was measured using a 500 μ L glass pipette. The density was calculated from the weight difference of pipette before and after it was filled with the compound.

Measurement of viscosity

Viscosity of an extractant influences mass transfer between phases. It plays a vital role in predicting the nature of flow in any process. Measuring viscosity is useful in the calculation of power requirements for the unit operations such as mixing, pipeline design and pump characteristics. Viscosity of a fluid can be determined by measuring the time of flow of a given volume of liquid through a vertical capillary under the influence of gravity:

$$\eta = \frac{\pi \Delta p t r^4}{8 l V}$$

Where η is the viscosity of the fluid, Δp is the difference in the pressure between two ends of the tube, t is the time for volume V to flow out, r is the radius of the capillary and l is the length of the capillary¹⁷⁶. With both ends of the viscometer tube open:

$$\eta = \frac{\pi h \rho g t r^4}{8 l V}$$

Where h is difference in height between the liquid levels in the two reservoirs used in the experiment, ρ is density of the liquid and g is acceleration due to gravity. For a given volume of liquid and a given viscometer

$$\eta = k \rho t$$

Where $k = \frac{\pi h g r^4}{8 l V}$

Additionally viscosity is related to the activation energy of liquid flow E_a , by the equation

$$\eta = A e^{\frac{E_a}{RT}}$$

Where A is a constant, T is the temperature and R is the gas constant.

The viscosity of the synthesised H-phosphonate and dialkylalkyl phosphonate extractants has been measured by Oswald viscometer¹⁷⁷. A known volume (~ 15 mL) of liquid was taken in the viscometer and time taken by the liquid to flow through the marked region of the Oswald viscometer was measured. The driving pressure p at all stages of the flow of a liquid is given

by $h\rho g$, where h is the difference in heights of liquid in upper and lower bulb, ρ density of liquid and g acceleration due to gravity. The viscosity of fluids can be evaluated by the comparative method where one of the fluids is water, whose density and viscosity as a function of temperature are well reported in the literature. The viscosity of the fluid of interest can be determined using the following expression.

$$\frac{\eta_e}{\eta_w} = \frac{\rho_e t_e}{\rho_w t_w}$$

Where η_e , ρ_e and t_e are the viscosity, density and time taken for an extractant to pass through marked region of viscometer of fluid to be determined. η_w , ρ_w and t_w are viscosity, density and the time for the water system under identical conditions. Viscosity measurements were carried out for the extractants and the natural logarithm of viscosity was plotted against the inverse of temperature. Linear plots were obtained and from the slope of the graphs, activation energy was calculated as slope of the graphs give Ea/R .

2.7 Extraction of metal ions

Measurement of aqueous solubility

An equal volume of extractant and distilled water were equilibrated in a glass equilibration tube for 8 h. The two phases were transferred to a separating funnel and allowed to settle for 24 h. Once the phase separation was complete, the aqueous layer was carefully separated using a pipette and analysed for the total carbon content using Total Organic Carbon (TOC) analyser. The solubilities of the H-phosphonates were determined by this method.

Extraction of Uranium tracer

Uranium extraction was carried out using ^{233}U isotope at tracer level. Its high specific activity allows D values to be measured using liquid scintillation counting (LSC). 1.1M solutions of three extractants (DBHP, DiBHP, and DsBHP) were prepared in toluene by taking the desired quantity of extractant on weight basis into a dry standard flask and making-up the volume with toluene. 1mL each of the extractant solutions were separately added to an equal

volume of nitric acid of different concentrations ranging from 0.01–8M. 10 μ L of ^{233}U tracer was added to each tube and the aqueous–organic systems were equilibrated for 1 hour. After equilibration, 100 μ L of liquid was pipetted from both phases, added to the LSC cocktail and homogenised thoroughly. The samples were subsequently counted and background correction was applied to obtain the distribution ratios for DBHP, DiBHP and DsBHP as a function of acid concentration. Dodecane was not used as the diluent for butyl H–phosphonates due to formation of third phase even at acidity below 1M.

Extraction of Americium

Americium was extracted from nitric acid medium using 1.1M solutions of DBHP, DiBHP and DsBHP in toluene. ^{241}Am isotope was used to measure the distribution ratio at tracer level. 1mL each of the extractant solutions were separately added to an equal volume of nitric acid of different concentrations ranging from 0.01–8M. 10 μ L of ^{241}Am tracer was added to each tube and the aqueous–organic systems were equilibrated for 1 hour. After equilibration, 100 μ L of liquid were pipetted from both phases into separate gamma–tubes and counted with a gamma counter with a well – type NaI(Tl) detector.

Extraction of Plutonium

The isotope composition of plutonium (atom%) used in the experiments is as follows: ^{238}Pu :0.017, ^{239}Pu :93.60, ^{240}Pu :6.24, ^{241}Pu :0.12, ^{242}Pu :0.023. High specific activity of Pu tracer allows that D values can be measured using liquid scintillation counting (LSC). 1mL each of the extractant solutions were separately added to an equal volume of nitric acid of different concentrations ranging from 0.01 – 8M. 20 μ L of Pu tracer was added to each tube and the aqueous-organic systems were equilibrated for 1 hour. After equilibration, 100 μ L of liquid were pipetted from both phases, added to the LSC cocktail and mixed thoroughly. The samples were counted and background correction was applied to obtain the distribution ratios for DiAiAP, DiBiBP, DiAHexylP and DiAButylP as a function of acid concentration. The

plutonium solution in IV oxidation state was prepared by taking an appropriate quantity of Pu stock in 1M nitric acid. The oxidation state of Pu was maintained as Pu(IV) by the addition of 0.1mL of 2.5M NaNO₂ and Pu(IV) was extracted with 0.5M TTA/xylene. The organic phase containing Pu(IV) was scrubbed with 1M nitric acid and stripped with 8M HNO₃. The aqueous phase (strip solution) was washed twice with equal volume of *n*-hexane to remove the entrained organic phase. The stock solution was used for preparing aqueous Pu(IV) solutions for solvent extraction experiments.

Extraction of Thorium in microgram quantities

Solutions of the extractants in *n*-dodecane were first pre-equilibrated with an equal volume of nitric acid ranging from 0.01M to 8M. Then the pre-equilibrated organic phases were separated and used for extraction of 200 ppm Th(IV) solutions. Th(IV) feed solutions used for extraction were prepared in nitric acid media with acidities varying from 0.01M to 8M. Equal volume of feed and pre-equilibrated organic phases were pipetted into glass tubes and equilibrated at room temperature for 1 h. The concentration of Th(IV) in equilibrated aqueous and organic phases was measured by pipetting aliquots of known quantity and estimating Th(IV) concentration spectrophotometrically using Thoron as the chromogenic agent. The Th(IV) concentration in the feed solutions of different acidity were also estimated by the same method, and all feed solutions had Th(IV) concentrations of 200 ± 5 ppm.

2.8 Analytical procedures

Determination of Th(IV)

Thorium concentrations in both the phases were estimated by complexometric titrations using DTPA (0.03 M and 0.01 M, respectively, for the analysis of concentrated and dilute thorium solutions) as titrant and xylenol orange as an indicator. Uranium concentrations in both phases were estimated by complexometric titrations using PDCA solution (0.01 M) using Arsenazo I as an indicator. Acid concentrations in organic samples were analysed by acid –

base titration with a standard dilute NaOH solution using phenolphthalein as an indicator. The U(VI) or Th(IV) metal ions were complexed with neutral saturated potassium oxalate solution prior to “free acidity” determination. Determination of Th(IV) in ppm was carried out spectrophotometrically using thoron reagent method.

Determination of acid

Acid concentrations in organic and aqueous samples were analyzed by acid-base titration using a dilute standardized NaOH solution (0.1M) after complexing the metal ions with neutral saturated potassium oxalate solution prior to analysis.

Determination of U(VI)

In order to enable determination of U(VI) in the presence of higher concentrations of Th(IV), a modified method was developed in our laboratory¹⁷⁸ based on the spectrophotometric determination of microgram amounts of U(VI) with Br-PADAP (originally developed by Johnson and Florence). The effects of ethanol content on the molar absorptivity of U(VI)-Br-PADAP complex and the interference of organic substances such as TBP and HNP are provided elsewhere¹⁷⁸. This modified method can be employed for the analysis of U(VI) both in aqueous and organic samples containing a large excess of Th(IV) (Th : U = 10000 : 1). Using this method, uranium in ppm concentrations (with and without thorium) in organic and aqueous samples was estimated by spectrophotometry using Br-PADAP as chromogenic agent. Absorbance maximum at a wavelength of 577 ± 1 nm¹⁷⁹ was used to get quantitative information. The lowest measurable concentration for the spectrophotometric analysis of uranium was found to be ≈ 1 ppm.

Determination of Ce(IV)

Ce(IV) in all the phases were analysed by redox titrimetry using barium diphenylamine sulphonate as the indicator. Back titration methodology was adopted due to the sluggish end point observed in the case of direct titration of Ce(IV) with ferrous ammonium sulphate.

Hence, excess ferrous ammonium sulphate (standardised 0.1M) was added so as to convert all the Ce(IV) in the analyte to Ce(III). The excess Fe(II) was back titrated with standard potassium dichromate solution (0.025N). Ce(IV) in ppm levels was analysed by spectrophotometry in acetic acid-acetate medium (pH~3) with Arsenazo-III as the chromogenic agent¹⁸⁰.

Analysis of Th and U in a mixture

During the analysis of U/Th mixtures, Th in the presence of U(VI) was spectrophotometrically estimated by thoron reagent and U(VI) in the presence of Th(IV) was estimated by the Br-PADAP method.

2.9 Computational methodology

The Turbomole program package¹⁸¹ or ORCA 3.0.3.^{182, 183} was used for all the calculations performed. For the U and Th atoms, the 60 core electrons approximated by pseudo potentials along with the corresponding def-SV(P) (14s13p10d8f1g)/ [10s9p5d4f1g] basis sets were used.^{184, 185} All main-group atoms were treated at the all-electron level employing the def2-SV(P) basis sets. The geometries of the bare ligands and their complexes with U(VI) and Th(IV) nitrate species were optimized using density functional theory (DFT) using Becke's exchange functional¹⁸⁶ in conjunction with Perdew's correlation functional¹⁸⁷ (BP86) with the generalized gradient approximation (GGA). The PBE^{188, 189} functional in conjunction with TZVP^{190, 191} basis set has been used for the optimization of Ce(IV) complexes. For cerium, 28 inner-shell core electrons were replaced by an effective core potential (ECP) generated by using quasi-relativistic methods¹⁸⁵ and the explicitly treated electrons were described by standard def-TZVP basis sets. All the geometries were verified as minima by computing their harmonic vibrational frequencies. Optimizations, as well as the calculation of complexation energies, were carried out by incorporating the D3 correction for the U(VI) and Th(IV) complexes with TBP and TsBP. Further, the energetics on the computed geometries were

evaluated using M06-2X functional in conjunction with the all-electron, SARC def2-TZVP basis set¹⁹². For reliable energetics such as redox potentials or binding energies or ionisation energies, density functionals with some amount of HF-exchange are mandatory. The choice of M06 suite functional has been used previously and benchmarked with respect to a series of experimental and CCSD(T) results¹⁹³. Very recently, a series of density functionals and ab initio methods have been benchmarked for the redox properties of uranyl complexes. The experimental quantities are derived from ESI-PES data and with CCSD(T) results. It has been found that with reference to Gold-standard CCSD(T) results, the performance of M06-2X and M06 functionals are good¹⁹⁴. Thus, this computational protocol has been chosen for the present study. Relativistic effects have been incorporated within ZORA as implemented in ORCA 3.0.3. The solvent effects were computed within the COSMO¹⁹⁵ model using the default radii of all atoms. For these, a dielectric constant of 80 and 5 were used to mimic the aqueous and organic phases, respectively. Energy decomposition analysis of the cerium complexes has been carried out using ADF 2016 programme employing the PBE functional and TZ2P basis set. Relativistic effects have been incorporated by the ZORA approximation in ADF. Atoms in Molecules (AIM) analysis has been carried out using the Multiwfn software¹⁹⁶, for which the .wfn files are generated from the ORCA output files using the orca_2aim utility. Frozen core approximations viz. 1s–5d for uranium atom, 1s for carbon, nitrogen, and oxygen and 1s-2p for phosphorous have been considered. Relativistic effects have been incorporated by the ZORA approximation as implemented in ADF¹⁹⁷⁻¹⁹⁹.

For heavy actinide complexes geometries of the bare ligands and the actinide complexes have been optimized using the ADF 2016 programme^{169, 200}. All calculations have been carried out by employing PBE functional in conjunction with TZ2P Slater type orbital (STO) basis sets²⁰¹. Frozen core approximations viz. 1s–5d for actinides, 1s for carbon, nitrogen, and oxygen and 1s-2p for phosphorous and sulphur have been considered. All the optimized

structures have been confirmed to be energy minima by running analytical frequency calculations²⁰²⁻²⁰⁴. Solvent effect has been incorporated using the COSMO approach²⁰⁵ with water as the solvent (epsilon = 78.39). The atomic radius values used in the COSMO model are 1.30, 2.00, 1.83, 1.72 and 2.16 Å for H, C, N, O and S, respectively. The radius for all the actinide atoms was taken as 2.223 Å¹⁶⁶. Relativistic effects have been incorporated by the ZORA approximation as implemented in ADF¹⁹⁷⁻¹⁹⁹.

Energy decomposition analysis has been performed in which the interaction energy between the ligands and the metal has been decomposed into individual components. This interaction energy ΔE_{int} can be broken down into components, *viz.*

$$\Delta E_{\text{int}} = \Delta E_{\text{elec}} + \Delta E_{\text{Pauli}} + \Delta E_{\text{orb}}$$

Where ΔE_{elec} and ΔE_{Pauli} denote the attractive electrostatic interaction energy and the Pauli repulsive energy, respectively, between the fragments, and ΔE_{orb} is the stabilizing orbital interaction term. ΔE_{orb} includes the polarization term and the empty/occupied mixing of orbitals belonging to one fragment due to the presence of the other. Therefore, this orbital component in the decomposition is a measure of the covalency in the interaction¹⁶⁹. For the bond energy decomposition calculations the open shell configuration of the central metal ion (6, 7, 6, and 5 unpaired electrons for Am, Cm, Bk, and Cf, respectively) has been defined for the explicitly treated electrons which are not considered in the frozen core. In complexes consisting of more than one kind of ligand, the different types of ligands have been considered as different fragments during the analysis. The effect of solvent (dielectric constant value of 78.39 corresponding to the aqueous phase) has been considered during the energy calculations for the fragment as well as the complex in the EDA.



Chapter 3



“I would rather have questions that can't be answered than answers that can't be questioned”

~ Richard Feynman

EXTRACTION OF THE TETRAVALENT METAL IONS Th(IV) AND Ce(IV): THIRD PHASE FORMATION AND QUANTUM CHEMICAL STUDIES

3.1. Introduction

The present study elucidates the behaviour of Tri-sec-butyl phosphate (TsBP) in the extraction of Th(IV) over the entire range of thorium concentrations, starting from ~ 5mg/mL up to the saturated aqueous concentration. The results obtained with TsBP are compared with earlier work on TBP⁶², which is conventionally used in the U/Th separation. The extraction of Th(IV) and nitric acid and the variation of density of organic phase for TsBP system have been investigated as a function of aqueous phase thorium concentration. In addition to TsBP, studies were also carried out with Tri-iso-butyl phosphate (TiBP) in order to understand the effects of branching in the carbon chain. Further, the extractant concentrations in third phase and diluent-rich phase as a function of thorium concentration are determined²⁰⁶.

Investigating the third phase formation behaviour of Pu(IV) is crucial for designing solvent extraction processes. In practice, handling higher concentrations of Pu(IV) is difficult due to its high specific activity and it is potentially unsafe as its build-up in the third phase can lead to criticality related issues. In this context, in this study, third phase formation behaviour of Ce(IV), which is chemically analogous to Pu(IV) and often used as surrogate for Pu(IV)^{122, 123, 207} has been examined. In this work, , extraction of Ce(IV) from 4M nitric acid medium has been carried out with the TsBP-dodecane system and the results compared under identical conditions with the extraction achieved by TBP. The concentration of Ce(IV) extracted into the organic phase, third phase and diluent-rich phases after their formation have been determined. The variation in the density of the phases and the acid extracted as a function of increasing concentration of Ce(IV) in the aqueous phase has also been measured.

In addition to experiments, quantum chemical calculations using DFT are employed to understand the electronic structure of Ce(IV) complexes and the extractants TBP and TsBP.

The solvent corrected energetics of complex formation for these extraction systems with Ce(IV) have been computed. The binding free energy as well as geometric parameters has been correlated with the experimental findings. To this day, third phase formation in metal-extractant systems has been an experimentalist's domain. In this investigation, DFT has widened perspectives on the understanding of third phase and provided an explanation for the differential tendency of metal-extractant systems to form aggregates leading to third phase.

3.2 Extraction of Th(IV) with TBP, TiBP and TsBP

Trends in the variation of extraction isotherms for the extraction of Th(IV) by solutions of TBP and its isomers (1.1M) in n-DD from thorium nitrate solution in 1M HNO₃ as a function of equilibrium aqueous phase Th(IV) concentration at 303 K are shown in Figure 3.1A. It can be seen that the metal loading in the organic phase at a particular equilibrium aqueous phase Th(IV) concentration was higher for TBP than TiBP, which in turn was higher than that of TsBP. These results confirm the lesser extraction tendency of TsBP compared to its isomers TiBP and TBP. Also in all the cases, organic phase metal loading increases with increase in the equilibrium aqueous phase Th(IV) concentration.

The variation of density of organic phases in the extraction of Th(IV) by 1.1M solutions of TBP, TiBP and TsBP in DD from thorium nitrate solution in 1M HNO₃ are depicted in Figure 3.1B. The trends in the variation of density of organic phases are similar to that of thorium loading as the major contribution to the density of the organic phase is from thorium. Figure 3.1C shows the variation of organic phase nitric acid concentration with increase in aqueous thorium concentration. In the case of TBP and TiBP, the acid concentration decreases with increase in aqueous thorium concentration. As more thorium is extracted to the organic phase, thorium competes for the available extractant molecules in the organic phase and less acid is extracted. However, TsBP exhibits a different trend for nitric acid extraction. In the case of TsBP, there is no significant change in the HNO₃ loading with

increase in aqueous phase Th(IV) concentration. Over the entire range, the HNO₃ loading in the organic phase was higher for TsBP compared to TiBP and TsBP. The study was carried out at 1M HNO₃ concentration in order to minimise the extracted acid, and hence maximise the range of metal concentrations in the aqueous and organic phases. Though TsBP extracts less Th(IV) compared to TBP, it extracts higher acid than TBP due to its higher basicity.

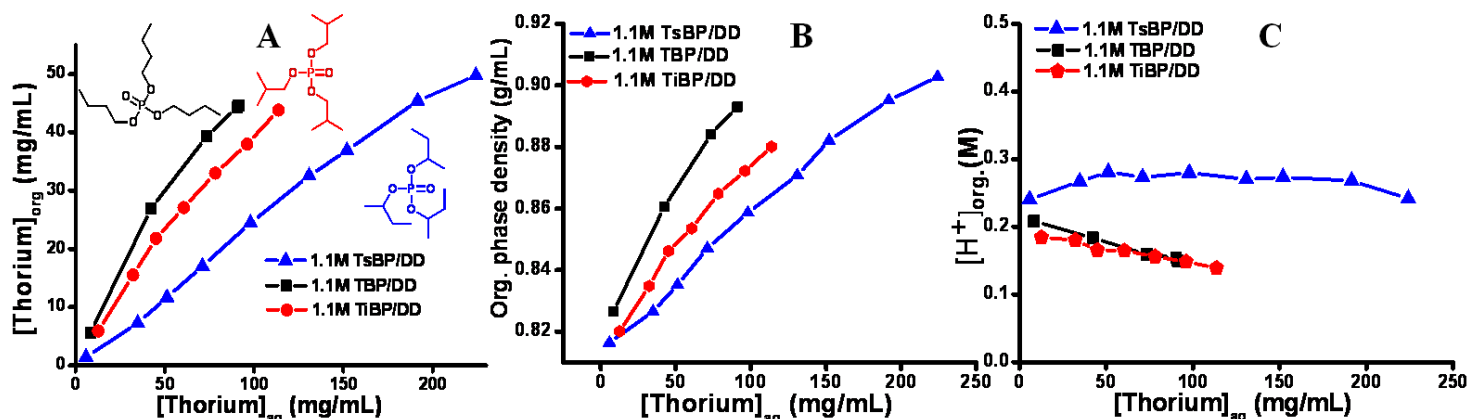


Figure 3.1: Variation of (A) organic phase Th(IV) concentration (B) density of the organic phase (C) organic phase nitric acid concentration as a function of equilibrium aqueous phase Th(IV) concentration in the extraction of Th(IV) for 1.1M TBP/DD, TiBP/DD and TsBP/DD systems in biphasic regions.

Figure 3.2A illustrates the organic phase concentration of thorium over the entire range of aqueous thorium concentrations from ~ 5 mg/mL up to the saturated aqueous concentration of ~530 mg/mL. The LOC and CAC points, third and diluent phase regions are indicated. It is clear that the LOC for TsBP is higher than for TBP. After the splitting of the organic phase, the concentration of thorium in the diluent-rich phase drops and the thorium concentration in the third phase start increasing drastically. The concentration of Th(IV) in diluent – rich phase for the TsBP/DD system are marginally higher than that of TBP/DD system all through the triphasic region. Earlier it has been observed in our laboratory that solvent system with higher third phase formation tendency splits with lesser metal concentration in diluent-rich phase compared to solvent with lesser third phase formation tendency [24]. The trend

observed in the present study also follows the above trend. The third phase in TsBP/DD initially has less thorium concentration than the third phase of TBP/DD at the same aqueous thorium concentration. Beyond an aqueous thorium concentration of 400 mg/mL, its concentration in third phase for TsBP/DD increases above that of the TBP/DD system. At higher thorium loading, the solvation number (the number of extractant molecules associated with a metal ion in the metal complex) decreases for TsBP system. Table 3.1 shows the extractant concentrations in the third phase at each thorium concentration. This decrease in the solvation number, allows more thorium nitrate to be taken up by the organic phase. The branched extractant TsBP, would prefer a lower solvation number compared to TBP, which contains a linear carbon chain. Hence, this effect of decreased solvation number is more pronounced in TsBP, leading to higher uptake of thorium into the third phase even at higher metal loading, whereas the same plot for TBP remains reasonably flat.

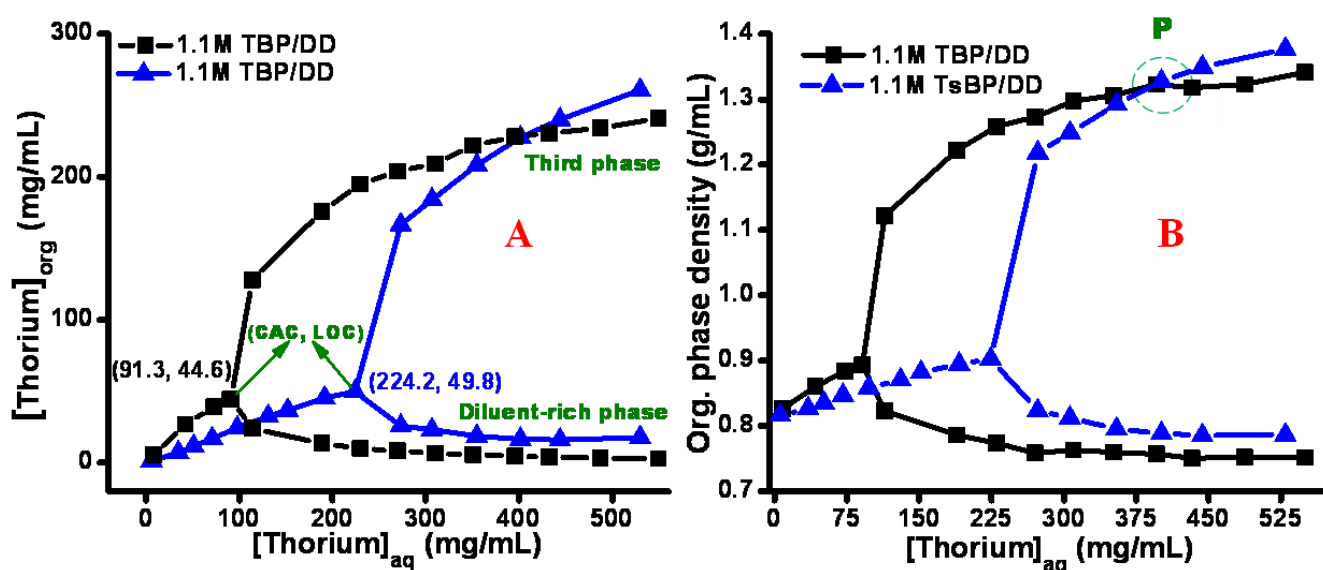


Figure 3.2: Variation of (A) organic phase Th(IV) concentration (B) density of the organic phase, third phase and diluent-rich phase as a function of equilibrium aqueous phase Th(IV) concentration in the extraction of Th(IV) for 1.1M TBP/DD and TsBP/DD systems in biphasic and triphasic regions.

As in the case of the biphasic region, organic phase thorium concentration can influence the density of organic phase in triphasic region. Hence one can expect an increase in density of third phase and a decrease in density of diluent-rich phase as a function of aqueous phase metal concentration. The trends in variation of density of organic phase, third phase and diluent-rich phase with increase in aqueous thorium concentration are shown in Figure 3.2B for both TBP/DD and TsBP/DD systems. The plot of density of organic phase vs. aqueous phase thorium concentration mimics the plot of thorium concentration in the phases, to an extent that there is a crossover in the densities of the TsBP/DD and TBP/DD at the point P (marked in Figure 3.2B), which occurs at an aqueous thorium concentration of 400mg/mL. This is the same aqueous concentration at which the triphasic plots in Figure 3.2B crossed each other. Hence, by monitoring the density of the organic phase for a given system, a quick and good estimate of the thorium concentration in the phase can be obtained without an explicit analysis.

Based on the above argument, a plot of organic density vs. organic metal loading can provide a calibration curve which can be used for the prediction of organic metal loading from organic phase density. Figure 3.3 represents the plot constructed for TsBP system and the calibration plot yields two straight lines; one for the biphasic region and the other for third phase. By monitoring the density of the phases, a good estimate for the concentration of thorium can be obtained quickly without an explicit analysis.

Figure 3.4A shows trends in the variation of acid concentration in third phase and diluent-rich phase with increase in the aqueous thorium concentration. In both the cases, there is a steep decrease in the nitric acid loading in diluent-rich phase with increase in aqueous phase thorium concentration. However, nitric acid loading in third phase of TsBP/DD system initially shows a sharp increase and after passing a through maximum, it decreases, whereas in the case TBP, the nitric acid loading in third phase remains same over a wide range of

aqueous phase thorium concentration. In general, concentration of nitric acid in the organic phase is decided by concentration of extractant and thorium in that phase.

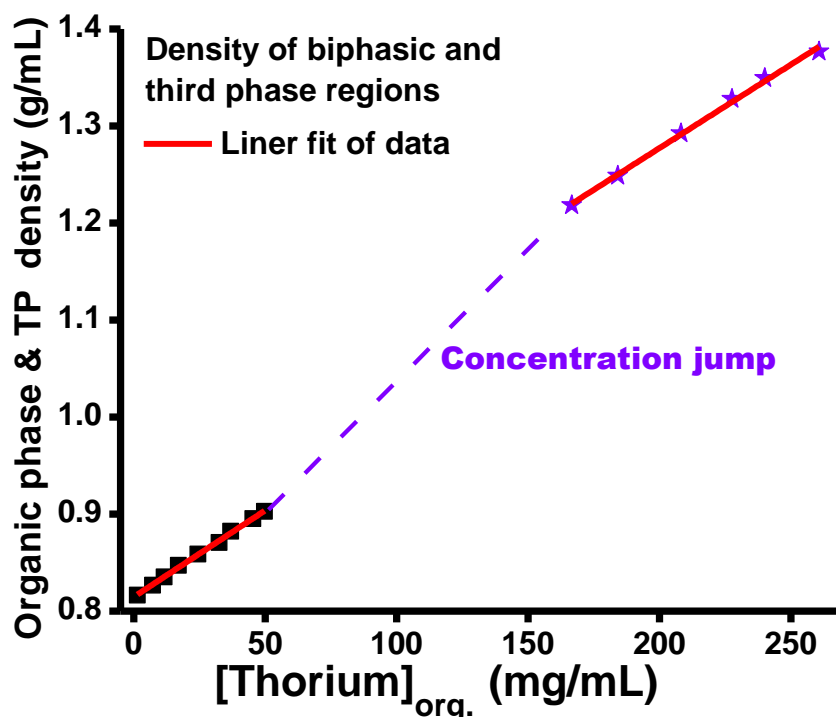


Figure 3.3: A fit of the organic phase thorium concentration against the organic phase density for the biphasic and third phase regions for 1.1M TsBP/DD system.

When the organic phase splits to form third phase and diluent-rich phase, the constituents of loaded organic phase (extractant, diluent, metal nitrate and nitric acid) unevenly distributes between the third phase and diluent-rich phase with unequal volume. In general, the volume of diluent-rich phase is higher than that of third phase and the ratio of volume of third phase to the volume of diluent-rich phase (V_{DP}/V_{TP}) depends on the nature of solvent system. The variations of V_{DP}/V_{TP} ratio as a function of equilibrium aqueous phase concentration for TBP and TsBP systems are shown in Figure 3.4B. When the concentration of extracted thorium is increased, more third phase is formed as the diluent-rich phase cannot accommodate much thorium. This can be seen from Figure 4 as well, in which as aqueous thorium concentration is increased beyond CAC, the third phase thorium concentration steadily increases whereas the diluent phase thorium remains more or less a constant. It follows, that the V_{DP}/V_{TP}

obtained at different thorium concentrations gives an indication of the third phase formation tendency. The higher the ratio of DP/TP volume, the lower is the tendency of the thorium complexes to go into the third phase. This trend is observed in Figure 3.4B for both TBP/DD and TsBP/DD extractants, with the TsBP system showing the starker trend in this case. The more prominent decrease of volume ratio in the case of TsBP over TBP is due to the concentration of Th(IV) increasing more drastically in the case of TsBP (Figure 3.2A). This leads to the expansion of the third phase volume to accommodate the larger amounts of thorium complex, making the ratio of V_{DP}/V_{TP} decrease sharply.

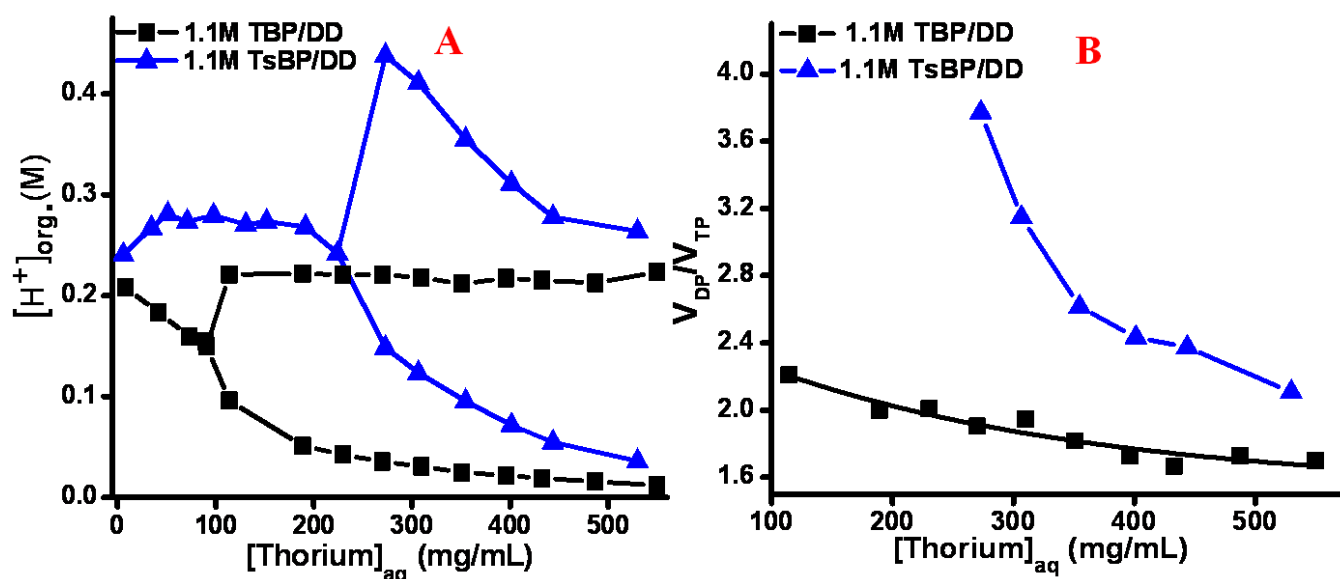


Figure 3.4: (A) The change in concentration of acid in the organic phase, third phase and diluent-rich phase with increase in the aqueous thorium concentration (B) The variation of V_{DP}/V_{TP} ratio as a function of function of equilibrium aqueous phase Th(IV) concentration

3.3 Measurement of extractant concentration in third phase and diluent-rich phase

After measuring the concentrations of Th(IV) and HNO_3 in organic phases, the extractant concentrations in the third phase and diluent-rich phase were determined. This was carried out by stripping the metal ion and nitric acid from organic phases with 0.01M nitric acid as the stripping agent. Once the thorium and acid were completely stripped into the aqueous phase, the organic phase is left with the free extractant in the diluent. The concentration of

extractant in the organic phase was determined by density calibration and nitric acid equilibration methods developed in our laboratory²⁰⁶. In the density calibration method, TsBP concentrations in third phase and diluent-rich phase were measured using calibration plots constructed by plotting density vs. extractant concentration of known samples. Calibration graph constructed by plotting organic phase nitric acid concentration vs. extractant concentration of known samples equilibrated with 8M HNO₃ was used for measuring TsBP concentration of unknown samples by acid equilibration methods. The concentrations of TsBP measured in third phase and diluent-rich phase by the above methods are shown in Table 3.1.

Table 3.1: Extractant concentrations in the diluent-rich phase and third phase obtained by density and nitric acid equilibration methods.

Aq. Thorium conc. (M)	Organic Thorium concentration (M)		[TsBP] (M) (after stripping) Density method	[TsBP] (M) (after stripping) Acid method
1.18	DP	0.11	0.15	0.18
	TP	0.72	3.27	3.23
1.32	DP	0.1	0.22	0.21
	TP	0.79	3.25	3.20
1.53	DP	0.08	0.25	0.25
	TP	0.90	3.20	3.19
1.73	DP	0.072	0.27	0.31
	TP	0.98	3.15	3.18
1.91	DP	0.069	0.38	0.40
	TP	1.03	3.04	3.06
2.28	DP	0.076	0.46	0.50
	TP	1.12	2.93	2.98

There is a fair match of extractant concentration values obtained by both the methods. The coordination number for Th with TsBP is 3, and it forms a complex Th(NO₃)₄.3TsBP in the organic phase. Theoretically, the concentration of extractant in each phase should be three

times the thorium concentration at each point, in that phase. At lower thorium concentrations, the third phase has more extractant concentration than expected and the diluent-rich phase has less than expected. At higher Th concentrations, this is reversed and the third phase has less extractant concentration than the expected $3 \times [\text{Th}]$, whereas the diluent-rich phase has more extractant concentration than the calculated value. This is due to three reasons. One being that when the thorium concentration is very high in the third phase, there is not enough extractant to compensate for the 1: 3 ratios in the complex; this causes the extractant concentration to fall below the expected value at higher Th concentration. The second reason could be attributed to increase in density of the third phase as thorium concentration increases. The diluent phase density does not change much with increasing Th concentration (Figure 3.2B), hence it is much less compacted than the corresponding third phase. The crowding in the third phase can cause some of the extractant molecules to enter the diluent phase. The third reason is that at higher Th loading, the third phase becomes increasingly more polar due to extraction of $\text{Th}(\text{NO}_3)_4$ and the relative decrease in the amount of non – polar diluent. TsBP is an organic compound soluble in the non – polar diluent, and it prefers the less polar diluent-rich phase at high Th concentrations.

Similar studies were carried out for TiBP based system with thorium nitrate solutions. As crud formation was observed beyond biphasic region ($\text{CAC} = 113.7 \text{ mg/mL}$ and $\text{LOC} = 43.8 \text{ mg/mL}$), it was difficult to measure Th(IV) concentration in the triphasic region. However, the LOC and CAC values for the above system have been measured by the usual method. While dissolving the organic phase (containing both third phase and diluent-rich phase) with distilled water or lean organic (1.1M TiBP/n-DD), the point at which the turbid organic phase transforms to a clear single organic phase has been taken as the threshold to get LOC and CAC values from organic and aqueous concentrations, respectively.

3.4 Extraction of Ce(IV) by TBP and TsBP as a function of aqueous Ce(IV)

Figure 3.5A shows the variation of organic cerium concentration as a function of $[\text{Ce(IV)}]_{\text{aq}}$ for TBP and TsBP systems and the critical aqueous concentration (CAC) and LOC values are marked. The CAC is the aqueous metal ion concentration above which the organic phase splits. There is more Ce(IV) loaded in the third phase than that in the diluent phase. The extraction isotherms indicated that the third phase formation limit as well as extraction of Ce(IV) by TsBP is higher than that of TBP. Branching in TsBP provides fewer surfaces for the inter-molecular interactions thereby reducing the tendency to form third phase. Further examinations into the aggregation between the cerium-organophosphate complexes have been carried out by density functional theory in order to elaborate on this aspect. The D value for TsBP is higher than TBP due to the higher basicity of the phosphoryl oxygen in the case of TsBP. The higher basicity of TsBP can be attributed to the higher inductive effect (electron donating ability) of sec-butyl groups in TsBP as compared to the n-butyl groups in TBP. Therefore, TsBP exhibits higher D values due to better binding of the ligand with the metal ion⁴².

Figure 3.5B depicts the variation of organic phase density for TBP and TsBP systems as a function of $[\text{Ce(IV)}]_{\text{aq}}$. It can be seen that Ce(IV) concentration and the density in the third phase are higher than those values for the diluent phase at a particular $[\text{Ce(IV)}]_{\text{aq}}$ for both the solvents systems. The density profiles mimic the profile of Ce(IV) loaded in the organic phase (Figure 3.5A). This is because density of the phases is dictated by the amount of metal complex present in that phase rather than the solvent which is of relatively lower density. Extrapolating this concept, a graph of organic phase cerium vs. density is plotted (Figure 3.6A). This gives a linear correlation between the organic cerium concentration and the density of the phase. In principle, an online density monitor is a quick and effective method to estimate the cerium in the phase without doing any explicit analysis. An unknown cerium

concentration in the organic phase can be computed from a linear fit $y = mx+c$ where y is density and x is cerium concentration (molar) in the organic phase.

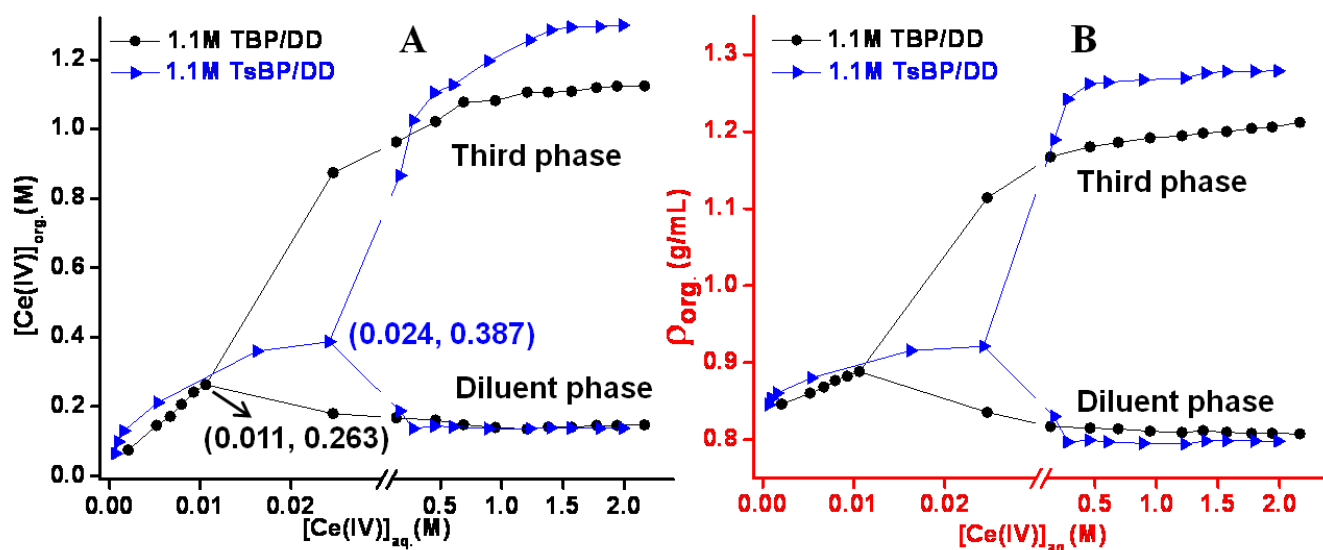


Figure 3.5: (A) Variation of Ce(IV) concentration in organic phase, third and diluent phases as a function of $[\text{Ce(IV)}]_{\text{aq}}$. The (CAC, LOC) points are marked in the inset for both the extractants. (B) Variation of the density in the organic phase, third and diluent phases as a function of $[\text{Ce(IV)}]_{\text{aq}}$.

Acid concentration in the third phase is much higher than the diluent-rich phase. The reason for this is the presence of higher extractant in the third phase which is responsible for the extraction of acid. Another reason is that the diluent-rich phase is mostly non-polar and will not stabilize the H^+ ion. The acid loaded in the organic phase is higher in the case of TsBP solvent system than TBP (Figure 3.6B).

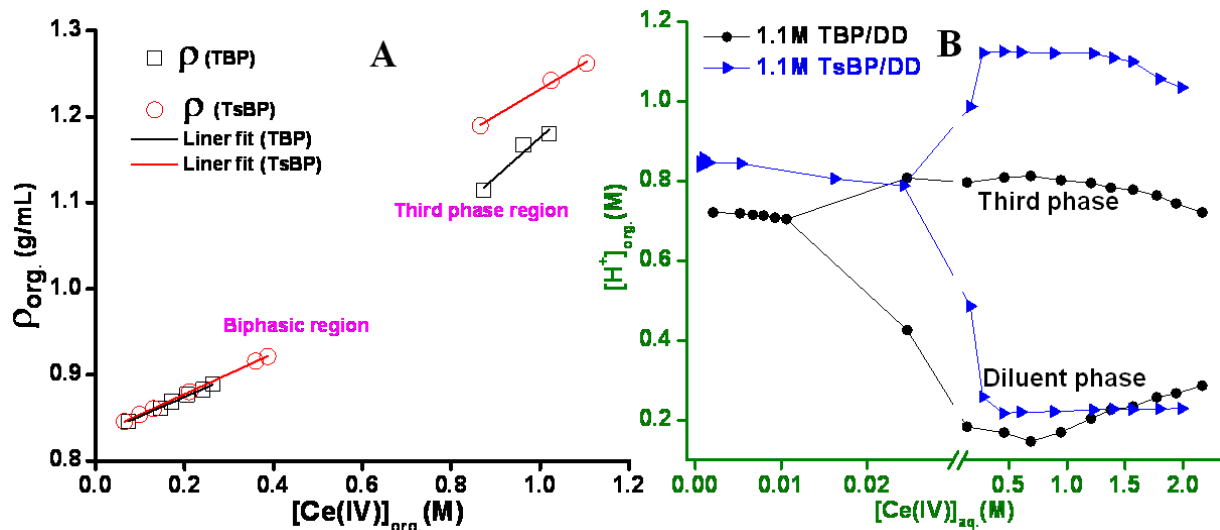


Figure 3.6: (A) Graph of the density of the phase vs. biphasic and third phase concentration of cerium (B) Concentration of acid in the organic phase, third and diluent phases as a function of $[Ce(IV)]_{aq}$.

3.5 Extraction of Ce(IV) by TBP and TsBP as a function of nitric acid

The extraction of Ce(IV) as a function of its feed concentration has been carried out for both the extractants and various parameters have been measured. In addition, the extraction of Ce(IV) as a function of nitric acid has been carried out for both 1.1M solutions of TBP and TsBP in dodecane and the D values have been measured (Figure 3.7). The extraction studies have been carried out for two different concentrations of Ce(IV) in the aqueous phase viz. 2000 and 10000 ppm solutions. The TsBP system shows higher extraction of Ce(IV) compared to TBP for both concentrations of Ce(IV). When extracted at higher concentrations, the distribution of Ce(IV) is higher. This could be attributed to the formation of Ce-O-Ce bridged cluster at higher concentrations of Ce in the organic phase. Generally as metal loading in the organic phase increases, free extractant availability reduces, leading to lower distribution. However, in the case of Ce(IV) extraction, dimer or higher clustering is formed in the organic phase leading to higher distribution for increased metal loading. The observation of these Ce complex clusters are also evidenced through the Ce-O-Ce bridged bond observed in the IR spectrum as reported by Antonio *et.al.*¹²⁴. The Ce-O-Ce stretching at $\sim 591\text{ cm}^{-1}$ is observed for such clusters and an IR peak corresponding to this has been observed for Ce(IV) third

phase with the TBP-dodecane system¹²⁴. Before the onset of third phase, at higher Ce(IV) concentrations in the biphasic region, evidence for the bridged cluster has been observed in our study (Figure 3.8). In the case of TBP based system, the bare ligand does not have a feature at 591cm^{-1} . However, in the case of TsBP system, the bare ligand has a feature at the above wavenumber, thereby masking Ce-O-Ce bridge stretching at 591cm^{-1} .

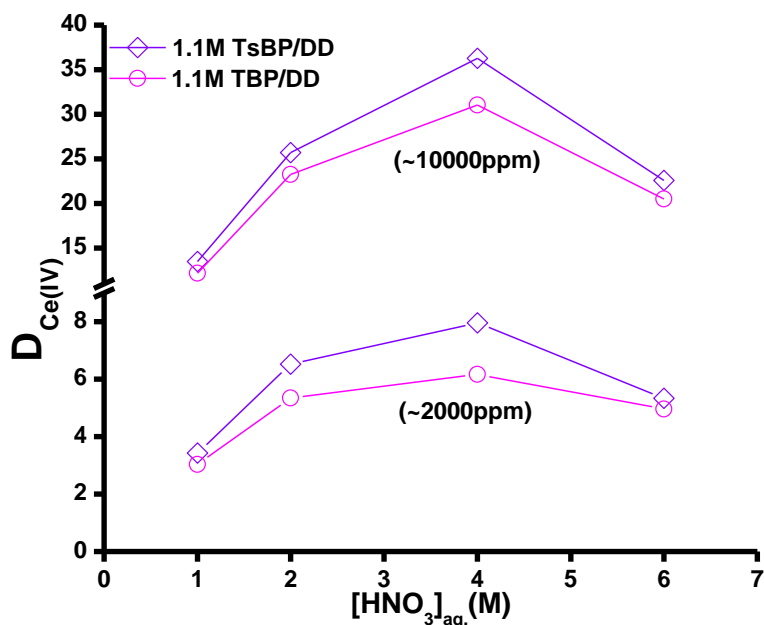


Figure 3.7: Distribution ratio of Ce(IV) as a function of nitric acid concentration. The insets indicate the initial aqueous concentration of Ce(IV).

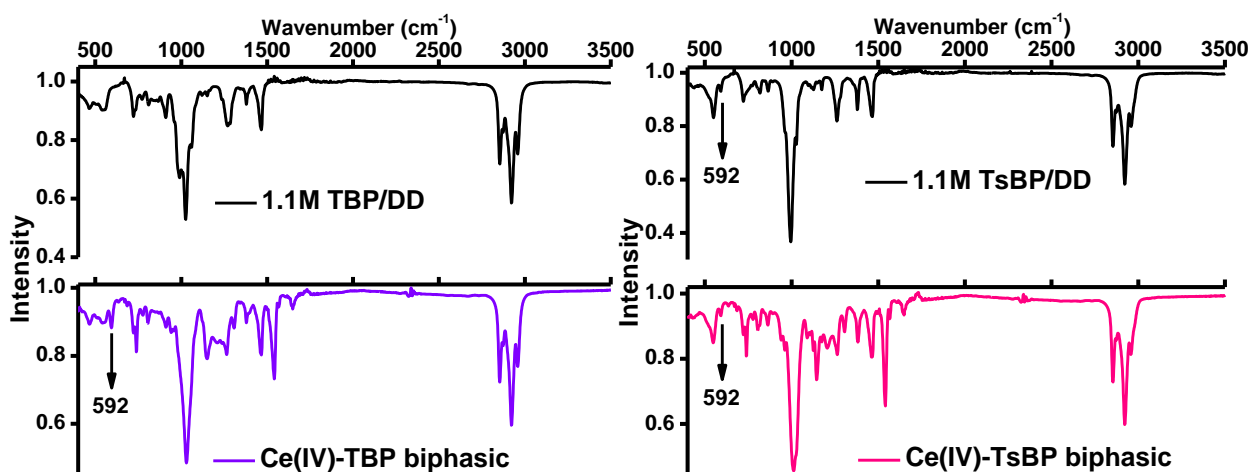


Figure 3.8: IR spectra for the cerium nitrate complex with TBP compared with 1.1M TBP/DD system. The peak corresponding to the Ce-O-Ce bridged bond is marked. The spectra for 1.1M TsBP/DD system and the corresponding Ce-complex are also shown. The bare TsBP extractant itself has a peak at 592cm^{-1} .

3.6 Computational results on Ce(IV) complexes and dimers

The estimated D values derived from solvent extraction experiments suggest that TsBP shows higher extraction of the $\text{Ce}(\text{NO}_3)_4$ species compared to TBP. Geometry optimizations have been carried out for the bare ligands, TBP and TsBP as well as the complexes of Ce(VI) with both TBP and TsBP. Subsequently the complexes were analysed for their bond lengths (Figure 3.9 and Table 3.2), and Hirshfeld charges (Table 3.3). $\text{M} - \text{O}_{\text{EXT}}$ and $\text{M} - \text{O}_{\text{NO}_3}$ refer to the bond between the metal and the phosphoryl (P=O) oxygen and metal and oxygen of nitrate group, respectively. There is no significant difference between the charges between the two complexes or between the two extractants. The calculated charges are not able to account for the difference in basicity between TBP and TsBP. In order to investigate if the difference in basicity of the P=O oxygen between the two extractants can be found computationally by other means, solvent corrected affinities for the protonation of phosphoryl oxygen in TBP and TsBP have been calculated. The P=O oxygen in TsBP extractant has a higher affinity towards proton by 1.5 kcal/mol compared to the P=O oxygen in TBP, which is in agreement with the experimentally observed higher acid extraction ability of TsBP.

The experiments are a determination of the distribution of metal species as a function of nitric acid between the aqueous and organic phase containing the extractant. The speciation of Ce(IV) nitrate depends on the acidity of the aqueous phase²⁰⁸. At lower acidity, cationic species (e.g. water solvated Ce^{4+} , $\text{Ce}(\text{NO}_3)_4\text{OH}^{2+}$) predominate. As acidity is increased higher than 2M, the nitrate species such as $\text{Ce}(\text{NO}_3)_4^{3+}$ are formed and eventually neutral $\text{Ce}(\text{NO}_3)_4$ water solvate predominates. The predominance of the charge neutral species of both Ce(IV) and its surrogate Pu(IV) causes neutral extractants such as TBP and TsBP to extract with higher distribution ratios for acidities of 1– 4M²⁰⁹. Neutral species alone are extracted to the nearly non-polar organic phase. At acidities above 6M, formation of anionic species of cerium, e.g. $\text{Ce}(\text{NO}_3)_6^{2-}$ will result in reduced extraction of metal ion into the organic phase.

For the given species present in the aqueous and organic phase under the conditions of the experiment (4M nitric acid) as discussed above, Equation (3.1) has been employed to compute the energies (B.E) of complex formation. Moreover, at every step the solvation energy for each species in the respective solvent medium has been considered in the calculations. In the past, this protocol has successfully explained the experimental observations on actinide complexation^{23, 42, 80, 210-212}

B. E for Ce(NO₃)₄ · 2TBP

$$= \Delta G_{solv}[Ce(NO_3)_4 \cdot 2TBP] + 2\Delta G_{solv}[H_2O] - \Delta G_{solv}[Ce(NO_3)_4 \cdot 2H_2O] - 2\Delta G_{solv}[TBP] \dots \dots \dots (3.1)$$

In the optimised structures of the Ce(IV) complexes, the two organophosphorous ligands are positioned diametrically opposite to each other causing the least steric repulsions that can arise by the interaction between carbon chains. The metal extractant bond length is lower in the case of the Ce(NO₃)₄·2TsBP complex compared to the Ce(NO₃)₄·2TBP complex by 0.02Å (comparing longer bond lengths on both complexes), indicating a stronger interaction between the metal centre and TsBP compared to TBP. The solvent corrected binding free energies are negative for the formation of both the complexes indicating that complex formation is favourable. However the binding free energy is higher in magnitude for the Ce(NO₃)₄·2TsBP complex compared to the Ce(NO₃)₄·2TBP complex; supporting the results obtained by the solvent extraction experiments in which the D values for TsBP are higher than TBP for the extraction of Ce(IV).

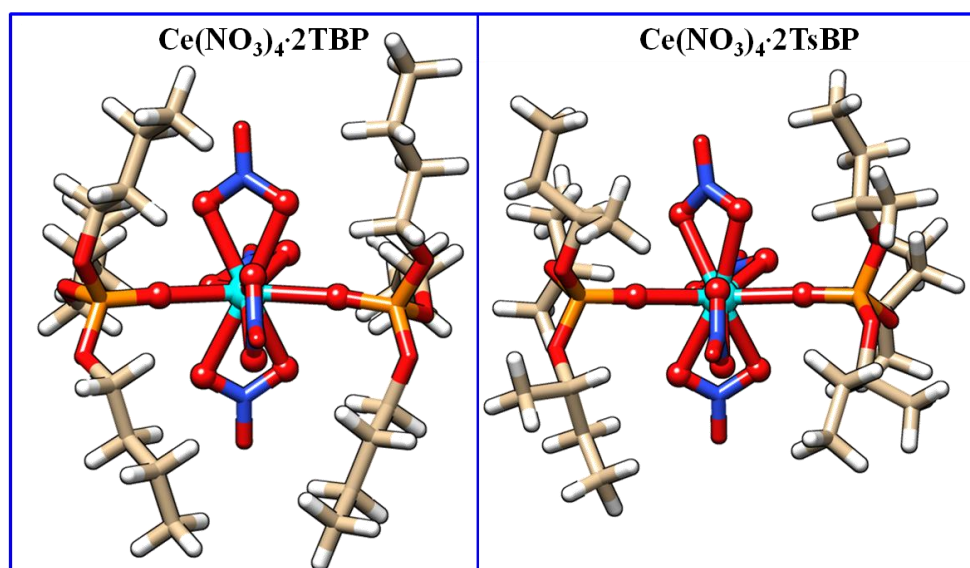


Figure 3.9: Optimized geometries of $\text{Ce}(\text{NO}_3)_4 \cdot 2\text{TBP}$ and $\text{Ce}(\text{NO}_3)_4 \cdot 2\text{TsBP}$ complexes.

Table 3.2: Solvent corrected binding free energies (kcal mol^{-1}) using M06-2X functional and computed structural parameters (\AA) of actinide extractant complexes.

Complex	$\text{Ce}(\text{NO}_3)_4 \cdot 2\text{TBP}$	$\text{Ce}(\text{NO}_3)_4 \cdot 2\text{TsBP}$	$\text{Ce}(\text{NO}_3)_3 \cdot 3\text{TBP}$
Bonds	Bond lengths (\AA)		
M – O _{Ext}	2.362 – 2.377	2.355 – 2.357	2.489 – 2.497
M – O _{NO₃}	2.493 – 2.534	2.471 – 2.544	2.556 – 2.576
Binding free energy	-5.52	-10.96	+50.16

Table 3.3: Hirshfeld charges on phosphorous and phosphoryl oxygen atoms in the bare ligand and after complexation calculated using M06-2X. Charges on the metal centre as well as nitrate oxygen atoms bound to the metal are also shown.

Complex	Q _P	Q _O (P=O)	Q _O (P-O)	Q _{N-O} (NO ₃)	Q _{N=O} (NO ₃)	Q _M
TBP	0.5001	-0.4317	-0.2039
TsBP	0.5001	-0.4317	-0.2021
$\text{Ce}(\text{NO}_3)_4 \cdot 2\text{TBP}$	0.5659	-0.3622	-0.1841	-0.2364	-0.2027	0.8804
$\text{Ce}(\text{NO}_3)_4 \cdot 2\text{TsBP}$	0.5628	-0.3648	-0.1802	-0.2396	-0.2012	0.8807

* The P=O oxygen in TsBP extractant has a higher affinity towards proton by 1.5 kcal/mol compared to the P=O oxygen in TBP.

As DFT predictions successfully interpreted the experimental trends for Ce(IV) complexation, a further venture has been undertaken to theoretically investigate the complexation behaviour of Ce(III). It has been found that organophosphates show negligible

extraction towards cerium in its trivalent oxidation state ($D < 0.05$)²¹³. The structure of the Ce(III)-TBP complex has been considered as a representative and its geometry has been optimised (Figure 3.10). The composition of trivalent lanthanide complexes with TBP has been established²¹⁴. The complex has been analysed for its geometric parameters (Table 1). The $M-O_{NO_3}$ bond lengths are reasonably close to those in the Ce(IV)-TBP complex, however $M-O_{Ext}$ bond lengths are greater in the Ce(III) complex by $\sim 0.13 \text{ \AA}$. In the Ce(III) complex as three extractant molecules are bound to the metal instead of two (as in the Ce(IV) complex), the steric and columbic effects near the metal centre are likely to result in longer bond lengths. Further, Ce is in a lower oxidation state and hence there is lower net positive charge to attract the phosphoryl oxygen of the extractant molecule. Binding free energy for the complex formation has been calculated (Table 3.2) and resulted in a positive value. This indicates unfavourable complex formation for Ce(III) and is well matched with the experimental results of the studies carried out earlier²¹³.

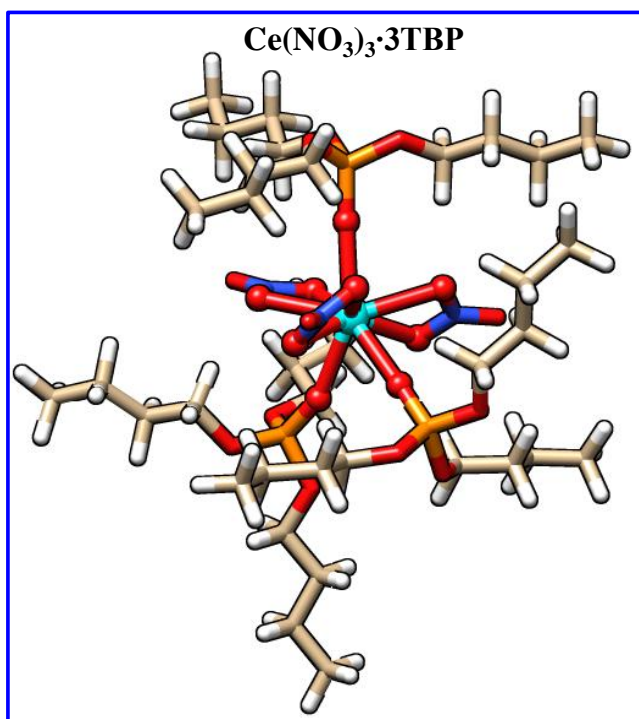


Figure 3.10: Optimized geometry of $Ce(NO_3)_3 \cdot 3TBP$ complex

The intermolecular interactions between metal-extractant complexes are a driving force for their aggregation which culminates in third phase formation. Moreover, this intermolecular interaction in the third phase is predominated by hydrogen bonding between the aggregating species²¹⁵. This has been shown through molecular dynamics simulations of metal free TBP-HNO₃ systems²¹⁵. It is well established that inter and intra molecular forces complement each other in a molecule such that the increasing number of one implies the decrease of the other^{216, 217}. Closer examination into the inter-atomic weak interactions within each of the two Ce(IV)-phosphate complexes revealed that the Ce(NO₃)₄·2TsBP complex possessed a number of weak-hydrogen bond interactions of the CH····O type. The distribution of these distances for both complexes is compared (Figure 3.11A). The Ce(NO₃)₄·2TsBP complex has more CH····O interactions in the shorter distance ranges including one within 2.4 Å. Between 2.4-2.6 Å there are only 3 weak hydrogen bonds in the TBP complex compared to 11 in the TsBP complex implying the larger number of short range interactions in the latter. At intermediate distances (2.6-2.8 Å), the numbers are comparable and at longer distances between 2.8-2.9 Å, there are more long bonds in the TBP complex. The combined effect of these interactions plays an important part in the overall stabilisation of the Ce(NO₃)₄·2TsBP by a staggering ~20 kcal/mol compared to the compositionally identical Ce(NO₃)₄·2TBP complex (Figure 3.12). Some of the CH····O interaction distances are indicated and showed generally shorter distances in the case of the Ce(NO₃)₄·2TsBP complex. These increased intra-molecular interactions in the Ce(NO₃)₄·2TsBP complex, collectively make the alkyl hydrogens on the surface of the complex less available for inter-molecular interactions. As a consequence, the aggregation of complexes which is the trigger for third phase onset is significantly reduced.

Third phase formation occurs due to the electrostatic interaction between polar cores of the metal extractant system. Energy decomposition analysis (EDA) has been used in the recent past to gain understanding about weak, non-covalent interactions²¹⁸ including hydrogen

bonding²¹⁹. Energy decomposition analysis on the two Ce(NO₃)₄·2TBP and Ce(NO₃)₄·2TsBP complexes has also been carried out in order to obtain the contributions of the three energy components to the total interaction energy. The total interaction energy between the nitrate fragments, ligand fragments and metal core can be decomposed into Pauli repulsion, steric, electrostatic, and orbital interaction. This interaction energy, ΔE_{int} can be broken down into three components *viz.*

$$\Delta E_{\text{int}} = \Delta E_{\text{elec}} + \Delta E_{\text{Pauli}} + \Delta E_{\text{orb}}$$

Where ΔE_{elec} and ΔE_{Pauli} denote the electrostatic interaction energy and the Pauli repulsive energy, respectively, between the fragments and ΔE_{orb} is the orbital interaction term. In the case of third phase, the polar metal-solvates mutually attract each other by predominantly electrostatic forces between polar cores in a non-polar diluent environment^{30, 59}. The results obtained by energy decomposition of the two isomeric Ce(IV) complexes reveal that the electrostatic interaction within the Ce(NO₃)₄·2TsBP complex is higher than the Ce(NO₃)₄·2TBP complex (Figure 3.11B). Increased electrostatic intra-molecular interaction indicates a lower tendency towards electrostatic attractions between neighbouring polar cores, in turn decreasing the driving force towards aggregation.

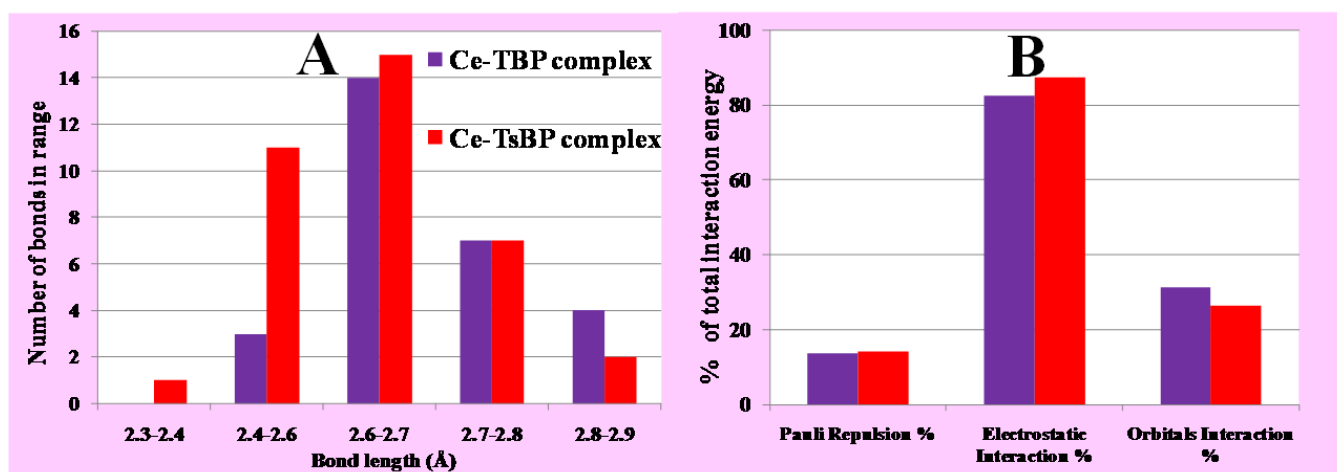


Figure 3.11: (A) Distribution of the number of CH...O interaction distances in each length range and (B) Energy decomposition components of the total interaction energy for complexes of Ce(IV) with TBP and TsBP.

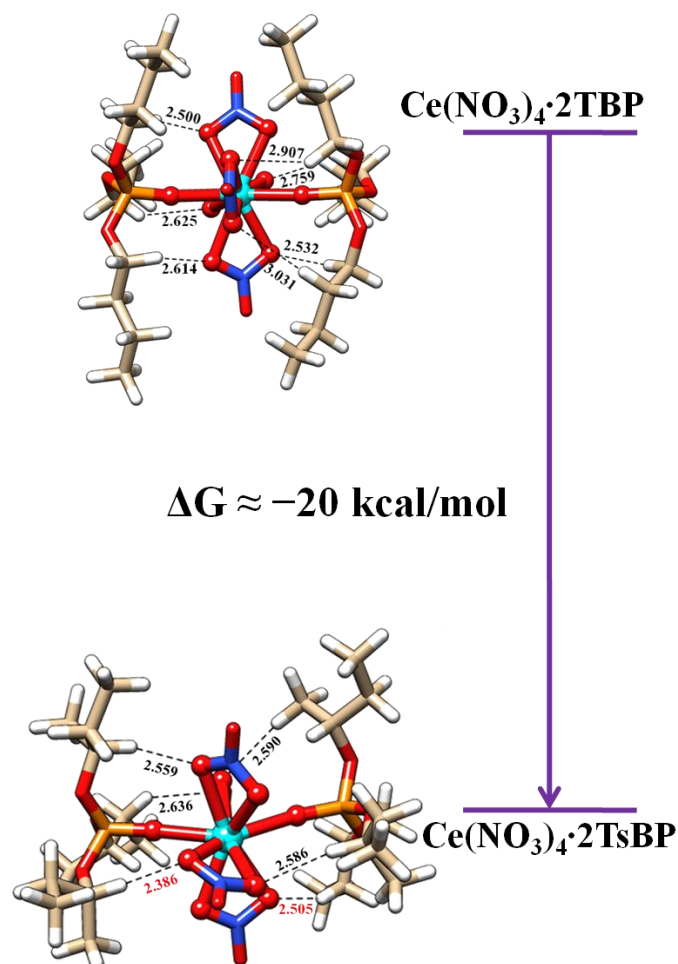


Figure 3.12: Representation of the relative energies of $\text{Ce}(\text{NO}_3)_4 \cdot 2\text{TBP}$ and $\text{Ce}(\text{NO}_3)_4 \cdot 2\text{TsBP}$ complexes. A few of the $\text{CH} \cdots \text{O}$ interaction distances are marked on the structures.

As dimer formation has been observed in the organic phase at higher concentrations of the Ce(IV) complexes, the dimers have also been considered in the theoretical calculations on third phase formation. The dimers are constructed such that an oxo-bridge exists between two Ce(IV) ions as observed from the IR and proposed by Antonio *et. al.*¹²⁴. The oxo-bridge carries a -2 charge shared between the two Ce atoms. In order to maintain Ce in the +4 oxidation state, the bridge replaces two negatively charged nitrate groups. Thus, structures of the cerium nitrate–TBP dimer of the composition $\text{TBP-Ce}(\text{NO}_3)_3\text{-O-Ce}(\text{NO}_3)_3\text{-TBP}$ and the corresponding TsBP dimer complex have been constructed and optimized. As D increases with increased loading, the 1:2 ratios in monomer must be reduced to 2:3 or 2:2 in dimer.

Generally a decrease in D for metal ions is due to the competition for the free extractant. In the case of Ce(IV), the increase in D at higher loading implies that metal: extractant ratio in the dimer, must decrease from the 1:2 ratio present in the monomer. For the sake of symmetry, dimers with 2:2 Ce: extractant ratio has been considered. As observed in the case of the monomer, the Ce–TsBP dimer is lower in energy than the Ce–TBP dimer. A stabilisation of ~25kcal/mol has been observed (Figure 3.13). The optimized structure of the Ce–TBP dimer have Ce–O_{NO3} bond lengths in the range 2.445–2.504 Å and Ce–O_{Ext} bond lengths between 2.316–2.323 Å. In the case of the Ce–TsBP dimer these bond lengths are 2.431–2.498Å and 2.315–2.365Å, respectively.

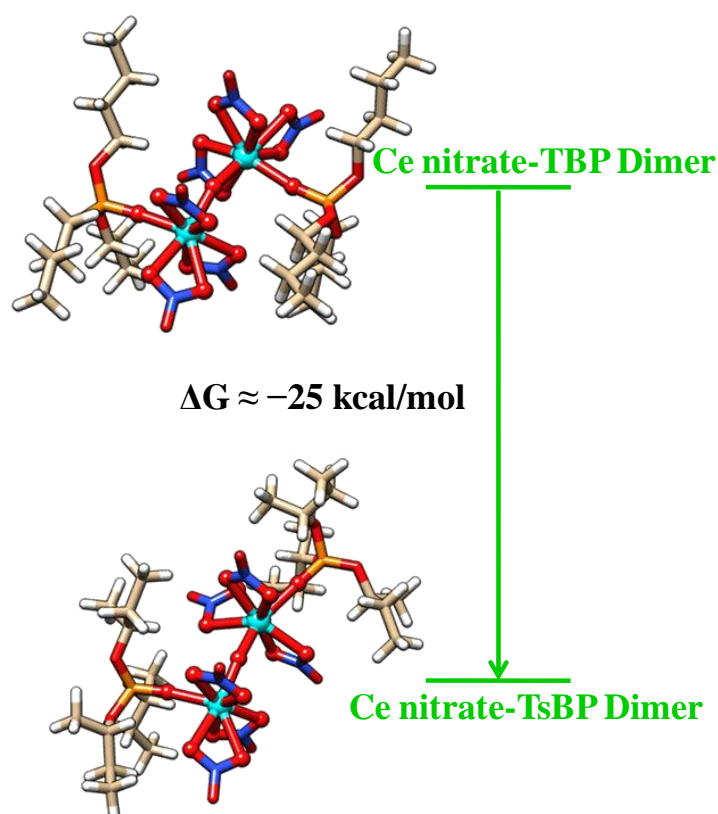


Figure 3.13: Representation of the relative energies of Ce nitrate–TBP and Ce nitrate–TsBP dimers. The energy scheme in the inset indicates the relative stabilisation of the Ce nitrate–TsBP dimer.

An analysis of the intra-molecular CH···O bond lengths has been carried out in order to understand the basis for this energy difference. As observed in the case of the monomers, the

shorter range CH \cdots O bond lengths (2.5–2.7Å) in the Ce–TsBP dimer are more than those in the Ce–TBP dimer (Figure 3.14). Conversely, in the longer range of bond distances (2.7–2.9Å), the Ce–TBP dimer has the larger number of such bonds. This is one of the factors for lowering of energy. Apart from the difference in CH \cdots O bond lengths, in the case of the dimer geometries (Figure 3.13), the optimized structures show a different orientation of one of the TsBP ligands in the dimer. In the Ce–TBP dimer, the two ligands are in ‘trans’ orientation. However, in the TsBP case due to steric effect of branched ligand, during the geometry optimization one of the ligands is oriented in a fashion such as to reduce the steric repulsion. This is an important factor that contributes to the absolute energy of the dimer. This difference of orientation was not there in monomer case; hence the weak interactions played a larger role in comparison with the dimers.

Further, energy decomposition analysis has been carried out by considering the monomers as fragments, and the results show a 20% increase in the electrostatic interaction component in the case of Ce–TsBP dimer. This is consistent with the increased electrostatic interaction observed in the case of monomeric Ce–TsBP over Ce–TBP complex.

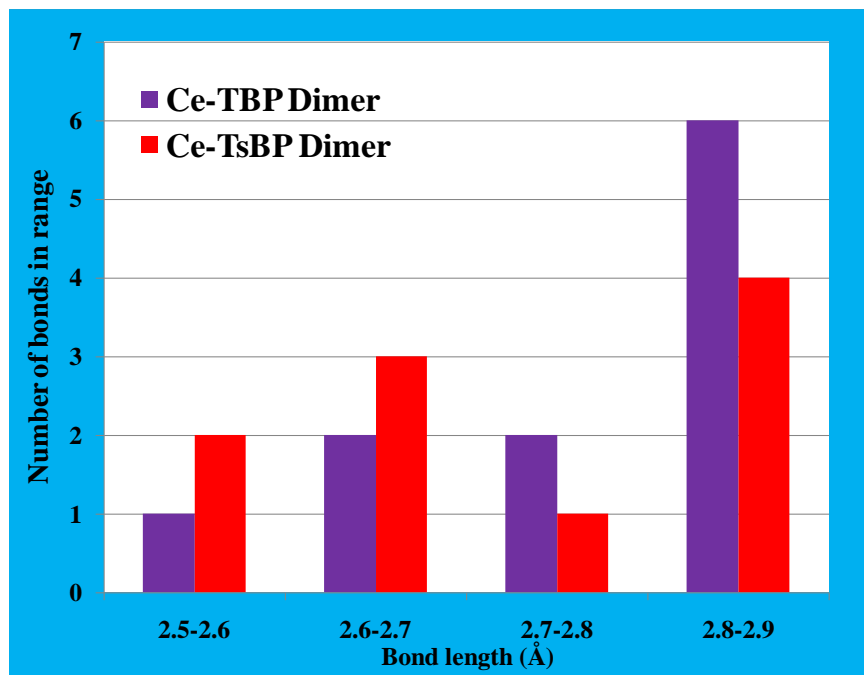


Figure 3.14: Distribution of the number of CH \cdots O interaction distances in each length range for Ce–TsBP and Ce–TBP dimers.

The calculated infra-red spectra of cerium nitrate complexes with TBP and TsBP and the bare ligands are shown (Figure 3.15) and compared with the experimentally recorded spectra for each compound. The peaks corresponding to the P=O stretching frequency are indicated in the insets. In the case of both TBP and TsBP complexes, there is a red shift in the P=O stretching frequency in comparison with the bare ligands.

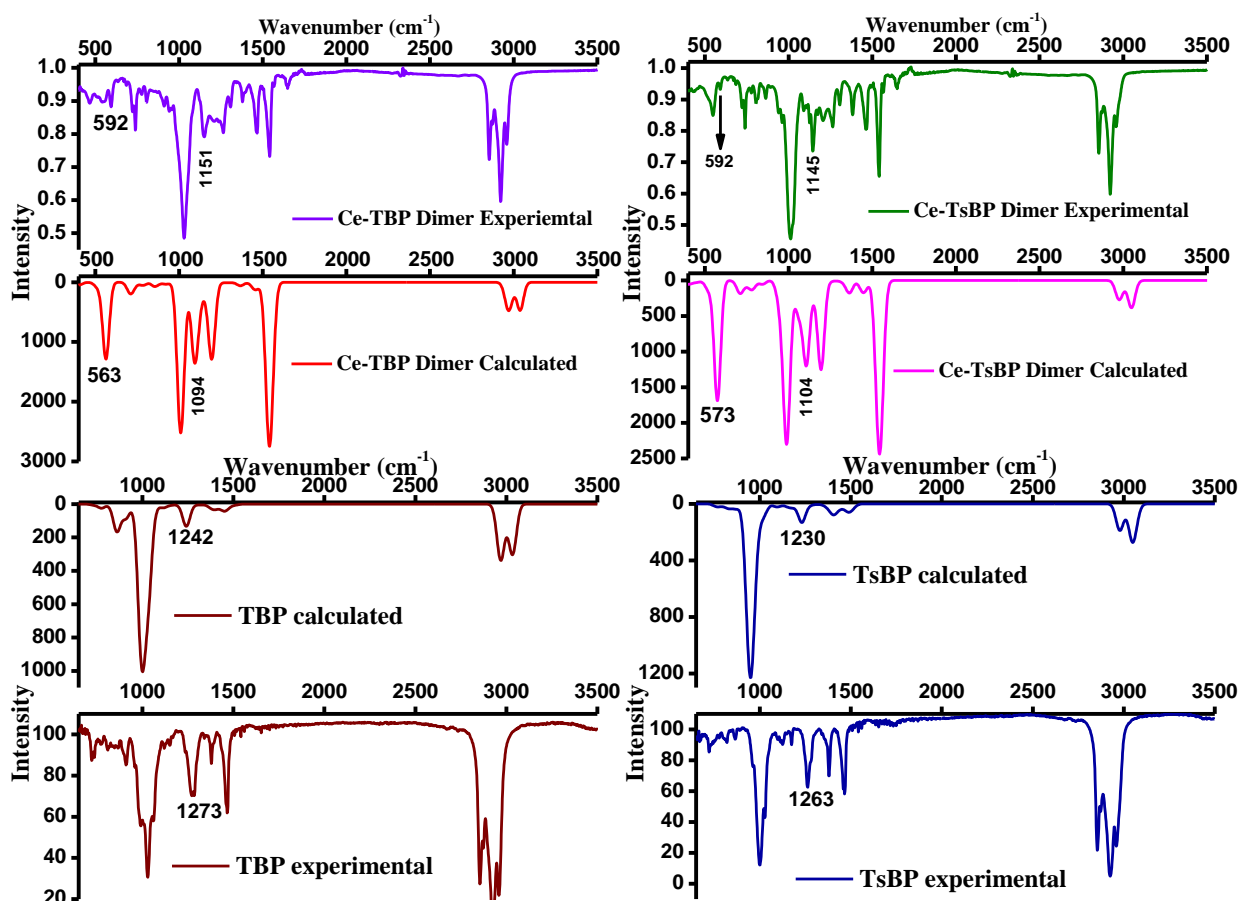


Figure 3.15: Experimentally observed and calculated IR spectra for the cerium nitrate complex dimer with TBP and TsBP. The peak corresponding to the Ce-O-Ce bridged bond is marked along with the P=O stretching peak. The experimental and calculated spectra for and the bare ligands TBP and TsBP are also shown. The frequencies shown mark the P=O stretch for the bare ligands.

3.7 Conclusion

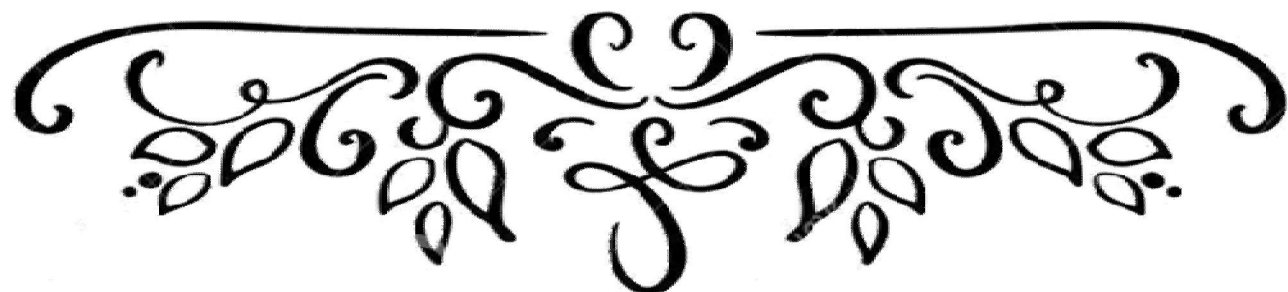
The distribution of Th(IV) and HNO₃ in the extraction with 1.1M TsBP/DD and 1.1M TiBP/DD systems are compared with the 1.1M TBP/DD system. The variation in density of organic phase and V_{DP}/V_{TP} ratios as a function of equilibrium aqueous phase Th(IV) concentration is also carried out. It has been shown that each extractant–diluent system can be calibrated such that a fair estimate for the concentration of thorium can be obtained from the density of the phase. Concentration of TsBP in organic phases after phase splitting has also been measured. The extraction of Ce(IV) as a function of aqueous Ce(IV) concentration ranging from 1-280mg/mL has been carried out from nitric acid medium by employing

TsBP-dodecane and compared with the conventional TBP-dodecane system. Third phase formation occurs in both extractant systems; however, TsBP has higher third phase limits compared to TBP in the extraction of Ce(IV). TsBP showed higher distribution ratios compared to TBP in both the biphasic and triphasic regions. The higher extraction of TsBP compared to TBP can be attributed to the higher basicity of the phosphoryl oxygen that arises due to the inductive effect of the secondary methyl branching. The acid extracted to the organic phase, by TsBP is higher compared to TBP, confirming the higher basicity of TsBP as an extractant.

In addition to experimental studies, theoretical investigations were carried out using DFT to understand the binding between ligand and metal. The data on extractant-metal bond distances suggest weaker binding of TBP to the Ce(IV) centre compared to TsBP. Binding energies obtained by DFT suggested the formation of the Ce(IV)-TsBP complex to be more favourable than the TBP complex corroborating well with experimental findings. Theoretical binding free energy for the Ce(III)-TBP complex has also been obtained for comparison and yielded a positive complexation energy value consistent with previous experimental reports. Beyond the purview of complexation energetics, our electronic structure calculation took its founding step into the theoretically unexplored domain of third phase formation in metal complexes. The calculations and geometric observations provide insights into the lower aggregation leading to higher third phase limits of Ce-TsBP complexes as compared to the Ce-TBP complexes. The entire quantum chemical study is in excellent agreement with experimental observations



Chapter 4



“And in the end it's not the years in your life that count; it's the life in your years”

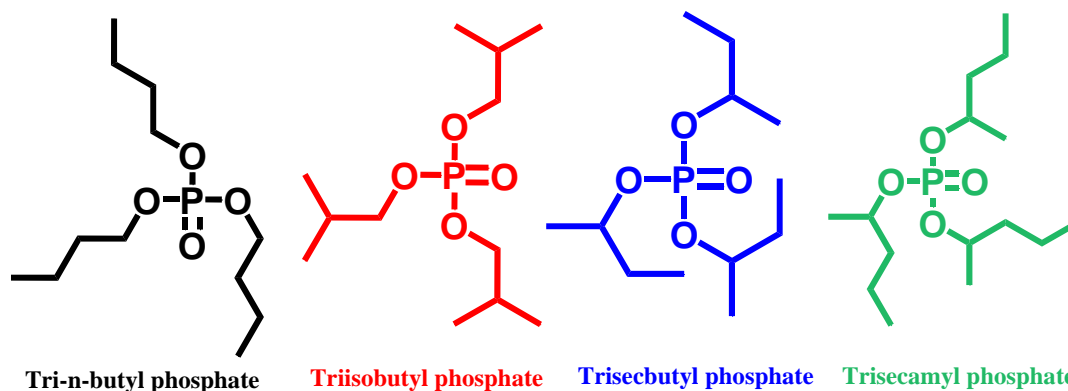
~ Abraham Lincoln

TRENDS IN SMALL ANGLE NEUTRON SCATTERING OF ACTINIDE – TRIALKYL PHOSPHATE COMPLEXES: A MOLECULAR INSIGHT INTO THIRD PHASE FORMATION

4.1 Introduction

The Small Angle Neutron Scattering (SANS) technique has been employed for a variety of applications, including study of polymers²²⁰⁻²²⁸, organic molecules^{229, 230}, gels²³¹, micro²³²⁻²³⁷ and nanoscale materials^{230, 238} and biomolecules^{239, 240}. A subset of these that pertain to the current work include, probing aggregation behaviour of micelles^{220, 241}, cloud point studies²⁴²⁻²⁴⁵ and temperature dependent aggregation^{243, 246}. Such aggregation leading to third phase formation during extraction of Th(IV) by organophosphates is a concern during the processing of Th(IV) solutions.

Tri-sec-butyl phosphate (TsBP) has shown higher U/Th separation factor and lesser third phase formation tendency compared to its isomers, TBP and tri-iso-butyl phosphate (TiBP)²⁴⁷. Tri-sec-amyl phosphate (TsAP), on the other hand, does not form third phase with both U(VI) and Th(IV) up to saturated metal concentrations when extracted from 1M nitric acid at 303 K⁶³. In the present work, SANS studies have been carried out using solutions of TBP, TiBP, TsBP and TsAP in n-C₁₂D₂₆ (deuterated dodecane) loaded with U(VI) as well as Th(IV). The structures of the trialkyl phosphates (TalP) used in this study are shown in Scheme 4.1. The variation in the SANS profiles, stickiness parameter and attraction potential energy have been examined as a function of three parameters influencing third phase formation phenomena. The effects of extractant, metal ion concentration and temperature have been systematically investigated.



Scheme 4.1: Structure of trialkyl phosphates studied in the present work

4.2 SANS Measurement

For the SANS measurements, organic phase containing metal complexes of known concentration in 1.1 M TalP/*n*-C₁₂D₂₆ was used. The neutron scattering experiments were carried out using the SANS facility at Dhruva reactor, Bhabha Atomic Research Centre (BARC), India²⁴⁸. A mean neutron wavelength of 5.2 Å with a resolution of ~ 15 % was used for the experiments. The scattered neutrons were measured using a one-dimensional ³He gas detector. The samples were scanned in the Q range from 0.017 to 0.35 Å⁻¹. A quartz cell with a thickness of 2 mm was used for containing the samples during the measurements. The diameter of micelle (σ), is calculated mathematically assuming the particles to be spherical and the width of the square-well potential (Δ), is taken as 3 Å for the potential energy calculations²⁴⁹. In order to calculate the aggregate diameter, volume of a single extractant molecule was first computed from its density and molecular mass. The aggregation number was taken as 3 for Th(IV) and 2 for U(VI)^{250, 251}. The expression for the volume of a sphere was used to obtain the size of aggregates. Throughout the data analysis, corrections were made for instrumental smearing by the appropriate resolution function. The parameters in the analysis were optimised by means of non-linear least-squares fitting program. As third phase formation is inherently an aggregation phenomenon, sticky hard sphere model has been used to fit the data for these systems.

The concentration of U(VI) and Th(IV) in the organic phase was varied so as to approach the third phase region with increasing metal concentration and test the aggregation parameters. The concentration of metal ions (Th and U) and HNO₃ of samples used for SANS experiments are shown in Table 4.1.

Table 4.1: Concentration of metal ions/acid in the samples used for SANS experiments

Organic phase	Concentration of metal ion		Metal free samples
	U(VI)	Th(IV)	Conc. of HNO ₃ (M) in the organic phase
1.1M TBP/ <i>n</i> -C ₁₂ D ₂₆	20g/L	20g/L	0.23
	30g/L	30g/L	
	40g/L	40g/L	
	120g/L		
1.1M TiBP/ <i>n</i> -C ₁₂ D ₂₆	20g/L	20g/L	0.20
	30g/L	30g/L	
	40g/L	40g/L	
	120g/L		
1.1M TsBP/ <i>n</i> -C ₁₂ D ₂₆	20g/L	20g/L	0.26
		30g/L	
		40g/L	
1.1M TsAP/ <i>n</i> -C ₁₂ D ₂₆	40g/L	20g/L	0.22
	80g/L	30g/L	
	120g/L	40g/L	

4.3 Study on metal free HNO₃ systems

Extraction of metal ions was carried out at 1M acidity to ensure higher loading of metal complexes in to the organic phase. At higher acidities, the H⁺ ion competes for the free extractant and less of the metal species are extracted into the organic phase. Moreover, at higher acidities, the third phase limit is lowered and a wide range of metal loading in the organic phase cannot be achieved. When metal ions are extracted, both the metal complex and the H⁺ species are present in the organic phase. Metal free organic phases of 1.1M TalP/*n*-C₁₂D₂₆ were also prepared by equilibrating with 1M HNO₃ and the scattering pattern was recorded. It is seen from Figure 4.1 that the rise of scattering intensity in the low Q region is highest for TBP, marginally lower for TiBP, and reduces further for TsBP and TsAP. The scattering intensity shows correlation with the tendency of each extractant to form

third phase with the metal ions. The higher scattering intensity in the low Q region is expected to arise from increase in size and/or increase in attractive interaction of the aggregates. SANS data are best fitted by considering the increase in the attractive interaction between the aggregates. The extractants, TBP and TiBP have a higher tendency to form third phase with Th(IV) compared to TsBP; TsAP does not form third phase with Th(IV)⁶³.

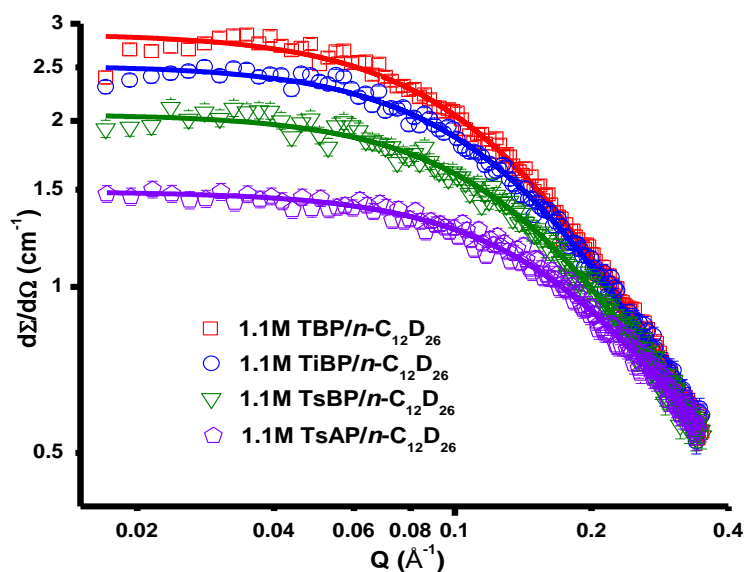


Figure 4.1: SANS data of metal free 1.1 M TalP/*n*-C₁₂D₂₆ -1M HNO₃ systems at 303K.

4.4 Aggregation behaviour of Th(NO₃)₄ systems

Effect of the structure of trialkyl phosphate

The scattering intensity for Th(IV) loaded sample changes with variation in structure of extractant, when all other factors are kept constant. Figure 4.2 shows the scattering profiles obtained at 303K for various TalP/ *n*-C₁₂D₂₆ systems, all loaded with same amount of metal ion (30 g Th(IV)/L). The highest scattering intensity in the low Q region is shown by TBP followed by TiBP, TsBP and TsAP respectively. The stickiness parameter (τ^{-1}) and the attractive potential energy (U_0) calculated for the four systems are shown (Table 4.2a).

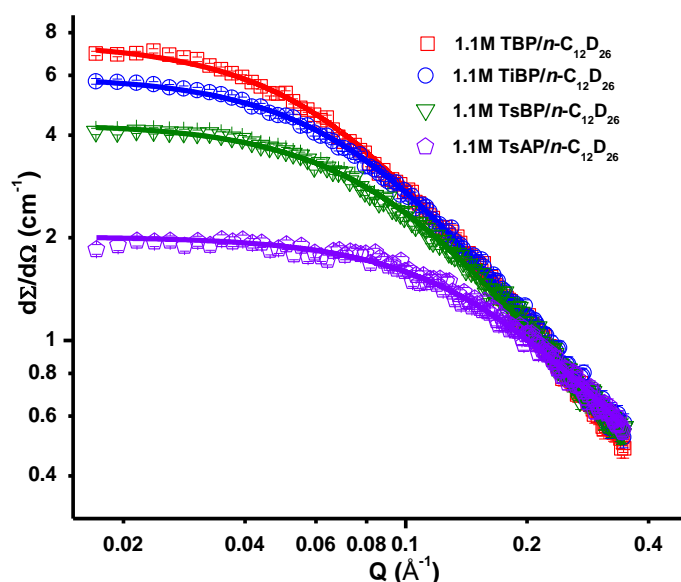


Figure 4.2: SANS data obtained for the 1.1 M TalP/n-C₁₂D₂₆ - Th(NO₃)₄/1M HNO₃ systems loaded with 30 g Th/L at 303K.

Highest stickiness parameter was observed with TBP, which has a higher third phase formation tendency with Th(IV). The interaction potential energy is the most negative indicating higher attraction between the micelles. The stickiness parameter decreases with branching in the alkyl chain as in the case of TiBP and is further lower for TsBP, which has lower third phase formation tendency with Th(IV). For TsAP, the value of stickiness parameter drops much lower and it is also observed from solvent extraction experiments that TsAP does not form third phase with Th(IV), when extracted from 1M HNO₃ at all metal ion concentrations. Based on the experimentally derived metal–ligand ratio in the complex, aggregation number was taken as 3 for Th(IV) complexes²⁴⁷. An aggregate diameter of 13.8Å was obtained for TBP, TiBP and TsBP and a diameter of 14.6Å for TsAP, based on the assumption that the micelles are spherical as discussed above. For a given system, the size of the aggregates does not change, though the potential varies depending on the conditions. This has been previously studied in the work of Verma *et. al.*^{250, 251} which showed that aggregate number changed only in the particle growth model applied to higher metal loading, e.g. third

phase regions. Our studies, however, are restricted to lower metal loading where radii remain constant as consistent with earlier study^{250, 251}.

Table 4.2: The fitted parameters of SANS data for (a) 1.1 M TalP/n-C₁₂D₂₆ - Th(NO₃)₄/1M HNO₃ systems, loaded with 30g/L of Th(IV) at 303K. (b) 20g/L and 40g/L Th(IV) loaded TalP/ n-C₁₂D₂₆ systems at 303K. (c) 1.1 M TalP/n-C₁₂D₂₆ - Th(NO₃)₄/1M HNO₃ systems, loaded with 40g Th/L as a function of temperature.

a) Conditions: TalP/n-C ₁₂ D ₂₆ /1M HNO ₃ systems, loaded with 30 g/L of Th(IV) at 303K.								
System		Aggregation number (N)	Aggregate Diameter (D)	Stickiness Parameter (1/τ)		Potential Energy [U₀ (k_BT)]		
1.1 M TBP/n-C ₁₂ D ₂₆		3	13.8 Å	9.3		-1.47		
1.1 M TiBP/n-C ₁₂ D ₂₆		3	13.8 Å	8.5		-1.38		
1.1 M TsBP/n-C ₁₂ D ₂₆		3	13.8 Å	7.7		-1.28		
1.1 M TsAP/n-C ₁₂ D ₂₆		3	14.6 Å	4.7		-0.84		
b) Conditions: 20g/L and 40g/L Th(IV) loaded TalP/ n-C ₁₂ D ₂₆ systems at 303K.								
Metal Conc.	TBP (N = 3, D = 13.8 Å)		TiBP (N = 3, D = 13.8 Å)		TsBP (N = 3, D = 13.8 Å)		TsAP (N = 3, D = 14.6 Å)	
	1/τ	U₀ (k_BT)	1/τ	U₀ (k_BT)	1/τ	U₀ (k_BT)	1/τ	U₀ (k_BT)
20g/L	7.4	-1.24	7.3	-1.23	6.9	-1.17	4.6	-0.81
40g/L	11.3	-1.66	9.2	-1.46	8.9	-1.42	4.9	-0.87
c) Conditions: 1.1 M TalP/n-C ₁₂ D ₂₆ - Th(NO ₃) ₄ /1M HNO ₃ systems, loaded with 40 g Th/L								
Temp(°C)	TBP (N = 3, D = 13.8 Å)		TiBP (N = 3, D = 13.8 Å)		TsBP (N = 3, D = 13.8 Å)			
	1/τ	U₀ (k_BT)	1/τ	U₀ (k_BT)	1/τ	U₀ (k_BT)	1/τ	U₀ (k_BT)
40	9.8	-1.52	8.4	-1.37	8.0	-1.32		
50	8.8	-1.41	7.6	-1.27	7.5	-1.25		
60	7.8	-1.29	7.2	-1.21	6.9	-1.17		
70	7.4	-1.24	6.7	-1.14	6.4	-1.10		

Effect of metal loading

For a given extractant system, the scattering intensity, stickiness parameter and attraction potential energy change when the metal concentration is varied. At higher concentration of Th(IV) in the organic phase (40g/L), scattering intensity in the low Q region is highest for all extractant systems at a fixed temperature of 303K, (Figure 4.3 (A–D)). Similar to the trend observed in Figure 4.2, TBP system shows highest scattering intensity for a given metal loading, and least for TsAP system. The difference in intensity between metal loading of 20g/L and 40g/L is most pronounced in the case of TBP (Fig.4.3 C), which has the highest

tendency to form third phase and the least difference was observed for TsAP system, which does not form third phase with Th(IV)/1M HNO₃ at all Th concentrations. From the patterns, it can be seen that for extractants such as TBP and TiBP which have higher third phase formation tendency, the scattering intensity is more sensitive to variation in organic metal concentration.

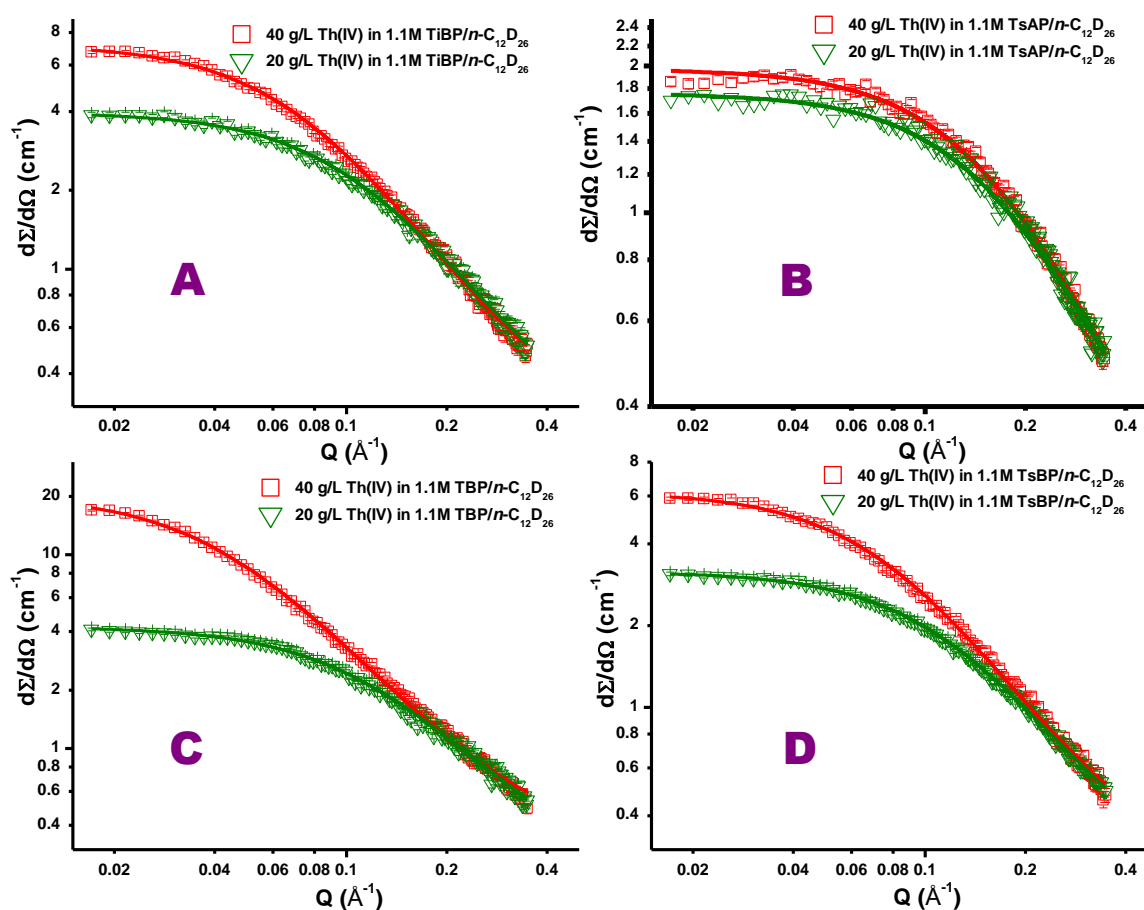


Figure 4.3: SANS plots of 1.1 M TalP/n-C₁₂D₂₆ - Th(NO₃)₄/1M HNO₃ systems with organic Th(IV) loading of 20g/L and 40g/L at 303K. (A) TiBP (B) TsAP (C) TBP and (D) TsBP

When the metal loading is higher, the tendency for the system to form third phase is higher, because of the stronger attractive interaction between the metal solvate species while approaching the LOC. When the number density of particles increase, they are forced to pack in such a way that they come closer, making this a factor for aggregation. In general, the attraction leading to third phase formation / aggregation can be prevented in metal-extractant systems by increasing the alkyl chain length of the extractant molecules, thus enhancing the

intermicellar distance making the central polar cores stay away from each other. In addition, for systems consisting of isomers of extractants with similar micellar radius, the structure of the extractant may influence the intermicellar distance, in a way this is achieved by introducing branching on the carbon chain close to the polar core. Thus the stickiness parameter increases from 7.7 in TsBP to 9.3 in TBP system. It is interesting to note that even in the nanoparticle systems, these are often capped with sterically bulky molecules to prevent them from coming close together, greatly reducing their tendency to aggregate^{252, 253}. For the four extractant systems (Figure 4.3), stickiness parameters have been computed and the results are shown in Table 4.2b. As expected, the stickiness parameter is higher at 40g/L metal loading compared to 20g/L for all the extractants. The attraction potential is larger at higher metal concentrations, indicating more attraction between the micelles. Among the extractants, TBP has the highest stickiness, followed by TiBP, TsBP and TsAP. This trend matches with the trends observed in solvent extraction experiments, which showed a similar trend for third phase formation tendency among these extractants⁶³. Stickiness parameter is markedly lower for TsAP than the other three phosphate systems with butyl carbon chain, indicating that its third phase limits are higher. This has been observed by earlier solvent extraction experiments carried out in our laboratory⁶².

Effect of temperature

Apart from investigating the effects of structure of alkyl groups of the extractant and organic metal loading on neutron scattering, a third parameter namely, temperature was probed in the present work using the same tool, keeping all other factors similar. Figure 4.4 (A, B and C) shows the variation in SANS patterns for TBP, TiBP and TsBP systems, as the temperature was increased from 313 to 343K in steps of 10K. For all extractant systems, the Th(IV) concentration was kept at 40g/L. As temperature was raised, the intensity of scattering

monotonically reduces for all extractants. Among these, TBP system is most sensitive to rise in temperature from 313 to 323K, as well as from 323 to 333K.

The increase in thermal energy suppresses aggregation in the solvent phase and hence prevents third phase formation. Thus, aggregation leading to third phase formation can be minimised by increasing the temperature as observed by our earlier solvent extraction experiments⁶³. The variations in stickiness parameter and attraction potential energy as a result of temperature increase are shown in Table 4.2c. The data indicate that there is a gradual decrease in the stickiness parameter with increase in temperature for all the three solvents.

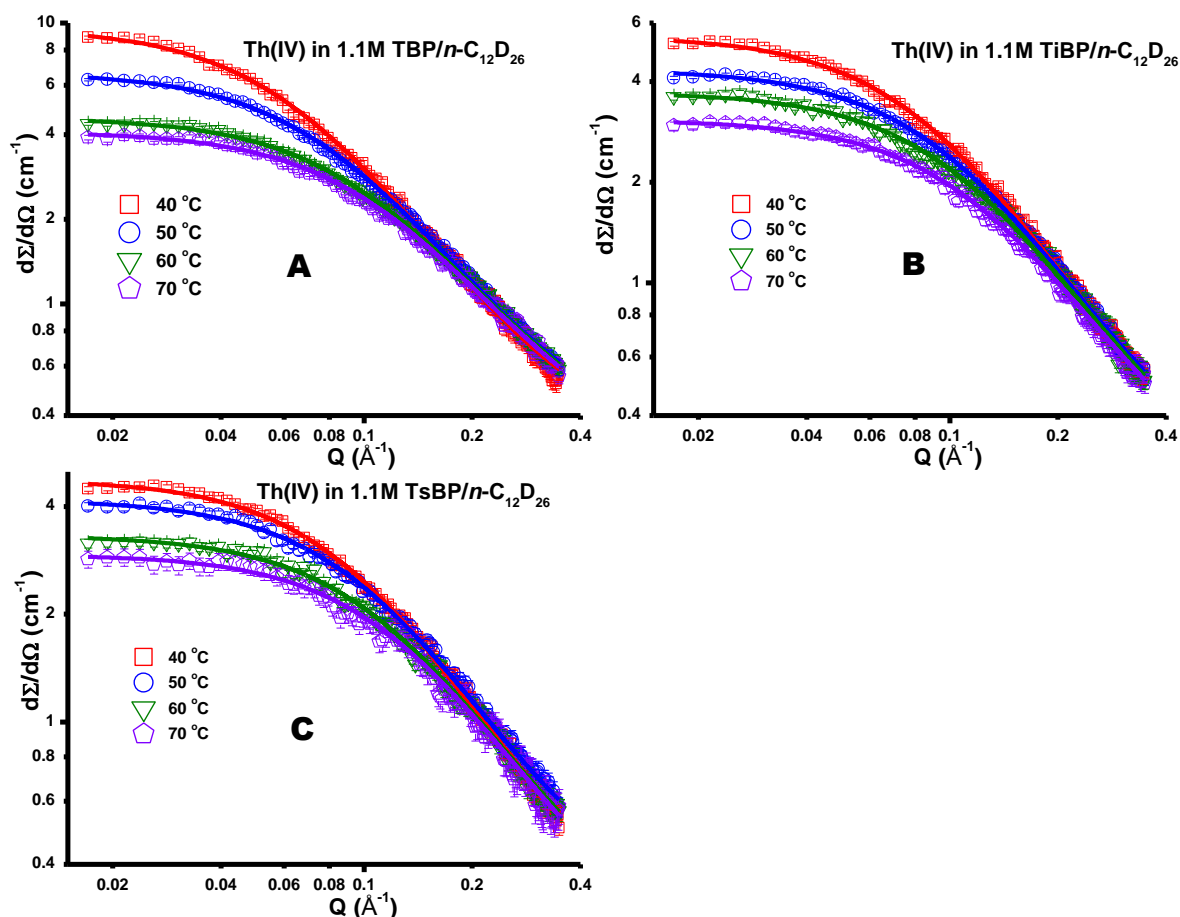


Figure 4.4: Variation in the scattering pattern as a function of temperature for 1.1 M TalP/ n-C₁₂D₂₆-Th(NO₃)₄/1M HNO₃ systems with a Th(IV) loading of 40g/L in the organic phase. (A) TBP (B) TiBP (C) TsBP systems are shown in the panels.

4.5 Investigations on $\text{UO}_2(\text{NO}_3)_2$ systems

Effect of metal loading

The third phase formation tendency of Th(IV) complexes showed a strong correlation with the stickiness parameter obtained from the SANS patterns. It has been observed from solvent extraction experiments that U(VI) does not form third phase with the 1.1M TalP/*n*-C₁₂D₂₆ in the extraction from 1M HNO₃. Hence to investigate our predictions, similar SANS experiments were carried out using samples loaded with U(VI). Figure 4.6 (A), (B) and (C) shows the fitted SANS plots obtained at 303K from TiBP, TBP and TsAP systems, respectively, as a function of increasing U(VI) concentration in the organic phase. TiBP and TBP systems were loaded with 20, 30 and 40g/L of U(VI). From the profiles it can be seen that there is a marginal increase in the scattering intensity as metal concentration was increased for all the three extractants. Stickiness parameter and attraction potential energy have been calculated for all metal concentrations (Figure 4.5 A to C) (Table 4.3a). For all the extractant systems, there is a small change in the stickiness and aggregation energy as the metal loading is increased, indicating that aggregation tendency of U(VI) loaded organic phase have a limited sensitivity to increasing metal loading. Aggregation number was taken as 2 for all extractant systems loaded with U(VI). For TBP and TiBP, the micelle diameter obtained was 12.0Å, and for TsAP it was calculated to be 12.7Å.

As 10g/L change in U(VI) had only a small effect on the intensity and fitted parameters obtained from the curves, 1.1M TsAP/*n*-C₁₂D₂₆ was loaded with 40 and 80g/L of U(VI). Figure 4.5C shows the SANS results obtained from these two systems and Table 4.3a shows the corresponding (τ^{-1}) and (U_0) values. The magnitude of (τ^{-1}) is lower for TsAP compared to TBP and TiBP, illustrating that its tendency to form third phase is even lower than the two butyl phosphates. It has also been observed experimentally that phosphates with a longer carbon chain are less susceptible to third phase formation⁶².

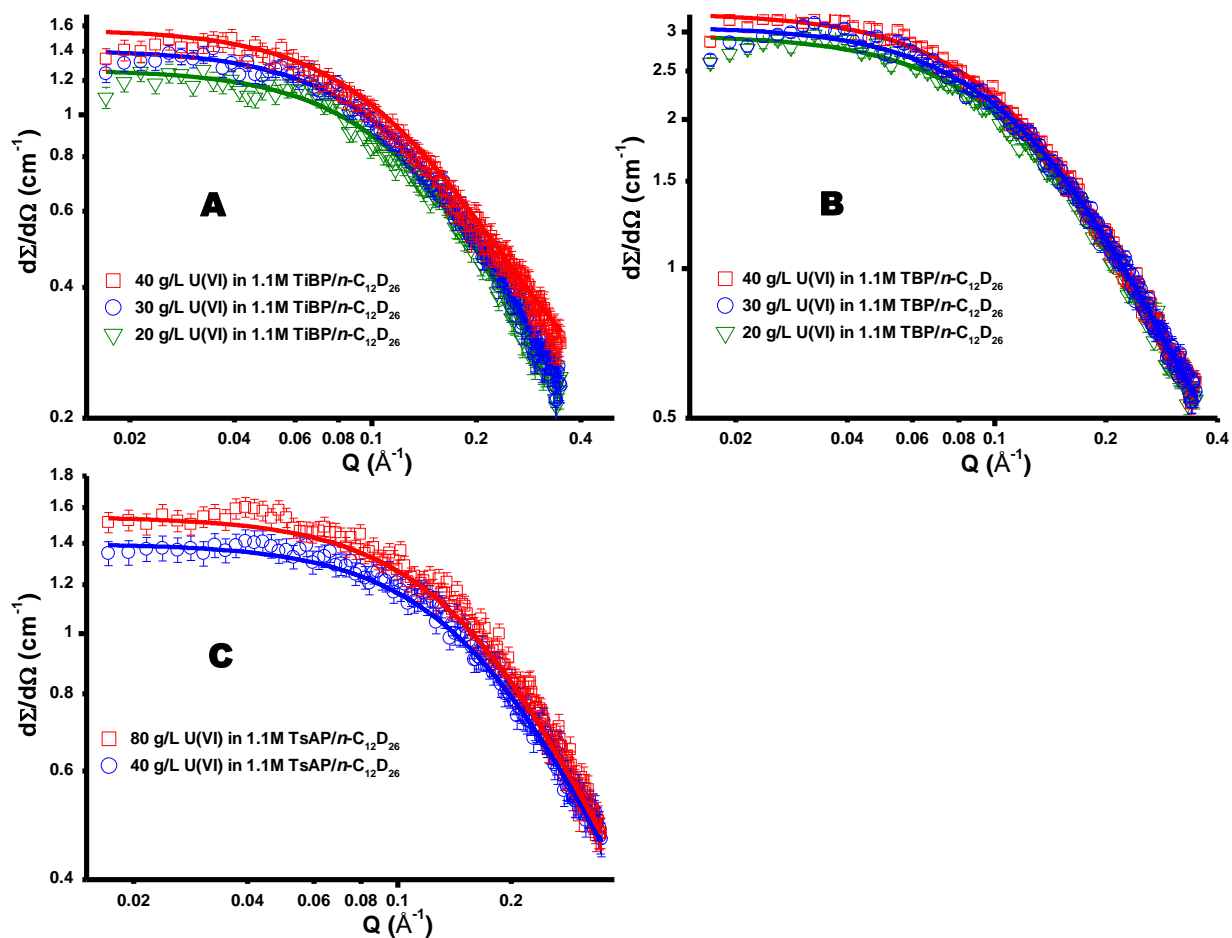


Figure 4.5: Variation of SANS curves as a function of metal loading obtained from 1.1 M TalP/ $n\text{-C}_{12}\text{D}_{26}$ – $\text{UO}_2(\text{NO}_3)_2/1\text{M HNO}_3$ systems at 303K (A) TiBP (B) TBP and (C) TsAP.

Table 4.3: The fitted parameters of SANS data for (a) 1.1 M TalP/n-C₁₂D₂₆-UO₂(NO₃)₂/1M HNO₃ systems at 303K. (b) 1.1M TalP/n-C₁₂D₂₆-UO₂(NO₃)₂/1M HNO₃ systems loaded with 120 g U/L at 303K. (c) 1.1 M TalP/n-C₁₂D₂₆ /1M HNO₃ systems with U(VI): 40g/L in TBP and TiBP and 20g/L in TsBP as a function of temperature. (d) 1.1 M TBP and TiBP in C₁₂D₂₆ loaded with 40g/L Th(IV) and U(VI)/1M HNO₃ at 308K.

a) Conditions: 1.1 M TalP/n-C₁₂D₂₆ – UO₂(NO₃)₂/1M HNO₃ at 303K						
U(VI) conc. (g/L)	TBP(N = 2,D = 12.0 Å)		TiBP(N = 2,D = 12.0 Å)		TsAP(N = 2,D = 12.7 Å)	
	1/τ	U ₀ (k _B T)	1/τ	U ₀ (k _B T)	1/τ	U ₀ (k _B T)
20	6.6	-1.02	6.6	-1.01	–	–
30	6.7	-1.03	6.8	-1.04	–	–
40	6.9	-1.06	7.2	-1.10	4.7	-0.72
80	–	–	–	–	4.9	-0.76
b) Conditions: 1.1M TalP/n-C₁₂D₂₆ /1M HNO₃ systems loaded with 120 g U/L at 303K						
System	Aggregation number (N)	Aggregate Diameter (D)	Stickiness Parameter (1/τ)	Potential Energy [U ₀ (k _B T)]		
1.1 M TBP/n-C ₁₂ D ₂₆	2	12.0	7.9	-1.2		
1.1 M TiBP/n-C ₁₂ D ₂₆	2	12.0	7.9	-1.2		
1.1 M TsAP/n-C ₁₂ D ₂₆	2	12.7	5.2	-0.81		
c) Conditions: 1.1 M TalP/n-C₁₂D₂₆ /1M HNO₃ systems with U(VI): 40g/L in TBP and TiBP and 20g/L in TsBP						
Temp(°C)	TBP		TiBP		TsBP	
	1/τ	U ₀ (k _B T)	1/τ	U ₀ (k _B T)	1/τ	U ₀ (k _B T)
40	5.5	-0.84	5.4	-0.82	5.3	-0.79
50	5.1	-0.76	4.9	-0.71	4.8	-0.69
60	5.0	-0.74	4.8	-0.70	-	-
70	-	-	-	-	4.4	-0.60
d) Conditions: 1.1 M TBP and TiBP in C₁₂D₂₆ loaded with 40g/L Th(IV) and U(VI)/1M HNO₃ at 308K						
Metal ion in the organic phase	1.1 M TBP/n-C ₁₂ D ₂₆		1.1 M TiBP/n-C ₁₂ D ₂₆			
	1/τ	U ₀ (k _B T)	1/τ	U ₀ (k _B T)		
40g/L Th(IV)	10.9	-1.63	8.7	-1.40		
40g/L U(VI)	5.8	-0.89	5.5	-0.83		

At lower concentrations of U(VI) in the organic phase, the stickiness parameter was lower, because at the given acid concentration, these extractants do not form third phase with uranium even with saturated aqueous concentration of the metal ion. SANS studies were carried out with samples loaded with 120 g/L of U(VI), which was the organic loading obtained with near saturated (saturated loading ~ 120 – 125 g/L) aqueous concentration of the

metal ion. The neutron scattering pattern obtained at 303K from TBP, TiBP and TsAP systems loaded with 120 g/L of U(VI) is shown in Figure 4.6. The data in Table 4.3b show the calculated values of (τ^{-1}) and (U_0) obtained after fitting the data. The scattering intensity is equally high for TBP and TiBP, and these have a stickiness parameter of 7.9 and attraction potential of -1.2 , which are higher in magnitude than the corresponding numbers shown in Figure 4.6, where the same extractants were loaded with a maximum of 40g/L of U(VI). The scattering intensity as well as the stickiness parameter is lower for TsAP compared to the two butyl phosphates at the same metal loading of 120g/L. This implies that TsAP has lower tendency to aggregate than butyl phosphates do⁶³.

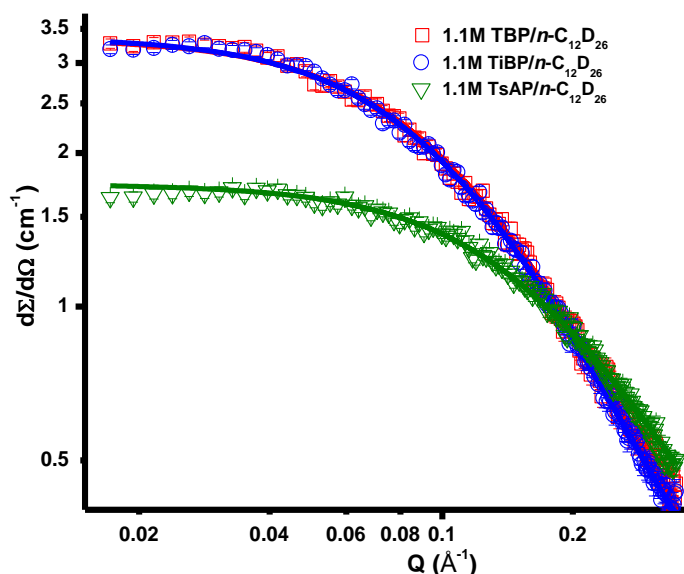


Figure 4.6: SANS data obtained for 1.1M TalP/n-C₁₂D₂₆ - UO₂(NO₃)₂/1M HNO₃ systems loaded with 120 g U/L at 303K.

Effect of temperature on U(VI) system

Increase in temperature lowers the stickiness in the Th(IV) systems, thereby reducing the third phase formation tendency. The effect of raising the temperature has a similar effect on U(VI) loaded organic phases containing 1.1M TalP/n-C₁₂D₂₆. Figure 4.7 A, and B, respectively, shows the scattering from TBP and TiBP extractant systems loaded with 40g/L of U(VI) at temperatures ranging from 313 to 333K. Figure 4.7 C shows 1.1M TsBP/ n-

$C_{12}D_{26}$ containing 20g/L of U(VI) at temperatures between 313 and 343K. For all the extractants, for a fixed metal loading, the scattering intensity decreases with increase in temperature. Table 4.3c shows the variation in stickiness parameter and attraction potential energy for systems at different temperatures shown in Figure 4.7. For all three phosphates, the stickiness parameter decreases with increase in temperature as enhancement in thermal energy reduces inter-particle attraction. The attractive energy becomes less with temperature rise.

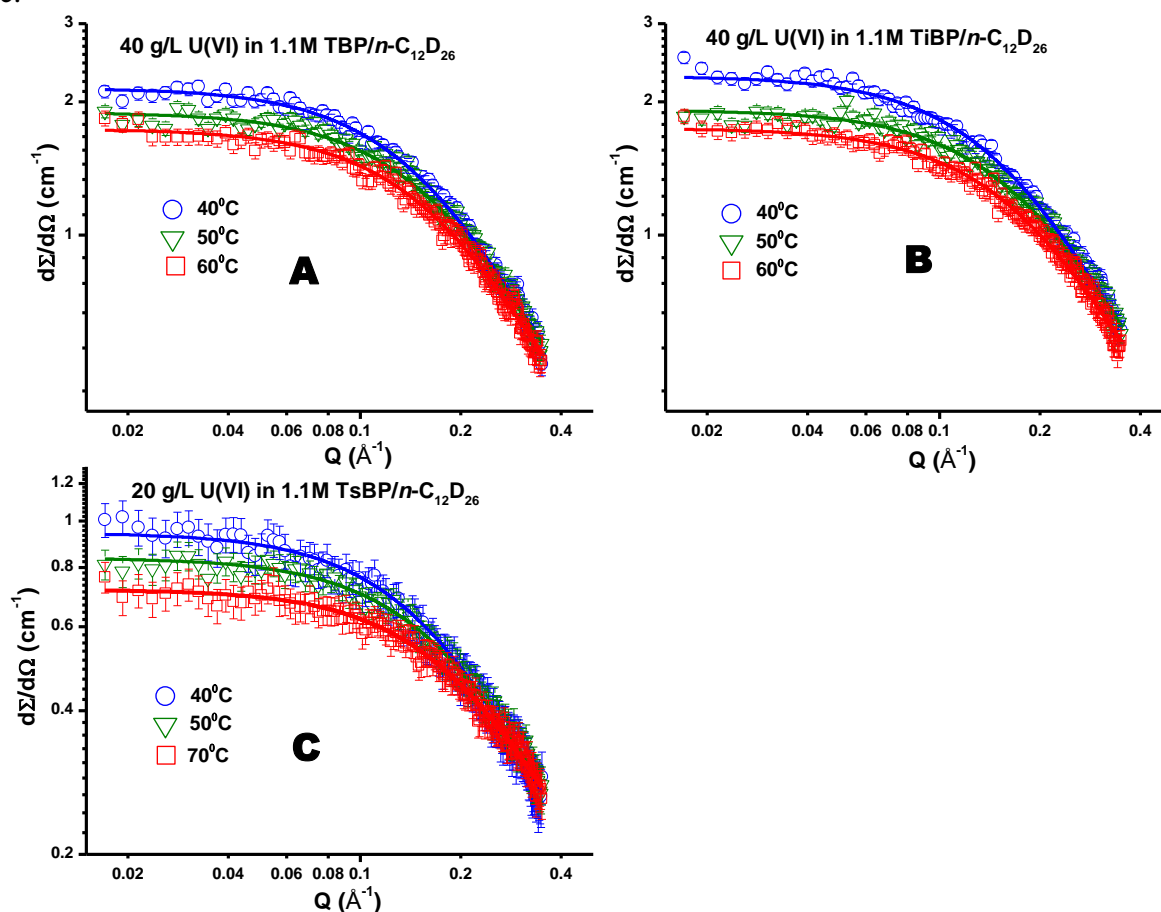


Figure 4.7: Temperature variants in SANS obtained from 1.1 M TalP/n- $C_{12}D_{26}$ – $UO_2(NO_3)_2/1M HNO_3$ systems with U(VI): (A) 40g/L U(VI) in TBP (B) 40g/L U(VI) in TiBP and (C) 20g/L U(VI) in TsBP.

4.6 Comparing U(VI) and Th(IV) SANS

As described in the previous sections, TBP and TiBP have high tendency to form third phase with Th(IV), whereas they do not form third phase with U(VI) under normal extraction

conditions. The SANS patterns obtained in the present study are in line with the above behaviour and show a clear difference between organic phases loaded with Th(IV) and U(VI) for these two extractant systems. Figure 4.8 A and B shows the SANS plot obtained at 308K for TBP and TiBP systems, respectively. Each organic phase was separately loaded with 40g/L of Th(IV) and U(VI). It can be seen that for both the extractant systems, the scattering intensity is much higher for Th(IV) loaded samples compared to samples loaded with U(VI). The data in Table 4.3d shows the corresponding stickiness parameter and attraction potential energy obtained for the above systems. The stickiness parameter is much higher for the Th(IV) loaded samples indicating a higher third phase formation tendency, whereas for the U(VI) loaded samples, stickiness is much lower, in agreement with the observation that two extractant systems do not form third phase with U(VI). From the SANS studies it is observed that tetravalent metals ions with higher ionic potential e.g. Th(IV) have higher tendency to form third phase.

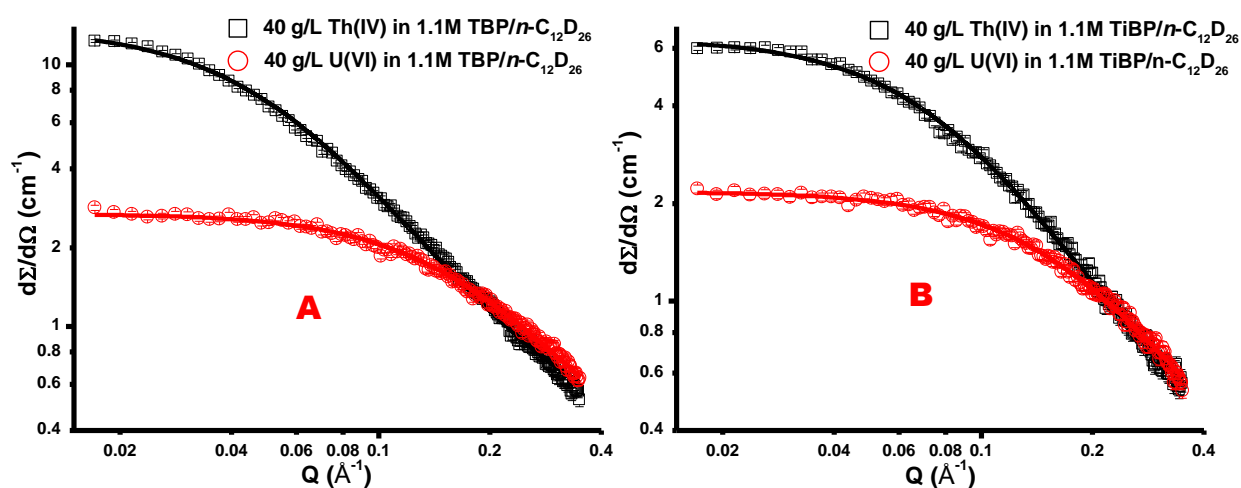


Figure 4.8: SANS patterns obtained at 35°C from 1.1 M TalP/ $\text{C}_{12}\text{D}_{26}$ (A) TBP and (B) TiBP loaded with 40g/L Th(IV) and U(VI)/1M HNO_3 .

4.7 Predictions on third phase formation

Interpretation of scattering intensity and stickiness parameter

Observations made from the SANS studies can be extended to predicting the likelihood of third phase formation phenomena. TBP loaded with 120g/L of U(VI) (Figure 4.6) shows scattering intensity ($Q \rightarrow 0$) less than 3.5, indicating that in general for systems with scattering intensity below 3.5 they are far from forming third phase. On the other extreme, systems with scattering intensity ($Q \rightarrow 0$) above 6 are close to the third phase limit as seen from Figure 4.3A, which shows the scattering for TiBP loaded with 40g/L of Th(IV), which is close to its limiting organic concentration of 43.8g/L. Similar threshold values can be set for the stickiness parameter (τ^{-1}). Systems with (τ^{-1}) less than 8 are not susceptible to third phase formation as seen from Table 4.3b, whereas a stickiness value greater than 9 would signal near third phase conditions. This can be seen from Table 4.2b which shows 9.2 to be the stickiness parameter for TiBP system loaded with 40g/L of Th (IV). Stickiness parameter for TBP is much higher than the threshold when loaded with 40g/L of Th (IV) which is close to its limiting organic concentration. The corresponding value for TsAP loaded with 40g/L Th(IV) is 4.9 which is way below the threshold, and agrees with the observations that TsAP does not form third phase with Th(IV) at 1M acid up to saturated aqueous concentration⁶³.

Effect of the extracted metal ion

From the SANS studies it is seen that tetravalent metal ions e.g. Th(IV) have higher tendency to form third phase as seen from its higher scattering intensities and stickiness parameter data. In this context, it will be interesting to explore the stickiness parameter details for the Zr(IV)–TBP system as it has been experimentally shown in our laboratory that Zr is bound to form third phase even at much lower metal ion concentration for e.g. above the LOC of 8.19g/L³². It is also interesting to compare the present study with a preliminary study on SANS of Zr(IV) loaded TBP/n-C₁₂D₂₆ system carried out earlier by Benadict et al³². The

studies on SANS of 1.1M TBP/n-C₁₂D₂₆ loaded with Zr (0.057 mol/L) before the LOC conditions indicated a scattering intensity of around 5 ($Q \rightarrow 0$) with a stickiness parameter of 9.7 and potential energy of -1.4. The above values of Zr-TBP system are higher than the corresponding values (stickiness parameter = 7.4 and potential energy = -1.24) reported in the present study for TBP-Th(IV) system loaded with higher Th concentration (20 mg Th/L which corresponds to 0.086 mol/L) with a scattering intensity of around 4 ($Q \rightarrow 0$).

Temperature and third phase formation

As temperature is one of the parameters influencing third phase formation, its effect have been extensively studied in this work and in all cases it has been observed that increasing temperature decreases the scattering intensity as well as stickiness parameter. From these studies it is observed that TiBP system loaded with 40g/L of Th (IV), at 313K its stickiness parameter is below the third phase limit of 9, and beyond 323K, τ^{-1} falls below 8. It could be possible that systems with stickiness parameter below 8 are not susceptible to third phase formation. Temperatures above 343K were not investigated in the present work as it is generally not recommendable operating temperature for solvent extraction system due to safety issues when employed under plant conditions.

Predictions when diluent is changed

Extending the diluent chain length decreases the LOC value for Th(IV)⁶². Hence, experiments with longer chain length diluents, e.g. tetradecane instead of dodecane, can lead to higher scattering intensity and τ^{-1} for the given metal loading especially with Th(IV) system^{62, 63}. Similarly, diluents with shorter chain length such as octane or decane, is expected to reduce scattering intensity at low region and stickiness.

4.8 Conclusion

SANS experiments were carried out to investigate the third phase formation tendency for 1.1M TalP extractants in deuterated dodecane. Three factors affecting third phase formation

were investigated in this study: nature of extractant, nature of metal ion and temperature. Comparison between U(VI) and Th(IV) complexes with the same extractant and comparison between the different phosphate extractants loaded with a given metal ion have been studied for the first time. The results obtained are in good agreement with our earlier solvent extraction experiments with respect to all the three parameters that were investigated. Further, the intensity of scattering and stickiness parameter data can be used for predicting the tendency of a system to form third phase. This study was also extended to set threshold values for scattering intensity and stickiness parameter below which third phase will not form, as well as the thresholds above which third phase is expected to form.



Chapter 5



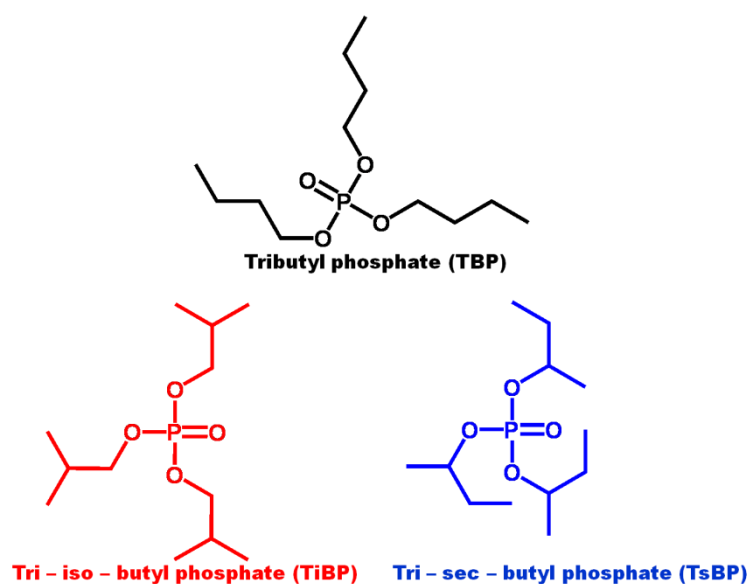
“Live as if you were to die tomorrow. Learn as if you were to live forever”

~ Mahatma Gandhi

SELECTIVE SEPARATIONS OF U(VI) FROM A Th(IV) MATRIX BY BRANCHED BUTYL PHOSPHATES: INSIGHTS FROM SOLVENT EXTRACTION, CHROMATOGRAPHY AND QUANTUM CHEMICAL CALCULATIONS

5.1. Introduction

In this study, the separation of trace amounts of U(VI) from a Th(IV) matrix by both solvent extraction as well as using coated polymer columns was studied; computational study relating the specificity of an extractant to the electronic structure of metal complexes was taken-up in connection with the above. The effect of extractant concentration as well as the acidity on the separation of U(VI) from a thorium matrix has been systematically investigated using TBP, Tri-iso-butyl phosphate (TiBP) and Tri-sec-butyl phosphate (TsBP). These molecules differ from each other in the position of methyl branching in their carbon chains (Scheme 5.1). The effect of acidity, coupled with varying extractant concentration on the separation factor has been carried out.



Scheme 5.1: Structures of TBP, TiBP and TsBP

Kinetics of uptake for U(VI) and Th(IV) by TsBP and TBP coated XAD-7 resins have been studied both for individual metal ions and for a mixture. Further, mixtures containing variable

U/Th ratios (1:100, 1:1000, 1:10000) were loaded on to the coated columns and isolation of U(VI) from a Th(IV) matrix has been examined.

To understand the basis for the separations from experimental work, density functional theory (DFT) calculations were carried out and the metal–extractant interactions were electronically modelled. The calculation of complexation energies followed by ligand deformation studies for the formation of uranium and thorium complexes is crucial in elucidating the metal-ligand interactions.

5.2 Solvent extraction studies on the separation of U(VI) from Th(IV)-Extraction and stripping

Extraction studies were carried out with feed solutions containing 180µg/mL of U(VI) and 160mg/mL of Th(IV) as this ratio (~1:800) simulates those in monazite ore as well as in the irradiated Th in the fast reactor which forms some amount of U²³³ by neutron capture. Extraction behavior was investigated as a function of extractant concentration, which was varied from 0.1mol/L to 0.5mol/L.

It can be seen (Table 5.1) that for both the metal ions (U(VI) and Th(IV)), the D value increases with an increase in extractant concentration. At extractant concentrations above 0.183M, TBP and TiBP formed third phase^{58, 59}, whereas TsBP remained in the biphasic regime at extractant concentrations above 0.55M. At a given extractant concentration, Th(IV) distribution ratio is highest for TBP, followed by TiBP and TsBP, whereas for U(VI) distribution this trend is reversed. D values for acid extraction are highest for TsBP, followed by TiBP lowest for TBP. U/Th separation factor is highest for TsBP and least for TBP, indicating that branching close to the phosphoryl group improves separation factor 'β' values. The D value increases with an increase in extractant concentration for U(VI), Th(IV) as well as H⁺. Separation factor decreases with an increase in extractant concentration due to poorer selectivity for U(VI) with the greater availability of extractant molecules. Nevertheless, at

3M, acidity ' β ' is much higher with 15% TsBP/DD than that with 3% TBP/DD or 3% TiBP/DD. Methyl branching near the phosphoryl group produces an inductive effect which increases the basicity of the phosphoryl oxygen which in turn increases the D values for U(VI) and H⁺.⁶⁰ In the case of Th(IV), three extractant molecules bind to the Th(NO₃)₄. Steric factors due to the presence of secondary carbon atoms near the central metal ion reduce the distribution ratio as compared to the U(VI)–TsBP system in which only two extractant molecules bind to the uranyl centre²⁴⁷.

Table 5.1: Extraction of U(VI) and Th(IV) as a function of extractants concentration (M) in dodecane. The aqueous phase contained initially a mixture of 180 $\mu\text{g/mL}$ U(VI) and 160 mg/mL Th(IV) in **3M nitric acid**.

	TBP		TsBP				TiBP	
	0.110 (3%)	0.183 (5%)	0.110 (3%)	0.183 (5%)	0.367 (10%)	0.550 (15%)	0.110 (3%)	0.183 (5%)
[H⁺] (M)								
[H ⁺] Org.	0.071	0.130	0.099	0.145	0.264	0.369	0.069	0.128
[H ⁺] Aq.	3.01	2.97	3.03	2.98	2.96	3.01	3.03	3.04
D _H	0.024	0.044	0.032	0.049	0.089	0.123	0.023	0.042
Th(IV) (mg/mL)								
Th(IV) Org.	2.20	7.46	1.00	2.65	11.1	25.4	1.74	5.81
Th(IV) Aq.	157	152	158	156	148	134	158	154
D _{Th(IV)}	0.014	0.049	0.006	0.017	0.075	0.19	0.011	0.038
U(VI) ($\mu\text{g/mL}$)								
U(VI) Org.	106	135	150	162	175	177	102	132
U(VI) Aq.	71.5	46.5	28.5	15.8	6.12	4.67	77.6	46.5
D _{U(VI)}	1.48	2.90	5.26	10.2	28.6	37.9	1.31	2.84
β	106	59.2	877	600	381	199	119	74.7

In order to investigate the effect of acidity, a feed solution with the U(VI) and Th(IV) concentration (180 $\mu\text{g/mL}$ of U(VI) and 160 mg/mL of Th(IV)) was prepared at 5M acidity, and extraction was carried out as a function of extractant concentration (Table 5.2). For a given extractant concentration, separation factors are higher at 3M than at 5M acidity. For example for 3% TsBP/DD, β is 877 when extraction is carried out from 3M HNO₃, and 522 from 5M HNO₃. More U(VI) is extracted to the organic phase from 3M acid compared to the

same at 5M. Further, Th(IV) loaded into the organic phase in the presence of U(VI) is lower than for neat Th(NO₃)₄.

Table 5.2: Extraction of U(VI) and Th(IV) as a function of extractants concentration (M) in dodecane. The aqueous phase contained initially a mixture of 180 µg/mL U(VI) and 160 mg/mL Th(IV) in **5M nitric acid**.

	TBP		TsBP				TiBP	
	0.110 (3%)	0.183 (5%)	0.110 (3%)	0.183 (5%)	0.367 (10%)	0.550 (15%)	0.110 (3%)	0.183 (5%)
[H⁺] (M)								
[H ⁺] Org.	0.131	0.155	0.153	0.186	0.314	0.426	0.125	0.148
[H ⁺] Aq.	5.03	5.03	5.04	5.01	4.96	4.99	5.05	4.96
D _H	0.026	0.031	0.030	0.037	0.063	0.085	0.025	0.030
Th(IV) (mg/mL)								
Th(IV) Org.	1.89	6.32	0.93	1.91	9.71	22.3	1.50	5.26
Th(IV) Aq.	158	154	158	159	152	139	158	154
D _{Th(IV)}	0.012	0.041	0.006	0.012	0.064	0.160	0.009	0.034
U(VI) (µg/mL)								
U(VI) Org.	92.8	112	136	151	167	170	90.5	108
U(VI) Aq.	87.6	67.3	43.5	29.5	14.3	9.5	88.7	70.9
D _{U(VI)}	1.06	1.66	3.13	5.12	11.7	17.9	1.02	1.52
β	88.3	40.5	522	427	183	112	113	44.7

Separation factor is found to be higher when the extractant concentrations are low. The highest β (522) seen for this feed solution (at 5M acidity) was achieved at 3% TsBP concentration. TBP and TiBP have comparable β, with TiBP having marginally higher values. U/Th separation factors achieved by TsBP are far higher than that of TBP and TiBP. Even at 15% TsBP/DD solution, β value is higher than the corresponding value for 3% TBP/DD, and almost equal to 3% TiBP/DD system. Lower extractant concentrations are ideal for good separation, but this has disadvantage with respect to throughput in large-scale systems as the absolute amounts of metals extracted at each step are reduced in this case. Thus, choosing a suitable extractant concentration for a separation process requires a balance between throughput and separation efficacy.

Earlier studies showed that the number of extractant molecules of any type bound to the metal species can be found from the slope of a $\log(D)$ vs. $\log(E)$ graph, where E is the free extractant concentration⁶⁰. Figure 5.1 (A) and (B) show a plot of the logarithm of extractant concentration vs. logarithm of D for Th(IV) and U(VI), respectively. In both cases, a linear fit of the data is obtained and the slope of the graph for Th(IV) is 2.11 and that for U(VI) is 1.27. However, Th(IV) forms a trisolvate with the extractant during complexation and U(VI) forms a disolvate⁶⁰. The slope values of 2 and 3, respectively for U(VI) and Th(IV) are obtained when the extraction is carried out at tracer levels (typically tens of micrograms) where the equilibrium free extractant concentration (after complex formation) can be approximated to initial extractant concentration. In the case of Figure 2 (A) and (B) the slopes [U(VI) = 1.27, Th(IV) = 2.11] have a lower value than the actual solvate formed as the equilibrium free extractant concentration cannot be approximated to the concentration of initial extractant. The feed solutions contain 160 mg/mL of Th(IV) which binds to a substantial quantity of extractant molecules, making the free extractant concentration after complexation to drop significantly from the initial concentration.

After the extraction of Th(IV) and U(VI) to organic phases, the back extraction of U(VI) from the loaded organic phases to the aqueous phase was carried out. The organic phases containing 3% TBP as well as 3% TsBP were taken as representatives since they contained the highest quantities of extracted U(VI). The loaded organic phases were initially equilibrated with 3M nitric acid to strip as much Th(IV) as possible to the aqueous phase. At 3M acid in the case of TsBP, D for Th(IV) (0.006) is much less than D for U(VI) (5.26); consequently thorium predominantly comes into the aqueous phase, along with a small percentage of uranium. U(VI) recovery was subsequently achieved by equilibrating the organic phase with a 0.01M HNO₃ solution because at this acidity D values for both U(VI) and Th(IV) are ~0.1[17]. Table 5.3 shows the concentration profiles of Th(IV), U(VI) and H+

on contact with 3M HNO₃ followed by equilibrating twice with fresh 0.01M HNO₃. Most of the Th(IV) leaves the organic phase into 3M HNO₃ and after equilibration with 0.01M HNO₃, the aqueous phase contains pure U(VI).

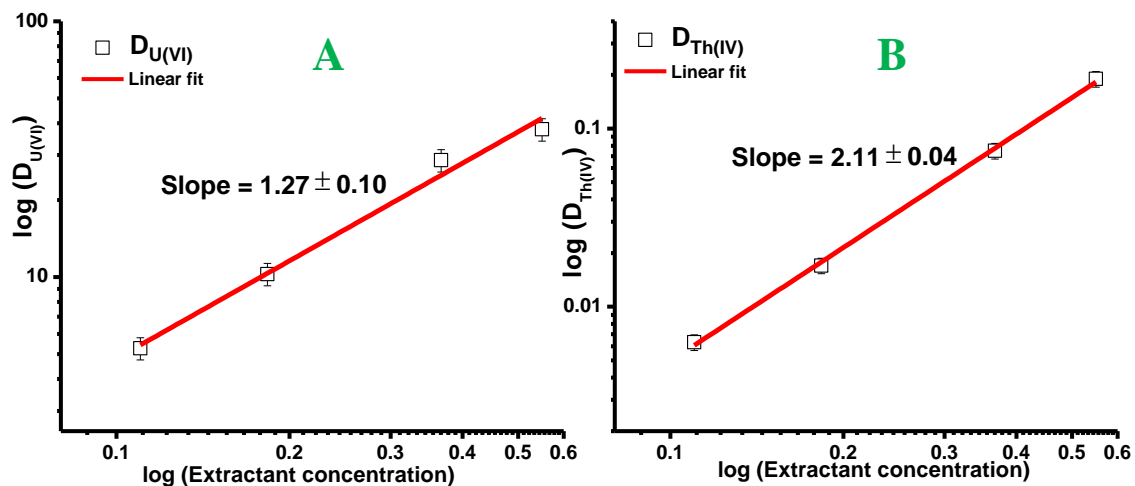


Figure 5.1: Plot of logarithm of D (distribution ratio) vs. logarithm of extractant concentration. The slope of the graph can be used to find the metal solvate composition in (A) Th(IV) extraction (B) for U(VI) extraction.

Table 5.3: Recovery of U(VI) from the organic phase 0.11 M (3%) TBP and TsBP solutions in dodecane after extraction from a feed solution containing 180 µg/mL U(VI) and 160 mg/mL Th(IV) in 3M nitric acid. The organic phase was then equilibrated with 3M HNO₃ followed by two stages of equilibration with 0.01 M HNO₃.

	TBP				TsBP			
	Extraction	3M scrub	0.01M (I) strip	0.01M (II) strip	Extraction	3M scrub	0.01M (I) strip	0.01M (II) strip
[H ⁺] (M)								
[H ⁺] Org.	0.071	0.083	0.013		0.099	0.124	0.028	
[H ⁺] Aq.	3.01	2.97	0.061		3.03	2.88	0.095	
D _H	0.024				0.033			
Th(IV) (mg/mL)								
Th(IV) Org.	2.20	0.382	0.011		1.00	0.184	0.008	
Th(IV) Aq.	157	1.94	0.310		158	0.874	0.104	
D _{Th(IV)}	0.014				0.006			
U(VI) (µg/mL)								
U(VI) Org.	106	90.1	26.9	15.8	150	136	38.2	21.9
U(VI) Aq.	71.5	15.1	62.8	10.2	28.5	12.8	97.6	15.5
D _{U(VI)}	1.48				5.26			

5.3 Electronic structure calculations on U(VI) and Th(IV) complexes

The estimated D values derived from solvent extraction experiments suggest that TsBP shows higher extraction for uranyl ion compared to TBP, whereas for thorium, TBP shows higher extraction compared to TsBP. The superior separation factors achieved with TsBP rests on its selectivity for U(VI) over Th(IV). This reversal of preferences of the ligands towards U(VI) and Th(IV) and selectivity of TsBP towards U(VI) with reduced binding to Th(IV) due to steric factors was probed by electronic structure calculations using density functional theory (DFT). The structures of the U(VI) and Th(IV) complexes with TBP and TsBP were optimized. The differences in their geometries (Figure 5.2 and Table 5.4) and Mülliken charge distribution (Table 5.5) were analysed. Binding free energies of complex formation were also calculated (Table 5.4).

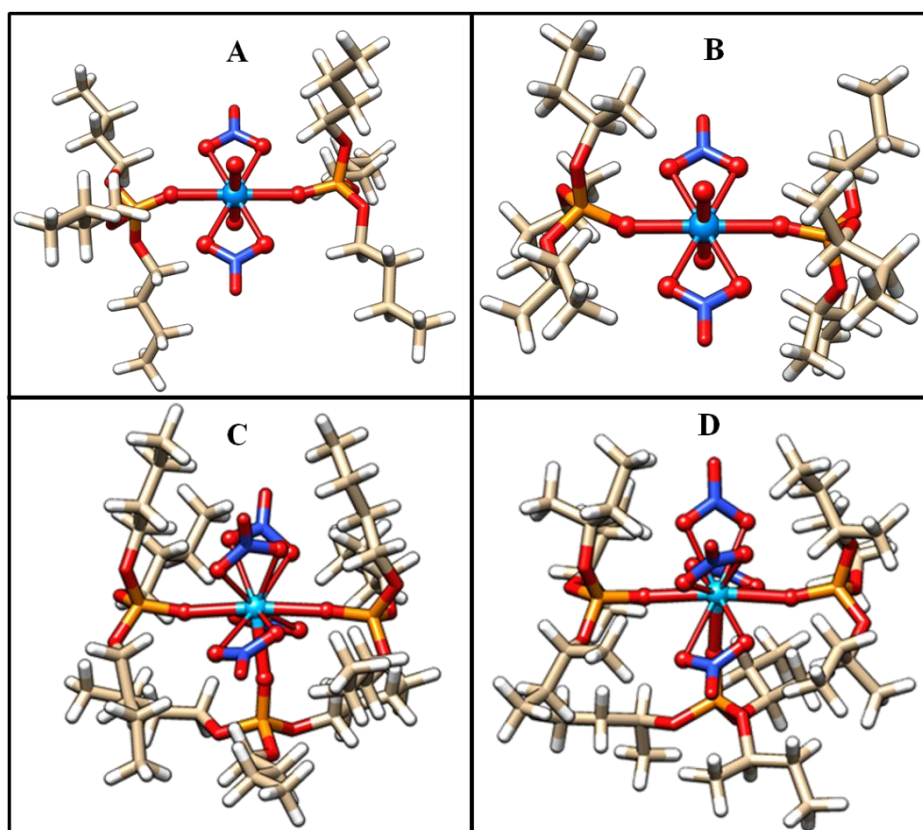


Figure 5.2: Optimized geometries of (A) $\text{UO}_2(\text{NO}_3)_2 \cdot 2\text{TBP}$ (B) $\text{UO}_2(\text{NO}_3)_2 \cdot 2\text{TsBP}$ (C) $\text{Th}(\text{NO}_3)_4 \cdot 3\text{TBP}$ and (D) $\text{Th}(\text{NO}_3)_4 \cdot 3\text{TsBP}$ complexes

The two organophosphorous ligands in the uranyl complexes are positioned opposite to each other causing the least steric repulsions between their carbon chains. There is a marginal elongation in the average $U - O_{NO_3}$ bond length in the case of the $UO_2(NO_3)_2 \cdot 2TsBP$ complex and a shortening of the $U - O_{Ext}$ bond length, both indicating a stronger complexation in the case of TsBP with uranyl nitrate (Table 5.4). On the other hand, in the thorium complexes, there is an elongation of $\sim 0.06 \text{ \AA}$ in the $Th - O_{Ext}$ bond length in the $Th(NO_3)_4 \cdot 3TsBP$ complex as compared to the $Th(NO_3)_4 \cdot 3TBP$ complex (considering largest bond distances in both complexes). This indicates a weaker binding between $Th-TsBP$ compared to $Th-TBP$.

Table 5.4: Solvent corrected binding free energies (kcal mol^{-1}) using M06-2X functional and computed structural parameters (\AA) of actinide extractant complexes.

Complex	$UO_2(NO_3)_2 \cdot 2TBP$	$UO_2(NO_3)_2 \cdot 2TsBP$	$Th(NO_3)_4 \cdot 3TBP$	$Th(NO_3)_4 \cdot 3TsBP$
Bonds	Bond lengths (\AA)			
$U = O_{yl}$	1.797 – 1.801	1.792 – 1.803	-	-
$M - O_{Ext}$	2.365 – 2.378	2.351	2.369 – 2.399	2.390 – 2.461
$M - O_{NO_3}$	2.500 – 2.527	2.524 – 2.529	2.533 – 2.697	2.544 – 2.648
Binding free energy	-11.67	-10.71	-35.75	-14.51

Table 5.4 also shows the solvent corrected energies of complexation as calculated for uranium and thorium complexes with TBP and TsBP using M06-2X functional and TZVP basis set. All the complexation energies are negative, indicating that the formation of the complexes is favorable under these solvent conditions. Dispersion effects were considered during the geometry optimization to account for steric factors which are believed to be the reason behind lower distribution ratios for Th(IV) extraction by TsBP⁵⁸. Indeed $Th(NO_3)_4 \cdot 3TBP$ complex formation is favored as opposed to the formation of $Th(NO_3)_4 \cdot 3TsBP$ complex. Computed binding affinities for both the extractants are very similar for uranyl nitrate. When the uranyl nitrate complexes were optimised in the absence of dispersion effects, it was found that the formation of $UO_2(NO_3)_2 \cdot 2TsBP$ complex was more favored than the $UO_2(NO_3)_2 \cdot 2TBP$ complex by $3.5 \text{ kcal mol}^{-1}$ in agreement with solvent

extraction results. There is no significant difference in the magnitude of charge localisation on the corresponding atoms between the uranyl nitrate complexes with TBP and TsBP and in the bare ligands TBP and TsBP as obtained from Mulliken charge analysis. The same is the case when comparing the thorium nitrate complexes with these ligands.

Table 5.5: Mulliken charges on phosphorous and phosphoryl oxygen atoms in the bare ligand and after complexation calculated using M06-2X. Charges on the metal centre, as well as uranyl and thorium nitrate oxygen atoms bound to the metal are also shown.

Complex	Q _P	Q _O (P=O)	Q _O (P-O)	Q _O (UO ₂)	Q _{N-O} (NO ₃)	Q _{N=O} (NO ₃)	Q _M
TBP	2.530	-1.104	-0.796
TsBP	2.548	-1.113	-0.812
UO ₂ (NO ₃) ₂ ·2TBP	2.625	-1.059	-0.795	-0.633	-0.466	-0.364	1.922
UO ₂ (NO ₃) ₂ ·2TsBP	2.644	-1.060	-0.813	-0.632	-0.470	-0.368	1.916
Th(NO ₃) ₄ ·3TBP	2.643	-1.102	-0.797		-0.477	-0.377	1.698
Th(NO ₃) ₄ ·3TsBP	2.663	-1.094	-0.817		-0.472	-0.382	1.718

Binding free energy for both ligands with a given metal ion can be compared. However, between two different metal ions the oxidation states as well as the number of ligands bound per complex specie are different. Hence, trends obtained from calculated binding energy values across U(VI) and Th(IV) for the same ligand are not expected to correlate with their respective distribution behaviour. Hence, ligand deformation energy per ligand was calculated for the complexes of U(VI) and Th(IV) with TBP and TsBP ligands (Table 5.6). This is a measure of the change in the ligands' deformation upon complex formation. Higher deformation energy is indicative that the ligand has altered its relaxed geometry more in order to adapt itself to the steric environment present in the complex. As predicted by solvent extraction and complexation energy calculations, the largest deformation energy was computed for the Th(NO₃)₄·3TsBP complex (12.5 kcal mol⁻¹) and the least for UO₂(NO₃)₂·2TBP complex (0.7 kcal mol⁻¹). For both metal nitrates, TsBP has the larger deformation energy as compared to TBP due to the effect of branching close to the phosphoryl group, which causes more steric strain. On comparing U(VI) and Th(IV), the

complexes of Th(IV) have the larger deformation energies as three ligands are accommodated around the Th centre as opposed to two ligands bound to the uranyl ion. For a given metal-ligand complex, larger deformation with reference to the ligands' relaxed geometry signifies lesser tendency of the ligand to participate in complexation with that particular metal ion. Thus, we have shown a direct correlation to the deformation of the ligand with their binding affinities. The difference in binding energy for the uranyl nitrate complexes with TBP and TsBP are negligible and within the computational error bar (~1kcal/mol). Though complexation energies are almost the same for the U(VI) complexes with TBP and TsBP, however, lower preference of TsBP over TBP towards binding with Th(IV) is clearly established from the calculated complexation energy values. Trends in binding free energy, coupled with deformation energetics indicate more affinity of TsBP towards U(VI) in presence of Th(IV).

Table 5.6: Deformation energy (kcal mol⁻¹) per ligand for TBP/TsBP ligands in U(VI) and Th(IV) complexes calculated using M06-2X.

Complex	Deformation Energy
UO ₂ (NO ₃) ₂ ·2TBP	0.75
UO ₂ (NO ₃) ₂ ·2TsBP	4.75
Th(NO ₃) ₄ ·3TBP	6.00
Th(NO ₃) ₄ ·3TsBP	12.50

For U(VI) and Th(IV) complexes with TBP and TsBP, IR spectra were calculated and compared with the experimental IR spectra (Figure 5.3). The features corresponding to P=O stretching (between 1100-1200 cm⁻¹) and U=O asymmetrical IR stretching (between 900-1000 cm⁻¹) are indicated in the figure. The calculated IR spectra for each of the four complexes were in good match with the spectrum of the corresponding complex obtained by experimental measurement.

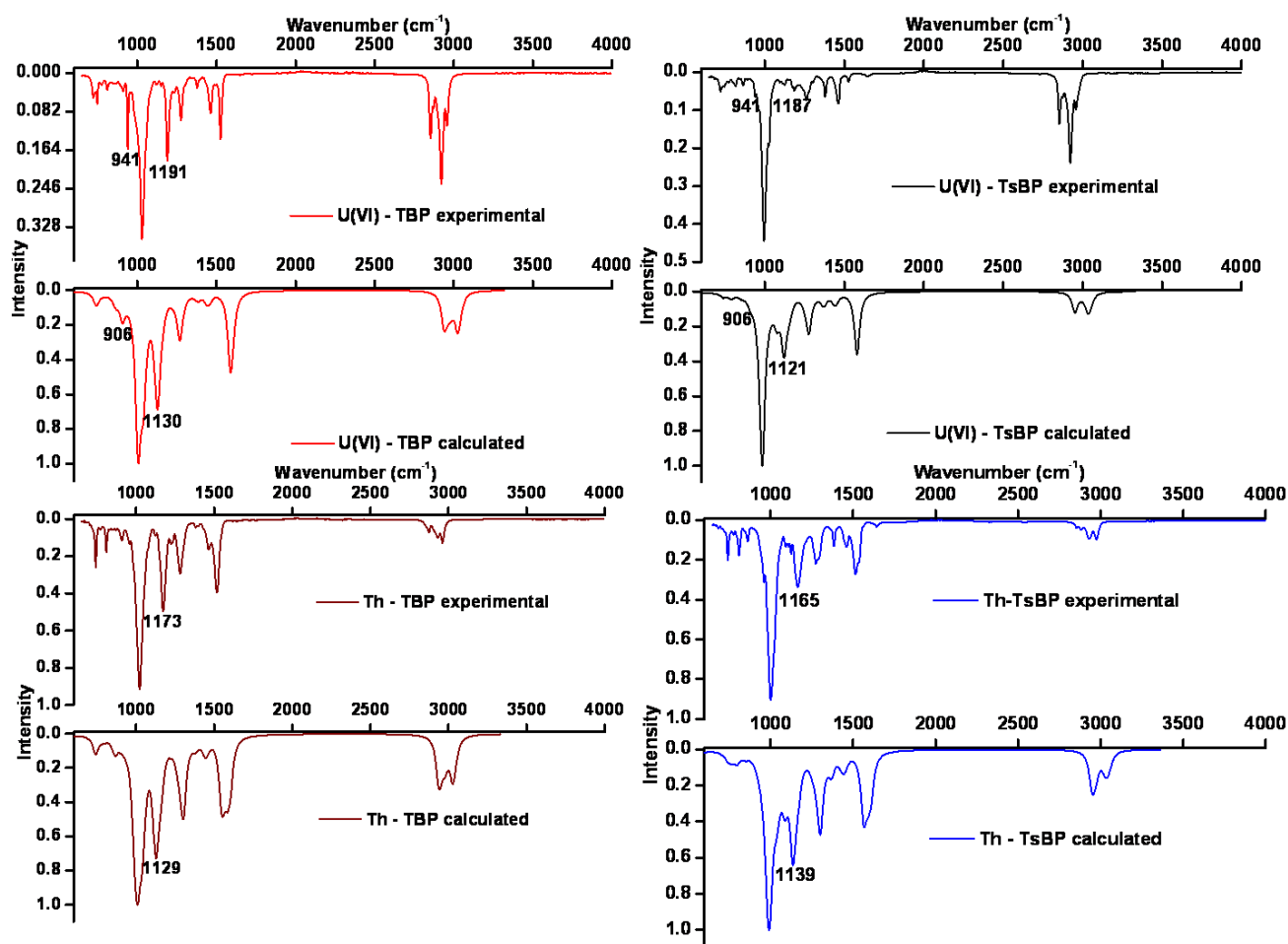


Figure 5.3: Comparison of experimental and calculated spectra for the complexes of U(VI) and Th(IV) with TBP and TsBP.

5.4 Demonstration U/Th separation by coated polymer support

On finding from the above solvent extraction experiments and DFT calculations that better separation factors can be achieved by TsBP as compared to TBP, extraction chromatography experiments were designed to demonstrate the separation of U(VI) from a large excess of Th(IV). Prior to carrying out column chromatography, the kinetics of extraction of both U(VI) and Th(IV) by impregnated TBP and TsBP resins were examined. In general, kinetics of extraction of a metal ion by an extraction chromatography resin (a solid-liquid extraction system) is slower than liquid-liquid extractions due to the restricted diffusion of the metal ions into the extractant molecules coated onto a solid support. Kinetics of U(VI) and Th(IV)

uptake with TsBP and TBP coated (40%) resins were studied in order to investigate the effects of branching near the co-ordination site in the case of TsBP in comparison with TBP. Figure 5.4A shows the plot of D values as a function of time for the extraction of U(VI) and Th(IV) ions by TBP and TsBP coated resins.

The highest D value is seen for U-TsBP system, which has the highest D value in solvent extraction as well compared to the other three cases. D value decreases in the order: U-TsBP, U-TBP, Th-TBP and Th-TsBP systems, respectively in agreement with the trends observed in solvent extraction for these extractant–metal pairs. The kinetics of U(VI) uptake is similar in the case of TBP and TsBP and the maximum capacity of the resin is achieved in ~1hr. In the case of the Th-TBP system, the resin reaches the maximum capacity in ~2hrs. The kinetics of Th-TsBP system, however, is much slower than Th-TBP system. This is due to the branching in the alkyl group on the first carbon atom in the case of TsBP, whose steric effect considerably slows down the kinetics in circumstances of the TsBP coated on a solid support. This difference, on the other hand, is not observed in solvent extraction as the equilibration time of ~15 minutes is more than adequate for liquid – liquid extraction systems to attain equilibrium. It is noteworthy that from our DFT studies, the steric effects in the formation of the Th(IV)–TsBP complex are reflected both in the binding as well as ligand deformation energies. Based on our computational study on the Th(IV)-TsBP complexation, we expect sorption of the Th species to be slow on the TsBP sorbed chromatographic support; as expected, the sorption of Th(IV) was found to be slower as seen from the kinetics.

As the sorption of Th(IV) on TsBP coated resin was slow, it was hypothesized that the presence of U(VI) may further affect the kinetics of Th(IV) extraction. This was investigated by equilibrating a 1:1 mixture of U(VI) and Th(IV) as the feed solution with TsBP and TBP coated (40%) resins. The D value for U(VI) in the mixture remains similar to the D obtained with a neat U(VI) solution for both TsBP and TBP, whereas the D value for Th(IV) in the

mixture decreased compared to the D obtained with neat Th(IV) for both TsBP and TBP (Figure 5.4B). Thus, the kinetics of U(VI) uptake is similar in the case of TBP and TsBP, however, the kinetics of Th-TsBP system is further slowed down in the presence of U(VI), which competes for TsBP. The sorption kinetics of thorium on the chromatographic column has been substantially lowered in the presence of uranium.

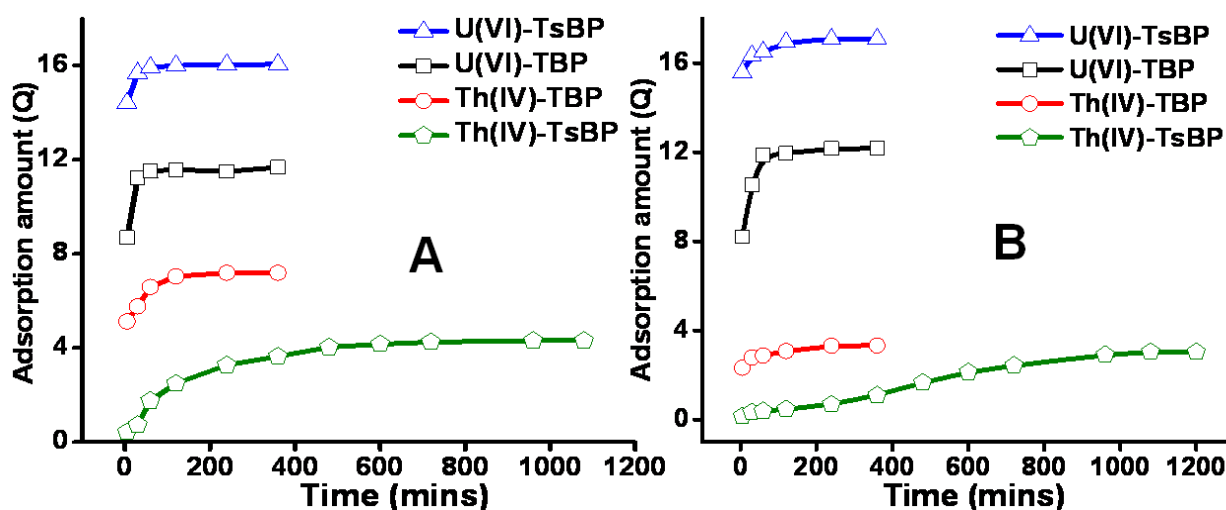


Figure 5.4: Kinetics of metal ion uptake from 4M HNO₃ solutions by TBP and TsBP coated XAD – 7 resins (A) Individual metal ions (B) From a 1:1 mixture.

Following the kinetic studies, TsBP impregnated XAD-7 polymer resin (40 wt% coating of TsBP on XAD-7) was packed in two glass columns (5g resin in each case) and two feed solutions containing 100 ppm of U(VI) and Th(IV) in 4M nitric acid were separately passed through the 40% TsBP coated resin columns. Once metal uptake saturation was reached, the column was washed with 4M acid, followed by elution of the metal ions by passing 0.01M nitric acid through the column. Figure 5.5A-C shows the loading and elution profiles for the two metal nitrate systems. TsBP coated resin showed higher loading of U(VI) compared to Th(IV), consistent with the data generated from solvent extraction experiments.

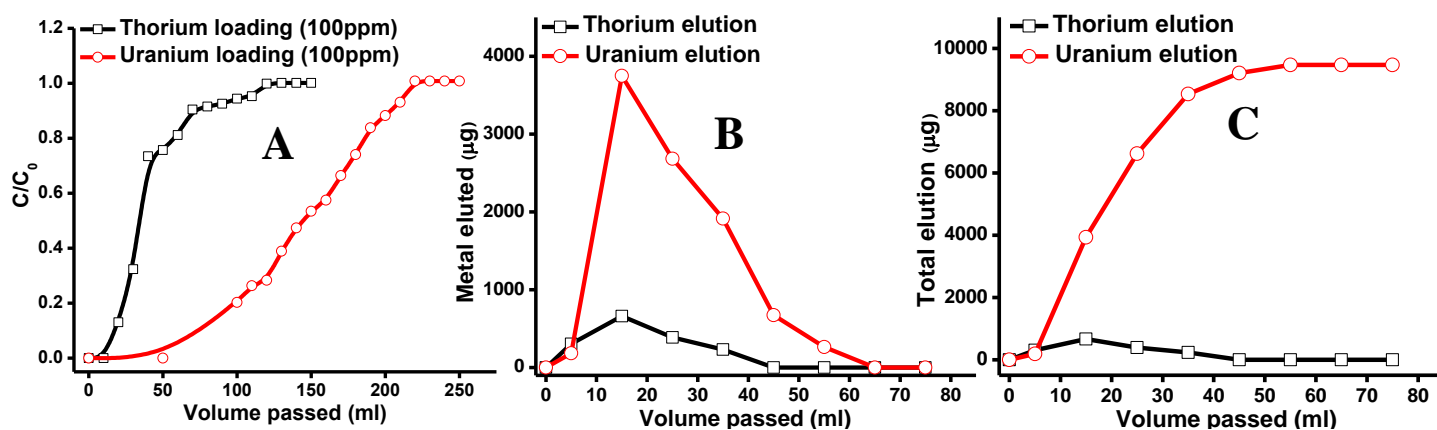
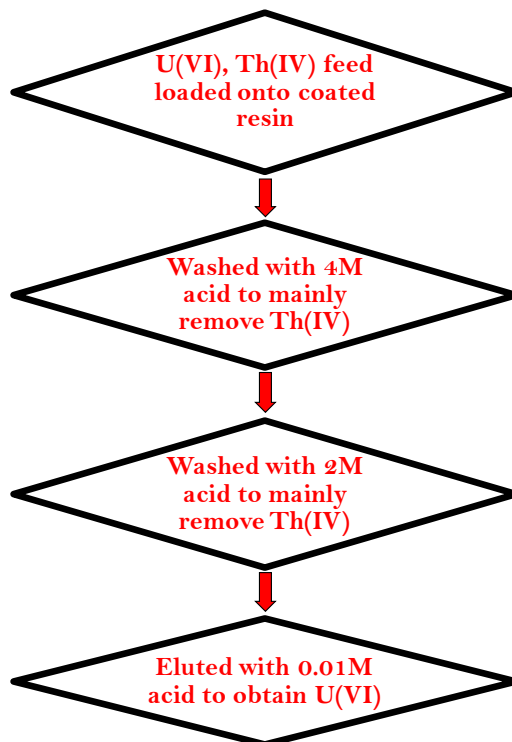


Figure 5.5: (A) Loading of U(VI) and Th(IV) from 4M HNO₃ medium on 40% TsBP coated resin columns followed by (B) Elution with 0.01M HNO₃ and (C) Total elution curve.

Subsequently, the separation of U(VI) from U-Th mixtures of varying U/Th ratios was carried out using TsBP coated XAD-7 columns. The acidity of the feed was maintained at 4M and the U/Th ratio of the feed solutions was varied as U: Th = 1:100, 1:1000 and 1:10000. From solvent extraction studies, it was observed that washing with nitric acid removes Th(IV) from the column and U(VI) is completely retained by the support. A mixture of U and Th can be continuously passed through a ligand coated column; however, unless the capacities are sufficiently high enough, it is difficult to achieve separation. Hence, only a fixed volume of the feed was loaded on to a column and the support was strategically washed with optimum volumes of 4M nitric acid to remove preferentially Th(IV), retaining the U(VI) in the column. Further, passing 2M HNO₃ removed substantial quantities of Th(IV) from the coated column. At lower HNO₃ concentrations, D values for both metal ions are lowered, but still substantially lowered for Th(IV) compared to U(VI); making the 2M washing more effective towards the elution of Th(IV). Finally, once most of the Th(IV) was removed from the column, the U(VI) retained in the column was eluted along with the remaining Th(IV) if any, by passing 0.01M nitric acid. Scheme 5.2 represents the flowchart for the strategy adopted in the separation of U(VI) from Th(IV) for the feed solutions containing excess of Th(IV). For each ratio the washing and elution stages which achieved the best separations are represented (Figure 5.6 A-D).



Scheme 5.2: Flow chart of the column chromatographic separation of U(VI) from Th(IV) in the mixtures by TBP or TsBP coated XAD – 7 columns.

Different U:Th ratios are considered and the results obtained from chromatographic studies are discussed:

(I) U:Th ratio of 1:100

Initially 1mL of the feed solution with a U: Th ratio of 1:100 (~10 μ g/mL of U(VI) and 1mg/mL of Th(IV)) was passed through the TsBP coated column. The fractions from the column were collected 5mL at a time (Figure 5.6A) and were analysed for their U(VI) and Th(IV) content. In the first such run, the column was washed with 20mL each of 4M and 2M acids followed by elution with 20mL of 0.01M HNO₃. Under these conditions 10 μ g of U(VI) was obtained in the eluate along with 312 μ g of Th(IV). In order to further reduce the Th(IV) retained in the column before eluting the U(VI), another experiment was carried out in which the column was washed with 20mL of 4M nitric acid and then with 40mL of 2M nitric acid instead of the 20mL used in the previous run. In this case the amount of total Th(IV) present with the eluted U(VI) was reduced to 126 μ g (Figure 5.6A). The details about the washing and elution volumes and the composition of the eluate are provided in Figure 5.6A-D.

(II) U:Th ratio of 1:1000

Subsequently 1mL of a feed solution with a U: Th ratio of 1:1000 containing $\sim 10\mu\text{g/mL}$ of U(VI) and 10mg/mL of Th(IV) was loaded onto the column. 20mL each of 4M and 2M acids were used to wash the column. Further, 20mL of 0.01M HNO_3 was used to elute the U(VI) along with the Th(IV) retained in the column (Figure 5.6B). In this run, $8\mu\text{g}$ of U(VI) was obtained with $\sim 2900\mu\text{g}$ of Th(IV) in the eluate. As Th(IV) was selectively removed from the column during the washing with 4M acid, it was hypothesized that more washing with 4 and 2 M acids can remove more Th(IV) before the U(IV) is eluted. In a second experiment with the same feed, 40mL of 4M nitric acid was passed through the column and the volume of 2M acid passed was also increased from 20 to 30mL in order to remove maximum Th(IV). In the second experiment $5\mu\text{g}$ of U(VI) was obtained with only $\sim 800\mu\text{g}$ of Th(IV) in the eluate (Figure 5.6B). As more 4M and 2M acid solutions were passed through the column, more Th(IV) was removed. However, at the cost of some U(VI) lost in the 2M acid wash.

(III) U:Th ratio of 1:10000

Finally the feed solution with a U:Th ratio of 1:10000 containing $\sim 10\mu\text{g/mL}$ of U(VI) and 100mg/mL of Th(IV) was loaded and the column was washed with 20mL each of 4M and 2M nitric acid solutions followed by elution with 20mL of 0.01M HNO_3 . In this case, half the initial U(VI) was lost in the 2M elution stages and $5\mu\text{g}$ of U(VI) remained in the eluate (Figure 5.6C) along with $1124\mu\text{g}$ of Th(IV). The U(VI) could have been lost mainly due to the large excess of Th(IV) concentration in comparison with U(VI), which significantly disabled the binding of U(VI) ions to the TsBP in the column. In order to avoid losing U(VI) before elution, in the next experiment the column was washed with only 4M HNO_3 . Furthermore, when U(VI) was first detected in the collected fraction, the column was eluted with 0.01M HNO_3 . After 35mL of 4M acid was passed through the column, U(VI) was found in the collected fraction and hence at this stage the column was eluted with 0.01M HNO_3 . In

this case 10 μ g of U(VI) was entirely recovered along with 2644 μ g of Th(IV) in the eluate (Figure 5.6C).

Generally the ligands coated onto the extraction chromatographic columns are stable for about six to eight runs and slowly the sorbed ligand will be leached out^{254, 255}. It has been confirmed that these resins can be recycled for good number of runs as mentioned above without much extractant loss and deterioration in the column performance. Both TBP and TsBP are not expected to come out from the resin matrix with the experimental conditions adopted in the present study. The TBP/ TsBP coated supports were examined for multiple column runs as well as distribution coefficient experiments. We have observed no change in D data for 5 runs. After that, slow leaching of ligand could take place. Thus, the supports can be used for about 5 experimental runs. The extractant leaching from the support depends on (i) hydrophobicity of the support (ii) hydrophobicity of ligand (iii) nature of medium used e.g. H₂O/HNO₃. Extractant leaching is expected to be lower from HNO₃ medium because of its higher dielectric constant.

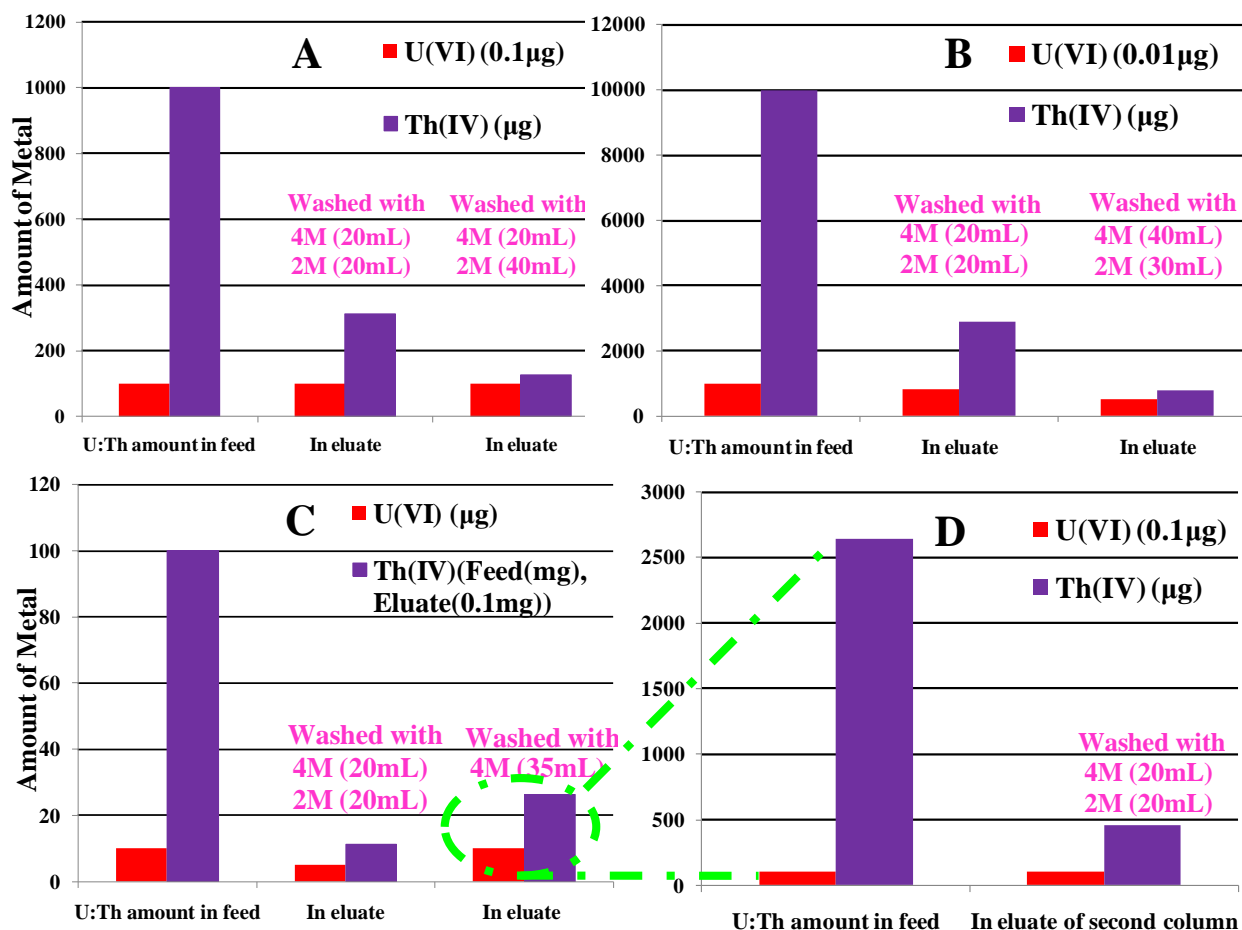


Figure 5.6: Eluent from two different column runs for the separation of U(VI) from Th(IV) from a feed solution containing (A) $\sim 10\mu\text{g/mL}$ of U(VI) and 1mg/mL of Th(IV) (B) $10\mu\text{g/mL}$ of U(VI) and 10mg/mL of Th(IV) (C) $10\mu\text{g/mL}$ of U(VI) and 100mg/mL of Th(IV). (D) U(VI) and Th(IV) concentrations in the eluate collected in the second column run carried for the 1:10000 mixture after the first step of separation. The feed used for this further purification is indicated. The acids used for washing and their volumes are provided in the insets. Uranium sorbed in the column runs have been eluted with 20mL of 0.01M HNO_3 (5.6A-D).

As seen from Figure 5.6, the uranium can be separated from thorium from a mixture of 1:100, 1:1000 and 1:10000 U:Th ratio, by using an appropriate washing of the loaded TsBP column with 4M and 2M HNO_3 . This leads to substantial reduction of thorium in the loaded column. Subsequently, sorbed uranium was eluted along with some thorium using 0.01M HNO_3 .

Thus, using a series of TsBP columns, U(VI) can be efficiently separated from a Th(IV) matrix.

Considering the 1:10,000 U:Th ratio in the feed, the results demonstrate that the U:Th ratio after purification by a second column reduces to 1:46 (where the eluate from second column contains 10 μ g U and 458 μ g Th). The actual U:Th ratios present in the monazite ore or irradiated thorium rods are in the order of 1:1000. Hence, certainly complete separation of U(VI) from Th(IV) can be achieved by employing TsBP coated support with additional column run. Thus a demonstration has been carried out with a huge U:Th ratio (1:10000) to show that uranium can be recovered even from a difficult proportion; though in reality from reactor samples, the U:Th ratio will be only in the order of ~1:800.

In order to demonstrate that U(VI) can be potentially separated and obtained in pure form from a feed solution with a 1:10000 U/Th ratio, the eluate from the TsBP column was passed through another fresh TsBP column (Figure 5.6D). The eluate with 10 μ g of U(VI) and 2644 μ g of Th(IV) was employed as the feed for the secondary column. The mixture was evaporated and its volume reduced from 20mL to 1mL before loading onto the column, in order to get sharper elution profiles. The column was washed with 20mL each of 4M and 2M acids followed by 20mL of 0.01M HNO₃. In the second stage of purification 10 μ g of U(VI) remained with a mere 458 μ g of Th(IV) in the eluate; a drastic reduction from the initial 100mg Th(IV) present in the primary feed. The U(VI) and Th(IV) present in the eluate for all the column runs discussed and summarised (Table 5.7a).

To quantify the superior separations displayed by TsBP with its linear isomer TBP, another experiment was conducted. A TBP coated column was loaded with the feed solution containing a U:Th ratio of 1:10000 (~10 μ g/mL of U(VI) and 100mg/mL of Th(IV)). Similar to the second column in Figure 5.6C, the TBP coated column was washed with 35mL of 4M HNO₃ and then eluted. These are identical to the conditions employed for the TsBP coated

column with the same U/Th ratio of 1:10000. The results obtained with TsBP are compared with those obtained with TBP (Figure 5.7). The U(VI) elutes from the TBP column much earlier than it does from the TsBP column. Consequently, there is less uranium in the eluate (0.01M fractions) in the case of the TBP coated column compared to the TsBP coated column. Furthermore, as TBP also retains Th(IV) better than TsBP, there is less Th(IV) in the eluate in the case of TsBP (10 μ g U(VI) and 2644 μ g Th(IV)) compared to TBP (3.5 μ g U(VI) and 9508 μ g Th(IV)). This consequently increases the final U(VI)/Th(IV) ratio in the eluate in the case of TsBP (Table 5.7b). Additionally, by employing this elution strategy the entire 10 μ g of U(VI) was recovered from the TsBP column. These data clearly indicate that TsBP coated resin is far superior to TBP coated one for the separation of U(VI) from Th(IV) from feed solutions containing uranium in a thorium matrix.

Table 5.7: (a) Summarised results for the separation of U(VI) from Th(IV) from TsBP coated columns. (b) Comparative study for TBP and TsBP column for isolation of U(VI) from 1:10000 U:Th ratio.

(a) Separation of U(VI) from Th(IV) from TsBP coated columns				
Initial composition of U(VI) and Th(IV) in the feed	U=10 μ g Th=1mg	U=10 μ g Th=10mg	U=10 μ g Th=100mg	
U and Th concentration in the elate (0.01M HNO ₃)				
Run I	U=10 μ g Th=0.312mg	U= 8 μ g Th= 2.88 mg	U=5 μ g Th=1.12mg	From second TsBP column
Run II	U=10 μ g Th=0.126mg	U= 5 μ g Th= 0.792 mg	U=10 μ g Th=2.64mg	 U=10 μ g Th=458 μ g
(b) Comparing TBP and TsBP for U=10 μ g, Th=100mg feed				
	TsBP		TBP	
U and Th concentration in the eluate (0.01M HNO ₃)	10 μ g U(VI), 2.64 mg Th(IV)		3.5 μ g U(VI) 9.51 mg Th(IV))	

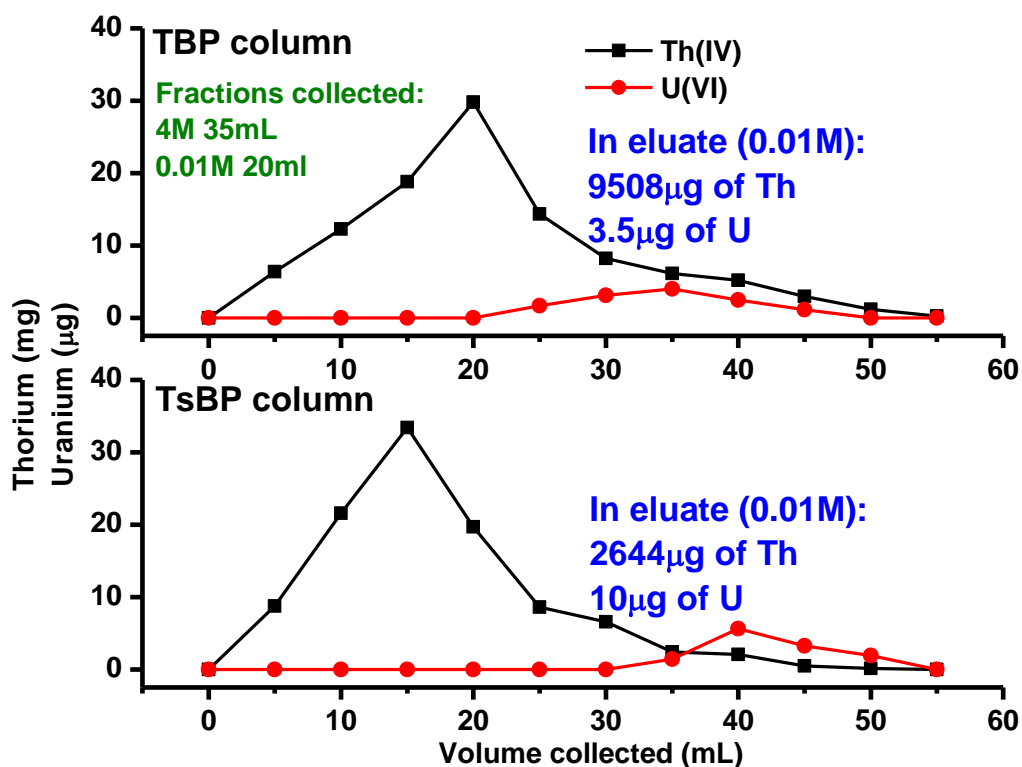


Figure 5.7: Comparison of the separation of U(VI) from Th(IV) by TBP and TsBP coated columns from a feed solution containing 10µg/mL of U(VI) and 100mg/mL of Th(IV).

5.5. Conclusion

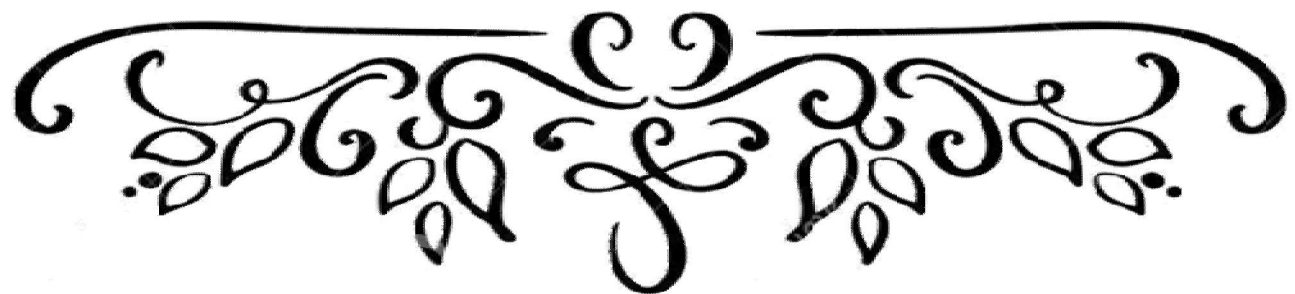
A comprehensive study on the separation of U(VI) from a Th(IV) matrix by solvent extraction, coated resins, and theoretical validations by DFT has been carried out. The effect of structure of extractant, concentration of extractant and acidity of feed solution on the separation of U(VI) from Th(IV) by solvent extraction has been systematically investigated for U:Th ratios that simulate those present in the major thorium ore and irradiated thorium material. The ligand TsBP exhibits highest separation factor with selectivity for U(VI) over Th(IV) which can be attributed to its methyl branching close to the phosphoryl group, increasing the basicity of phosphoryl oxygen. With TsBP, the extraction of U(VI) is enhanced, but not Th(IV) as the steric effect of branching reduces $D_{Th(IV)}$ for TsBP as compared to TBP. The effect of steric hindrance on structure and complexation energy has been revealed through density functional results. The solvent and dispersion corrected calculated binding affinities of Th(IV) complexes with both TBP and TsBP ligands showed

that Th(IV) has a stronger affinity for TBP compared to TsBP. Theoretical deformation energies of bare ligand on complexation revealed lower steric strain on forming uranyl complexes compared to the Th complexes, particularly for the branched TsBP ligand. These trends clearly indicate higher affinity of TsBP towards U(VI) in presence of Th(IV).

The separation of U(VI) from Th(IV) was demonstrated by TsBP coated XAD-7 columns for a series of U:Th ratios. Though U:Th ratios of ~1:1000 are found in monazite as well as in irradiated Th in the nuclear reactor, present study extends further to demonstrate effective separation of uranium from thorium for a U:Th ratio of 1:10000. The final U:Th ratio was reduced 200-fold (1:48 from 1:10000) by merely 2 stages of column purification, indicating that coated columns of TsBP on XAD-7 have immense potential to separate U(VI) from Th(IV). Kinetic studies carried out on the sorption of U(VI) and Th(IV) on TBP and TsBP coated columns revealed the steric factors that slow down the uptake of Th(IV) by TsBP; the same was also confirmed by the quantum chemical calculations.



Chapter 6



“The people who are crazy enough to think they can change the world are the ones who do”

~ Steve Jobs

STRUCTURAL EFFECTS ON THE COMPLEXATION OF ACTINIDES WITH BRANCHED PHOSPHONATES: A COMBINED EXPERIMENTAL AND QUANTUM CHEMICAL STUDY

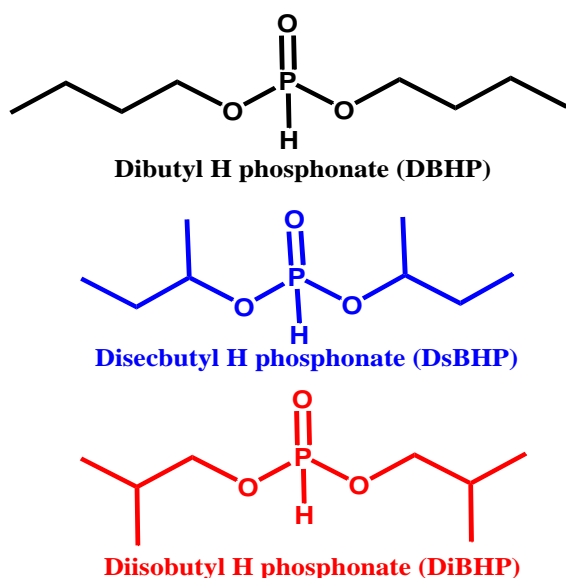
(A) H-PHOSPHONATES

6A.1 Introduction

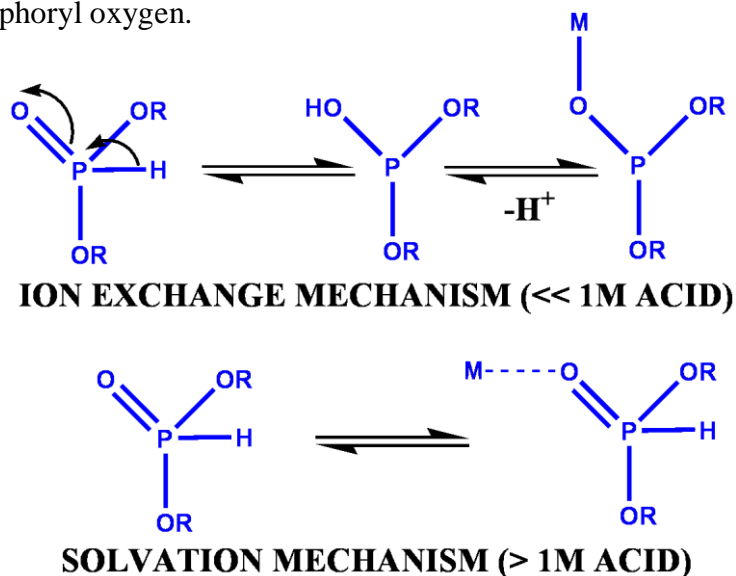
Studies in the past have mainly been on phosphate ligands, and little has been explored on phosphonates, and particularly H-phosphonates. In general higher homologs within a given class of compounds have been examined, but not the effects of branching at different positions in the alkyl chain in phosphonates. In the present study, ligands resulting from branching in 4-carbon chain of DBHP, namely DiBHP and DsBHP (Scheme 6A.1), were examined for the extraction of U(VI) and Am(III) from nitric acid. These three extractants were synthesised and their physical properties *viz.* density, aqueous solubility, viscosity and activation barrier to flow was measured as these characterize the suitability of an extractant used for solvent extraction. A systematic study on the variation in D as a function of HNO₃ concentration (0.01–8M) was carried out for U(VI) and Am(III) ions. The D is strongly dependent on the acidity of the aqueous phase and therefore in order to establish the optimum conditions for each extractant, varying the aqueous acidity is a vital investigation. To gauge our experimental studies, density functional theory (DFT) based calculations were employed to understand the energetics of complex formation for both the metal ions and explain the trends observed in solvent extraction experiments. DFT calculations were carried out for both the keto and enol mechanisms of extraction. The mechanism of extraction that operates depends on the pH of the aqueous phase as shown in Scheme 6A.2.

For H-phosphonates, two mechanisms of extraction operate depending on the acidity. Acidic extractants extract with a higher D value at lower acidity due to the ion-exchange mechanism, and at higher acidities, they extract through solvation mechanism⁵¹. Ion-exchange between the metal and H⁺ ion is the result of *keto-enol* tautomerism of phosphoryl

group, leading to the formation of O–H group^{256, 257}, i.e. at acidities below 1M, enol tautomerisation of the H – phosphonate occurs, and extraction is primarily through exchange of H⁺. At higher acidities, the keto tautomer predominates in the extraction; this tautomer binds to the metal nitrate species via the phosphoryl oxygen.



Scheme 6A.1: Structure of the H-phosphonates employed for the study



Scheme 6A.2: Mechanisms by which H-phosphonates extract metal ions in different pH

6A.2 Physico-chemical properties of butyl H-phosphonates

The physicochemical properties viz. density, viscosity and aqueous solubility of H-phosphonates were measured as these are important parameters that decide the efficacy of an organic phase during solvent extraction. Density of the three H-phosphonates DBHP, DiBHP and DsBHP are listed in Table 6A.1. The density of the phosphonates decreases with the branching due to reduced packing efficiency as the branching increases. The density difference is especially pronounced in the case of DsBHP due to the branching close to the P=O group.

Table 6A.1: Density, viscosity at 31°C, activation energy and aqueous solubility of various H-phosphonates.

Extractant	Density (g/mL)	Viscosity (cP) (@31⁰C)	Activation Energy (E_a) (kJ/mol)	Aqueous solubility (g/L) at 298K
DBHP	0.970	1.45	10.38	38.03
DiBHP	0.968	1.89	11.92	54.4
DsBHP	0.957	1.39	9.19	39.23

Viscosity measurements were made for DBHP, DiBHP and DsBHP and the activation barrier to flow was calculated from the slope of logarithm of viscosity vs 1/T graph (Figure 6A.1). The viscosity of the solvent determines the mass transfer, and the activation barrier to fluid flow affects the phase disengagement time. The activation barrier for DsBHP is less than that of DBHP as the effects of branching near the polar groups causes a reduction in packing density and intermolecular interactions. DiBHP, however, shows a higher activation barrier than the other two extractants. Table 6A.1 lists the viscosity at 31⁰C and activation energies for the three H-phosphonates.

The aqueous solubility of the H-phosphonates were measured and the results are listed in Table 6A.1. In general, the H-phosphonates have higher aqueous solubility compared to the phosphates of similar chain length. It is to be noted that tri butyl phosphate (TBP) has an aqueous solubility of 0.4 g/L²⁹. The highest aqueous solubility was observed with DiBHP followed by DsBHP and DBHP.

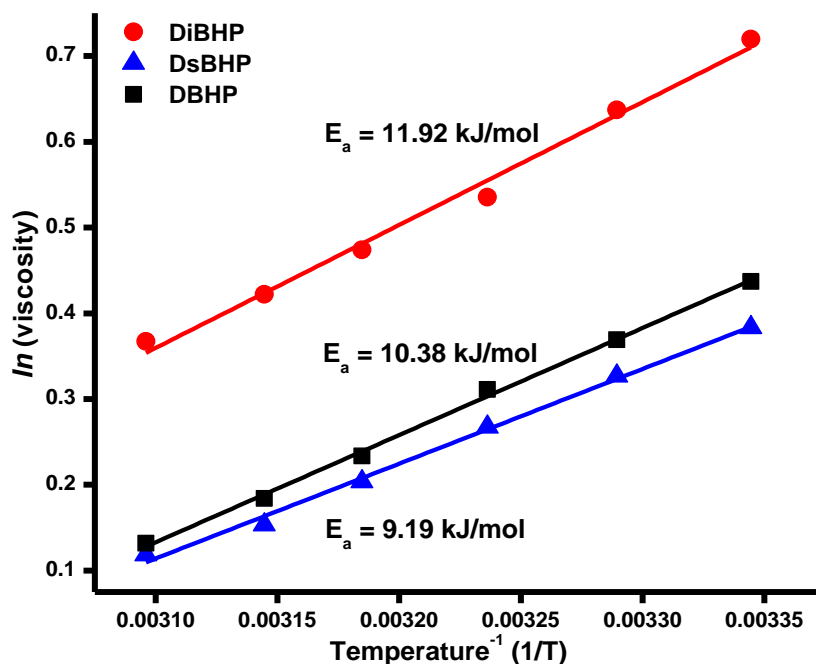
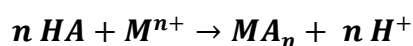


Figure 6A.1: Logarithm of viscosity against 1/T for the three H-phosphonates, DBHP, DiBHP and DsBHP. The activation energies are calculated from the slopes

6A.3 Extraction of U(VI)

Variation in D as a function of nitric acid concentration for the extraction of U (VI) by 1.1M DBHP, DiBHP, and DsBHP, respectively, in toluene are shown in Figure 6A.2. Toluene was used as the diluent because these extractants formed the third phase at acidities below 1M, when the extraction was carried out with dodecane diluent. Acidic extractants extract with a high D value at lower acidities due to the ion-exchange mechanism, and at higher acidities, they extract through the solvation mechanism. Ion-exchange between the metal and H⁺ ion is possible because of *keto-enol* tautomerism of the phosphoryl group, leading to the formation of the O-H group.

For example and acidic extractant HA undergoes an extraction event represented by the equation:



The equilibrium constant for the reaction is given as:

$$K = \frac{[MA_n][H^+]^n}{[M^{n+}][HA]^n} = K_D \frac{[H^+]^n}{[HA]^n}$$

$$K_D = K \frac{[HA]^n}{[H^+]^n}$$

$$\log K_D = \log K + n \log HA - n \log H^+$$

From the above equation, a plot of $\log K_D$ vs. pH for an acidic extractant would yield a straight line in the pH range (i.e. at acidities below 1M). Other kinds of extractants will not give a straight line.

The extractants DBHP and DiBHP behaves as acidic extractant and show higher extraction values in the lower acid region. On the other hand, DsBHP shows neutral extractant characteristics. In the case of the latter, lower distribution ratios are observed at lower acid concentrations, whereas highest D values are observed for acidities ranging from 4 to 6 M. When the solvation mechanism operates *i.e.* at higher acidities, DsBHP has a higher D value than DiBHP, which in turn has a higher D value than DBHP. The inductive effect due to the branching increases the basicity of the phosphoryl group and hence the D value. This has also been observed in the case of phosphates where tri-sec-butyl phosphate has a higher D value than tributyl phosphate for the extraction of U(VI)²⁵⁸. The experimentally observed higher D value for DiBHP at 0.01M acidity makes it a suitable candidate for the recovery of uranium from matrices in the pH range e.g. mine water. The speciation of uranyl nitrate depends on the acidity of the aqueous phase²⁵⁹. At lower acidities cationic species predominate, and at acidities above 6M, anionic species also will be present. Coupled with this, our extractants tautomerise at lower acidities to form the anionic species which is why extraction is enhanced due to cation-anion binding. Between 1-6 M HNO₃ concentrations, the charge neutral metal nitrates are extracted to the organic by the neutral keto tautomer. Charged species cannot be stabilized in the nearly non-polar organic medium. Above 6M, anionic species of uranyl ion also exist and this is one of the reasons for the decrease in the distribution ratios of UO₂²⁺ at acidities greater than 6M.

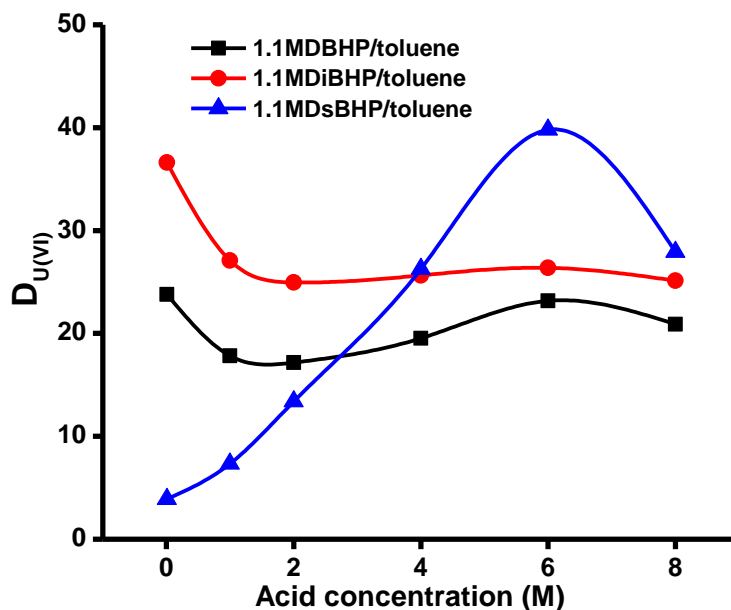


Figure 6A.2: Variation in D values as a function of HNO₃ concentration in the extraction of U(VI) by butyl H-phosphonates

6A.4 Explorations into the acid-dependent mechanism of extraction

The extractant DsBHP shows behaviour similar to a neutral extractant like TBP (Figure 6A.2). Extraction of the U(VI) was carried out at 0.001M acidity where it was expected that DsBHP will not show extraction, but DBHP will. This was expected by extrapolating the graphs in Figure 6A.2. The IR spectrum of 1.1M DsBHP and DBHP after extraction of U(VI) from 0.001M acid are compared with free DsBHP and DBHP in Figure. 6A.3. After extraction of uranium with DBHP and DiBHP, a red shift of 68cm⁻¹ and 59cm⁻¹ respectively is observed for the P=O stretching, whereas there is no change in the corresponding region in the case of DsBHP, suggesting poor or no extraction of uranium by DsBHP at low acidities consistent with Figure 6A.11.

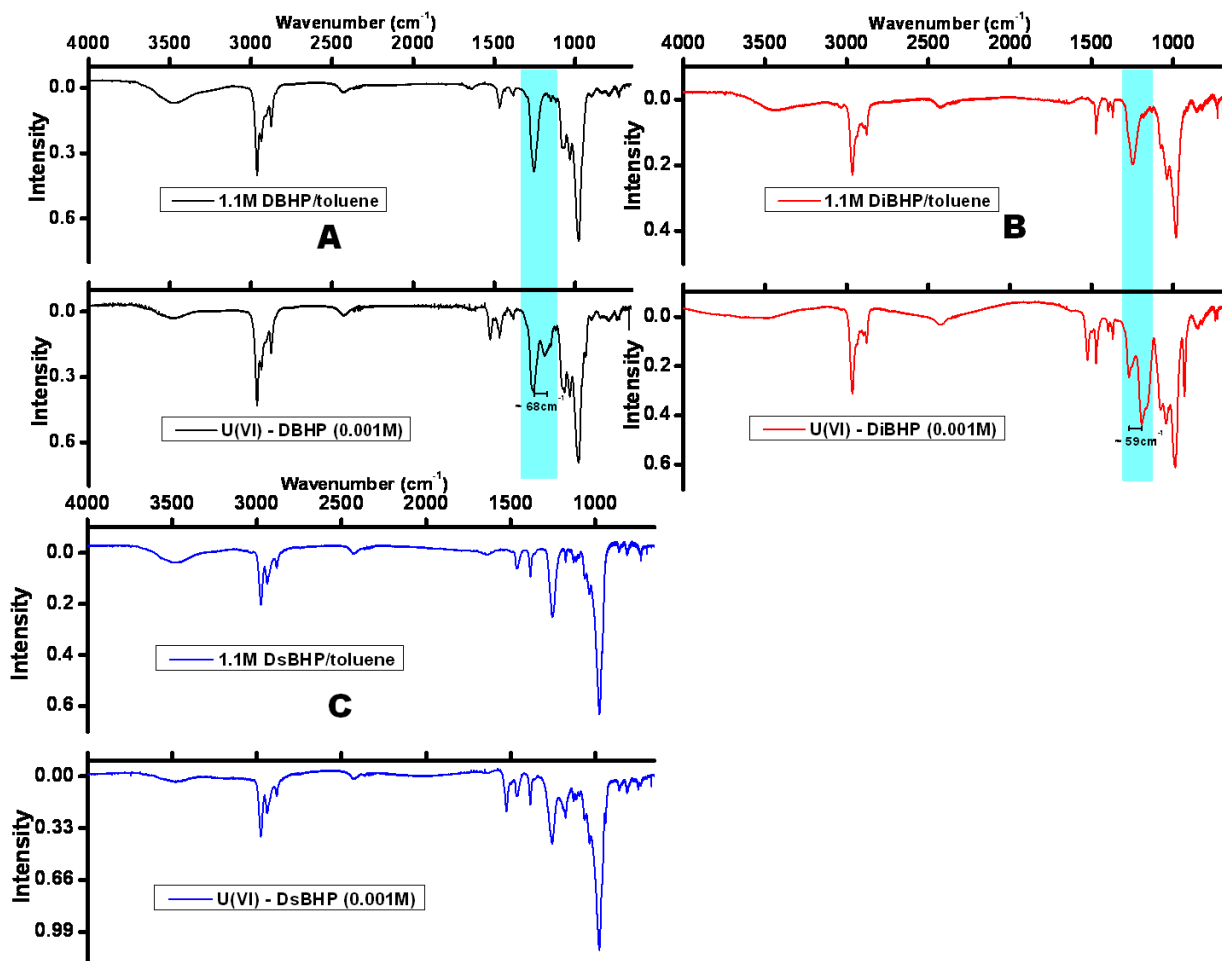


Figure 6A.3: (A) IR spectrum of DBHP, (B) DsBHP and (C) DiBHP before and after extraction of U(VI) from 0.001M nitric acid

By delving deeper into the reasons for the extraction trend observed at lower acidity, it can be hypothesized that there is a variation in the formation tendency of the *enol* tautomer among the extractants, as the cation exchange mechanism predominates the extraction in this zone. It can be expected from the extraction trends at lower acidity that DiBHP forms more *enol*, followed by DBHP and then DsBHP as it shows the poorest extraction of U(VI) at low acidities.

This claim was assessed by designing another simple yet insightful experiment in which the concentrations of *enol* tautomer could be estimated. 1.1M solutions of the extractants in toluene were first equilibrated with a 0.01M HNO₃ solution, enabling them to tautomerise to the *enol* form. The organic phases were then separated and equilibrated with an equal volume

of standardized (1.6M) NaOH. The *enol* form of the extractants alone can exchange the proton with sodium from the aqueous alkali. The difference in hydroxyl ion concentration in the aqueous phase is equal to the sodium extracted to the organic phase by the exchange of H⁺ ion. This is the amount of *enol* tautomer present in the organic phase. The percentage of *enol* tautomer formed for the three extractants DBHP, DiBHP and DsBHP are reported (Table 6A.2). The highest percentage of *enol* tautomer is formed in the case of DiBHP, followed by DBHP and DsBHP shows the least tendency for tautomerisation. This is the same as the trend in D values observed for uranium by solvent extraction experiments at lower acidity. The reduced formation of *enol* tautomer in the case of DsBHP was also predicted by theoretical calculations (refer section 6A.6).

Table 6A.2: The percentage of *enol* tautomer formed for the three extractants based on titration of NaOH before and after extraction

Extractant	[NaOH] _{aq} (M) (Before extraction)	[NaOH] _{aq} (M) (After extraction)	[NaOH] _{org} (M)	Percentage of <i>enol</i> tautomer formed
DBHP	1.645	1.117	0.528	48%
DiBHP	1.645	0.924	0.721	66%
DsBHP	1.645	1.335	0.310	28%

The marginally higher viscosity and activation barrier to the flow of DiBHP as compared to the other two extractants could also be attributed to a higher percentage of *enol* form in the case of DiBHP. In the *enol* tautomeric form, there exists a prerequisite for hydrogen bonding manifest in the O–H bond. Hydrogen bonding, known to be the strongest among intermolecular forces²⁶⁰ can cause a significant rise in the attractive interactions between DiBHP molecules. A consequence of this is its higher viscosity (Figure 6A.1).

As the acidity is increased and reaches about 4–6M, DsBHP extracts with a higher distribution ratio than DiBHP followed by DBHP. The trend in D values for the three extractants at 4M is different from the trend observed at 0.01M. This could be due to a set of different reasons, or their effective combination. One of the reasons D values increase in

general at higher acidity is due to the increase in the total nitrate concentration as detailed in a report by Benadict *et. al.*³². Another reason for the higher D specifically for DsBHP is due to the higher basicity of the phosphoryl oxygen^{61, 258} which will bind more readily to the metal cation which acts as a Lewis acid. Other factors include steric interactions around the metal centre, the electronic environment and strength of the M–O bond^{33, 261}. Having examined the tautomerism and its effects on the D value at low acidity, the strength of the U–O bond in the U---O=P moiety was investigated by IR spectroscopy at 4M acid. The extraction of U(VI) was carried out at 4M acid by 1.1M solutions of DBHP, DiBHP and DsBHP by equilibrating equal volumes of the aqueous and organic phases. The IR spectra of 1.1M solutions of DBHP, DiBHP and DsBHP in toluene before and after extraction of U(VI) from 4M acid are shown in Figure 6A.4 (A-C). Upon complex formation, at 4M acidity, P=O stretching frequency shows redshift for all the three extractants indicating M···O=P binding. This is consistent with the observation that at 4M acidity, the mechanism of extraction will be primarily through solvation (Figure 6A.2).

Figure 6A.5 shows the ESI mass spectrum of the organic phase after extraction of U(VI) by DiBHP from 0.01M HNO₃ as well as 4M HNO₃ media. These spectra are compared with the equivalent spectrum obtained for the bare ligand DiBHP. In the case of the bare ligand (L), monomer, dimer and trimer peaks were found in the gas phase and are assigned. For the uranyl complex formed from the extraction at 0.01M HNO₃, the enolic complex is observed at m/z 673 and the corresponding keto complex is observed at m/z 795.

TBP is a neutral extractant and shows optimum extraction at acidities of 4-6M. The class of extractants examined in this work are acidic in nature, generally showing higher distribution in the pH range, besides extraction at 4-6M. These extractants thus have potential application in pre-concentration of actinides. In addition, the ligand in extraction chromatography mode can be used for recovery of uranium even from lower acidic streams as the loaded uranium

from a chromatographic column can be recovered in a small volume using appropriate eluting agent.

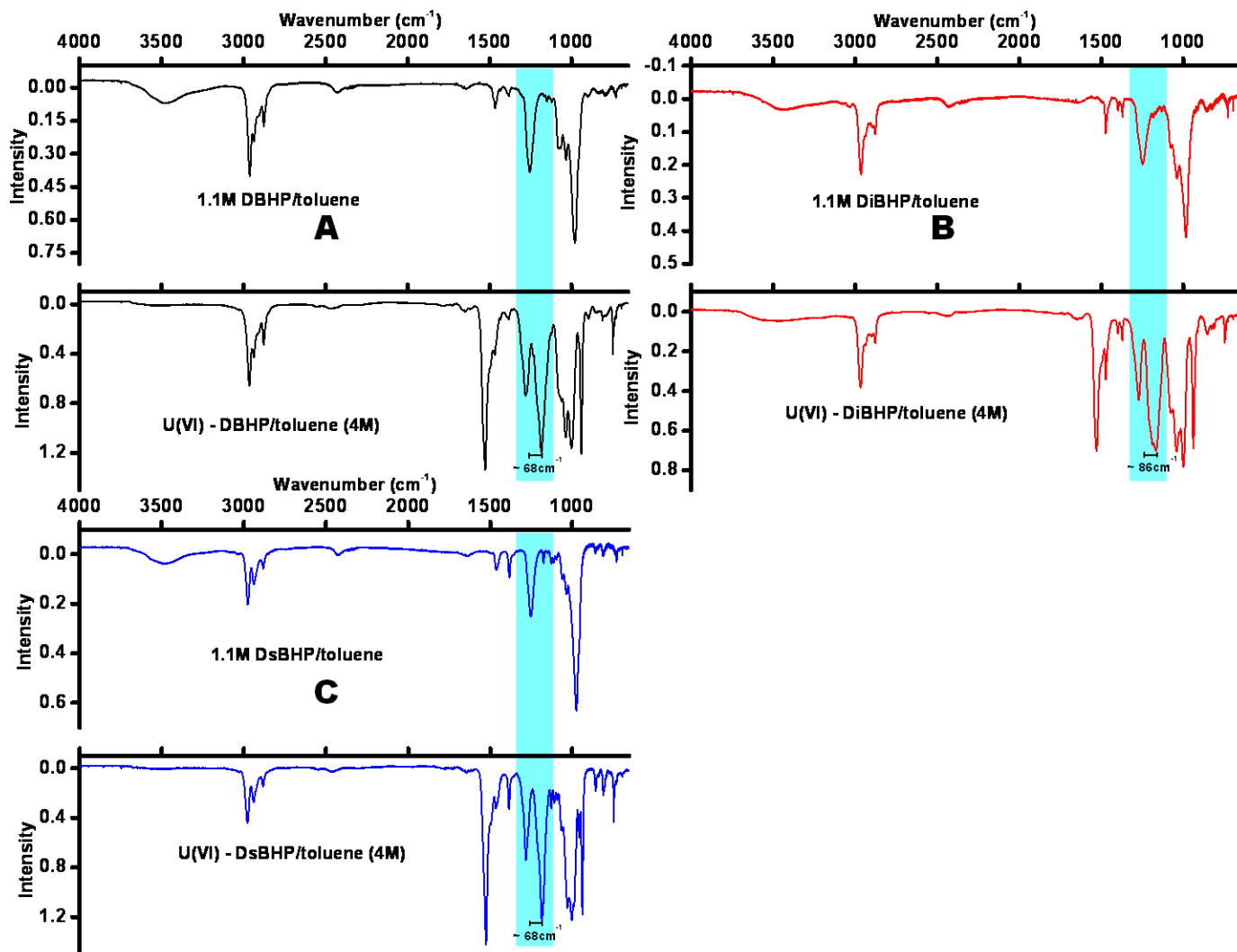


Figure 6A.4: (A) IR spectrum of 1.1M DBHP/toluene (B) 1.1M DiBHP/toluene and (C) 1.1M DsBHP/toluene before and after extraction of U(VI) from 4M nitric acid

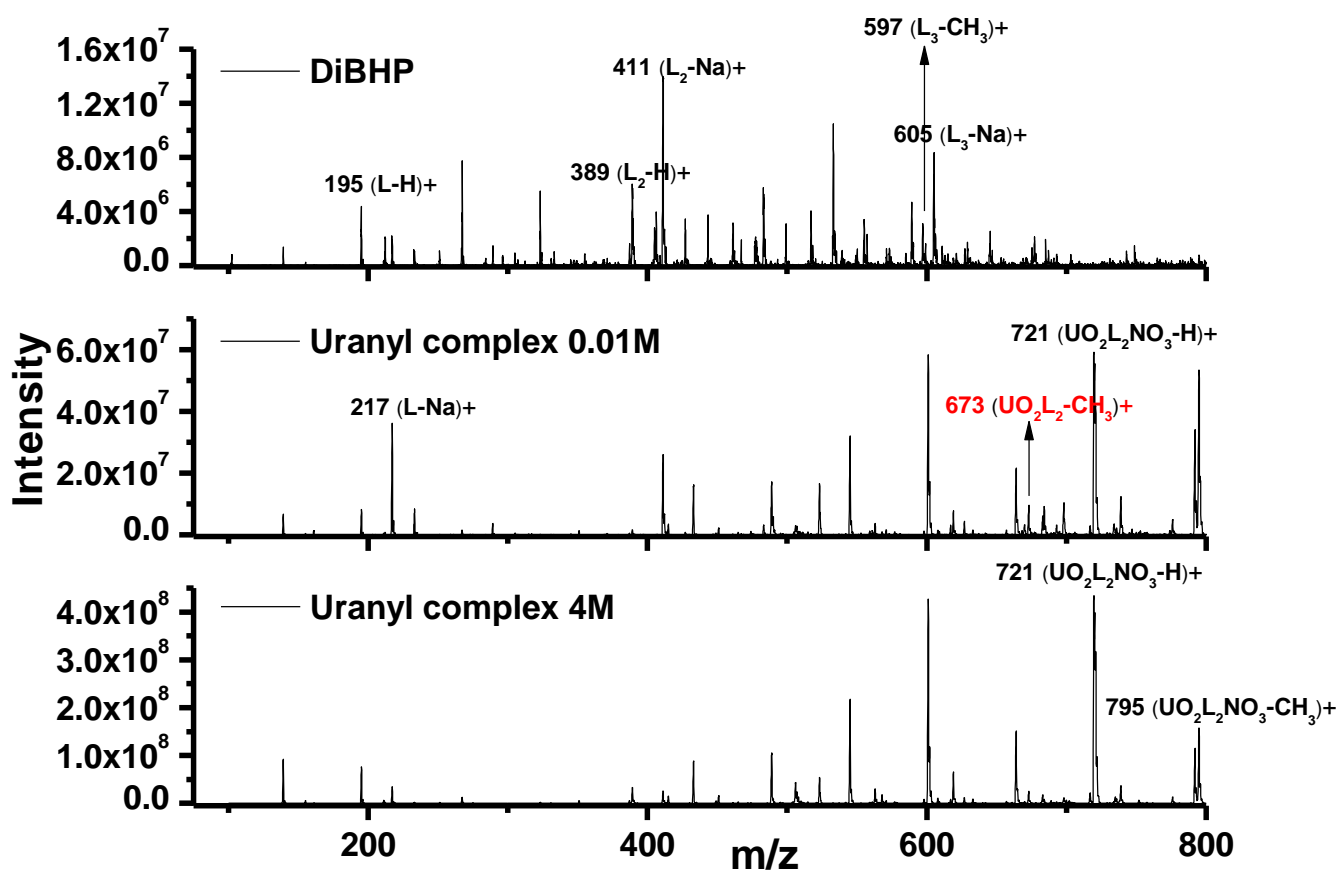


Figure 6A.5: ESI mass spectra for the bare ligand DiBHP compared with the organic phase uranyl complexes extracted from 0.01M and 4M nitric acid

6A.5 Extraction of Am(III)

Variation in D values as a function of nitric acid concentration in the extraction of Am (III) is shown in Figure 6A.6. The butyl-H-phosphonates have D values less than 0.1 and show negligible extraction of Am (III), compared to U(VI). Among the H-phosphonates, DiBHP is marginally higher than DBHP and DsBHP. DsBHP exhibits neutral extractant behaviour with Am(III) as it did in the case of U(VI). One of the reasons for the poor extraction of Am(III) is due to the binding of three extractants with Am(III) nitrate. This sterically hinders the extractants around the metal core, reducing the probability of complex formation and in turn its extraction. On the other hand, during the extraction of U(VI) two extractants are bound to the uranyl nitrate and hence extraction is much higher^{61, 258}. The effect of solvate was further investigated by choosing another trivalent metal similar to Am(III) and measuring its D value at 0.01M. It has been seen in the past that Am(III) shares a similar chemistry to

the trivalent lanthanide ions^{83, 262}. The extraction of Ce(III) nitrate at tracer level from the 0.01M acid by DsBHP was carried out, and the concentration of Ce(III) in the aqueous phase before and after extraction were measured by ICP–OES (Inductively Coupled Plasma–Optical Emission Spectroscopy). There was no change observed in the aqueous concentrations of Ce(III) before and after the extraction experiment indicating negligible extraction of the trivalent lanthanide. The difference in D values between U(VI) and Am(III) at acidities near 4M shows promising separation abilities of these phosphonates to separate U(VI) from a mixture containing Am(III). DsBHP, with branching close to the phosphoryl group is especially suited for this purpose as seen from a comparison of Figures 6A.2 and 6A.6.

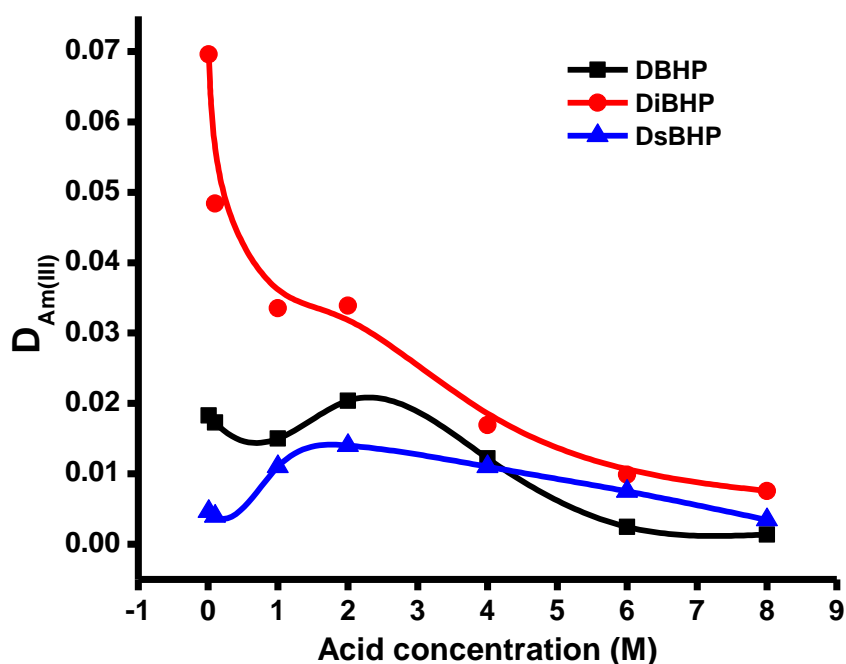


Figure 6A.6: Variation in D values as a function of HNO₃ concentration for the extraction of Am (III) by butyl H-phosphonates.

6A.6 Theoretical predictions

The optimized structure of DBHP and DsBHP binding to uranyl ion in keto and enol form, respectively are shown in Figures 6A.7 and 6A.8. Two nitrate anions are found to be in first coordination shell for the keto form, whereas in the corresponding enol form, the nitrates are

not found in first coordination shell. Only charge neutral complexes are stabilised in the organic medium. In the enol form the hydrogen ions are replaced by the extracted metal species. In order to maintain charge neutrality, nitrates are not extracted to the organic phase due to the anionic nature of the enolic tautomer of the extractant. The optimized geometry of uranyl ($U=O$) bond distance in both linear DBHP and branched DsBHP in keto form is found to be very similar ($\sim 1.797\text{\AA}$). However, $U-O_{\text{H-phosphonate}}$ is somewhat strongly bound in DsBHP complex (2.416\AA) as compared to DBHP (2.424\AA). Further, the two nitrates are symmetrically bound in both uranyl complexes.

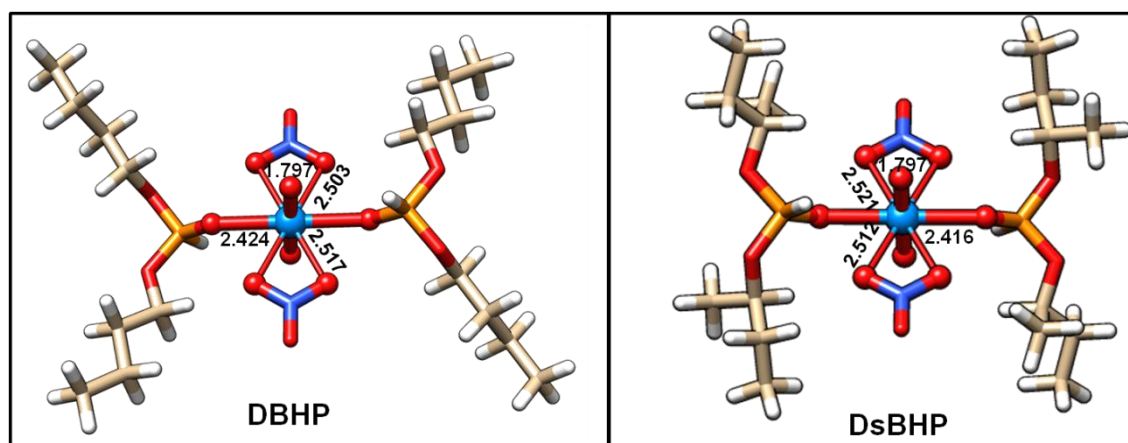


Figure 6A.7: Optimized structures of DBHP and DsBHP bound with uranyl nitrate (keto form)

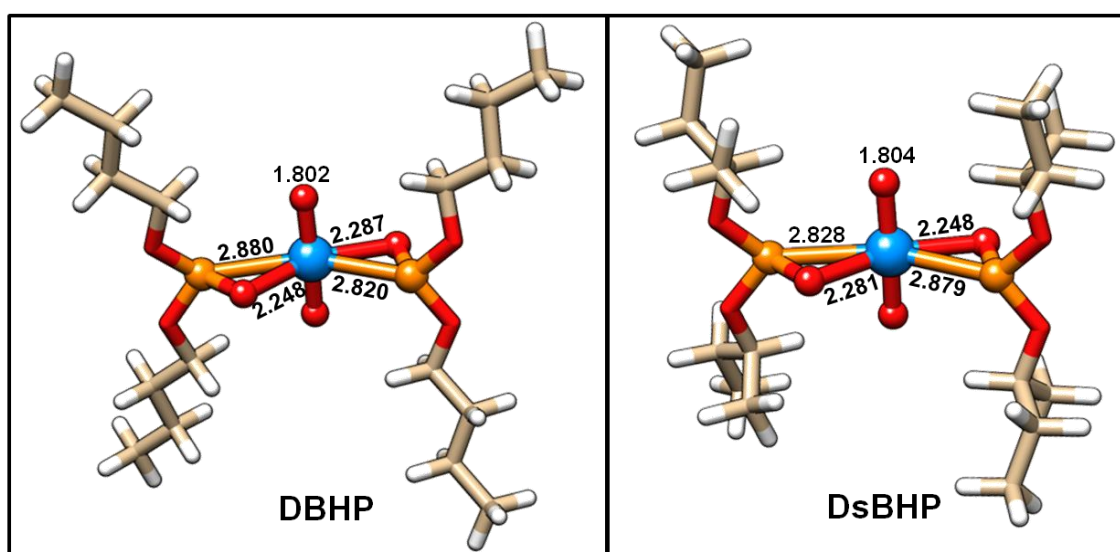


Figure 6A.8: Optimized structures of DBHP and DsBHP bound with uranyl nitrate (enol form)

In the corresponding enolic form, the extractant molecules are strongly bound to uranyl due to its anionic nature of the H-phosphonate. In this complexation, both oxygen ($\sim 2.3 \text{ \AA}$) and phosphorus ($\sim 2.8 \text{ \AA}$) are found to interact with uranyl centre in an asymmetric fashion due to differing covalent radii of phosphorous (107 pm)²⁶³ and oxygen (66 pm)²⁶⁴.

The extractant binding strength to uranyl in both keto and enol forms are reflected in the computed asymmetric vibrational frequencies (ν_{asym}) of uranyl oxygens ($\text{U=O}(\nu_{\text{asym}})$) and the ($\text{P=O}(\nu_{\text{asym}})$). As a general rule of thumb, the stronger the equatorial coordination of the extractant will weaken the axial U=O bond. As shown in Table 6A.3, the $\text{P=O}(\nu_{\text{asym}})$ is redshifted by $\sim 200 \text{ cm}^{-1}$ in the enolic form as compared to the keto-form. As expected the binding of H-phosphonate is weaker in the keto-form, but are still red-shifted (by $\sim 100 \text{ cm}^{-1}$) as compared to the free-extractant. As far as the uranyl vibrational frequencies are concerned, the ($\text{U=O}(\nu_{\text{asym}})$) for the enolic form is red shifted by $30\text{-}40 \text{ cm}^{-1}$, whereas for the corresponding keto form the red shifting less ($< 20 \text{ cm}^{-1}$). Within the two extractants, the $\text{U=O}(\nu_{\text{asym}})$ is more red-shifted by 10 cm^{-1} in DsBHP as compared to DBHP which is again reflected in the ($\text{P=O}(\nu_{\text{asym}})$) of the two extractants. Further, the computed vibrational frequencies are in line with our experimental IR data within a few wave numbers ($\sim 10 \text{ cm}^{-1}$ for U=O and $20\text{-}30 \text{ cm}^{-1}$ for the P=O) (Figure 6A.9). These variations in the predicted geometries between the two extractants will be reflected in the computed binding affinities.

Table 6A.3: IR stretching and shifts: Theoretical and experimental P=O and U=O stretching frequencies in cm^{-1} . Corresponding experimental values are in parenthesis

Molecule	P=O stretching frequencies			U=O stretching frequencies		
	Bare ligand	Complexed form	Red shift in P=O stretch	Uranyl nitrate	Complexed form	Red shift in U=O stretch
DBHP keto	1228 (1254)	1135 (1184)	93 (70)	937 (950)	921 (940)	16 (10)
DsBHP keto	1234 (1253)	1126 (1184)	108 (69)	937 (950)	918 (939)	19 (11)
	P=O stretching frequencies in cm^{-1}			U=O stretching frequencies in cm^{-1}		
DBHP enol	1068	881	187	937 (950)	907 (934)	30 (16)
DsBHP enol	1070	869	201	937 (950)	897 (934)	40 (16)

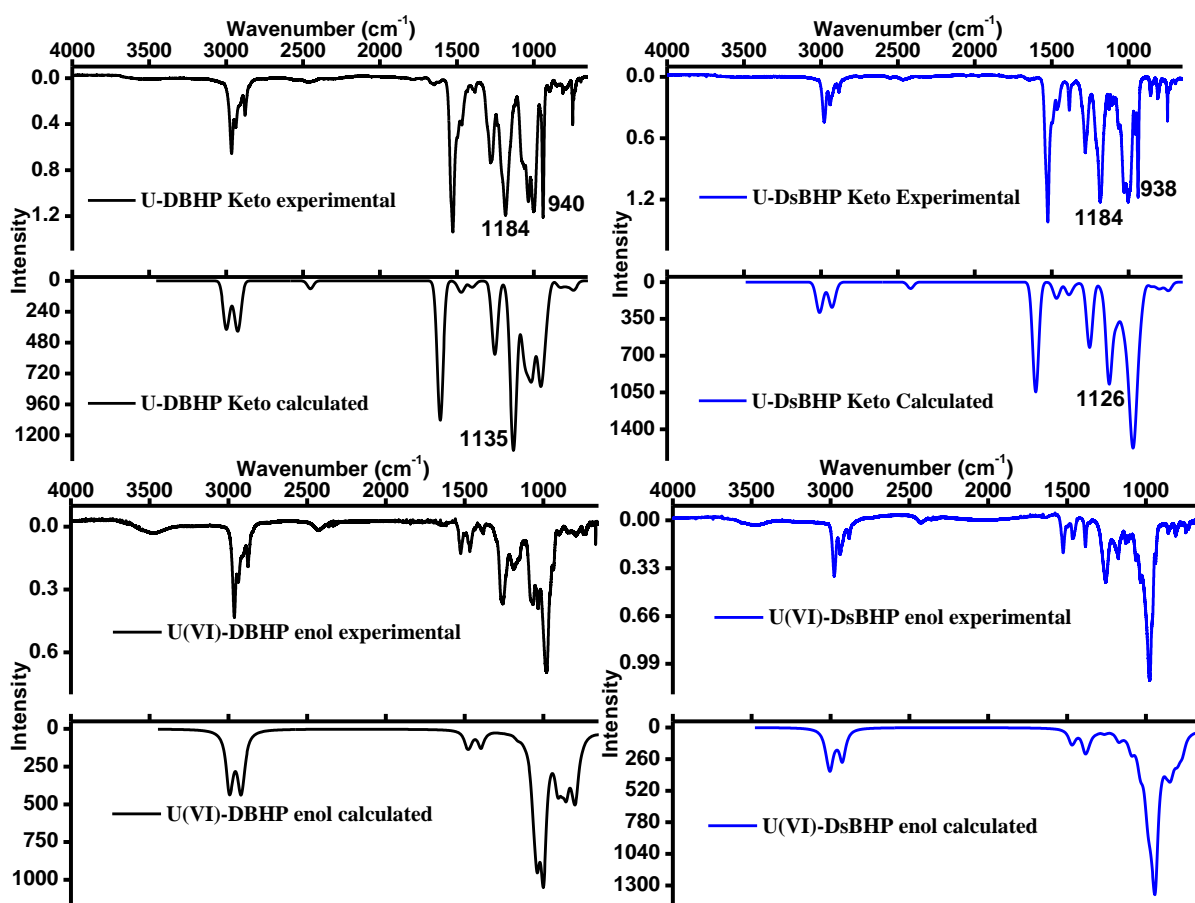


Figure 6A.9: Comparison of experimental and calculated IR spectra for uranyl nitrate complexes of DBHP and DsBHP both in the keto and enol forms

The binding free energies of uranyl (solvent corrected) with DsBHP complex is higher (-16.5 kcal mol⁻¹) as compared to DBHP extractant (-7.8 kcal mol⁻¹) (Table 6A.4). Due to the *sec*-butyl branch, the inductive effect of the secondary methyl group can increase the basicity of the DsBHP phosphoryl group and make this a stronger complexing ligand. For the corresponding enolic form, the binding is very strong due to the expected anionic nature of the ligand. Unlike the ketone form, the binding affinities are very similar in both DBHP and DsBHP extractant. The complexation energies of DBHP and DsBHP in the enolic form are similar despite the lower tendency of the latter to form the enolic tautomer, as the computational study does not take into account the proportion of enolic tautomer.

Table 6A.4: Computed binding free energies for uranyl nitrate complexes (kcal mol⁻¹)

UO₂(NO₃)₂ complexes	DBHP	DsBHP
Keto	-7.87	-16.52
Enol	-42.33	-41.93

From solvent extraction studies, it is observed that the *sec*-butyl isomer of DBHP shows less extraction at lower acidities and more extraction at higher acidities above 4M. At lower acidities (~0.01 – 0.1M) the enol tautomer is responsible for the higher extraction showed by H-phosphonates in general⁵¹. In the experiments, the percentage enol formation (28%) of DsBHP is lesser as compared to DBHP extractant. The α/β -hydrogens in DsBHP extractant are forming somewhat stronger hydrogen bonding (<2.65 Å) with the phosphoryl oxygens (P=O...H). However, in DBHP ligand, the hydrogens attached to alpha carbons are weakly interacting (>~2.85Å) as shown in Figure 6A.10. This weak hydrogen bonding can be one of the reasons why the formation of the enol tautomer is hindered in the case of DsBHP, as the phosphoryl oxygen is engaged in the hydrogen bonding interactions.

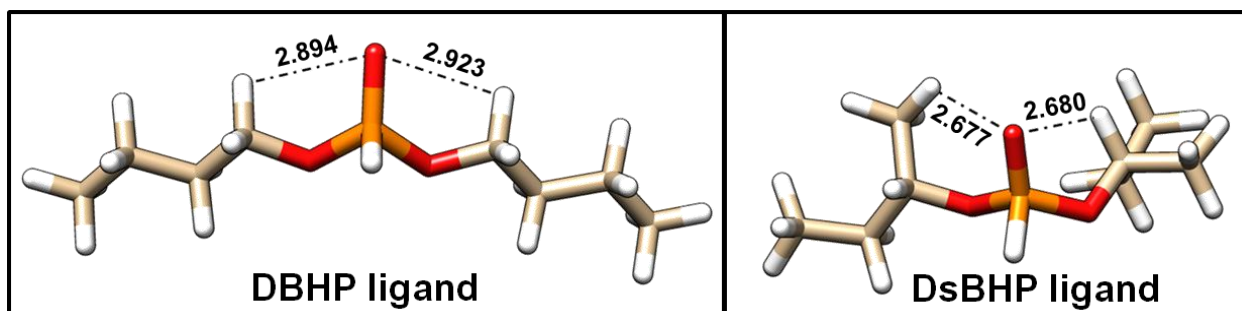


Figure 6A.10: Optimized structures of bare DBHP and DsBHP ligands indicating the P=O---H hydrogen bonding

The D values for the extraction of Am were less than 0.1 for all the three extractants, DBHP, DiBHP and DsBHP. To understand the possible structure and binding affinities, we have optimized the Am-extractant species (Figure 6A.11). A nine-coordinated (3 extractants and 6 oxygens of three nitrate moieties) Am³⁺ species is found in our optimized structure. The Am-O bonds with DBHP lie in the range 2.420 to 2.454 Å and the Am-O bonds with the nitrate groups are in the bond length range of 2.469-2.569 Å. The Am(III) complex with DBHP was examined, and the complexation energy for this complex was calculated as +8.03 kcal mol⁻¹ which indicates that the binding is unfavourable. The computed binding free energies are consistent with the experimental data where negligible D values are found in solvent extraction studies.

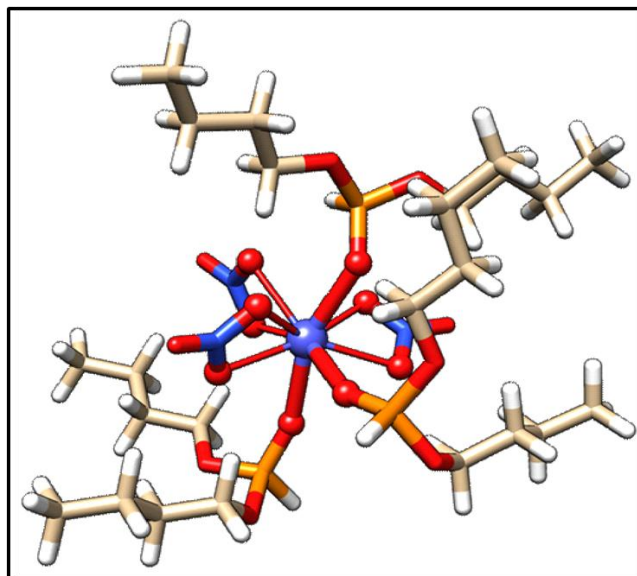


Figure 6A.11: Optimized structures of DBHP bound with Am(III)nitrate in keto form

6.A7 Conclusion

Branched butyl H-phosphonates, *viz.* DiBHP and DsBHP and their linear chain isomer, *n*-butyl H-phosphonate (DBHP), were synthesised and characterized. These phosphonates were used for the extraction of U(VI) and Am(III) and their distribution ratios were studied as a function of nitric acid concentration. It was observed that DsBHP interestingly showed neutral extractant behaviour for the extraction of both uranium and americium, though H-phosphonates are generally categorized as acidic extractants. At higher acidity, U(VI) was extracted with highest D value by DsBHP followed by DiBHP and DBHP, indicating that branching in the carbon chain increases the extractability of U(VI). All the three phosphonates showed negligible extraction for Am(III). Computational results from which binding energies for both metal ions were predicted, matched well with the experimental findings. Further, our electronic structure calculations also elucidated a plausible reason for the unexpected extraction trend shown by DsBHP.

Structural effects due to branching were examined more closely by understanding its role in the mechanisms of extraction. Branching at the *iso* position ensures higher D values for the extraction of U(VI) at lower acidity. This implies that these phosphonates can be used as an

effective ligand for the extraction and concentration of U(VI) from aqueous streams in the pH range. Our combined experimental and theoretical studies also indicated that methyl branching close to the phosphoryl group hinders the formation of the *enol* tautomer to a certain extent.

STRUCTURAL EFFECTS ON THE COMPLEXATION OF ACTINIDES WITH BRANCHED PHOSPHONATES: A COMBINED EXPERIMENTAL AND QUANTUM CHEMICAL STUDY

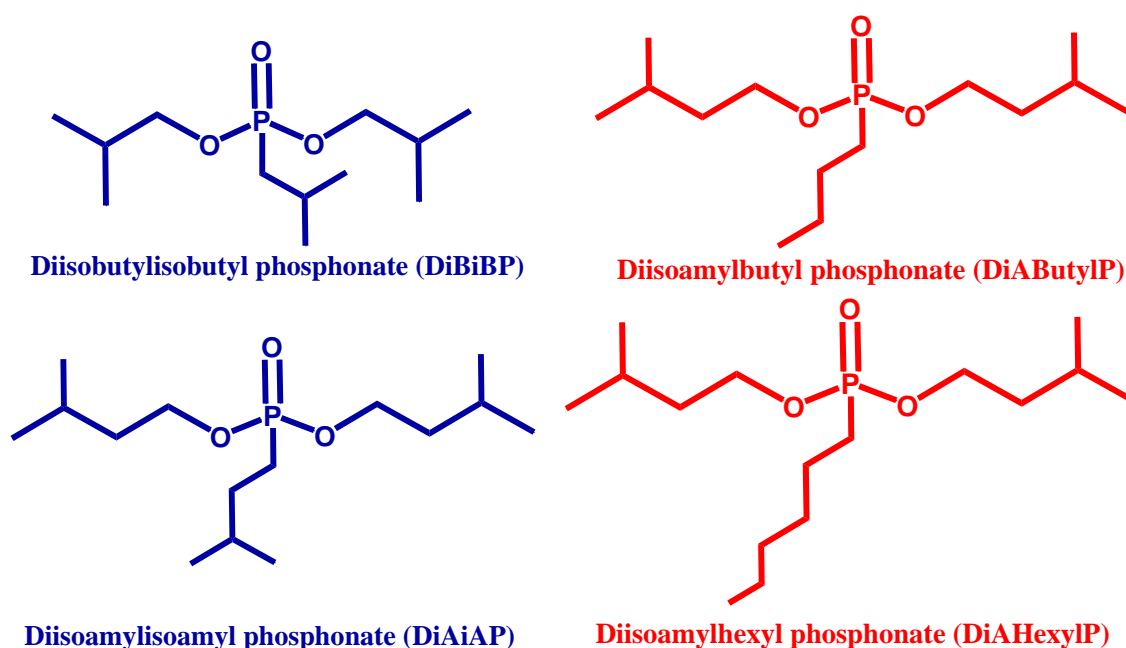
(B) DIALKYLALKYL PHOSPHONATES

6B.1 Introduction

Unlike phosphates, phosphonates allows us to tailor-make the molecules by choosing appropriate ligands around the central phosphoryl group and hence modulate the electron density around the coordinating group, which in turn dictates the physical properties of ligand and its extraction capability. Phosphinates and phosphine oxides are prepared by a Grignard reagent mediated route, whereas phosphonates are prepared from H-phosphonates that can be converted to dialkylalkyl phosphonates by a two step process in which an alkyl group replaces hydrogen. The multiple advantages of phosphonates as actinide binders were a motivation to study their structural behaviour on extraction.

The present study investigates extraction behaviour of actinides with dialkylalkyl phosphonates where both branched symmetrical and branched unsymmetrical carbon chains have been considered. When all the carbon chain substituents are the same, a symmetrical phosphonate is formed and when at least one of the carbon chains is different an unsymmetrical phosphonate is formed. For the first time, symmetrical Diisobutylisobutyl phosphonate (DiBiBP), Diisoamylisoamyl phosphonate (DiAiAP) and unsymmetrical Diisoamylhexyl phosphonate (DiAHexylP) and Diisoamylbutyl phosphonate (DiAButylP) have been investigated in the extraction of U(VI), Th(IV), Pu(IV) and Am(III). For this purpose dialkylalkyl phosphonates with branched symmetrical and unsymmetrical carbon chains have been synthesised in pure form by Michelis–Arbuzov reaction and characterised by NMR and GC – MS. The structures of these phosphonates are depicted in Scheme 6B1. The extraction ability of these compounds has been found to strikingly correlate with the length of their carbon chains bound to the phosphoryl group. These structural correlations

have been probed further by employing density functional theory (DFT). For the first time, structures of DiBiBP (symmetrical) and DiAHexylP (unsymmetrical) phosphonate and their complexes with U(VI) and Th(IV) have been investigated. In addition, the energetics of binding associated with U(VI) and Th(IV) complex formation have been calculated and the complexation energies obtained by DFT corroborated with distribution ratios obtained from experiment.



Scheme 6B.1: Structures of the dialkylalkyl phosphonates synthesised and used for the extraction studies.

6B.2 Physico-chemical properties of dialkyl alkyl phosphonates

Density of the dialkylalkyl phosphonates DiBiBP, DiAiAP, DiAButylP and DiAHexylP are shown in Table 6B.1. The density of DiAHexylP is the highest among the four, followed by DiBiBP, DiAiAP and the least dense is DiAButylP. The density decreases with the branching as well as with shorter carbon chains. Viscosity measurements were made for DiBiBP, DiAiAP, DiAButylP and DiAHexylP and the activation energy was calculated using the slope obtained in the plot. Figure 6B.1 shows the graphs of the logarithm of viscosity vs. $1/T$ and the activation energy that is calculated from the slopes. The activation energy for

DiAiAP is the highest among the four, followed by DiAButylIP, DiBiBP and then DiAHexylIP. Unsymmetrical dialkylalkyl phosphonates have lower viscosity and among the symmetrical phosphonates the ones with the shorter alkyl chains have the lower viscosity. Table 6B.1 shows the viscosity at 31⁰C and activation energies for the dialkylalkyl phosphonates.

Solubility of the compounds in 4M HNO₃ was measured and the results are shown in Table 1. DiAiAP shows the lowest aqueous solubility followed by DiBiBP, DiAHexylIP and DiAButylIP. Symmetrical dialkylalkyl phosphonates have lower aqueous solubility than the unsymmetrical ones. This could be due to a better solute-solute contact and hence more interaction between phosphonate molecules in the symmetrical phosphonates, making them less likely to dissolve in the aqueous phase. Among both the symmetrical and unsymmetrical phosphonates the ones with the longer carbon chains are less soluble in the aqueous phase.

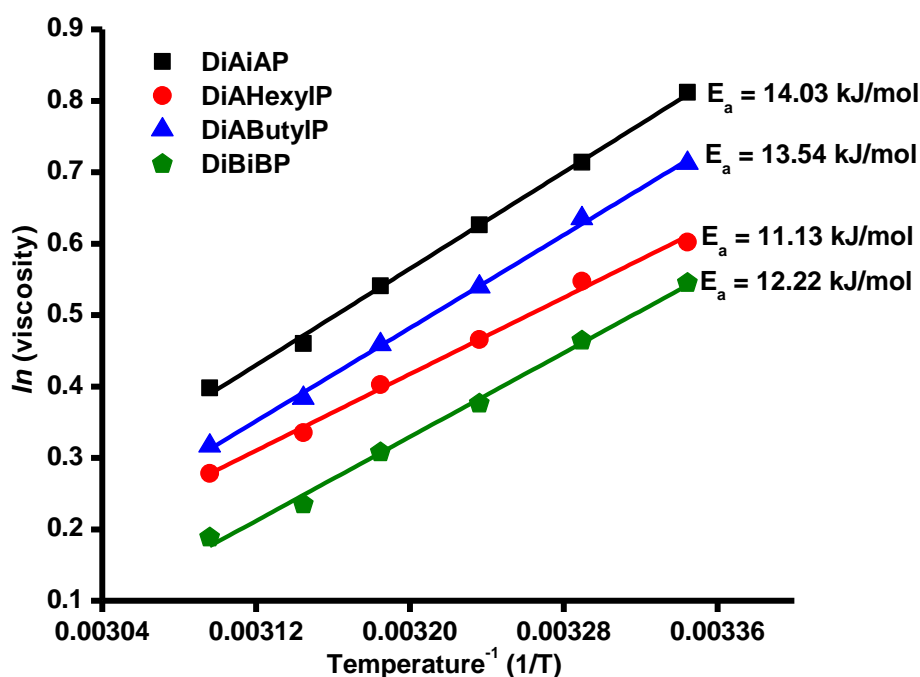


Figure 6B.1: Logarithm of viscosity against 1/T for the dialkylalkyl phosphonates DiBiBP, DiAiAP, DiAButylIP and DiAHexylIP. The activation energy is calculated from the slopes.

Table 6B.1: Density (g/mL), viscosity (cp) at 304K, activation energy (kJ/mol), aqueous solubility (g/L) and dielectric constant of DiBiBP, DiAiAP, DiAButylP and DiAHexylP.

Extractant	Density	Viscosity	Activation Energy	Aqueous solubility	Dielectric const.
DiAiAP	0.9088	2.04	14.03	0.7761	4.97
DiBiBP	0.9126	1.59	12.22	0.7858	5.27
DiAHexylP	0.9250	1.73	11.13	0.8127	5.08
DiAButylP	0.9076	1.89	13.54	0.8541	6.09

6B.3 Extraction of U(VI), Th(IV), Pu(IV) and Am(III)

Variation in D as a function of nitric acid concentration in the extraction of U(VI) by 1.1M extractants in dodecane is shown in Figure 6B.2. At 0.01M nitric acid concentration, all the extractants showed a D value less than 1. The extraction by dialkylalkyl phosphonates increases with increase in acidity and shows a maximum distribution ratio at 6M nitric acid. On further increasing the acidity to 8M the extraction of U(VI) drops as HNO₃ competes with the extractants. DiAHexylP shows the maximum extraction of U(VI) followed by DiAiAP, DiAButylP and DiBiBP. The order of extraction mainly shows dependence on the length of the alkyl chain directly attached to the phosphorous in the extractant molecule and also on the phospho diester carbon chain. A longer alkyl carbon chain bound to phosphorous increases the basicity of the phosphoryl oxygen due to the inductive effect and this increases the binding ability of the phosphoryl oxygen to the uranyl group. The effect of the phospho diester carbon chain has a less dramatic effect as the carbon chain is attached via a P–O linkage. However, between DiAButylP and DiBiBP, DiBiBP shows lower extraction as the isobutyl group is shorter than the isoamyl group in the phospho diester linkage in the two extractants.

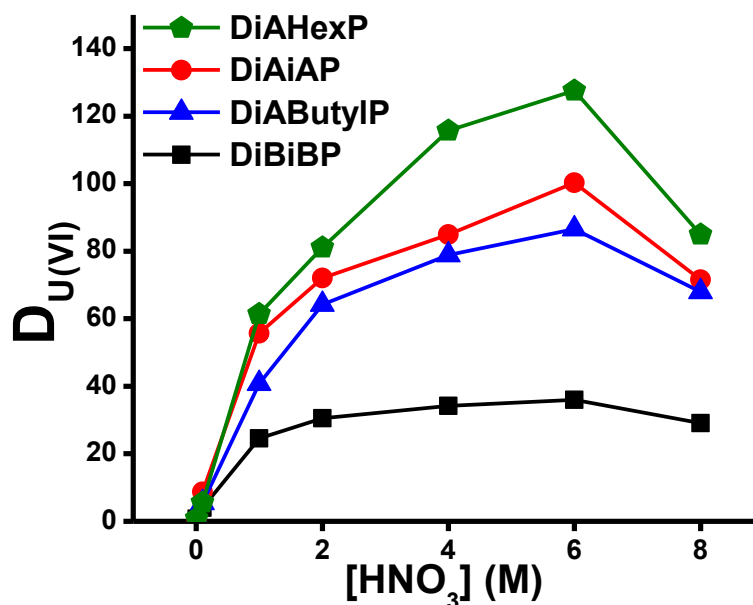


Figure 6B.2: Variation in D values as a function of HNO₃ concentration in the extraction of U(VI) by unsymmetrical and symmetrical branched dialkylalkyl phosphonates.

The graph of D value vs. nitric acid concentration in the extraction of Th(IV) for all the four dialkylalkyl phosphonate extractants is shown in Figure 6B.3. The maximum D value occurs at 4M acidity in all the four extractants. Th(IV) extraction is similar to U(VI) system where DiAHexylP shows the maximum extraction followed by DiAiAP, DiAButylP, and DiBiBP. The D for Th(IV) is lower than D for U(VI) by the corresponding extractants in the case of all the four extractants. For both U(VI) and Th(IV), DiBiBP shows the lowest extraction for the metal ions and DiAHexylP shows the highest extraction. The peak at which the maximum extraction occurs is at 6M acid in the case of U(VI), compared to 4M for Th(IV). This is because Th(IV) binds with three extractant molecules during its extraction, whereas U(VI) binds to two extractant molecules. Hence, in general the competition for the extractant by the acid is more pronounced in the case of Th(IV) and the D value starts decreasing at 6M instead of 8M nitric acid.

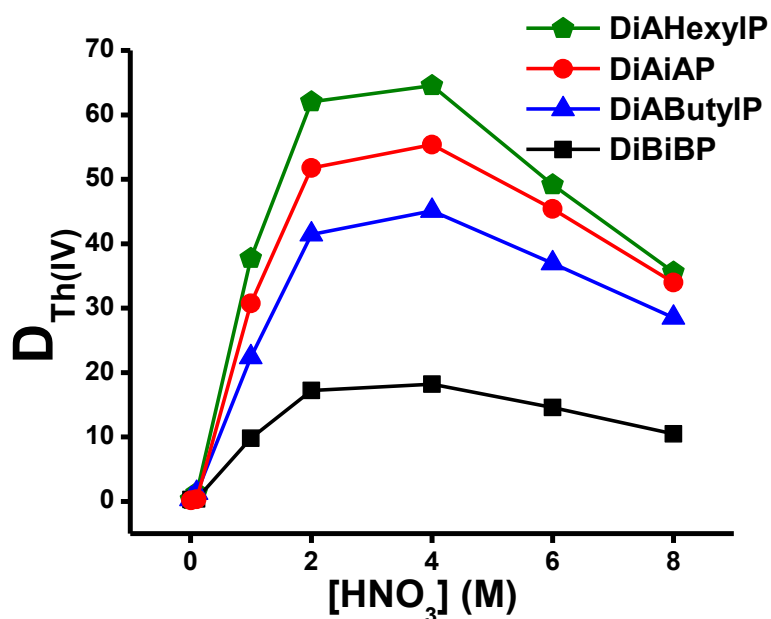


Figure 6B.3: Variation in D values as a function of HNO₃ concentration in the extraction of Th(IV) by unsymmetrical and symmetrical branched dialkylalkyl phosphonates.

Figure 6B.4 shows the D values for the four dialkylalkyl phosphonates in the extraction of Pu(IV). In this case as well, DiAHexylIP shows the maximum extraction of Pu(IV) followed by DiAiAP, DiAButylIP, and DiBiBP. All the extractants show a maximum extraction at 4M acidity. This is consistent with the order of extraction showed by U(VI) and Th(IV). The D values for the extraction of Pu(IV) are higher than those of Th(IV) and lower than those of U(VI) for a given extractant.

Figure 6B.5 shows the variation in distribution ratio in the extraction of Am(III) by DiBiBP, DiAiAP, DiAButylIP and DiAHexylIP. The maximum D value occurs at 4M acidity. All the four extractants show negligible extraction of Am(III) and have D values below 1, nevertheless, trends remain the same as observed for the other metal ions.

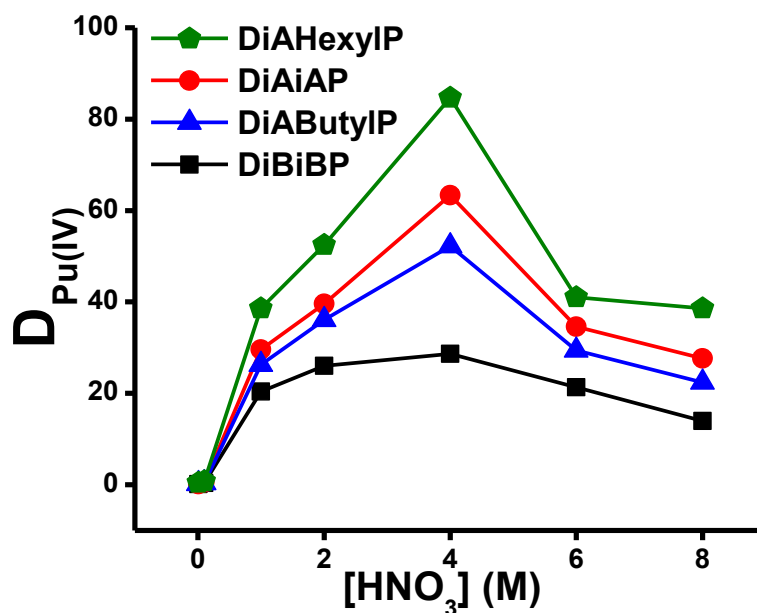


Figure 6B.4: Variation in D values as a function of HNO₃ concentration in the extraction of Pu(IV) by unsymmetrical and symmetrical branched dialkylalkyl phosphonates.

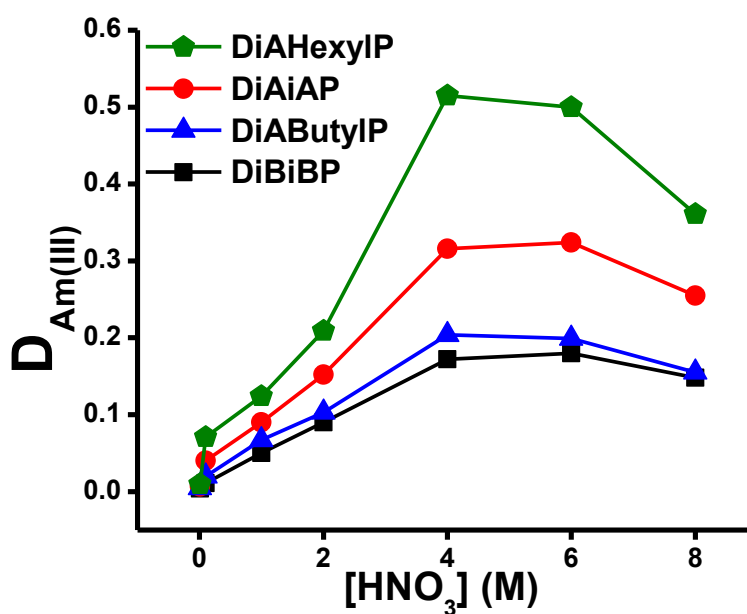


Figure 6B.5: Variation in D values as a function of HNO₃ concentration in the extraction of Am(III) by unsymmetrical and symmetrical branched dialkylalkyl phosphonates.

Figure 6B.6 shows the extraction of nitric acid by the four dialkylalkyl phosphonates as a function of equilibrium HNO₃ concentration in the aqueous phase. In general the effect of basicity on the extraction of nitric acid is not as pronounced as it is in the case of extraction of U(VI), Th(IV) and Pu(IV). However, DiAHexylIP and DiAiAP show a slightly higher

extraction of nitric acid compared to DiBiBP and DiAButylP. For all the extractants as the equilibrium HNO_3 concentration in the aqueous phase increases the concentration of HNO_3 in the organic phase increases. This validates the general drop in D values of the metal ions at acids concentrations of around 6–8 M. As more nitric acid binds to the extractants at these acidities, the acid competes for the free extractant and the D values for the metal ion are thus lowered.

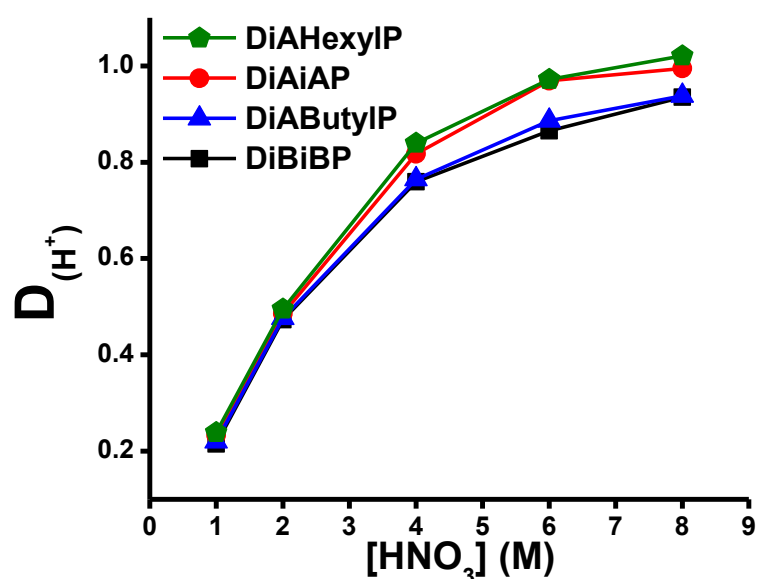


Figure 6B.6: Extraction of nitric acid by the four dialkylalkyl phosphonates as a function equilibrium HNO_3 concentration in the aqueous phase.

6B.4 Computational results

Solvent extraction distribution ratios reveal that highest metal ion extraction is obtained when DiAHexylP extractant is used, whereas DiBiBP shows the least. This may be due to the higher inductive effect of the longer carbon chains in DiAHexylP leading to increased basicity of the phosphoryl oxygen than in the case of DiBiBP. As representatives for this extraction behaviour, U(VI) and Th(IV) were examined by DFT in order to understand the electronic structure of the complexes as well as the binding energetics associated with the complex formation.

Complexes of both U(VI) and Th(IV) with DiBiBP as well as DiAHexylP have been optimized (Figures 6B.7 and 6B.8, respectively) and subsequently, their bond distances (Table 6B.2) and Mulliken charges (Table 6B.3) have been analysed.

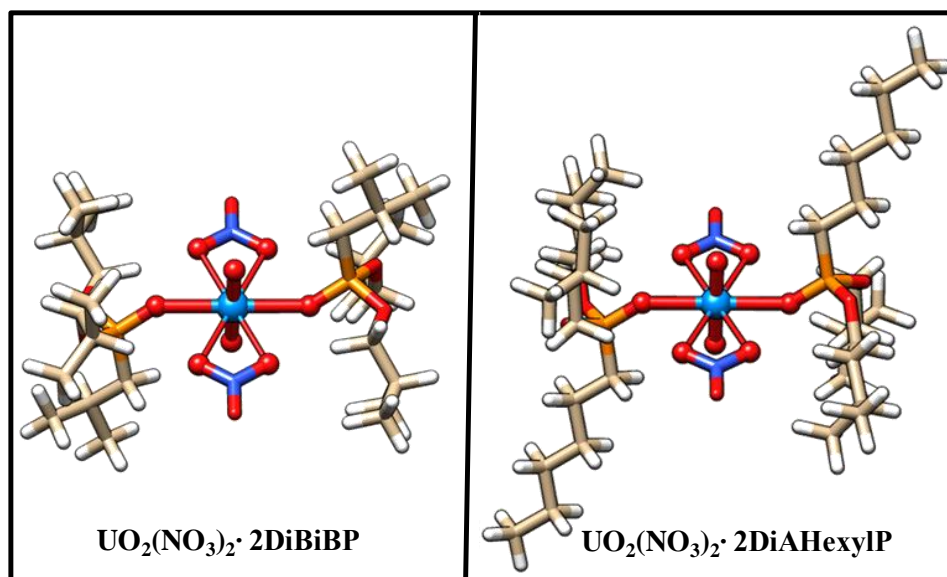


Figure 6B.7: Optimized geometries of the UO₂(NO₃)₂·2DiBiBP and UO₂(NO₃)₂·2DiAHexylP complexes

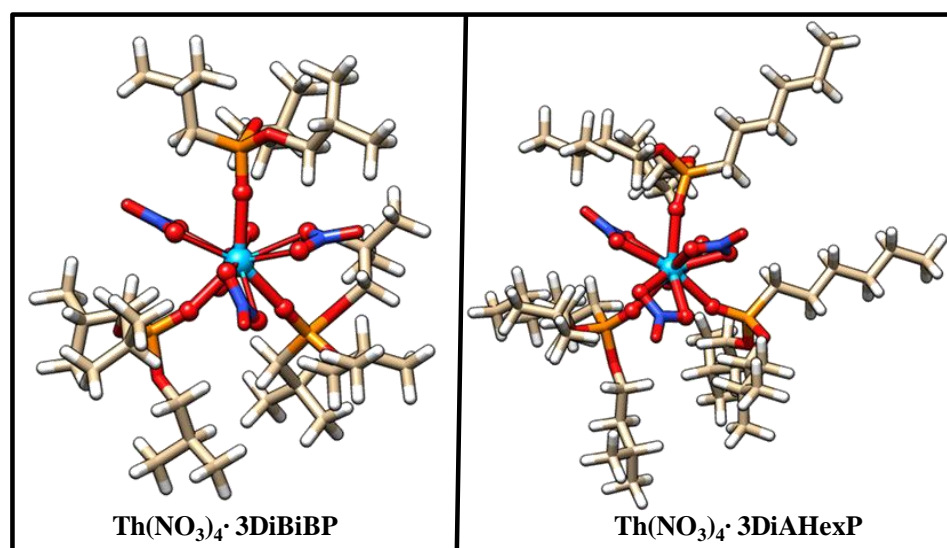


Figure 6B.8: Optimized geometries of the Th(NO₃)₄·3DiBiBP and Th(NO₃)₄·3DiAHexylP complexes

Table 6B.2: Structural parameters of actinide extractant complexes calculated using BP86 functional and SVP basis set.

Bond	Bond lengths (Å)			
	UO ₂ (NO ₃) ₂ ·2DiBiBP	UO ₂ (NO ₃) ₂ ·2DiAHexylP	Th(NO ₃) ₄ ·3DiBiBP	Th(NO ₃) ₄ ·3DiAHexylP
U = O _{yl}	1.804	1.804	-	-
M – O _{Ext}	2.402	2.392	2.408 – 2.426	2.417 – 2.446
M – O _{NO3}	2.522 – 2.541	2.534 – 2.542	2.559 – 2.655	2.541 – 2.670

Table 6B.3: Mulliken charges on phosphorous and phosphoryl oxygen atoms in the bare ligand and after complexation calculated using M06-2X. Charges on the metal centre, as well as uranyl and thorium nitrate oxygen atoms bound to the metal are also shown.

Molecule	Q _P	Q _O (P=O)	Q _O (P-O)	Q _O (UO ₂)	Q _{N-O} (NO ₃)	Q _{N=O} (NO ₃)	Q _M
DiBiBP	0.8342	-0.6262	-0.3602	-----	-----	-----	-----
DiAHexP	0.8117	-0.6231	-0.3616	-----	-----	-----	-----
UO ₂ (NO ₃) ₂ ·2 DiBiBP	0.7998	-0.6472	-0.3220	-0.6286	-0.4464	-0.3598	2.2299
UO ₂ (NO ₃) ₂ ·2 DiAHexP	0.8190	-0.6504	-0.3391	-0.6157	-0.4471	-0.3648	2.2073
Th(NO ₃) ₄ ·3DiBiBP	0.7645	-0.6774	-0.3259	-----	-0.4322	-0.3727	2.3768
Th(NO ₃) ₄ ·3 DiAHexP	0.7906	-0.6682	-0.3313	-----	-0.4373	-0.3743	2.3042

In both uranyl complexes, the two dialkylalkyl phosphonate ligands are positioned *trans* to each other to minimize its steric repulsion (Figure 6B.8). In UO₂(NO₃)₂·2DiBiBP complex, the predicted U-O_{Ext} bond length is marginally longer (by 0.01 Å) than in the case of the UO₂(NO₃)₂·2DiAHexylP complex. This suggests a marginally stronger binding of DiAHexylP which is also reflected in longer U-O_{NO3} bonds in the UO₂(NO₃)₂·2DiAHexylP complex compared to UO₂(NO₃)₂·2DiBiBP on an average.

The binding free energies (ΔG) are computed using the following equations (6B.1) and (6B.2):

$$\Delta G = E[\text{UO}_2(\text{NO}_3)_2 \cdot 2\text{DiBiBP}] + 2E[\text{H}_2\text{O}] - E[\text{UO}_2(\text{NO}_3)_2 \cdot 2\text{H}_2\text{O}] + 2E[\text{DiBiBP}] \dots \dots \dots (6B.1)$$

$$\Delta G = E[\text{Th}(\text{NO}_3)_4 \cdot 3\text{DiBiBP}] + 3E[\text{H}_2\text{O}] - E[\text{Th}(\text{NO}_3)_4 \cdot 3\text{H}_2\text{O}] + 3E[\text{DiBiBP}] \dots \dots \dots (6B.2)$$

Positive and negative binding energies indicate an unfavourable and favourable complex formation, respectively (Table 6B.4). From the table it can be seen that the formation of all the four complexes are favourable. The complexation energy obtained for the

$\text{UO}_2(\text{NO}_3)_2 \cdot 2\text{DiAHexylP}$ complex is more negative than that obtained for the $\text{UO}_2(\text{NO}_3)_2 \cdot 2\text{DiBiBP}$ complex, strongly suggesting that the formation of the uranyl nitrate complex with DiAHexylP is preferred over DiBiBP. Similarly, in the case of the two thorium nitrate complexes, the complexation energy values point to a stronger $\text{Th}(\text{NO}_3)_4 \cdot 3\text{DiAHexylP}$ complex formation as opposed to the formation of the $\text{Th}(\text{NO}_3)_4 \cdot 3\text{DiBiBP}$ complex. Both the trends obtained, for uranium as well as thorium complexes are in good agreement with the trends in the distribution ratio found by solvent extraction.

Infrared spectra of the extractants DiBiBP, DiAHexylP and their complexes with U(VI) were recorded and the calculated spectra were found to be in good agreement (Figure 6B.9). The peaks corresponding to asymmetric U=O and P=O stretching are indicated. Both DiBiBP and DiAHexylP showed a red shift in the P=O stretching frequency on complexation with uranyl nitrate.

Table 6B.4: Computed binding affinities (ΔG , kcal mol⁻¹) for uranium and thorium complexes with DiBiBP and DiAHexylP using M06-2X.

Complex	ΔG
$\text{UO}_2(\text{NO}_3)_2 \cdot 2\text{DiBiBP}$	-7.06
$\text{UO}_2(\text{NO}_3)_2 \cdot 2\text{DiAHexylP}$	-11.65
$\text{Th}(\text{NO}_3)_4 \cdot 3\text{DiBiBP}$	-29.19
$\text{Th}(\text{NO}_3)_4 \cdot 3\text{DiAHexylP}$	-43.53

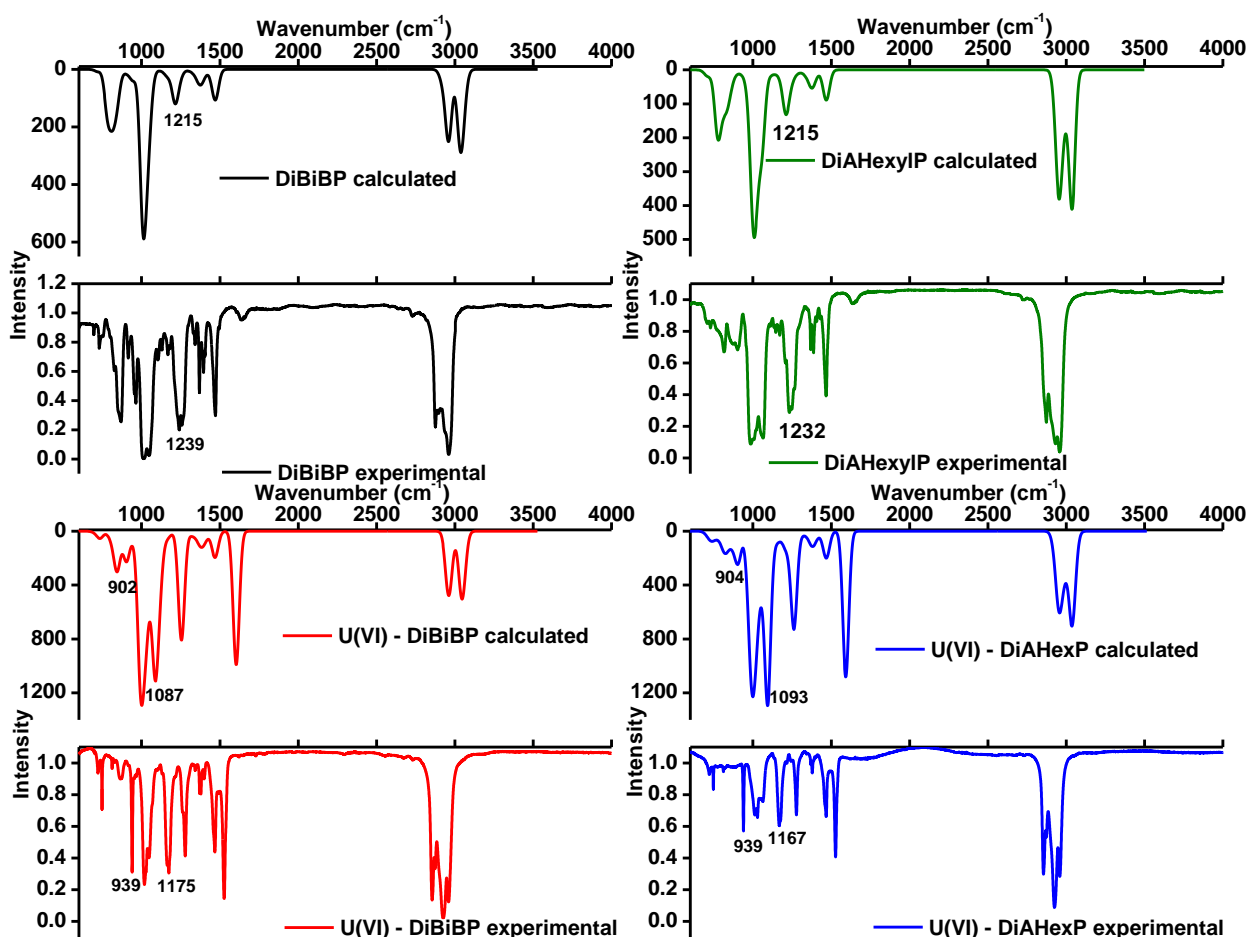


Figure 6B.9: Comparison of experimental and calculated spectra for the extractants DiBiBP, DiAHexylP and their complexes with U(VI).

6B.5 Conclusion

Phosphonates are an ideal class of organophosphorous extractants in which organic chain can be fine-tuned with ease to investigate their effects on extraction. The effects of carbon chain structure on the extraction behaviour of dialkylalkyl phosphonates have been systematically investigated by synthesizing symmetrical and unsymmetrical phosphonates with branched carbon chains. These ligands were employed in the extraction of actinide ions *viz.* U(VI), Th(IV), Pu(IV) and Am(IV). Actinide metal ions have been chosen in the present study as their specific complexation has numerous applications towards reprocessing and management of nuclear waste. It has been found that the chain length of alkyl chain has a significant effect on the distribution ratio of all four actinide ions; longer the carbon chain, higher the extraction. Extending the chain length by even a single carbon atom has visible

effects on the extraction. An increase in the inductive effect with increase in chain length increases the basicity of phosphoryl oxygen, thereby leading to higher extraction.

Additionally, quantum chemical studies have been carried out to probe the structure modulated effects on extraction behaviour obtained by solvent extraction. Electronic structure and complexation behaviour of these extractants with actinides revealed that indeed increasing the carbon chain length in this class of extractants enhances the binding of extractant to the metal ion; this was clearly reflected in the computed binding energies obtained for the complexes investigated in this work.



Chapter 7



“The two most important days in your life are the day you are born and the day you find out why”

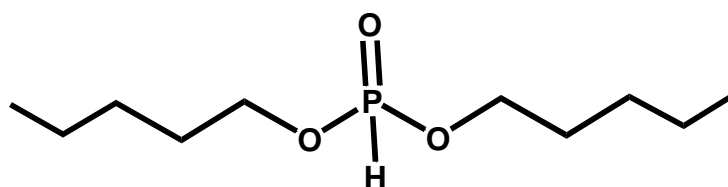
~ Mark Twain

DENSITY FUNCTIONAL THEORY AS A PREDICTIVE TOOL IN ACTINIDE CHEMISTRY

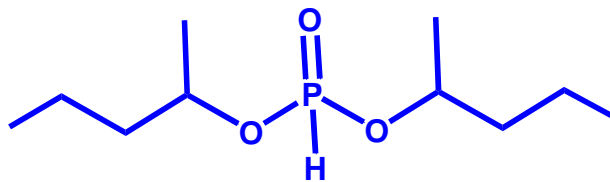
(A) THE INFLUENCE OF WEAK HYDROGEN BONDING ON THE EXTRACTION BEHAVIOUR OF H-PHOSPHONATES TOWARDS ACTINIDES

7A.1 Introduction

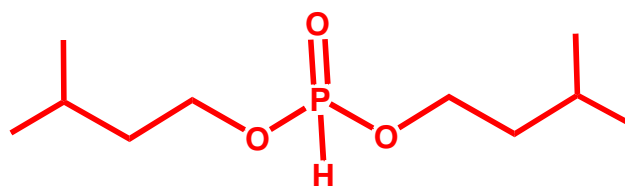
The structures and complexation abilities of Diamyl-H-phosphonate (DAHP) and Disecamyl-H-phosphonate (DsAHP) with uranyl nitrate have been investigated through DFT calculations. Theoretical calculations predict an unexpectedly higher stability for the uranyl-DsAHP complex compared to compositionally analogous uranyl-DAHP complex. The interactions leading to stabilisation of uranyl complex with the branched isomer have been examined. Calculations involving Diisoamyl-H-phosphonate (DiAHP) and its complexes have also been performed for comparison. Theoretical predictions have been further tested with experimental work. The ligands DAHP, DsAHP and Diisoamyl-H-phosphonate (DiAHP) (Scheme 7.A1) have been synthesised and solvent extraction experiments as a function of nitric acid concentration (0.01-8M) have been performed with uranyl nitrate. Interestingly, acid dependent extraction experiment revealed an anomaly of poor extraction in the lower acid region for the otherwise acidic DsAHP ligand. The causes for this behaviour have been probed by specific experiment and DFT that delve into the tautomeric extraction mechanism. In addition to U(VI), extraction experiments involving Pu(IV) and Th(IV) with the three H-phosphonates have also been performed. Solvent extraction behaviour of Am(III) has also been studied with all the three ligands.



Diamyl H phosphonate



Disecamyl H phosphonate



Diisoamyl H phosphonate

Scheme 7A.1: Structural representation of the three H-phosphonates synthesised and employed in the extraction studies.

7A.2 Theoretical insights and predictions

The optimized geometries of the $\text{UO}_2(\text{NO}_3)_2 \cdot 2\text{DAHP}$, $\text{UO}_2(\text{NO}_3)_2 \cdot 2\text{DiAHP}$ and $\text{UO}_2(\text{NO}_3)_2 \cdot 2\text{DsAHP}$ complexes are shown in (Figure 7A.1) and the relative energies with respect to the energy of the $\text{UO}_2(\text{NO}_3)_2 \cdot 2\text{DAHP}$ complex are given in Table 7A.1.

Table 7A.1: Solvent corrected relative energies of the uranyl nitrate complexes with DsAHP and DiAHP with respect to the energy of the $\text{UO}_2(\text{NO}_3)_2 \cdot 2\text{DAHP}$ complex by using different functionals

Complex	ΔG (kcal/mol) relative to $\text{UO}_2(\text{NO}_3)_2 \cdot 2\text{DAHP}$ complex		
	M06-2X	BP86-D3BJ	PBE0-D3BJ
$\text{UO}_2(\text{NO}_3)_2 \cdot 2\text{DsAHP}$	-14.23	-15.29	-13.68
$\text{UO}_2(\text{NO}_3)_2 \cdot 2\text{DiAHP}$	-1.01	-0.69	1.07

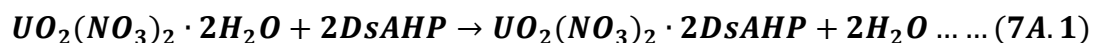
The structural analysis of bond lengths are listed (Table 7A.2). The composition of the metal ligand complex for this class of extractant has been established⁴². The two extractant molecules are positioned at opposite sides of the central atom so as to cause least steric repulsions. There is no significant difference in the $\text{U}=\text{O}$ or $\text{U}-\text{O}_{\text{NO}_3}$ bond lengths between

the two complexes; however the U–O_{Ext} bond is shorter by ~0.01 Å in the case of the UO₂(NO₃)₂·2DAHP complex.

Considering the energies of the two uranyl complexes alone, a strong lowering of energy has been observed with UO₂(NO₃)₂·2DsAHP in spite of both complexes possessing the same chemical composition. The solvent corrected energy of the UO₂(NO₃)₂·2DsAHP complex was lower than its counterpart by ~14 kcal/mol with the M06-2X functional. Here it may be noted that the performance of M06 and M06-2X types of functional is reasonably accurate in predicting the energetics such as redox potentials, binding energies, ionisation energies etc.^{193, 194}. Further observation on the structure led to finding that the CH···O_{NO3} intra-molecular interaction distances between the nitrate oxygen and the nearest α-hydrogen atoms were shorter in the UO₂(NO₃)₂·2DsAHP complex compared to the equivalent bonds in the UO₂(NO₃)₂·2DAHP complex by ~0.2 Å on an average. Among these, especially two of the CH···O_{NO3} intra-molecular distances in the UO₂(NO₃)₂·2DsAHP complex possessed bond lengths as short as 2.38 Å which is the order of the U–O_{Ext} covalent bond. These considerably short range intra-molecular interactions coupled with the marked stability of the UO₂(NO₃)₂·2DsAHP complex uncovered the possible existence of a weak intra-molecular hydrogen bond in the complex.

Apart from the energy difference between the UO₂(NO₃)₂·2DAHP and UO₂(NO₃)₂·2DsAHP complexes, the relative energy of the UO₂(NO₃)₂·2DiAHP complex with respect to the UO₂(NO₃)₂·2DAHP complex has also been calculated (Table 7A.1). The UO₂(NO₃)₂·2DsAHP complex is more stable compared to both UO₂(NO₃)₂·2DAHP and UO₂(NO₃)₂·2DiAHP complexes, which is clearly due to the presence of shorter CH···O hydrogen bonds in the UO₂(NO₃)₂·2DsAHP complex. Among other factors, relative strength of the weak –H bonding dictates the relative stability of the complexes. In addition to the M06-2X functional, where dispersion correction is implicit, explicit dispersion corrected

GGA and hybrid functionals, viz., BP86-D3BJ and PBE0-D3BJ for calculation of the relative energies in presence of solvent have been considered. The relative energies of the $UO_2(NO_3)_2 \cdot 2DsAHP$ and $UO_2(NO_3)_2 \cdot 2DiAHP$ with respect to the $UO_2(NO_3)_2 \cdot 2DAHP$ complexes are reported in the same Table 7A.1. It is interesting to note that the trend obtained by using the M06-2X functional is well reproduced with the dispersion corrected BP86-D3BJ and PBE0-D3BJ functionals. Subsequent to obtaining the optimized geometries, solvent corrected binding free energy of complexation for the uranyl complexes with DAHP and DsAHP have been calculated (Table 7A.2). The chemical reaction corresponding to the complexation/binding energy calculation is (Equation 7A.1):



Hence the equation derived for the calculation of the binding free energy is as follows (Equation 7A.2):

$$B.E \text{ for } UO_2(NO_3)_2 \cdot 2DsAHP = \Delta G_{solv}[(UO_2(NO_3)_2 \cdot 2DsAHP)] + 2\Delta G_{solv}[H_2O] - \Delta G_{solv}[(UO_2(NO_3)_2 \cdot 2H_2O)] - 2\Delta G_{solv}[DsAHP] \dots \dots (7A.2)$$

DFT predicts that the $UO_2(NO_3)_2 \cdot 2DsAHP$ complex has a higher complexation energy compared to the $UO_2(NO_3)_2 \cdot 2DAHP$ and the $UO_2(NO_3)_2 \cdot 2DiAHP$ complexes at the M06-2X level of theory.

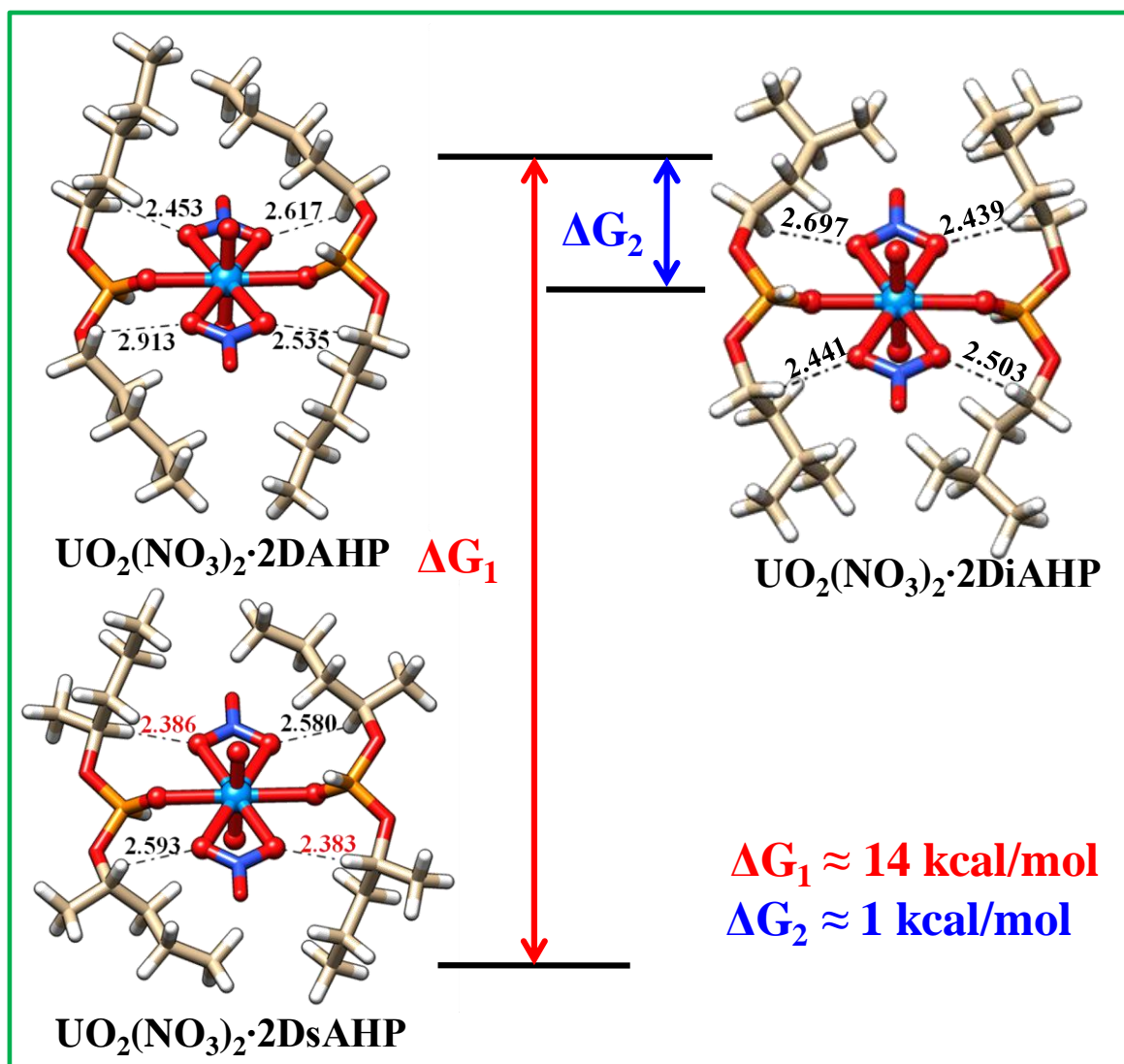


Figure 7A.1: Optimized structures of DAHP and DsAHP bound with uranyl nitrate. The energy schematic represents the stability of the $\text{UO}_2(\text{NO}_3)_2 \cdot 2\text{DsAHP}$ and $\text{UO}_2(\text{NO}_3)_2 \cdot 2\text{DiAHP}$ complex compared with the uranyl nitrate complex formed by the linear chain isomer DAHP.

Table 7A.2: Solvent corrected binding free energies (kcal mol^{-1}) using M06-2X functional and computed structural parameters (\AA) of uranyl nitrate complexes with the keto tautomer of DAHP, DsAHP and DiAHP.

Complex	$\text{UO}_2(\text{NO}_3)_2 \cdot 2\text{DAHP}$	$\text{UO}_2(\text{NO}_3)_2 \cdot 2\text{DsAHP}$	$\text{UO}_2(\text{NO}_3)_2 \cdot 2\text{DiAHP}$
Bonds	Bond lengths (\AA)		
U=O _{v1}	1.803–1.806	1.805	1.804–1.808
U–O _{Ext}	2.377–2.390	2.392	2.383
U–O _{NO3}	2.512–2.530	2.511–2.531	2.504–2.528
Binding free energy	-9.22	-13.41	-10.45

Apart from this, two types of DFT functionals with dispersion corrections incorporated (GGA type BP86-D3-BJ functional and hybrid type PBE0-D3-BJ functional) are used and the binding free energies are compared in Table 7A.3. It is to note that the binding free energy trend obtained by using the M06-2X functional, where the $\text{UO}_2(\text{NO}_3)_2 \cdot 2\text{DsAHP}$ complex is associated with a higher complexation energy, is reproduced in both BP86-D3-BJ and PBE0-D3-BJ functionals, though the absolute values of binding free energies are different from one functional to another.

Table 7A.3: Solvent corrected binding free energies (kcal mol^{-1}) using M06-2X and DFT-D3 functionals BP86 and the hybrid PBE0 functional of uranyl nitrate complexes with DAHP and DsAHP.

Complex	Binding free energy (kcal/mol)		
	M06-2X	BP86-D3BJ	PBE0-D3BJ
$\text{UO}_2(\text{NO}_3)_2 \cdot 2\text{DAHP}$	-9.22	-27.78	-16.18
$\text{UO}_2(\text{NO}_3)_2 \cdot 2\text{DsAHP}$	-13.41	-30.41	-19.03

To confirm the higher stability of the $\text{UO}_2(\text{NO}_3)_2 \cdot 2\text{DsAHP}$ complex, atoms-in-molecule (AIM) model developed by Bader^{265, 266} has been used to calculate electron density based parameters at the bond critical point (BCP). For this purpose, the electron density [ρ] and the Laplacian of the electron density [$\nabla^2\rho$] at the BCP for the identified $\text{CH}\cdots\text{O}$ hydrogen bonds have been calculated and the results have been reported in Table 7A.4. A small positive value of $\nabla^2\rho$ at the BCPs corresponding to the $\text{CH}\cdots\text{O}$ BCP clearly indicates the existence of weak intermolecular interaction of “closed-shell” in nature, *viz.*, hydrogen bond. The local energy density $E_d(\mathbf{r})$, which is defined as $E_d(\mathbf{r}) = G(\mathbf{r}) + V(\mathbf{r})$, is considered to determine the nature of a chemical bond. Here $G(\mathbf{r})$ and $V(\mathbf{r})$ denote the local kinetic energy and potential energy densities, respectively^{267, 268}. A positive value of local energy density at the BCPs implies that the nature of bonding is either ionic or vdW type denoting a “closed-shell” interaction, which is consistent with the trend in the variation of $\nabla^2\rho$ at the BCPs. Now it is interesting to

compare the ρ and $\nabla^2\rho$ values at the BCPs. From the reported values, it is evident that the CH...O hydrogen bonds in the $\text{UO}_2(\text{NO}_3)_2 \cdot 2\text{DsAHP}$ complex are associated with slightly larger electron density values (at BCPs) compared to that in the $\text{UO}_2(\text{NO}_3)_2 \cdot 2\text{DAHP}$ complex. Moreover, no BCP has been found for one of the hydrogen bonds in the $\text{UO}_2(\text{NO}_3)_2 \cdot 2\text{DAHP}$ complex with a bond distance of 2.913 Å. These trends are consistent not only with the corresponding smaller CH...O bond distances in the $\text{UO}_2(\text{NO}_3)_2 \cdot 2\text{DsAHP}$ complex, but also from the energy difference between the two complexes (Figure 7A.1) and the calculated complexation free energy values (Table 7A.2). All these evidences clearly indicate that the stability of the $\text{UO}_2(\text{NO}_3)_2 \cdot 2\text{DsAHP}$ complex over its compositionally equivalent counterpart.

Table 7A.4: Calculated Values of Bond Critical Point Electron Density (ρ in $e a_0^{-3}$), Laplacian of Electron Density ($\nabla^2\rho$ in $e a_0^{-5}$), and Local Electron Energy Density (E_d in au), in au) of $\text{UO}_2(\text{NO}_3)_2 \cdot 2\text{DAHP}$ and $\text{UO}_2(\text{NO}_3)_2 \cdot 2\text{DsAHP}$ as obtained by using BP86 functional.

Systems	R(H...O)	Bond	ρ	$\nabla^2\rho$	G(r)	V(r)	$E_d(\mathbf{r})$
$\text{UO}_2(\text{NO}_3)_2 \cdot 2\text{DAHP}$	2.453	CH...O _{NO3}	0.0108	0.036	0.0084	-0.008	0.0006
	2.535	CH...O _{NO3}	0.0095	0.033	0.0076	-0.007	0.0008
	2.617	CH...O _{NO3}	0.0069	0.026	0.0057	-0.005	0.0009
	2.913	CH...O _{NO3}
$\text{UO}_2(\text{NO}_3)_2 \cdot 2\text{DsAHP}$	2.383	CH...O _{NO3}	0.0126	0.041	0.0097	-0.009	0.0004
	2.386	CH...O _{NO3}	0.0125	0.040	0.0096	-0.009	0.0004
	2.580	CH...O _{NO3}	0.0073	0.027	0.0060	-0.005	0.0008
	2.592	CH...O _{NO3}	0.0072	0.027	0.0059	-0.005	0.0008

Further to calculations, experimental studies were taken-up to support the findings. In this connection, extraction of uranyl nitrate from nitric acid media has been experimentally carried out by DAHP, DsAHP and in addition another branched isomer, DiAHP.

7A.3 Physicochemical properties of amyl H–phosphonates

Prior to the extraction studies, the synthesised H-phosphonates have been evaluated for their physico-chemical properties viz. density, viscosity and aqueous solubility. Density of the three H–phosphonates DAHP, DiAHP and DsAHP (Table 7A.5) decreases with the introduction of a methyl branch. Branching in the carbon chain reduces the packing efficiency thereby a reduction in density. Viscosity measurements have been made for DAHP, DiAHP and DsAHP (Figure 7A.2) and the activation barrier to flow have been calculated from the slope of logarithm of viscosity vs. $1/T$ graph. The viscosity of the solvent governs the mass transfer, and the activation barrier to fluid flow (E_a) affects phase disengagement time during the solvent extraction process. E_a for DiAHP is less than that of DAHP which is in turn less than for DAHP. Branching causes less scope for the intermolecular dispersive forces to act. Moreover branching near the polar phosphoryl group as in the case of DsAHP has more marked effects and shows a considerable reduction in E_a . The aqueous solubility of the H-phosphonates is most for DsAHP and least for the linear chain isomer DAHP. The solubility in water is higher for the branched compounds and more so if the branching is closer to the polar phosphoryl group. The branching in the carbon chains reduces the packing thereby reducing the effective surface area for intermolecular interactions between the extractant molecules and increasing the possibility of water-extractant interactions.

Table 7A.5: Density (g/mL), viscosity (cP) at 31°C, activation energy (kJ/mol) and aqueous solubility (g/L) at 298K of the H–phosphonates.

Extractant	Density	Viscosity	Activation Energy (E_a)	Aqueous solubility
DAHP	0.958	3.30	13.58	10.78
DiAHP	0.947	2.01	13.36	15.14
DsAHP	0.944	1.37	8.75	17.54

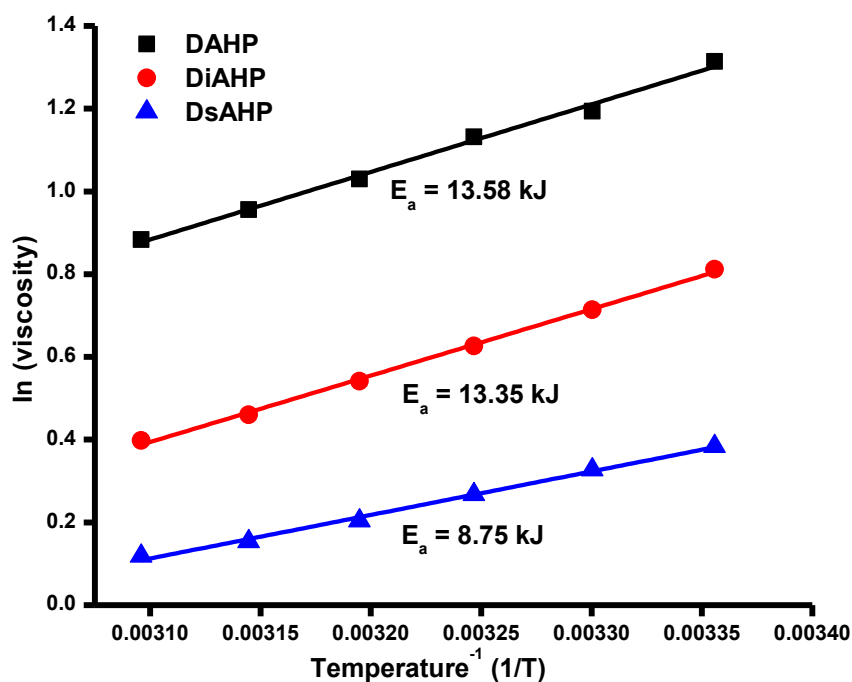


Figure 7A.2: Logarithm of viscosity against $1/T$ for the three H-phosphonates, DAHP, DiAHP and DsAHP. The activation energies are calculated from the slopes.

7A.4 Extraction of uranyl nitrate from nitric acid medium

The extraction of U(VI) as a function of nitric acid concentration, by 1.1M DAHP, DiAHP and DsAHP in n-dodecane are shown in Figure 7A.3. The H-phosphonate class of extractants are classified as acidic extractants due to the ion-exchange between the metal ion and H^+ ion occurring at lower acidities. The extractants DAHP and DiAHP behave as acidic extractants and show higher D values in the lower acid region ($\sim 0.01M$) as expected for these types of extractants. However, surprisingly DsAHP mainly shows neutral extractant characteristics, and has an extraction profile similar to the well known neutral, phosphate extractant TBP, which is also plotted for comparison. The extraction by DsAHP is marginally higher than that of TBP due to the greater basicity of the phosphoryl oxygen in the phosphonate class of extractants compared to phosphates. In the case of DsAHP, poor distribution ratios are estimated at lower acid concentrations, whereas highest D values are measured for acidities ranging from 4 to 6M. To understand this extraction behaviour in greater depth, it is useful to turn to the mechanism of extraction by H-phosphonates (Scheme 6A.1).

At lower acidities, the phosphoryl group tautomerises in such a way that the P=O functional group is converted to a P-O-H group in a *keto-enol* like tautomerisation. Hence, at lower acidities the extraction of the positive metal ions is enabled via H^+ exchange in what is called as an ion-exchange mechanism. At higher acidities, H-phosphonates extract through the formation of a P=O–M coordinate bond, which is known as the solvation mechanism. Therefore it is important to obtain the distribution ratios as a function of nitric acid concentration.

On examining the trend in the D values at higher acidities, it can be seen that DsAHP has higher extraction than DAHP, validating the predictions made by DFT on the complexation energies. One of the reasons for this trend is possibly the remarkable stability of the uranyl nitrate complex with DsAHP. Another reason could be the inductive effect introduced by the branching near the phosphoryl group in the DsAHP extractant. This methyl group can contribute to increasing the basicity of the phosphoryl oxygen and hence the D value. The branching in DiAHP is further away from the phosphoryl binding site and this effect is less pronounced.

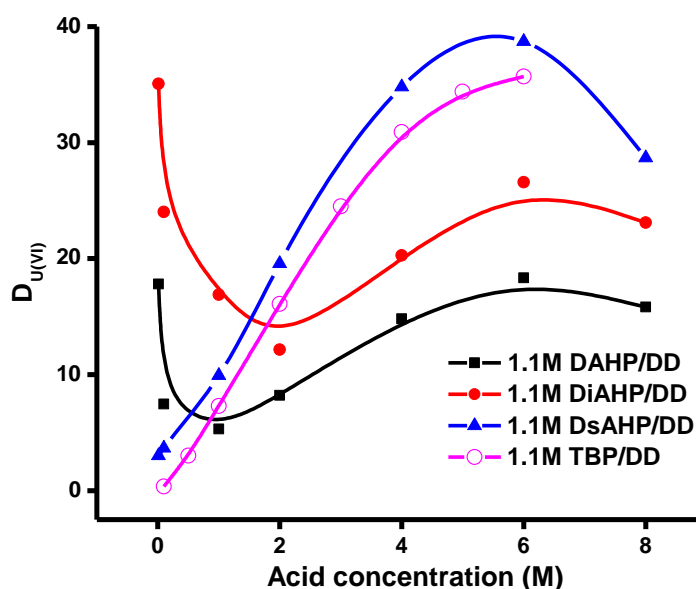


Figure 7A.3: Variation in D values as a function of HNO_3 concentration in the extraction of U(VI) by 1.1M solutions of amyl H-phosphonates in n-dodecane. The extraction of U(VI) by 1.1M TBP/DD is also shown.

The calculated infrared spectra of uranyl nitrate complexes with DAHP and DsAHP are compared with the experimentally recorded spectra for each compound (Figure 7A.4). The spectra for the bare ligands are also shown. The peaks corresponding to the P=O stretching frequencies ($\sim 1200\text{ cm}^{-1}$) are indicated in the insets and the U=O ($\sim 900\text{ cm}^{-1}$) stretching is also shown for the complexes. In the case of both DAHP and DsAHP complexes, there is a red shift in the P=O stretching frequency in comparison with the bare ligands in both the experimental as well as calculated spectra.

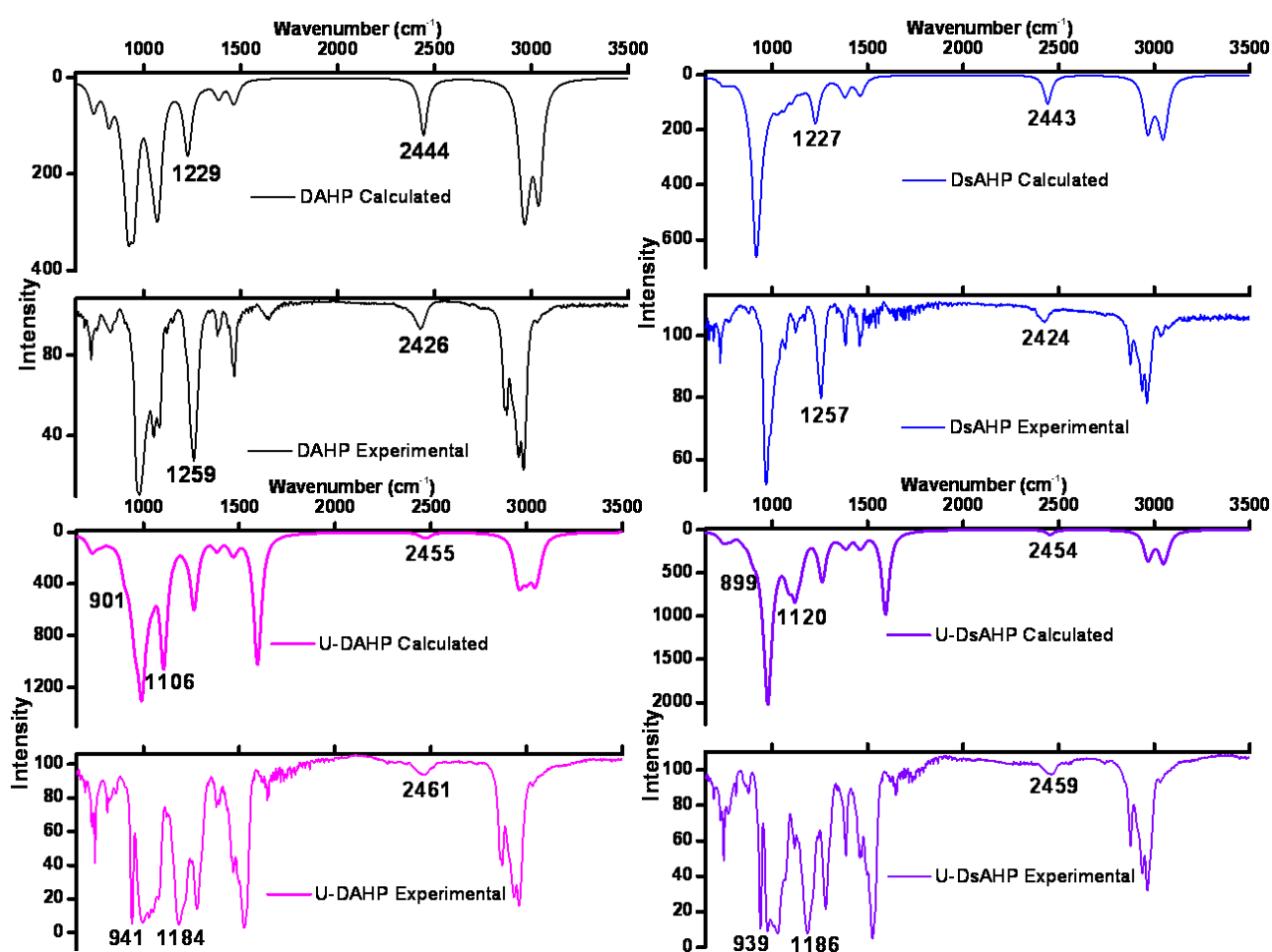


Figure 7A.4: Calculated IR spectra for the uranyl nitrate complexes of DAHP and DsAHP and the bare ligands. The calculated spectra are compared with those experimentally measured for each compound. The frequencies marked are the U=O asymmetric stretch, P=O stretch and P-H stretch.

Apart from the extraction behaviour at higher acidities where the experimental observations matched those predicted by computation, one cannot help but notice the poor extraction shown by DsAHP at lower acidity. The extraction mechanism here is ion-exchange in which the enol tautomer is responsible for the extraction of the metal ion. Therefore it could be that the enol tautomer is formed in lower quantities in the case of DsAHP.

This claim was put to test by an insightful experiment⁴², which estimates the percentage of enol tautomer formed in the case of each or the three extractants when contacted with aqueous medium at lower acidities. The results of these experiments are reported (Table 7A.6). The highest percentage of *enol* tautomer is formed in the case of DiAHP, followed by DAHP. The least enol formed is by DsAHP as reflected in the trend in D values observed for uranium extraction.

Table 7A.6: The percentage of *enol* tautomer formed for DAHP, DiAHP and DsAHP based on titration of NaOH before and after extraction.

Extractant	[NaOH] _{aq} (M) (Before extraction)	[NaOH] _{aq} (M) (After extraction)	[NaOH] _{org} (M)	Enol tautomer formed
DAHP	1.553	1.102	0.451	41%
DiAHP	1.553	0.915	0.638	58%
DsAHP	1.553	1.269	0.284	26%

7A.5 Extraction of Th(IV) and Pu(IV) from nitric acid medium

In addition to U(VI), other actinides viz. Th(IV), Pu(IV) have also been examined for their extraction behaviour with the H-phosphonates. The D values obtained as a function of nitric acid concentration are shown for Pu(IV) and Th(IV) (Figure 7A.5). The tetravalent metal ion Pu(IV) shows much higher D values than uranyl nitrate in the lower acid region (0.01M). This is because the enolic form of the extractant is anionic in nature and has much stronger coulombic interactions with the tetravalent metal centre than the UO₂²⁺ species, where the effective positive charge is less. Interestingly, the enol population (Table 7A.6) shows a proportionality to the extraction of Pu(IV) at lower acidities (0.01M). Even in the higher

acidity regions, Pu(IV) is extracted with higher D than U(VI) (Figure 7A.5B). Phosphates and dialkylalkyl phosphonates show a marginally higher extraction of U(VI) than the extraction of Pu(IV)^{41, 258}. On the other hand, in the case of H-phosphonates, Pu(IV) is extracted with significantly higher D values than U(VI). Th(IV) also shows higher extraction by H-phosphonates compared to phosphates and dialkylalkyl phosphonates^{23, 50}. In general the tendency of H-phosphonates to extract tetravalent metal ion with higher D values can be attributed to the acidic P-H hydrogen that can increase the charge on the phosphoryl oxygen by electron donation.

In the case of both Th(IV) and Pu(IV), DiAHP extracts with higher D than DAHP which in turn is higher than DsAHP. At higher concentrations of nitric acid (4-6M), DsAHP extracts Th(IV) and Pu(IV) less compared to DAHP. This is unlike the trend observed in the case of U(VI) extraction. The reason for poorer extraction by DsAHP in the case of the tetravalent ions can be attributed to steric factors associated with the metal nitrate. For charge neutrality, the tetravalent Pu(IV) and Th(IV) are bound to four bidentate nitrate groups making the metal core region sterically hindered. The secondary methyl branching in the DsAHP isomer is more prone to steric hindrances as the branching is close to the phosphoryl binding site. A recent study from our laboratory on the phosphate class of compounds shows a similar effect of the secondary branched carbon chain in the extraction of Th(IV)²³. Tri-sec-butyl phosphate (TsBP) showed drastically lower extraction of Th(IV) compared to TBP, whereas TsBP extracted U(VI) with higher D values than did TBP. For all the metal ions, DsAHP shows the least D value at lower acidities consistent with the observations that the percentage of the enol tautomer is the least among the three extractants investigated.

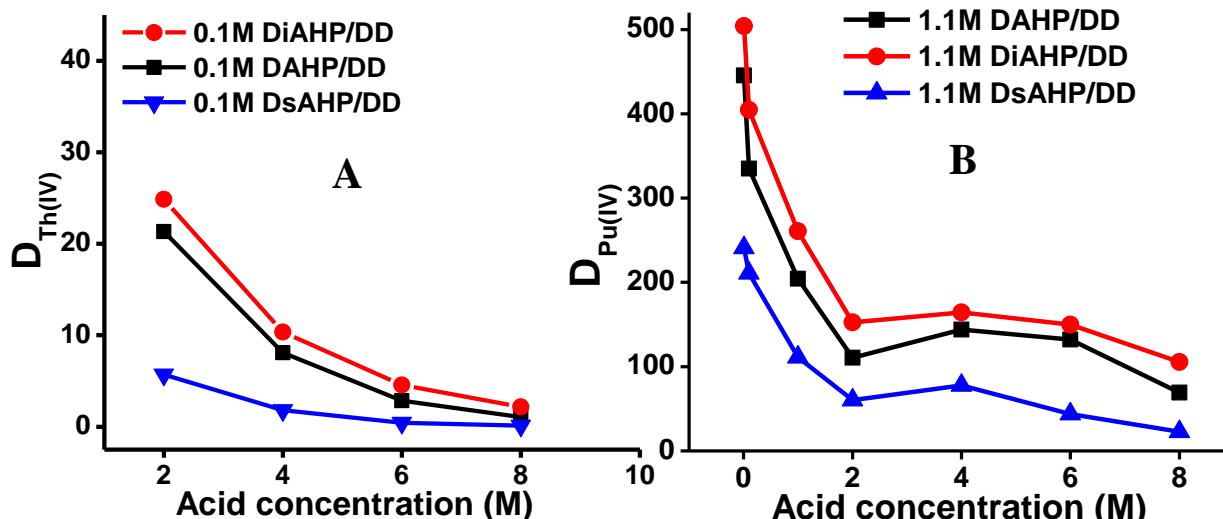


Figure 7A.5: Variation in D values as a function of HNO₃ concentration in the extraction of (A) Th(IV) by 0.1M solutions of amyl H- phosphonates in n-dodecane and (B) Pu(IV) by 1.1M solutions of amyl H- phosphonates in n-dodecane

Electrospray ionisation mass spectrometry (ESI-MS) which characterises the composition of the complexes of larger molecular mass has been carried out. The spectra have been recorded for a ligand and metal complexes using methanol as the solvent. The spectra for the extractant (Figure 7A.6), uranyl complex (Figure 7A.7) and thorium nitrate complex (Figure 7A.8) are shown. In the ESI-MS spectra, the free extractant's protonated molecular peak is seen at m/z 223 (M.W. for extractant = 222). In addition, the protonated dimer peak is also seen at m/z 445. Further, sodium bound and methanol bound peaks are also seen and marked in Figure 7A.6. The uranyl nitrate complex (M.W = 838) has also been characterised and the protonated peak at m/z 839 is present along with higher m/z peaks; the stoichiometry of the complex is thus UO₂(NO₃)₂·2L. The ESI-MS of the Th(NO₃)₄·3L (M.W = 1146) has also been obtained and showed protonated (+1), CH₃⁺ (+15) and sodium (+23), bound mass peaks. Several higher mass peaks are also present due to the tendency to form cluster in the gas phase and have been assigned in Figure 7A.8.

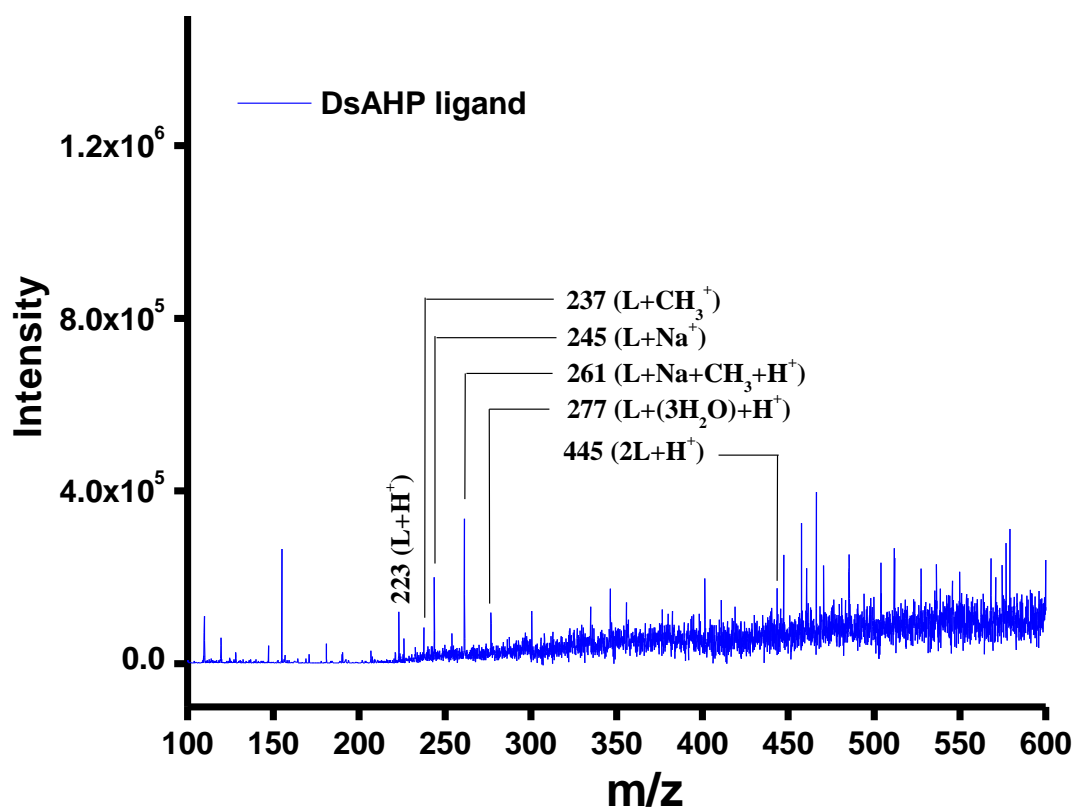


Figure 7A.6: ESI-MS spectra for the DsAHP bare ligand denoted as (L). The peaks corresponding to the relevant m/z are assigned.

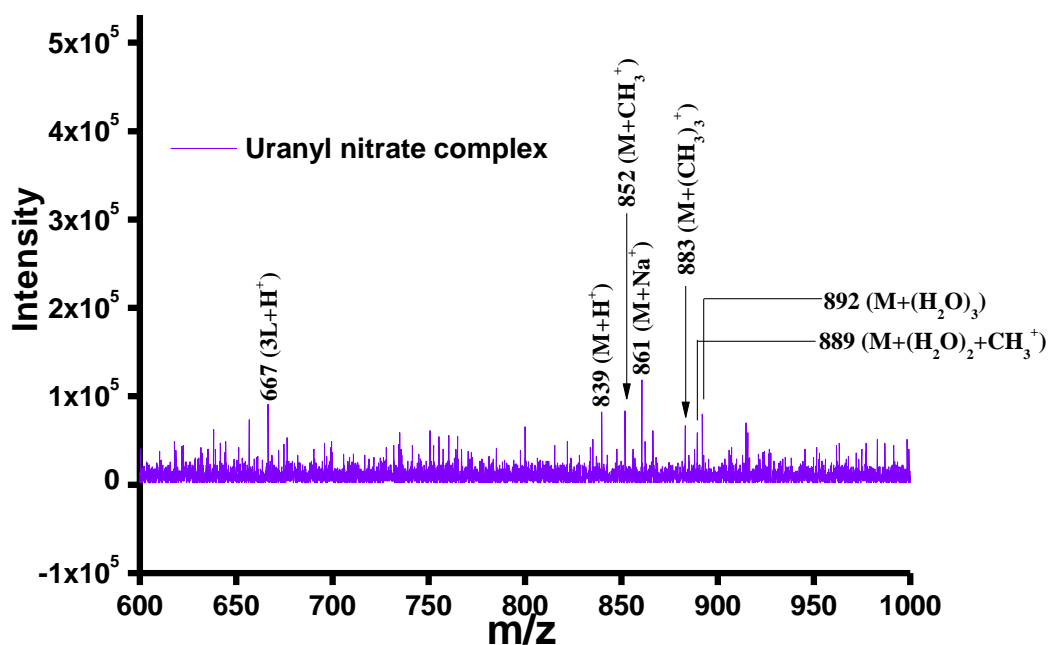


Figure 7A.7: ESI-MS spectra for the DsAHP bound uranyl nitrate complex denoted as (M). The peaks corresponding to the relevant m/z are assigned.

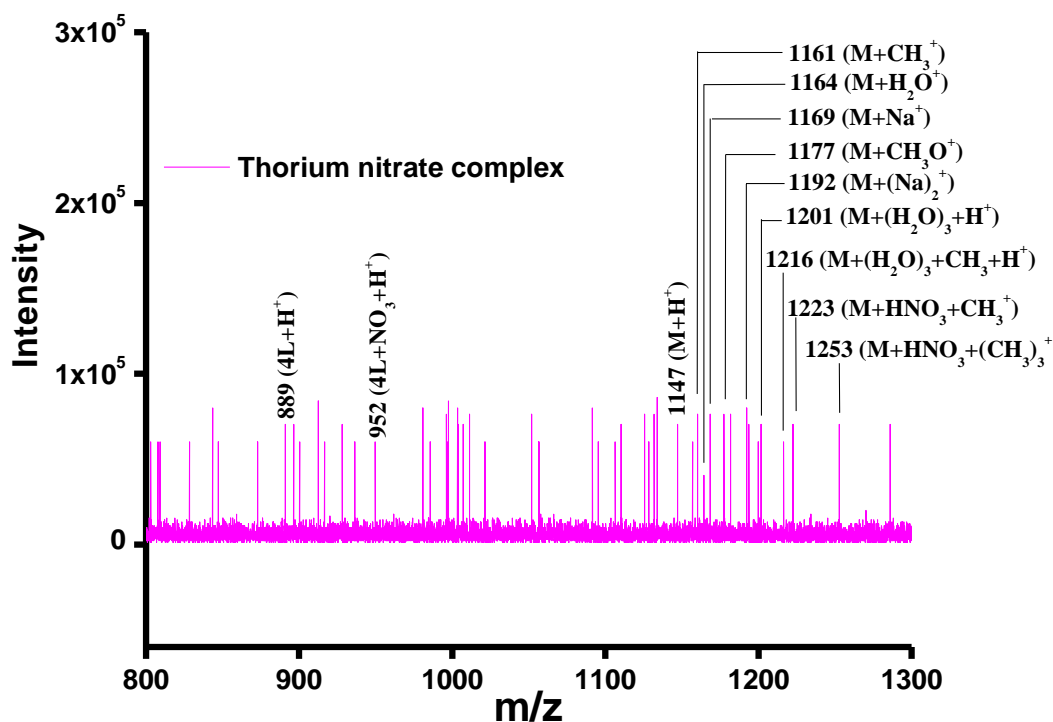


Figure 7A.8: ESI-MS spectra for the DsAHP bound thorium nitrate complex denoted as (M). The peaks corresponding to the relevant m/z are assigned.

7A.6 Extraction of Am(III) and theoretical studies

U(VI), Th(IV) and Pu(IV) are extracted effectively by the H-phosphonates, whereas Am(III) shows very low extraction with all the three extractants investigated (Figure 7A.9). The maximum extraction is shown by DiAHP in the enol form (i.e. acidity $\sim 0.01\text{M}$), followed by DAHP and DsAHP. This might be due to the formation of more enol tautomer in the case of DiAHP. DAHP and DsAHP showed poorer extraction of Am(III) in the higher acidities ($>2\text{M}$).

A theoretical study on the extraction of Am(III) has been carried out in order to explore the possible structures and binding energies. As all the three extractants have shown lower D values (< 0.1) in the keto form (i.e. acidities $> 1\text{M}$), the Am-DAHP complex has been investigated in the keto form. The Am(III) cation when extracted from nitric acid medium binds to three extractant molecules of the organophosphonate class of compounds[37]. The Am(III) cation is nine-coordinate with three bidentate nitrate groups and three extractant molecules (Figure 7A.10). The M-O_{NO_3} bond distances are in the range $2.486\text{--}2.570 \text{ \AA}$ and

the $M-O_{Ext}$ bond distances are in the range 2.420–2.452 Å. The binding free energy associated with complex formation has been calculated as 149.77 kcal/mol. The positive value of binding energy suggests the unfavourable formation of the Am(III) complex. This is in agreement with the experimentally observed D values.

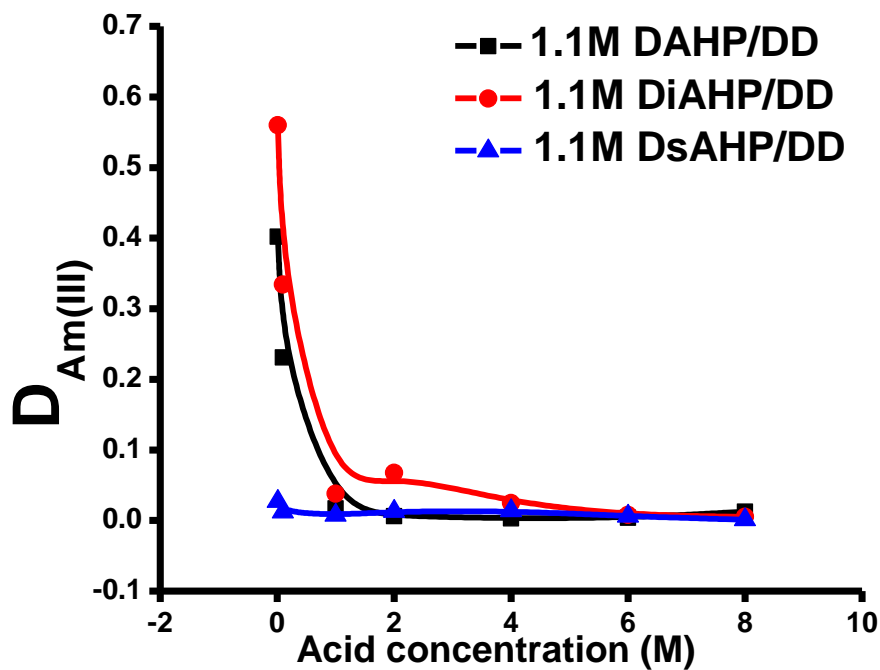


Figure 7A.9: Variation in D values as a function of HNO_3 concentration in the extraction of Am(III) by 1.1M solutions of amyl H- phosphonates in n-dodecane.

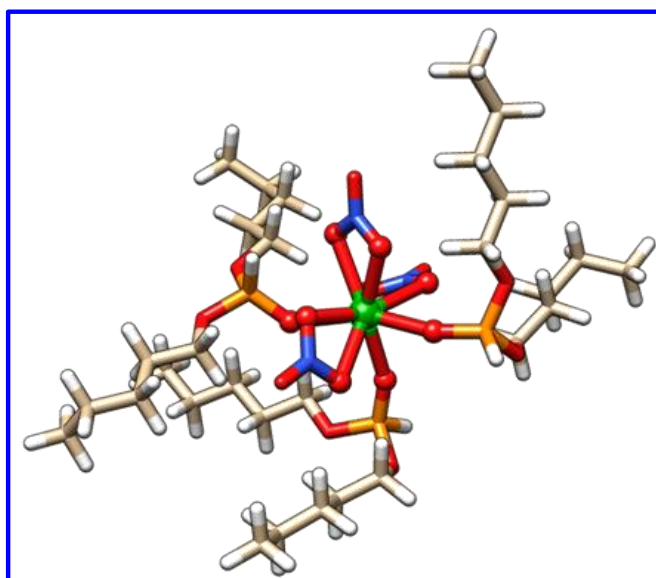


Figure 7A.10: The optimized structure for the $Am(NO_3)_3 \cdot 3DAHP$ complex

7A.7 Keto-enol tautomerisation of amyl H-phosphonates

Apart from the experiments, the bare ligands DAHP, DiAHP and DsAHP have been optimized by DFT and examined for their geometry (Figure 7A.11). The distance between the phosphoryl oxygen atoms in each ligand and the nearest hydrogen are indicated in the figure. The interaction distances between P=O and α -hydrogens are marginally increased for both the ligands in the presence of solvent. This might be because the interaction with the solvent reduces the extent of the intra-molecular interaction. The average CH \cdots O hydrogen-bond distance is the largest for DiAHP, followed by DAHP and the least for DsAHP. In the case of DsAHP ligand the α -hydrogens are closer to the oxygen atom; one of them being as near as 2.373Å. The phosphoryl oxygen is engaged in this interaction and is hence less available for the enol tautomerisation in the case of DsAHP. Accordingly, the percentage of enol tautomer is the least for the DsAHP and the most for the DiAHP. All these trends are consistent with the experimentally determined percentage of enol tautomers as reported in Table 7A.6.

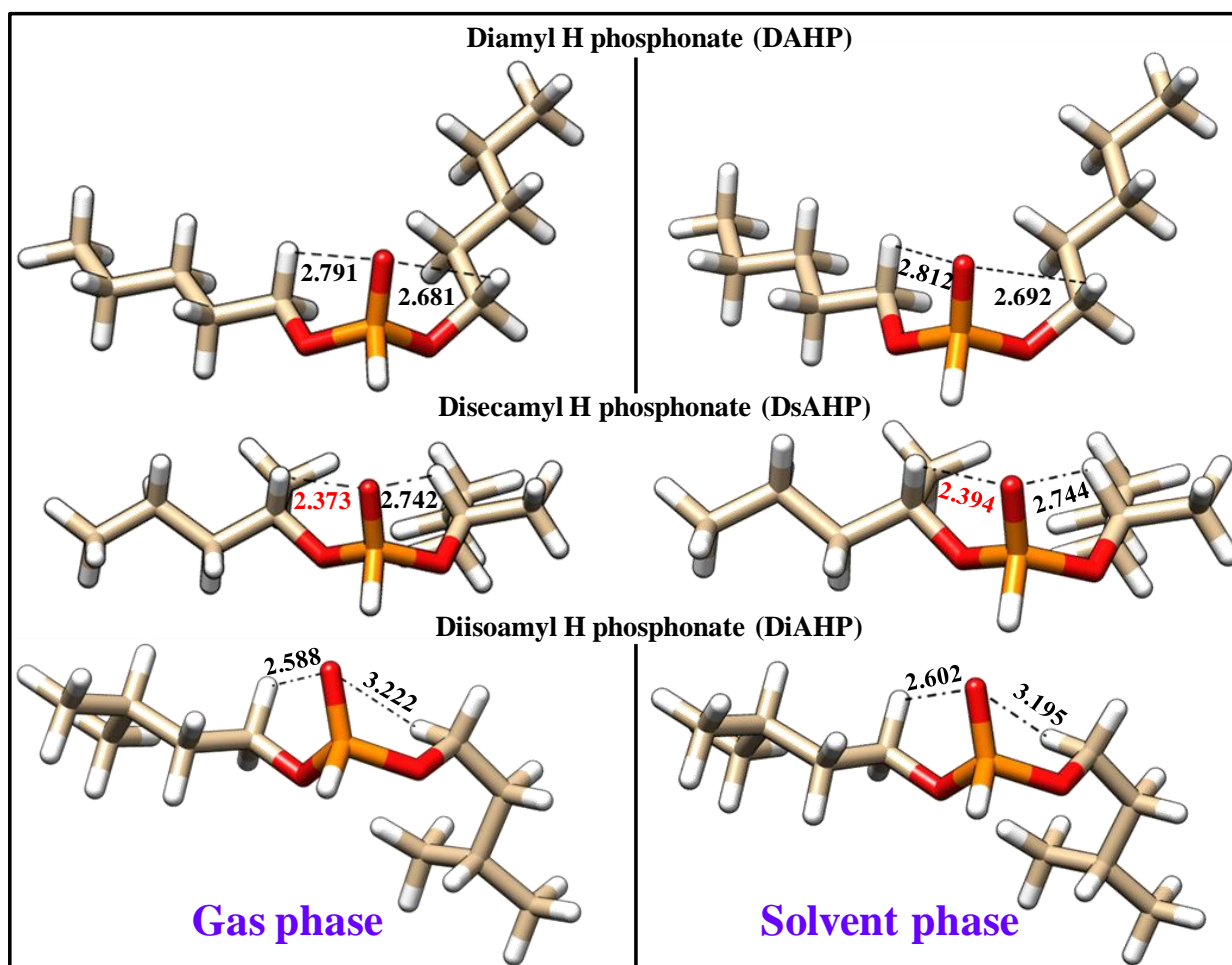


Figure 7A.11: Optimized structures (gas phase and solvent phase) of DAHP, DsAHP and DiAHP bare ligands in. The marked CH...O hydrogen-bond distances between the phosphoryl oxygen and the α -hydrogen atoms are indicated.

The binding free energy for the uranyl complexes formed with the keto tautomers of the two ligands has been established and successfully predicts the distribution ratios in the higher acid region. However, the enol tautomer of the H-phosphonates form complexes through the cation exchange mechanism and extract the UO_2^{2+} cationic species to the organic phase. The optimized geometries (Figure 7A.12) and the structural parameters (Table 7A.7) are shown. In the enol form, oxygen ($\sim 2.3 \text{ \AA}$) and phosphorus ($\sim 2.8 \text{ \AA}$) bind to the metal centre in an asymmetric arrangement due to difference in covalent radii of oxygen (66 pm)²⁶⁴ and phosphorous (107 pm)²⁶³. Binding free energies of complexation for the enol form of the extractants are shown in Table 7A.7. The columbic nature of the metal-ligand interaction is

reflected in the magnitude of complexation energies in the enol form. These values are significantly higher than those in the keto form. The anionic enol tautomer of the H-phosphonate interacts with the cationic UO_2^{2+} species. Moreover, the complexation energies of DAHP, DiAHP and DsAHP in the enolic complexes are similar as the effects of branching are not prominent in the charge controlled complexation. Despite the lower tendency of DsAHP to form the enol tautomer, the complexation energies are similar as the computational study does not account for the proportion of enol tautomer formed in each extractant in the employed experimental conditions.

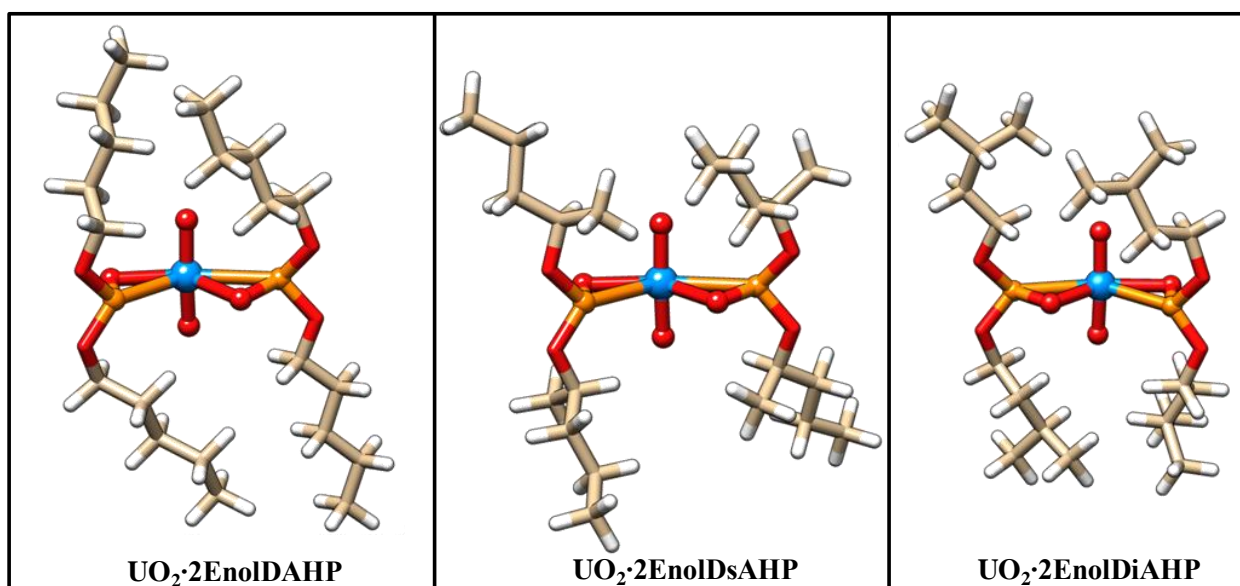


Figure 7A.12: Optimized structures of $\text{UO}_2 \cdot 2\text{EnolDAHP}$, $\text{UO}_2 \cdot 2\text{EnolDsAHP}$ and $\text{UO}_2 \cdot 2\text{EnolDiAHP}$ complexes.

Table 7A.7: Solvent corrected binding free energies (kcal mol^{-1}) using M06-2X functional and computed structural parameters (\AA) of uranyl nitrate complexes with the enol tautomers of DAHP and DsAHP and DiAHP.

Complex	$\text{UO}_2 \cdot 2\text{EnolDAHP}$	$\text{UO}_2 \cdot 2\text{EnolDsAHP}$	$\text{UO}_2 \cdot 2\text{EnolDiAHP}$
Bonds	Bond lengths (\AA)		
$\text{U}=\text{O}_{\text{yl}}$	1.810–1.813	1.812–1.815	1.812
$\text{U}-\text{O}_{\text{Ext}}$	2.248–2.290	2.242–2.293	2.245–2.291
$\text{U}-\text{P}_{\text{Ext}}$	2.772–2.855	2.773–2.864	2.776–2.858
Binding free energy	-30.41	-30.55	-30.63

7A.8 Conclusion

Uranyl nitrate complexes of DAHP and DsAHP have been quantum chemically investigated in the framework of DFT. On comparing the energies of two optimized complexes possessing the same chemical composition, the unexpected stability of $\text{UO}_2(\text{NO}_3)_2 \cdot 2\text{DsAHP}$ complex by 14 kcal/mol was discovered. Delving deeper into the intra-molecular interactions revealed weak $\text{CH} \cdots \text{O}$ hydrogen bonds in both $\text{UO}_2(\text{NO}_3)_2 \cdot 2\text{DAHP}$ and $\text{UO}_2(\text{NO}_3)_2 \cdot 2\text{DsAHP}$ complexes. Comparatively stronger such bonds in the $\text{UO}_2(\text{NO}_3)_2 \cdot 2\text{DsAHP}$ complex could be one of the important factors for its remarkable stability over the other complex with the linear chain isomer. Further, complexation energy of both the uranyl nitrate complexes which predicted formation of DsAHP complex to be more favourable than the DAHP complex was computed. Calculations involving Diisoamyl-H-phosphonate (DiAHP) and its complexes have also been performed for the comparison.

Theoretical predictions were tested by carrying out extraction of uranyl nitrate with DAHP, DsAHP and DiAHP experimentally. The experiments confirmed superior extraction by DsAHP as predicted by DFT through solvation mechanism at 4-6M. However, surprisingly DsAHP showed lower extraction in the lower acid region. This behaviour is unexpected for the H-phosphonate class of extractants which extract by forming the enol tautomer at lower acidities. This anomaly was further examined by experiments as well as DFT, through which it was discovered that formation of enol tautomer in DsAHP ligand is limited by the phosphoryl group which is engaged in interactions with the α -hydrogen, making it less available for the enol tautomerisation. Lower extraction by the enol form has also been experimentally observed in the extraction of Pu(IV) and Th(IV) ions in addition to U(VI) extraction. Uranyl nitrate complexes with the enol tautomer of DAHP, DiAHP and DsAHP have also been optimized and the computed binding free energies reflected the columbic nature of interactions compared to complexes with the keto tautomer. The complexation

energy of Am(III) has also been theoretically computed and yielded a positive value. This suggested an unfavourable extraction of Am(III), which was also established from the experimental studies.

DENSITY FUNCTIONAL THEORY AS A PREDICTIVE TOOL IN ACTINIDE CHEMISTRY

(B) COMPLEXATION BEHAVIOUR OF TRANSPLUTONIUM ACTINIDES

7B.1 Introduction

In the present study, Am^{3+} , Cm^{3+} , Bk^{3+} and Cf^{3+} complexes with ligands suited for minor actinide partitioning have been evaluated for their geometry, structure and interaction energy to understand various chemical interactions that exist in the metal-ligand bonding and particularly, the change in the extent of covalency while moving along the series in the complexes. Geometry optimization followed by EDA has been carried out for these actinides in their complexes with dipicolinic acid (DPA), Cyanex 301, 302 and 272 and N,N,N',N'-tetrakis[(6-carboxypyridin-2-yl)methyl]ethylenediamine (TPAEN) ligands. The choice of ligands selected for this study facilitates the effect of different donor atom and denticity to be taken into account as these parameters vary for the different complexes. Calculations have been carried out for both, in gas and solvent phases. It remains to be seen whether the results obtained from the EDA are able to provide important insights on the increase in the extent of covalency along the series as continue to be reported in literature from time to time.

7B.2 Heavy actinide complexes with cyanex ligands

The heavy actinide ion (Am^{3+} , Cm^{3+} , Bk^{3+} and Cf^{3+}) complexes with the bidentate cyanex 272, cyanex 302 and cyanex 301 ligands have been optimized and analysed for their geometry (Table 7B.1). As a representative of other actinide structures which have similar geometry, Figure 7B.1 shows the optimized structures for Cf complexes with cyanex 272, cyanex 302 and cyanex 301 ligands. The binding site changes in the case of each ligand. Cyanex 301 binds via two sulphur atoms, cyanex 302 binds via one sulphur and one oxygen atom and cyanex 272 binds via two oxygen atoms. The actinides form charge neutral 1:3 complexes with the cyanex extractants as reported earlier for the Cyanex 301 complexes with

trivalent lanthanides and actinide⁷⁷. Truncated forms of the cyanex ligands have been used for the theoretical calculations. The metal-oxygen bond lengths are shorter than those between metal-sulphur. For metal-oxygen as well as metal-sulphur bonds, the actinide-extractant bond lengths decrease monotonically from Am to Cf complexes. The shrinking ionic radii from Am through Cf are one of the causes for the shortening in bond length. The M-O/M-S bond distance is reduced in Cm in comparison with Am. However, the reduction in bond distance from Cm to Bk is more drastic. The trend is not gradual due to the effect of half-filled f7 configuration of Cm(III). Since half-filled f7 states of actinides are more stable, the M-O/M-S bond becomes relatively large in the complexes of Cm.



Figure 7B.1: Optimised geometries of Cf complexes with cyanex 272, cyanex 302 and cyanex 301 ligands.

Table 7B.1: Computed structural parameters (Å) of actinide cyanex complexes using PBE/TZ2P method.

	Cyanex 301	Cyanex 302		Cyanex 272
	Bond lengths			
Actinide	M – S	M – O	M – S	M – O
Am	2.829	2.338	2.909	2.408
Cm	2.818	2.327	2.902	2.403
Bk	2.797	2.306	2.881	2.381
Cf	2.794	2.308	2.866	2.373

Figure 7B.2 shows the EDA of heavy actinide complexes with cyanex 272, cyanex 302 and cyanex 301 ligands. The variation in interaction components *viz.* Pauli repulsion, electrostatic interaction and orbital interaction are shown from Am-Cf. The results indicate that on moving towards the heavy actinides, the electrostatic interaction decreases. The orbital interaction is more and suggests more overlap and hence extensive covalent interactions. On changing the binding site from oxygen to sulphur, there is increased covalency *viz.* orbital overlap and less electrovalence. The increased covalency is a reflection of the higher polarizability of sulphur as an electron donor due to its large size compared to oxygen. The same factor makes the electrostatic interaction the highest in the cyanex 272 complexes and least in the cyanex 301 complexes for all the actinides. Oxygen being a harder electron donor makes the actinide-oxygen interaction more electrostatic than the metal-sulphur interaction.

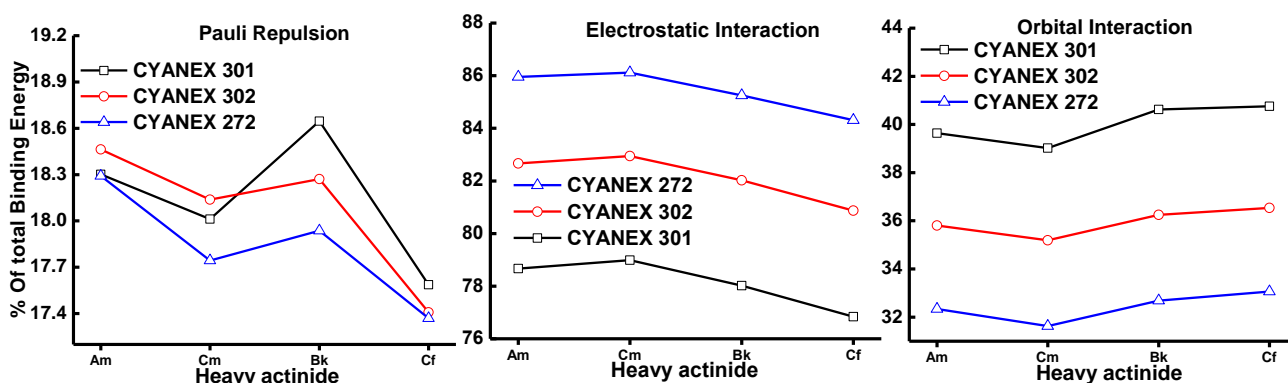


Figure 7B.2: EDA of heavy actinide complexes with cyanex 272, cyanex 302 and cyanex 301 ligands. The different interaction components are plotted from Am-Cf.

7B.3 Heavy actinide complexes with DPA ligand

The complexes of trivalent heavy actinide ions with DPA have been investigated. In these complexes there is a flexibility to vary the number of DPA ligands bound to the metal as the complexes are formed and stabilized in the aqueous phase. Hence, the actinide coordination is completed by complexing water molecules. Figure 7B.3 shows the optimized geometries of Am complexes with DPA in the ration 1:0, 1:1, 1:2 and 1:3. The other heavy actinide complexes have similar orientations and are hence not shown in the figure. The DPA ligand

donates electron density to the trivalent actinide through two carboxylate oxygens and an aromatic nitrogen, making it a tri-coordinate ligand with a charge of -2. Accordingly the net charges on the DPA complexes with triply charged actinide ions are +3, +1, -1 and -3 for the 1:0, 1:1, 1:2 and 1:3 complexes, respectively.

The metal-extractant bond lengths are shown in Table 7B.2 where M is the metal. M-O bond lengths are shorter than the M-N bond lengths in all the structures. In general, on moving from Am to Cf, the M-O bond lengths are shortened with the exception of Cm complexes, where there is an increase in the bond length. Unlike M-O bond lengths, the M-N bond lengths tend to decrease from Am to Bk, and show a marginal increase at Cf. As Cf^{3+} is a hard acid due to its smallest radius, it has a slightly lower tendency to bind with N which is a relatively soft donor compared to oxygen. For a given actinide, as the number of DPA ligands in the complex increases, the M-O as well as the M-N bond lengths increase. As more DPA ligands are available for electron donation to the cationic metal centre, the electron donation from the ligands is distributed. Consequently, the contribution from each DPA ligand is reduced, in turn increasing the bond lengths.

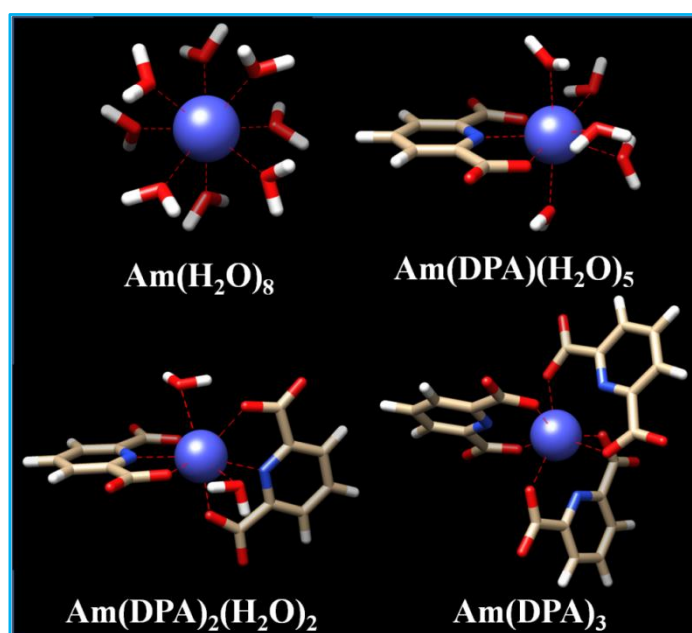


Figure 7B.3: The optimized geometries of 1:0, 1:1, 1:2 and 1:3 complexes of Am(III) with DPA

Table 7B.2: Computed structural parameters (Å) of actinide-DPA complexes using PBE/TZ2P method.

	$M(DPA)(H_2O)_5$		$M(DPA)_2(H_2O)_2$		$M(DPA)_3$	
	Bond lengths					
Actinide	M – O	M – N	M – O	M – N	M – O	M – N
Am	2.296	2.494	2.395	2.539	2.522	2.632
Cm	2.304	2.444	2.392	2.544	2.521	2.626
Bk	2.288	2.437	2.373	2.508	2.492	2.598
Cf	2.272	2.442	2.378	2.522	2.495	2.602

The gas phase EDA of the heavy actinide-DPA complexes with 1:0, 1:1, 1:2 and 1:3 metal:DPA ratios are shown in Figure 7B.4. On moving from Am to Cf there is a decrease in the electrostatic interaction component and an increase in the orbital overlap. This shows an increase in covalency in the actinide-DPA interaction. As the number of DPA ligands in the complex is increased from 0 to 3, the orbital overlap and hence covalency is systematically decreased. The increase in the bond distances from 1:1 to 1:3 DPA consequently leads to less overlap between the ligand and metal orbitals.

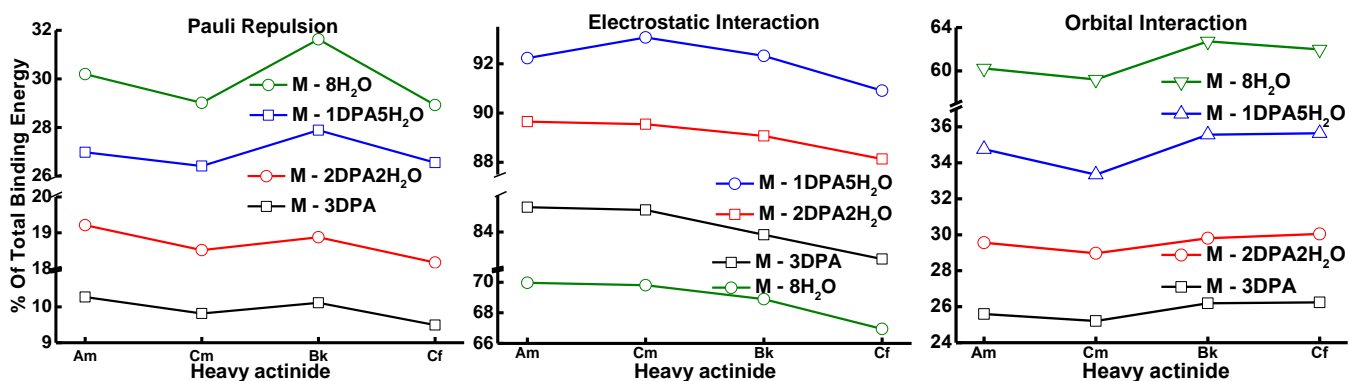


Figure 7B.4: Gas phase EDA of actinide–DPA complexes for Am, Cm, Bk and Cf.

EDA has been performed in solvent phase for all the metal-DPA systems (Figure 7B.5) with water as the solvent. The trends observed in the gas phase are retained in the solvent phase as well. The electrostatic interaction in the actinide-water complexes is significantly reduced in the solvent phase compared to the gas phase. In the $M(H_2O)_8$ complexes there is a significant decrease in the electrostatic interaction energies from the gas to the solvent phase. As the solvent medium is water, which has high dielectric constant the electrostatic interactions between the polar metal complex and solvent increase. This decreases the intra-complex electrostatic interactions.

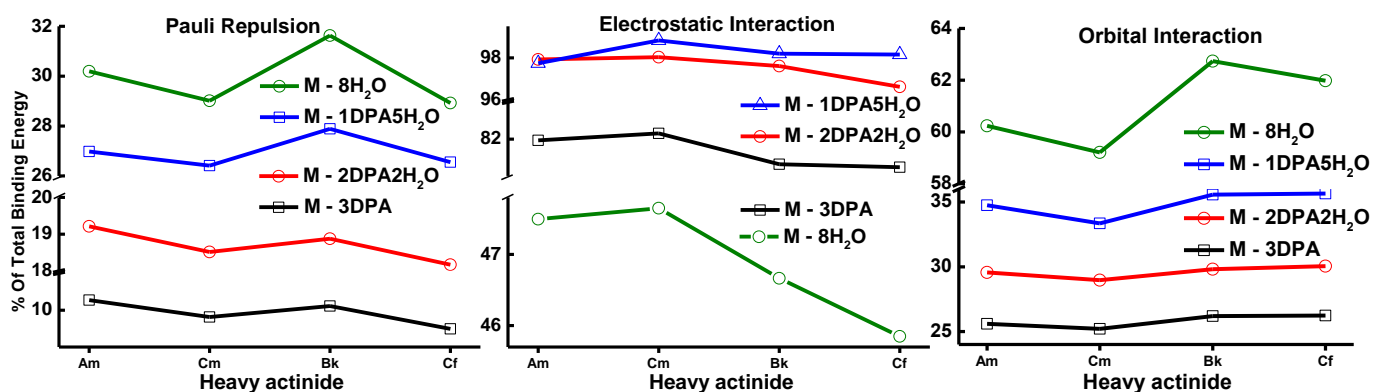


Figure 7B.5: Solvent corrected EDA of actinide–DPA complexes for Am, Cm, Bk and Cf.

7B.4 Heavy actinide complexes with TPAEN ligand

Subsequently the ligand, *viz.* TPAEN was taken-up and the complexation of heavy actinides with this ligand was investigated. As mentioned before, the complexation study of trivalent lanthanides and actinides with this ligand has been reported recently (27). Choice of this ligand is also motivated by the fact that in a single ligand, there are eight donor sites, making the structure of the complex more rigid. Moreover, choice of ligands in the present work has been made in such a way so that the effect of denticity on the trends in the variations of different energy components can be accomplished in a systematic way, starting from bidentate cyanex ligands, tridentate DPA and octadentate TPAEN. Figure 7B.6 shows the optimized geometries of the heavy actinide complexes with TPAEN octadentate ligand. The

ligand donates electrons to the triply charged actinide through 4 carboxylate oxygens and 4 nitrogen atoms as shown. The net charge on the complexes is -1 .

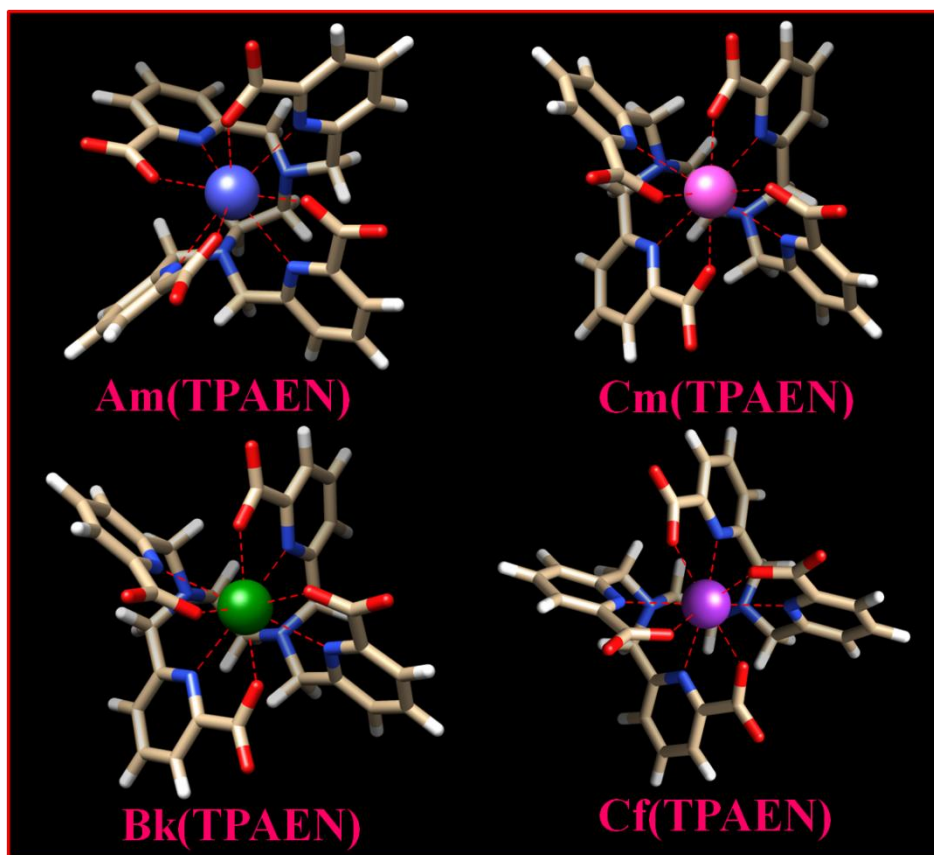


Figure 7B.6: Optimised geometries of Am^{3+} , Cm^{3+} , Bk^{3+} and Cf^{3+} complexes with the octa-coordinate TPAEN ligand.

Table 7B.3 shows the M-O and M-N bond distances between the actinide and ligand atoms at the binding site. From Am to Cf, the M-O and M-N bond distances decrease. In the cases of both cyanex and TPAEN complexes with actinides, there is an overall decrease in the average bond length from Am to Cf complexes. The decrease in bond length is more than the contraction of the ionic radii which is 0.025 \AA (53). From Tables 7B.1 and 7B.3, it can be seen that the decrease in the average bond length is 0.035 \AA in cyanex 301, 0.043 \AA (M-S bond), 0.030 \AA (M-O bond) in cyanex 302 complexes and 0.035 \AA in cyanex 272 complexes. In the case of the TPAEN ligand the decrease in average bond length from Am to Cf

complexes are 0.044 Å and 0.014 Å for the M-N and M-O bonds, respectively. The additional decrease in bond length is reflected in the complexation energy trends (Figure 7B.7). From Am to Cf, the complexes are more stabilised. The increasing complexation energy across the actinide series has been experimentally shown for the DPA ligand(27). The shortening in bond lengths over and above the shrinking of the ionic radii across Am-Cf is hence a consequence of enhanced covalency as predicted by the energy decomposition results.

Table 7B.3: Computed bond lengths (Å) of actinide-TPAEN complexes obtained using PBE/TZ2P method.

Actinide	$M(DPA)(H_2O)_5$	
	Bond lengths	
	M – O	M – N
Am	2.352	2.872
Cm	2.362	2.847
Bk	2.333	2.840
Cf	2.338	2.828

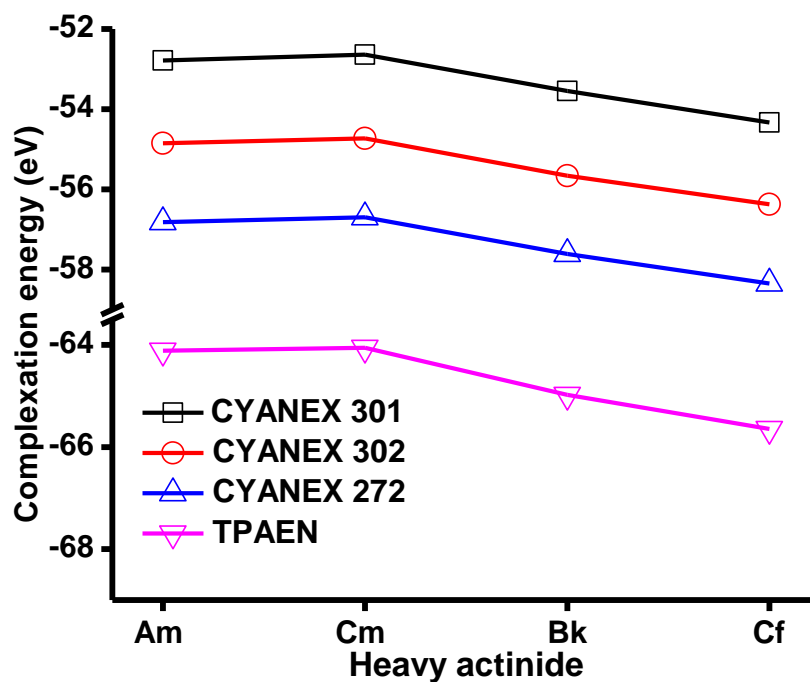


Figure 7B.7: Complexation energy for the heavy actinides with the Cyanex 301 Cyanex 302, Cyanex 272 and TPAEN ligands.

The gas and solvent phase EDA of the heavy actinide-TPAEN complexes are shown in Figure 7B.8. In both cases, on moving from Am to Cf, there is a decrease in the electrostatic interaction component and an increase in the orbital overlap. It is interesting to note that similar trend is followed in the gas phase as well as in the presence of solvent.

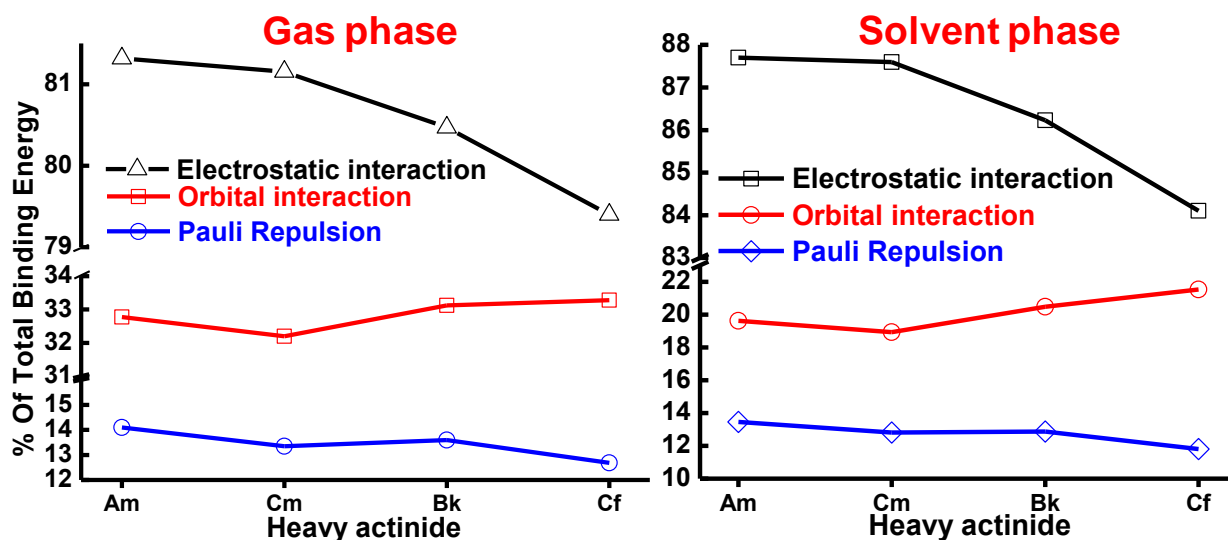


Figure 7B.8: EDA of actinide-TPAEN complexes for Am, Cm, Bk and Cf in gas phase and solvent phase.

For all the ligands studied, the effect of spin-orbit coupling has been investigated (Figure 7B.9-7B.11). The trends of lowering in the electrostatic interaction and increase in the orbitals interaction towards the heavy actinides is followed even in the presence of spin-orbit effects. The contribution from the orbital component is lower for Cm and the contribution of the electrostatic component is marginally higher than the expected trend line in the case of all the ligands. This behaviour could be due to the half-filled f orbitals in the Cm^{3+} ion which is not present in the other three ions studied. The effect of spin-orbit coupling on the EDA components has also been investigated. This lowering in the orbital contribution in the case of Cm is less pronounced when spin-orbit effects are introduced. In general there is an anomaly in the Cm-Bk region as far as few compounds reported in the literature are concerned. This deviation has been attributed to the near half-filled like configuration in the Cm-Bk region²⁶⁹. Very recently, an unusual trend in the variation of thermodynamic

properties has also been observed in the Cm-Bk region in their complexes with hydroxypyridinone ligand²⁷⁰. Exceptional behaviour of Bk can be attributed to that fact that Bk often assumes +IV state instead of +III state, which gives rise to half-filled f7 electronic shells for the Bk ion.

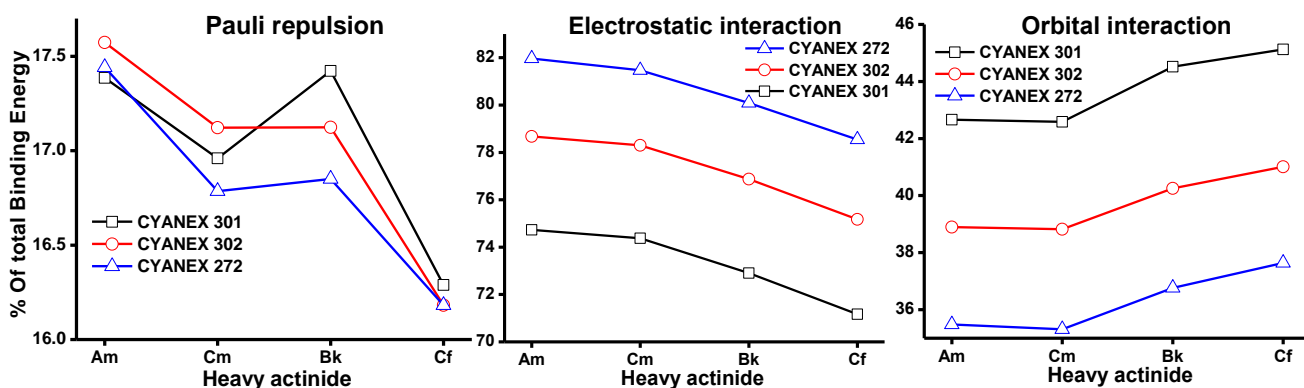


Figure 7B.9: EDA of heavy actinide complexes with cyanex 272, cyanex 302 and cyanex 301 ligands on incorporating spin-orbit coupling. The different interaction components are plotted from Am-Cf.

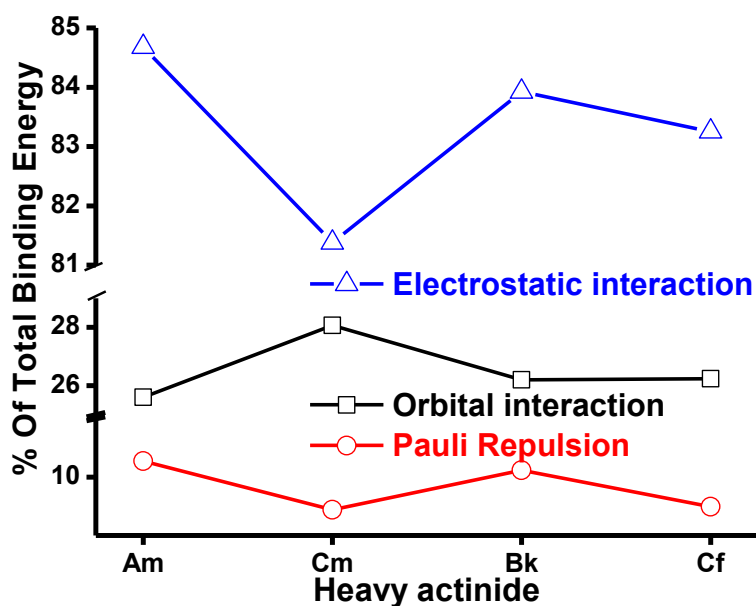


Figure 7B.10: EDA of Am-Cf complexes with 3DPA ligands on incorporating spin-orbit coupling. The different interaction components are plotted from Am-Cf

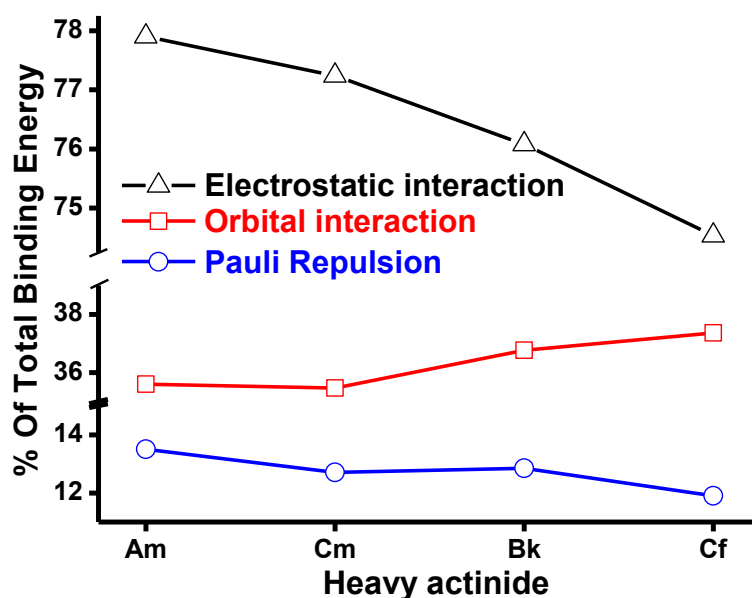


Figure 7B.11: EDA of heavy complexes with TPAEN ligand on incorporating spin-orbit coupling. The different interaction components are plotted from Am-Cf

7B.5 Analysis of energy levels

All the ligands investigated above, with varied binding site atoms and denticity show that the covalency in the metal-ligand bond increases towards the heavy actinide. This is completely unexpected as the actinides become harder acids across the period and are hence much more inclined to electrostatic interactions with anionic ligands. The basis for the covalency in heavy actinide complexes has been further probed by undertaking an energy level analysis, where the valence orbitals of the actinides Am-Cf are compared with the HOMO of the ligands. The results obtained succeeded in providing some ground on the reason behind the covalent interactions. Very recently, Batista and co-workers have performed similar kind of actinide and ligand energy level analysis for the complexes of Am-Cf with the DPA ligand¹⁶⁶ for the trivalent oxidation state of the actinides and also shown for the trivalent and tetravalent oxidation states using the hydroxypyridinone ligand²⁷⁰. Figure 7B.12 shows the energy level diagram for the heavy actinides, DPA and TPAEN ligands in solvent phase. The energy difference between the 5f energy level of Cf and the HOMO of DPA and TPAEN are schematically indicated. The energy difference between the ligand (DPA and TPAEN) HOMO and actinide energy levels is the maximum for Am, and decreases monotonically.

The energy difference between the 5f orbitals of Cf and the ligands is the least compared to the other actinides. Though the actinides contract across the period and are believed to participate in more electrostatic interactions with anionic ligands, they show greater covalency. This unexpected covalency is attributed to the near degeneracy of metal and ligand orbitals on moving across the actinide period from Am to Cf. Increased closeness of energy levels facilitates greater overlap of orbitals, which in turn leads to more covalent nature in the heavy actinide–ligand interaction.

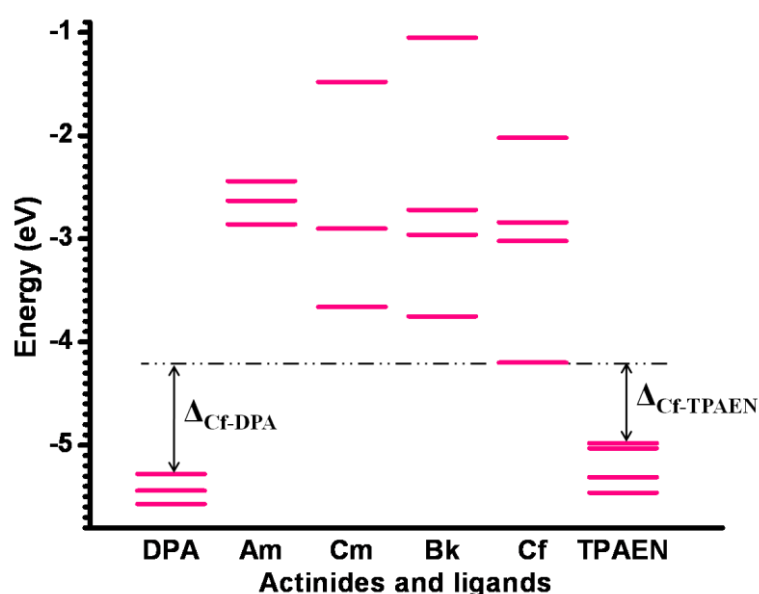


Figure 7B.12: Energy level diagram for the heavy actinides, DPA and TPAEN ligands in solvent phase. The energy difference between the Cf 5f energy level and the HOMO of DPA and TPAEN are schematically indicated.

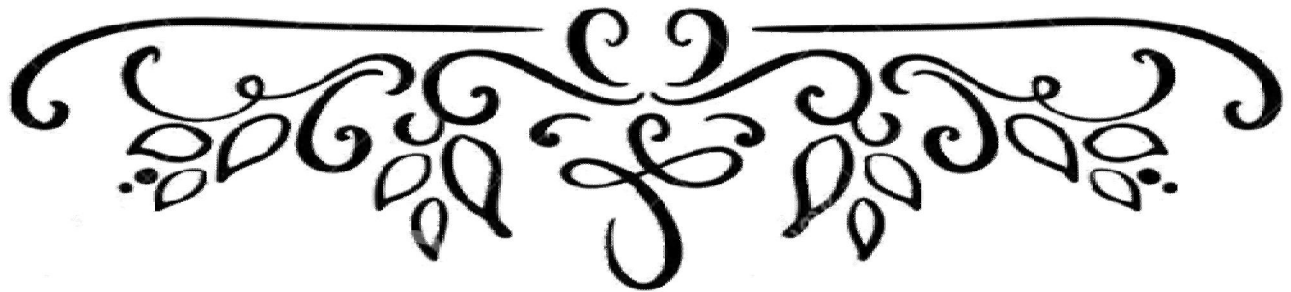
7B.6 Conclusion

Heavy actinides become harder acids due to contraction of the 5f orbitals, making their interactions with anionic ligands more electrostatic. Coupled with this, their dominant trivalent chemistry makes minor actinide partitioning all the more cryptic. Determination of electronic structures of lanthanide and actinide compounds and understanding their complexation chemistry with various ligands is crucial towards screening the right extractants.

The present work explicitly decomposed the actinide-ligand interaction into components viz. electrostatic, orbital overlap and Pauli repulsion. Ligands of different denticity and binding site atoms have been judiciously chosen. Counter-intuitive to the popular belief, our results uncovered decreased electrostatic interaction between ligand and actinide across Am to Cf and increased orbital interactions within the framework of EDA scheme, shown for the first time. These findings established greater covalency in the heavy actinide-ligand interaction. Further, observations on the ligand and metal energy levels clearly showed that from Am to Cf, actinide energy level was increasingly closer to the ligand HOMO. Total bonding energy has also been computed for all actinide-ligand systems. The overall bonding is increased along the series, and also the orbital contribution. It is clearly due to the enhancement in covalency, which is complimentary to the orbital degeneracy induced covalency.



Chapter 8



“Great beauty captures me, but a beauty still greater frees me even from itself”

~Kahlil Gibran

SUMMARY AND CONCLUSION

8.1 Conclusions

The present work effectively elaborates both experimentally as well as quantum chemically, the effects of carbon chain structure on the complexation of actinides. The results of SANS study provide insights into interparticle interactions that operate in the nanoscale regime through quantification of stickiness parameter. The threshold aggregation parameters quantified in this work is a stepping stone to create predictive models that anticipate aggregation in metastable solutions and suspensions. The changes in aggregation tendencies observed due to structural variation in the ligands may be extended to include a wide range of materials and provide means of overcoming aggregation by fine tuning the molecular structure of interacting surfaces. Apart from SANS, a theoretical perspective on third phase in metal-extractant systems is elaborated through the investigation of both Ce(IV) monomers and dimers. Aggregation tendencies are predicted by interpretation of single-molecule parameters. This study though pertaining to one kind of metal-ligand system, in its essence emphasises a consensus between theory and experiments, forming a basis for theoretically predicting properties of many atom complexes. Meticulous geometric analysis of intramolecular interactions in the Ce(IV) complexes, and energy decomposition of the interaction energy between the metal and ligands led to significant implications on the aggregation behaviour. This extended theoretical dimension successfully explains trends observed in the present work pertaining to tri-n-butyl phosphate (TBP) and tri-sec-butyl phosphate (TsBP) complexes with Ce(IV). The drastic effect of solely changing the oxidation state on the metal extraction energetics is clearly derived from calculations and corroborates well with experimental findings.

On establishing the effect of alkyl chain structure on the extraction of individual metal ions, separation of U(VI) from a Th(IV) matrix was subsequently carried out. Solvent extraction, quantum chemistry as well as demonstrations using extraction chromatography columns, confirmed that TsBP is a superior extractant for the separation of U(VI) from Th(IV) compared to TBP. This work elucidates the effect of complexing ligands' structure on the separation of elements which are conventionally very similar in their chemical behaviour. The separation of f-block elements has been a constant challenge due to their closely related chemistry. In this study, the same has been achieved by controlled parameters implemented at both liquid-liquid as well as solid-liquid interfaces and elucidated the importance of structure through DFT. The results obtained in this work are a classic example of the correlation between "structure and binding", a central and deeply investigated concept in the important field of separation science.

Having examined the effect of carbon chain structure on actinide extraction and separation within the phosphate family of compounds, a different class of organophosphorous extractants namely, phosphonates have been studied. Among these, the H-phosphonates that extract by two distinct extraction mechanisms, revealed striking structural effects. The hindrance in keto-enol tautomerism process and modulation of the P=O---H hydrogen bonding has surprisingly large implications on the extraction behaviour of secondary branched isomer Di-sec-butyl H-phosphonate (DsBHP) which does not show the dual extraction behaviour of classical H-phosphonates. This observation opens new avenues leading to a different class of extractants which can be tailor-made in a single step reaction, resulting in ligands with a desired level of selectivity. Further emphasising the effects of alkyl chain, investigation on dialkylalkyl phosphonates establishes variation in metal complexation behaviour and its sensitivity to extractant structure. Changes in extractant structure as far as five or six atoms away from the complexing site affect complexation affinities significantly

in the extractant-metal systems chosen. The DFT studies related to complexation energies corroborate well with the experimental findings. The implication of structural changes on the behaviour of ligands towards metal ions remains a valid question to this day and our results provide avenues for fine tuning metal specific complexation in the microgram regime.

DFT is most useful when its predictive element is taken advantage of. Especially the complexes studied in this work are of immediate interest in the processing of nuclear fuels where a plethora of organophosphorous extractants are still screened by involved experimental procedures. In the present study, DFT rightly predicts preferential stability of a uranyl nitrate complex with Disecamyl H-phosphonate (DsAHP) over its linear chain isomer Diamyl H-phosphonate (DAHP). The weak-hydrogen-bond mediated stability of this complex plays a role in its complexation behaviour, which was subsequently validated by performing complexation experiments. The results exemplify the predictive powers of DFT applied in the realm of actinide-organophosphorous complexes. Though this particular study pertains to uranyl complexes, the ideas presented therein can potentially be extended to other actinides, weaving a predictive future for actinide specific extractions and separations.

Experimental investigations using minor actinides involve great care due to their higher radiotoxicity. Moreover, due to the closeness in chemistry between minor actinides and lanthanides, several ligands require to be screened for identifying those specific to the actinides. Considering these challenges, a DFT platform to study minor actinide specific ligands is a wise alternative. In this work, deeper investigations into interaction energy have been elaborated and proved successful in predicting an increase in the covalency along the heavy actinide series though it is counter-intuitive from the view point of actinide contraction. The findings create a new direction for the search and evaluation of minor actinide specific extractants which are of immense utility in their partitioning from high-active nuclear waste streams. Results of the present work along with experimental reports on

the same lines suggest a rethinking of the decades old proposition in designing minor actinide selective ligands for use in back-end nuclear fuel cycle.

8.2 Future Directions

The initial studies with the solvent, TsBP have indicated potential prospects of preparative scale separation of uranium from thorium matrix using solvent extraction and extraction chromatographic technique. Further, the same can be extended to extraction of thorium from monazite and separation of uranium from thorium matrix of irradiated thorium rods.

There is need for development of methods for the removal of uranium from mine water samples and aqueous waste streams. Extraction chromatographic technique using phosphonate anchored XAD-7 support can be employed for this application. In this connection, it will be useful to chemically anchor these molecules on modified silica or reverse phase silica supports for extending the stability of resin material. These modified chromatographic supports can be used for removal of actinide elements e.g. actinide recovery from various aqueous streams. Additional solvent extraction studies with higher homologues of H-phosphonates would be preferable as these have lower aqueous solubility. Presently, the effect of branching in the carbon chain on the extraction behaviour has been investigated in both H-phosphonates and dialkylalkyl phosphonates. Further studies could include the effects of functionalising the carbon chain (e.g. with electron withdrawing vs. electron donating groups) and examining the extraction behaviour of actinides.

Investigations on the third phase formation behaviour of Pu(IV) are important for designing solvent extraction processes. In this connection extraction of Pu(IV) from nitric acid medium with TsBP-dodecane system and comparison with TBP/n-DD will be of immense importance for developing solvent extraction processes with alternate solvents. Similarly understanding and generation of data relating to third phase formation during solvent extraction of tetravalent metal ions such as U(IV), Th(IV), Zr(IV) and Pu(IV) with phosphate and

phosphonate based solvents are crucial for their extraction and purification. In this context, it is important to employ ligands which preferably do not form third phase during solvent extraction process.

Computational studies will be of immense help in screening ligands which can be employed for the above. Subsequent to that the ligand-diluent system can be employed for effective extraction with higher throughput. In the present thesis, in addition to exhaustive experimental studies, for the first time an attempt has been made to explain the third phase formation phenomena at the molecular level through DFT calculations. This computational study is a preliminary one and additional intensive computational study on the mechanism of third phase formation might be important to solve some of the issues of third phase formation.

Another area concerned with the covalency in heavy actinide complexes, shows a phenomenon counter-intuitive to the concept of “actinide contraction”. This field is challenging because of the difficulties in carrying out experimental work associated with higher radiotoxicity and short half-life of the heavier actinides like Bk, Cf etc. Thus, computational exploration could play a major role in this field. Specifically, molecular dynamic simulations for mimicking the heavy actinide complexes in realistic environments would be immensely beneficial in view of separation science.

References

1. P. Garg, *Journal of Sustainable Energy & Environment*, 2012, **3**, 7-17.
2. R. B. Grover and S. Chandra, *Energy Policy*, 2006, **34**, 2834-2847.
3. J. P. Dorian, H. T. Franssen and D. R. Simbeck, *Energy Policy*, 2006, **34**, 1984-1991.
4. M. Meinshausen, N. Meinshausen, W. Hare, S. C. B. Raper, K. Frieler, R. Knutti, D. J. Frame and M. R. Allen, *Nature*, 2009, **458**, 1158.
5. J.-C. Chen, Z.-S. Liu and J.-S. Huang, *Journal of Hazardous Materials*, 2007, **142**, 266-271.
6. S. O. Akansu, Z. Dulger, N. Kahraman and T. N. Vezirođlu, *International Journal of Hydrogen Energy*, 2004, **29**, 1527-1539.
7. R. G. Papagiannakis and D. T. Hountalas, *Energy Conversion and Management*, 2004, **45**, 2971-2987.
8. P. F. Kingston, *Spill Science & Technology Bulletin*, 2002, **7**, 53-61.
9. N. L. Panwar, S. C. Kaushik and S. Kothari, *Renewable and Sustainable Energy Reviews*, 2011, **15**, 1513-1524.
10. N. Armaroli and V. Balzani, *Angewandte Chemie International Edition*, 2007, **46**, 52-66.
11. Z. Guo, X. Xiao and D. Li, *Ecological Applications*, 2000, **10**, 925-936.
12. D. K. Okot, *Renewable and Sustainable Energy Reviews*, 2013, **26**, 515-520.
13. T. Ackermann and L. Söder, *Renewable and Sustainable Energy Reviews*, 2000, **4**, 315-374.
14. G. M. Joselin Herbert, S. Iniyar, E. Sreevalsan and S. Rajapandian, *Renewable and Sustainable Energy Reviews*, 2007, **11**, 1117-1145.
15. A. N. Celik, *Journal of Wind Engineering and Industrial Aerodynamics*, 2003, **91**, 693-707.
16. B. van der Zwaan, *Energy Strategy Reviews*, 2013, **1**, 296-301.
17. A. Verbruggen, *Energy Policy*, 2008, **36**, 4036-4047.
18. R. Chidambaram and C. Ganguly, *Current Science*, 1996, **70**, 21-35.
19. S. C. Chetal, P. Chellapandi, P. Puthiyavinayagam, S. Raghupathy, V. Balasubramanian, P. Selvaraj, P. Mohanakrishnan and B. Raj, *Energy Procedia*, 2011, **7**, 64-73.
20. H. S. Kamath, *Energy Procedia*, 2011, **7**, 110-119.
21. J. J. Laidler, J. E. Battles, W. E. Miller, J. P. Ackerman and E. L. Carls, *Progress in Nuclear Energy*, 1997, **31**, 131-140.
22. M. Salanne, C. Simon, P. Turq and P. A. Madden, *The Journal of Physical Chemistry B*, 2008, **112**, 1177-1183.
23. C. Aditi, A. Suresh, M. Joshi, M. Sundararajan, T. K. Ghanty and N. Sivaraman, *Separation and Purification Technology*, 2019, **210**, 182-194.
24. D. Serrano-Purroy, P. Baron, B. Christiansen, J.-P. Glatz, C. Madic, R. Malmbeck and G. Modolo, *Separation and Purification Technology*, 2005, **45**, 157-162.
25. M. R. Yaftian, L. Hassanzadeh, M. E. Eshraghi and D. Matt, *Separation and Purification Technology*, 2003, **31**, 261-268.
26. Z. Wang, J. Wang, S. Ding, Y. Liu, L. Zhang, L. Song, Z. Chen, X. Yang and X. Wang, *Separation and Purification Technology*, 2018, DOI: <https://doi.org/10.1016/j.seppur.2018.04.065>.
27. A. E. V. Gorden, M. A. DeVore and B. A. Maynard, *Inorganic Chemistry*, 2013, **52**, 3445-3458.
28. P.-W. Huang, C.-Z. Wang, Q.-Y. Wu, J.-H. Lan, G. Song, Z.-F. Chai and W.-Q. Shi, *Dalton Transactions*, 2018, **47**, 5474-5482.
29. W. W. Schulz, Berger, L. L., and Navratil, J. D, *RC Press*, 1990, **3**.
30. P. R. V. Rao and Z. Kolarik, *Solvent Extraction and Ion Exchange*, 1996, **14**, 955-993.
31. T. G. Srinivasan and P. R. Vasudeva Rao, *Separation Science and Technology*, 2014, **49**, 2315-2329.
32. K. B. Rakesh, A. Suresh, N. Sivaraman, V. K. Aswal and P. R. V. Rao, *Journal of Radioanalytical and Nuclear Chemistry*, 2016, DOI: 10.1007/s10967-016-4728-2.
33. C. V. S. Brahmmananda Rao Chirag K. Vyas, S. Jayalakshmi, P. M. Joshirao, and V. K. Manchanda, *Radiochim. Acta*, 2015, **103**, 277-285.
34. T. H. Siddall, *Industrial & Engineering Chemistry*, 1959, **51**, 41-44.
35. G. W. Mason and H. E. Griffin, in *Actinide Separations*, American Chemical Society, 1980, vol. 117, ch. 7, pp. 89-99.
36. L. L. Burger, *The Journal of Physical Chemistry*, 1958, **62**, 590-593.
37. L. L. Burger, *Nuclear Science and Engineering*, 1963, **16**, 428-439.
38. T. H. Siddall, *The Journal of Physical Chemistry*, 1960, **64**, 1863-1866.
39. D. C. Madigan and R. W. Catrall, *Journal of Inorganic and Nuclear Chemistry*, 1961, **21**, 334-338.
40. C. V. S. Brahmmananda Rao, A. Suresh, T. G. Srinivasan and P. R. V. Rao, *Solvent Extraction and Ion Exchange*, 2003, **21**, 221-238.
41. C. V. S. Brahmmananda Rao, T. G. Srinivasan and P. R. V. Rao, *Solvent Extraction and Ion Exchange*, 2012, **30**, 262-277.

42. C. Aditi, C. V. S. Brahmmananda Rao, M. Sundararajan, T. K. Ghanty and N. Sivaraman, *Dalton Transactions*, 2018, **47**, 3841-3850.
43. L. Burger, *The Journal of Physical Chemistry*, 1958, **62**, 590-593.
44. D. Madigan and R. Catrall, *Journal of Inorganic and Nuclear Chemistry*, 1961, **21**, 334-338.
45. T. Siddall, *Industrial & Engineering Chemistry*, 1959, **51**, 41-44.
46. M. E. Cabanela and J. Jowsey, *Calcified Tissue Research*, 1971, **8**, 114-120.
47. M. Pazianas, P. Miller, W. A. Blumentals, M. Bernal and P. Kothawala, *Clinical Therapeutics*, 2007, **29**, 1548-1558.
48. B. Nowack, *Water Research*, 1998, **32**, 1271-1279.
49. B. Nowack, *Water Research*, 2003, **37**, 2533-2546.
50. C. V. S. Brahmmananda Rao, S. Jayalakshmi, N. Sivaraman and P. R. V. Rao, *Journal*, 2015, **103**, 235.
51. C. V. S. Brahmmananda Rao, S. Jayalakshmi, S. Subramaniam, N. Sivaraman and P. R. V. Rao, *Radiochimica Acta*, 2015, **103**, 345-358.
52. E. M. Villa, S. Wang, E. V. Alekseev, W. Depmeier, and T. E. Albrecht-Schmitt, *European Journal of Inorganic Chemistry*, 2011, **2011**, 3749-3754.
53. C. Xu and L. Rao, *Chemistry – A European Journal*, 2014, **20**, 14807-14815.
54. M. Starck, F. A. Laporte, S. Oros, N. Sisommay, V. Gathu, P. L. Solari, G. Creff, J. Roques, C. D. Auwer, C. Lebrun and P. Delangle, *Chemistry – A European Journal*, 2017, **23**, 5281-5290.
55. J. D. Burns and B. A. Moyer, *Inorganic Chemistry*, 2016, **55**, 8913-8919.
56. B. Arunasis, M. Manoj, P. K. Mohapatra, G. Trilochan, S. K. Ghosh, M. Debashree, T. K. Ghanty, R. Neetika and B. S. Tomar, *European Journal of Inorganic Chemistry*, 2017, **2017**, 820-828.
57. J. Bisson, J. Dehaut, M. C. Charbonnel, D. Guillaneux, M. Miguiditchian, C. Marie, N. Boubals, G. Dutech, M. Pipelier, V. Blot and D. Dubreuil, *Chemistry – A European Journal*, 2014, **20**, 7819-7829.
58. C. Aditi, A. Suresh and N. Sivaraman, *Radiochimica Acta*, 2016.
59. C. Aditi, A. Suresh, N. Sivaraman and V. K. Aswal, *RSC Advances*, 2016, **6**, 92905-92916.
60. A. Suresh, T. G. Srinivasan and P. R.V. Rao, *Solvent Extraction and Ion Exchange*, 2009, **27**, 258-294.
61. A. Suresh, T. Srinivasan, P. R. V. Rao, C. Rajagopalan and S. Koganti, *Separation science and technology*, 2005, **39**, 2477-2496.
62. K. B. Rakesh, A. Suresh and P. R.V. Rao, *Solvent Extraction and Ion Exchange*, 2014, **32**, 249-266.
63. A. Suresh, T. G. Srinivasan and P.R.V. Rao, *Solvent Extraction and Ion Exchange*, 2009, **27**, 132-158.
64. A. S. Kertes, *The chemistry of the formation and elimination of a third phase in organophosphorous and amine extraction systems*, McMillan, London, 1965.
65. Z. Kolarik, ed., *The formation of a third phase in the extraction of Pu(IV), U(IV) and Th(IV) nitrates with tributyl phosphate in alkane diluents*, Can. Inst. Mining Metallurgy, Toronto, Canada, 1979.
66. T. G. Srinivasan, M. K. Ahmed, A. M. Shakila, R. Dhamodaran, P.R.V. Rao and C. K. Mathews, *Radiochimica Acta*, 1986, **40**, 151-154.
67. R. Chiarizia, M. P. Jensen, M. Borkowski, J. R. Ferraro, P. Thiyagarajan and K. C. Littrell, *Solvent Extraction and Ion Exchange*, 2003, **21**, 1-27.
68. J. Plaque, *Separation Science and Technology*, 2006, **41**, 2065-2074.
69. R. Chiarizia, M. P. Jensen, P. G. Rickert, Z. Kolarik, M. Borkowski and P. Thiyagarajan, *Langmuir*, 2004, **20**, 10798-10808.
70. R. J. Ellis, *The Journal of Physical Chemistry B*, 2013, **118**, 315-322.
71. R. J. Ellis, T. L. Anderson, M. R. Antonio, A. Braatz and M. Nilsson, *The Journal of Physical Chemistry B*, 2013, **117**, 5916-5924.
72. S. Subbuthai, R. Ananthanarayanan, P. Sahoo, A. N. Rao and R. S. Rao, *Journal of Radioanalytical and Nuclear Chemistry*, 2012, **292**, 879-883.
73. L. Lefrançois, J.-J. Delpuech, M. Hébrant, J. Chrisment and C. Tondre, *The Journal of Physical Chemistry B*, 2001, **105**, 2551-2564.
74. R. Baxter, *The Journal of Chemical Physics*, 1968, **49**, 2770-2774.
75. P. Kumar, P. G. Jaison, V. M. Telmore, D. Alamelu, S. K. Aggarwal, B. Sadhu and M. Sundararajan, *Journal of Radioanalytical and Nuclear Chemistry*, 2016, **308**, 303-310.
76. P. Kumar, P. G. Jaison, V. M. Telmore, B. Sadhu and M. Sundararajan, *Rapid Communications in Mass Spectrometry*, 2017, **31**, 561-571.
77. A. Bhattacharyya, T. K. Ghanty, P. K. Mohapatra and V. K. Manchanda, *Inorganic Chemistry*, 2011, **50**, 3913-3921.
78. A. Bhattacharyya, M. Mohapatra, P. K. Mohapatra, T. Gadly, S. K. Ghosh, D. Manna, T. K. Ghanty, N. Rawat and B. S. Tomar, *European Journal of Inorganic Chemistry*, 2017, **2017**, 820-828.
79. C.-Z. Wang, J.-H. Lan, Y.-L. Zhao, Z.-F. Chai, Y.-Z. Wei and W.-Q. Shi, *Inorganic Chemistry*, 2013, **52**, 196-203.

80. B. G. Vats, D. Das, B. Sadhu, S. Kannan, I. C. Pius, D. M. Noronha, M. Sundararajan and M. Kumar, *Dalton Transactions*, 2016, **45**, 10319-10325.
81. D. L. Clark and S. A. Kozimor, 2016.
82. E. R. Batista, R. L. Martin, D. L. Clark and S. A. Kozimor, Abstracts of papers of the American Chemical Society, 2014.
83. M. L. Neidig, D. L. Clark and R. L. Martin, *Coordination Chemistry Reviews*, 2013, **257**, 394-406.
84. P. F. Weck, C.-M. S. Gong, E. Kim, P. Thuery and K. R. Czerwinski, *Dalton Transactions*, 2011, **40**, 6007-6011.
85. M. Azam, S. I. Al-Resayes, G. Velmurugan, P. Venuvanalingam, J. Wagler and E. Kroke, *Dalton Transactions*, 2015, **44**, 568-577.
86. S. Hohloch, M. E. Garner, B. F. Parker and J. Arnold, *Dalton Transactions*, 2017, **46**, 13768-13782.
87. J. Narbutt and W. P. Oziminski, *Dalton Transactions*, 2012, **41**, 14416-14424.
88. T. S. Franczyk, K. R. Czerwinski and K. N. Raymond, *Journal of the American Chemical Society*, 1992, **114**, 8138-8146.
89. M. Iqbal, R. G. Struijk, J. Huskens, M. Sypula, A. Wilden, G. Modolo and W. Verboom, *New journal of chemistry*, 2012, **36**, 2048-2059.
90. J. Luo, C.-Z. Wang, J.-H. Lan, Q.-Y. Wu, Y.-L. Zhao, Z.-F. Chai, C.-M. Nie and W.-Q. Shi, *Dalton Transactions*, 2015, **44**, 3227-3236.
91. Q.-Y. Wu, F.-W. Zhai, Y. Liu, L.-Y. Yuan, Z.-F. Chai and W.-Q. Shi, *Dalton Transactions*, 2016, **45**, 14988-14997.
92. Q.-Y. Wu, C.-Z. Wang, J.-H. Lan, Z.-F. Chai and W.-Q. Shi, *RSC Advances*, 2016, **6**, 69773-69781.
93. J. A. Macor, J. L. Brown, J. N. Cross, S. R. Daly, A. J. Gaunt, G. S. Girolami, M. T. Janicke, S. A. Kozimor, M. P. Neu, A. C. Olson, S. D. Reilly and B. L. Scott, *Dalton Transactions*, 2015, **44**, 18923-18936.
94. E. C. Uribe, H. E. Mason, J. A. Shusterman and W. W. Lukens, *Dalton Transactions*, 2017, **46**, 5441-5456.
95. T. Zheng, Y. Gao, L. Chen, Z. Liu, J. Diwu, Z. Chai, T. E. Albrecht-Schmitt and S. Wang, *Dalton Transactions*, 2015, **44**, 18158-18166.
96. W. Yang, H. Wang, Z.-Y. Du, W.-G. Tian and Z.-M. Sun, *CrystEngComm*, 2014, **16**, 8073-8080.
97. H. Hall, J. C. Sullivan, P. G. Rickert and K. L. Nash, *Dalton Transactions*, 2005, **11**, 2011-2016
98. J. Chow, R. J. Kopp and P. R. Portney, *Science*, 2003, **302**, 1528.
99. S. Şahin, K. Yıldız, H. M. Şahin and A. Acır, *Energy Conversion and Management*, 2006, **47**, 1661-1675.
100. T. Ünak, *Progress in Nuclear Energy*, 2000, **37**, 137-144.
101. J. H. Cavendish, in *Science and technology of tributyl phosphate*, eds. W. W. Schulaz, J. D. Navratil and T. Bess, CRC Press, Boca Raton, FL, 1987, vol. II, Part-A, pp. 1-41.
102. W. D. Bond, ed., *The Thorex process*, CRC Press, Boca Raton, Florida, USA, 1990.
103. P. V. Achuthan, Janardanan, C., Vijaykumar, N., Kutti, P.V.E., Mukherjee, A., Ramanujam, A., *BARC Report: Mumbai*, 1993, **BARC-1993/E/029**.
104. R. V. Chitnis, Rajappan, K.G., Kumar, S.V., Nadkarni, M.N., *BARC Report, Mumbai*, 1979, **BARC-1003**.
105. A. Ramanujam, P.S. Dhami, V. Gopalakrishnan, A. Mukherjee, R.K. Dhumwad, *BARC Report, Mumbai*, 1989, **BARC-1486**.
106. J. C. Shafer, J. Sulakova, M. D. Ogden and K. L. Nash, *Separation and Purification Technology*, 2018, **202**, 157-164.
107. J. Serrano and T. Kimura, *Journal of radioanalytical and nuclear chemistry*, 1993, **172**, 97-105.
108. M. Yamaura and H. Matsuda, *Journal of radioanalytical and nuclear chemistry*, 1997, **224**, 83-87.
109. J. L. Cortina, N. Miralles, M. Aguilar and A. M. Sastre, *Solvent Extraction and Ion Exchange*, 1994, **12**, 371-391.
110. A. G. Strikovskiy, K. Jeřábek, J. L. Cortina, A. M. Sastre and A. Warshawsk, *Reactive and Functional Polymers*, 1996, **28**, 149-158.
111. E. P. Horwitz, M. L. Dietz, R. Chiarizia, H. Diamond, A. M. Essling and D. Graczyk, *Analytica Chimica Acta*, 1992, **266**, 25-37.
112. L. Pietrelli, A. Salluzzo and F. Troiani, *Journal of radioanalytical and nuclear chemistry*, 1990, **141**, 107-115.
113. A. Zhang, Y. Wei, H. Hoshi and M. Kumagai, *Separation science and technology*, 2005, **40**, 811-827.
114. A. Zhang, C. Xiao, E. Kuraoka and M. Kumagai, *Journal of hazardous materials*, 2007, **147**, 601-609.
115. A. Zhang, C. Xiao, W. Xue and Z. Chai, *Separation and Purification Technology*, 2009, **66**, 541-548.
116. M. El Absy, I. El Naggat, M. Hamid and H. Aly, *Journal of radioanalytical and nuclear chemistry*, 1993, **172**, 145-153.

117. J. Mathur, M. Murali, G. Rizvi, R. Iyer, K. Michael, S. Kapoor, R. Dhumwad, L. Badheka and A. Banerji, *Solvent Extraction and Ion Exchange*, 1994, **12**, 745-763.
118. A. Warshawsky, A. G. Strikovskiy, K. Jerabek and J. L. Cortina, *Solvent Extraction and Ion Exchange*, 1997, **15**, 259-283.
119. R. G. Bautista, *Handbook on the Physics and Chemistry of Rare Earths*, 1995, **21**, 1-27.
120. Z. O. U. Dan, C. Ji and L. I. Deqian, *Journal of Rare Earths*, 2014, **32**, 681-685.
121. R. Marsac, F. Real, N. L. Banik, M. Pedrot, O. Pourret and V. Vallet, *Dalton Transactions*, 2017, **46**, 13553-13561.
122. J. N. Cross, P. M. Duncan, E. M. Villa, M. J. Polinski, J.-M. Babo, E. V. Alekseev, C. H. Booth and T. E. Albrecht-Schmitt, *Journal of the American Chemical Society*, 2013, **135**, 2769-2775.
123. M. Šulka, L. Cantrel and V. Vallet, *The Journal of Physical Chemistry A*, 2014, **118**, 10073-10080.
124. M. R. Antonio, T. J. Demars, M. Audras and R. J. Ellis, *Separation Science and Technology*, 2017, **153**, 1834-1847.
125. L. Gagliardi, *Theoretical Chemistry Accounts*, 2006, **116**, 307-315.
126. D. Manna and T. K. Ghanty, *Physical Chemistry Chemical Physics*, 2012, **14**, 11060-11069.
127. D. Manna, S. Mula, A. Bhattacharyya, S. Chattopadhyay and T. K. Ghanty, *Dalton Transactions*, 2015, **44**, 1332-1340.
128. A. D. Buckingham, J. E. Del Bene and S. A. C. McDowell, *Chemical Physics Letters*, 2008, **463**, 1-10.
129. G. Desiraju and T. Steiner, *Monographs on Crystallography. 9th ed. International Union of Crystallography*, 1999.
130. J. Joseph and E. D. Jemmis, *Journal of the American Chemical Society*, 2007, **129**, 4620-4632.
131. S. Scheiner, *Hydrogen bonding: a theoretical perspective*, Oxford University Press on Demand, 1997.
132. L. Turi and J. J. Dannenberg, *The Journal of Physical Chemistry*, 1993, **97**, 7899-7909.
133. I. Ahmed and S. H. Jhung, *Chemical Engineering Journal*, 2017, **310**, 197-215.
134. X. Sui, M. Ji, X. Lan, W. Mi, C. Hao and J. Qiu, *Inorganic Chemistry*, 2013, **52**, 5742-5748.
135. Y. Ye, S. Xiong, X. Wu, L. Zhang, Z. Li, L. Wang, X. Ma, Q.-H. Chen, Z. Zhang and S. Xiang, *Inorganic Chemistry*, 2016, **55**, 292-299.
136. K. T. Mahmudov, M. N. Kopylovich, M. F. C. Guedes da Silva and A. J. L. Pombeiro, *Coordination Chemistry Reviews*, 2017, **345**, 54-72.
137. J. Reedijk, *Chemical Society Reviews*, 2013, **42**, 1776-1783.
138. A. J. Kendall, L. N. Zakharov and J. D. Gilbertson, *Inorganic Chemistry*, 2010, **49**, 8656-8658.
139. V. W. L. Ng, M. K. Taylor, J. M. White and C. G. Young, *Inorganic Chemistry*, 2010, **49**, 9460-9469.
140. N. Nasser, A. Borecki, P. D. Boyle and R. J. Puddephatt, *Inorganic Chemistry*, 2013, **52**, 7051-7060.
141. S. Kannan, M. Kumar, B. Sadhu, M. Jaccob and M. Sundararajan, *Dalton Transactions*, 2017, **46**, 16939-16946.
142. A. C. Sather, O. B. Berryman and J. Rebek, *Journal of the American Chemical Society*, 2010, **132**, 13572-13574.
143. A. C. Sather, O. B. Berryman and J. Rebek, *Chemical Science*, 2013, **4**, 3601-3605.
144. P. H. Walton and K. N. Raymond, *Inorganica Chimica Acta*, 1995, **240**, 593-601.
145. J. N. Mathur, M. S. Murali and K. L. Nash, *Solvent Extraction and Ion Exchange*, 2001, **19**, 357-390.
146. K. Nagarajan, B. P. Reddy, S. Ghosh, G. Ravisankar, K. S. Mohandas, U. K. Mudali, K. V. G. Kutty, K. V. K. Viswanathan, C. A. Babu, P. Kalyanasundaram, P. R. V. Rao and B. Raj, *Energy Procedia*, 2011, **7**, 431-436.
147. D. D. Sood and S. K. Patil, *Journal of Radioanalytical and Nuclear Chemistry*, 1996, **203**, 547-573.
148. F. Chartier, M. Aubert and M. Pilier, *Fresenius' Journal of Analytical Chemistry*, 1999, **364**, 320-327.
149. A. Afsar, D. M. Laventine, L. M. Harwood, M. J. Hudson and A. Geist, *Chemical Communications*, 2013, **49**, 8534-8536.
150. S. A. Ansari, P. Pathak, P. K. Mohapatra and V. K. Manchanda, *Separation & Purification Reviews*, 2011, **40**, 43-76.
151. F. W. Lewis, L. M. Harwood, M. J. Hudson, M. G. B. Drew, V. Hubscher-Bruder, V. Videva, F. Arnaud-Neu, K. Stamberg and S. Vyas, *Inorganic Chemistry*, 2013, **52**, 4993-5005.
152. J. Chen, S. Wang, C. Xu, X. Wang and X. Feng, *Procedia Chemistry*, 2012, **7**, 172-177.
153. G. Modolo and S. Nabet, *Solvent Extraction and Ion Exchange*, 2005, **23**, 359-373.
154. G. R. Choppin, *Marine Chemistry*, 2006, **99**, 83-92.
155. K. L. Nash and G. R. Choppin, *Separation Science and Technology*, 1997, **32**, 255-274.
156. W. Shuao, E. V. Alekseev, L. Jie, S. Skanthakumar, L. Soderholm, D. Wulf and T. E. Albrecht-Schmitt, *Angewandte Chemie International Edition*, 2010, **49**, 1263-1266.
157. C. Hill, C. Madic, P. Baron, M. Ozawa and Y. Tanaka, *Journal of Alloys and Compounds*, 1998, **271-273**, 159-162.

158. M. J. Hudson, L. M. Harwood, D. M. Laventine and F. W. Lewis, *Inorganic Chemistry*, 2013, **52**, 3414-3428.
159. C. Madic, M. J. Hudson, J.-O. Liljenzin, J.-P. Glatz, R. Nannicini, A. Facchini, Z. Kolarik and R. Odoj, *Progress in Nuclear Energy*, 2002, **40**, 523-526.
160. Y. Wei, M. Kumagai, Y. Takashima, G. Modolo and R. Odoj, *Nuclear Technology*, 2000, **132**, 413-423.
161. X. Cao, D. Heidelberg, J. Ciupka and M. Dolg, *Inorganic Chemistry*, 2010, **49**, 10307-10315.
162. T. Sun, C. Xu, X. Xie, J. Chen and X. Liu, *ACS Omega*, 2018, **3**, 4070-4080.
163. X. Cao, J. Zhang, D. Weissmann, M. Dolg and X. Chen, *Physical Chemistry Chemical Physics*, 2015, **17**, 20605-20616.
164. M. P. Jensen and A. H. Bond, *Journal*, 2002, **90**, 205.
165. G. Modolo and R. Odoj, *Solvent Extraction and Ion Exchange*, 1999, **17**, 33-53.
166. M. P. Kelley, J. Su, M. Urban, M. Luckey, E. R. Batista, P. Yang and J. C. Shafer, *Journal of the American Chemical Society*, 2017, **139**, 9901-9908.
167. N. Boubals, C. Wagner, T. Dumas, L. Chanèac, G. Manie, P. Kaufholz, C. Marie, P. J. Panak, G. Modolo, A. Geist and P. Guilbaud, *Inorganic Chemistry*, 2017, **56**, 7861-7869.
168. C. Nicholas, B. Yann, P. Jacques and M. Marinella, *Angewandte Chemie*, 2005, **117**, 7767-7770.
169. G. T. Te Velde, F. M. Bickelhaupt, E. J. Baerends, C. Fonseca Guerra, S. J. van Gisbergen, J. G. Snijders, T. Ziegler, *Journal of Computational Chemistry*, 2001, **22**, 931-967.
170. M. B. Brands, J. Nitsch and C. F. Guerra, *Inorganic Chemistry*, 2018, **57**, 2603-2608.
171. G. Cavigliasso and N. Kaltsoyannis, *Inorganic Chemistry*, 2007, **46**, 3557-3565.
172. P. R. Horn, Y. Mao and M. Head-Gordon, *Physical Chemistry Chemical Physics*, 2016, **18**, 23067-23079.
173. M. J. S. Phipps, T. Fox, C. S. Tautermann and C.-K. Skylaris, *Chemical Society Reviews*, 2015, **44**, 3177-3211.
174. J.-P. Dognon, C. Clavaguéra and P. Pykkö, *Chemical Science*, 2012, **3**, 2843-2848.
175. J.-P. Dognon, C. Clavaguéra and P. Pykkö, *Journal of the American Chemical Society*, 2008, **131**, 238-243.
176. C. A. Sorrell, *J. Chem. Educ*, 1971, **48**, 252.
177. F. Wes, J. Jeanne, K. Cheryl, O. Patrice and L. Monty, *J. Chem. Educ*, 1997, **74**, 224.
178. A. Suresh, D. K. Patre, T. Srinivasan and P. V. Rao, *Spectrochimica Acta Part A: Molecular and Biomolecular Spectroscopy*, 2002, **58**, 341-347.
179. D. A. Johnson and T. Florence, *Talanta*, 1975, **22**, 253-265.
180. E. Bobrowska-Grzesik, A. M. Grossman and J. Ciba, *Fresenius' journal of analytical chemistry*, 1993, **345**, 614-615.
181. R. Ahlrichs, M. Bär, M. Häser, H. Horn and C. Kölmel, *Chemical Physics Letters*, 1989, **162**, 165-169.
182. F. Neese, *ORCA Version 3.0.3, An ab initio density functional and semiempirical program package*, 2015.
183. F. Neese, *Wiley Interdisciplinary Reviews: Computational Molecular Science*, 2012, **2**, 73-78.
184. X. Cao, M. Dolg and H. Stoll, *The Journal of Chemical Physics*, 2003, **118**, 487-496.
185. W. Küchle, M. Dolg, H. Stoll and H. Preuss, *The Journal of Chemical Physics*, 1994, **100**, 7535-7542.
186. A. D. Becke, *Physical Review A*, 1988, **38**, 3098-3100.
187. J. P. Perdew, *Physical Review B*, 1986, **33**, 8822-8824.
188. J. P. Perdew, K. Burke and M. Ernzerhof, *Physical review letters*, 1996, **77**, 3865.
189. J. P. Perdew and Y. Wang, *Physical Review B*, 1992, **45**, 13244.
190. A. Schäfer, H. Horn and R. Ahlrichs, *The Journal of Chemical Physics*, 1992, **97**, 2571-2577.
191. F. Weigend and R. Ahlrichs, *Physical Chemistry Chemical Physics*, 2005, **7**, 3297-3305.
192. D. A. Pantazis and F. Neese, *J. Chem. Theory and Computat.*, 2011, **7**, 677-684.
193. J. P. Austin, N. A. Burton, I. H. Hillier, M. Sundararajan and M. A. Vincent, *Physical Chemistry Chemical Physics*, 2009, **11**, 1143-1145.
194. B. Khungar, A. Roy, A. Kumar, B. Sadhu and M. Sundararajan, *International Journal of Quantum Chemistry*, 2017, **117**, e25370.
195. A. Klamt and G. Schuurmann, *Journal of the Chemical Society, Perkin Transactions 2*, 1993, **5**, 799-805.
196. T. Lu and F. Chen, *Journal of computational chemistry*, 2012, **33**, 580-592.
197. E. van Lenthe, E.-J. Baerends and J. G. Snijders, *The Journal of chemical physics*, 1993, **99**, 4597-4610.
198. E. van Lenthe, E.-J. Baerends and J. G. Snijders, *The Journal of chemical physics*, 1994, **101**, 9783-9792.
199. E. van Lenthe, A. Ehlers and E.-J. Baerends, *The Journal of chemical physics*, 1999, **110**, 8943-8953.

200. C. Fonseca Guerra, J. G. Snijders, G. te Velde and E. J. Baerends, *Theoretical Chemistry Accounts*, 1998, **99**, 391-403.
201. E. van Lenthe, Erik, and E. J. Baerends, *Journal of Computational Chemistry*, 2003, **24**, 1142-1156.
202. A. Bérces, R. M. Dickson, L. Fan, H. Jacobsen, D. Swerhone and T. Ziegler, *Computer Physics Communications*, 1997, **100**, 247-262.
203. H. Jacobsen, A. Bérces, D. P. Swerhone and T. Ziegler, *Computer Physics Communications*, 1997, **100**, 263-276.
204. S. K. Wolff, *International Journal of Quantum Chemistry*, 2005, **104**, 645-659.
205. C. C. Pye and T. Ziegler, *Theoretical Chemistry Accounts*, 1999, **101**, 396-408.
206. K. B. Rakesh, A. Suresh and P. R. V. Rao, *Solvent Extraction and Ion Exchange*, 2014, **32**, 703-719.
207. J. Xu, E. Radkov, M. Ziegler and K. N. Raymond, *Inorganic Chemistry*, 2000, **39**, 4156-4164.
208. L. O. Tuazon, *The nature of cerium (IV) in aqueous nitric acid solution*, 1959.
209. T. Healy and H. McKay, *Transactions of the Faraday Society*, 1956, **52**, 633-642.
210. M. Sundararajan, G. Rajaraman and S. K. Ghosh, *Physical Chemistry Chemical Physics*, 2011, **13**, 18038-18046.
211. P. K. Verma, P. N. Pathak, N. Kumari, B. Sadhu, M. Sundararajan, V. K. Aswal and P. K. Mohapatra, *The Journal of Physical Chemistry B*, 2014, **118**, 14388-14396.
212. C. Aditi, C.V.S. Brahmmananda Rao, M. Sundararajan, T. K. Ghanty and S. Nagarajan, *ChemistrySelect*, 2018, **3**, 11309-11315.
213. B. Sreenivasulu, A. Suresh, N. Sivaraman and P. V. Rao, *Journal of Radioanalytical and Nuclear Chemistry*, 2015, **303**, 2165-2172.
214. W. W. Schulz, K. Bender, L. Burger and J. Navratil, 1990.
215. M. J. Servis, D. T. Wu and J. C. Braley, *Physical Chemistry Chemical Physics*, 2017, **19**, 11326-11339.
216. R. Chelli, P. Procacci, G. Cardini and S. Califano, *Physical Chemistry Chemical Physics*, 1999, **1**, 879-885.
217. T. Steiner and W. Saenger, *Journal of the American Chemical Society*, 1992, **114**, 10146-10154.
218. M. J. Phipps, T. Fox, C. S. Tautermann and C.-K. Skylaris, *Chemical Society Reviews*, 2015, **44**, 3177-3211.
219. Y. P. Yurenko, J. Novotný, V. Sklenář and R. Marek, *Physical Chemistry Chemical Physics*, 2014, **16**, 2072-2084.
220. J. Dey, N. Sultana, S. Kumar, V. K. Aswal, S. Choudhury and K. Ismail, *RSC Advances*, 2015, **5**, 74744-74752.
221. J. Habel, A. Ogbonna, N. Larsen, S. Cherre, S. Kynde, S. R. Midtgaard, K. Kinoshita, S. Krabbe, G. V. Jensen, J. S. Hansen, K. Almdal and C. Helix-Nielsen, *RSC Advances*, 2015, **5**, 79924-79946.
222. F. Kahnamouei, K. Zhu, R. Lund, K. D. Knudsen and B. Nystrom, *RSC Advances*, 2015, **5**, 46916-46927.
223. Y. V. Kulvelis, S. S. Ivanchev, V. T. Lebedev, O. N. Primachenko, V. S. Likhomanov and G. Torok, *RSC Advances*, 2015, **5**, 73820-73826.
224. H.-J. Lee, Y. Kwon, S. Y. Lee, J. Choi, B. H. Kim, D. Henkensmeier, J. H. Jang, S. J. Yoo, J.-Y. Kim, H.-J. Kim, H. Kim and M.-H. Kim, *RSC Advances*, 2016, **6**, 46516-46522.
225. J. Li, M. Pan and H. Tang, *RSC Advances*, 2014, **4**, 3944-3965.
226. G. Meleshko, J. Kulhavy, A. Paul, D. J. Willock and J. A. Platts, *RSC Advances*, 2014, **4**, 7003-7012.
227. R. A. Ramli, W. A. Laftah and S. Hashim, *RSC Advances*, 2013, **3**, 15543-15565.
228. X. Zhang, J. F. Douglas, S. Satija and A. Karim, *RSC Advances*, 2015, **5**, 32307-32318.
229. W. Marczak, M. Lezniak, M. Zorebski, P. Lodowski, A. Przybyla, D. Truszkowska and L. Almasy, *RSC Advances*, 2013, **3**, 22053-22064.
230. D. K. Patel, R. K. Singh, S. K. Singh, V. K. Aswal, D. Rana, B. Ray and P. Maiti, *RSC Advances*, 2016, **6**, 58628-58640.
231. C. V. Nikiforidis, E. P. Gilbert and E. Scholten, *RSC Advances*, 2015, **5**, 47466-47475.
232. D. G. Abebe, K.-Y. Liu, S. R. Mishra, A. H. F. Wu, R. N. Lamb and T. Fujiwara, *RSC Advances*, 2015, **5**, 96019-96027.
233. J. Bahadur, J. Prakash, D. Sen, S. Mazumder, P. U. Sastry, B. Paul, J. K. Chakravarty and H. Lemmel, *RSC Advances*, 2014, **4**, 13231-13240.
234. J. Bhattacharjee, G. Verma, V. K. Aswal, V. Patravale and P. A. Hassan, *RSC Advances*, 2013, **3**, 23080-23089.
235. A. Das, D. Sen, S. Mazumder, A. K. Ghosh, C. B. Basak and K. Dasgupta, *RSC Advances*, 2015, **5**, 85052-85060.
236. D. Sen, H. Lakhotiya, A. Das, J. Bahadur, S. Mazumder and C. B. Basak, *RSC Advances*, 2015, **5**, 22884-22891.

237. Z. Yang, S. Chaieb, Y. Hemar, L. de Campo, C. Rehm and D. J. McGillivray, *RSC Advances*, 2015, **5**, 107916-107926.
238. M. Z. Oskolkova, A. Stradner, J. Ulama and J. Bergenholtz, *RSC Advances*, 2015, **5**, 25149-25155.
239. J. Pathak, K. Rawat, V. K. Aswal and H. B. Bohidar, *RSC Advances*, 2015, **5**, 13579-13589.
240. D. R. Ratnaweera, D. Saha, S. V. Pingali, N. Labbe, A. K. Naskar and M. Dadmun, *RSC Advances*, 2015, **5**, 67258-67266.
241. T. A. Wagay, J. Dey, S. Kumar, V. K. Aswal and K. Ismail, *RSC Advances*, 2016, **6**, 66900-66910.
242. A. Bhadoria, S. Kumar, V. K. Aswal and S. Kumar, *RSC Advances*, 2015, **5**, 23778-23786.
243. R. Ganguly, S. Kumar, S. Nath, J. N. Sharma and V. K. Aswal, *RSC Advances*, 2015, **5**, 8063-8069.
244. N. Kumari, P. K. Verma, P. N. Pathak, A. Gupta, A. Ballal, V. K. Aswal and P. K. Mohapatra, *RSC Advances*, 2015, **5**, 95613-95617.
245. K. Thakkar, V. Patel, D. Ray, H. Pal, V. K. Aswal and P. Bahadur, *RSC Advances*, 2016, **6**, 36314-36326.
246. N. Arfin, V. K. Aswal and H. B. Bohidar, *RSC Advances*, 2014, **4**, 11705-11713.
247. A. Suresh, S. Subramaniam, T. G. Srinivasan and P. R. V. Rao, *Solvent Extraction and Ion Exchange*, 1995, **13**, 415-430.
248. V. K. Aswal and P. Goyal, *Curr Sci*, 2000, **79**, 947-953.
249. G. Verma, V. K. Aswal, S. Kulshreshtha, P. Hassan and E. W. Kaler, *Langmuir*, 2008, **24**, 683-687.
250. P. Verma, N. Kumari, P. Pathak, B. Sadhu, M. Sundararajan, V. K. Aswal and P. K. Mohapatra, *The Journal of Physical Chemistry A*, 2014, **118**, 3996-4004.
251. P. Verma, P. Pathak, P. Mohapatra, V. K. Aswal, B. Sadhu and M. Sundararajan, *The Journal of Physical Chemistry B*, 2013, **117**, 9821-9828.
252. P. Raveendran, J. Fu and S. L. Wallen, *Journal of the American Chemical Society*, 2003, **125**, 13940-13941.
253. J. Y. Chong, X. Mulet, L. J. Waddington, B. J. Boyd and C. J. Drummond, *Soft Matter*, 2011, **7**, 4768-4777.
254. A. Zhang, W. Wang, Z. Chai and M. Kumagai, *Journal of separation science*, 2008, **31**, 3148-3155.
255. A. Zhang, W. Wang, Z. Chai and E. Kuraoka, *European Polymer Journal*, 2008, **44**, 3899-3907.
256. G. Doak and L. D. Freedman, *Chemical Reviews*, 1961, **61**, 31-44.
257. J. P. Guthrie, *Canadian Journal of Chemistry*, 1979, **57**, 236-239.
258. A. Suresh, T. G. Srinivasan and P. R. V. Rao, *Solvent Extraction and Ion Exchange*, 1994, **12**, 727-744.
259. A. Ikeda-Ohno, C. Hennig, S. Tsushima, A. C. Scheinost, G. Bernhard and T. Yaita, *Inorganic Chemistry*, 2009, **48**, 7201-7210.
260. M. Walther, B. M. Fischer and P. U. Jepsen, *Chemical Physics*, 2003, **288**, 261-268.
261. D. G. Kalina, Mason, G.W., and Horwitz, E. P., *J. Inorg. Nucl. Chem.* , 1981, **43**, 159-163.
262. G. R. Choppin, *Journal of Alloys and Compounds*, 2002, **344**, 55-59.
263. C. H. Choi, M. W. Chung, S. H. Park and S. I. Woo, *Physical Chemistry Chemical Physics*, 2013, **15**, 1802-1805.
264. I.-Y. Jeon, S.-Y. Bae, J.-M. Seo and J.-B. Baek, *Advanced Functional Materials*, 2015, **25**, 6961-6975.
265. R. F. Bader, *Chemical Reviews*, 1991, **91**, 893-928.
266. F. W. Biegler-könig, R. F. Bader and T. H. Tang, *Journal of Computational chemistry*, 1982, **3**, 317-328.
267. X.-H. Kong, Q.-Y. Wu, J.-H. Lan, C.-Z. Wang, Z.-F. Chai, C.-M. Nie and W.-Q. Shi, *Inorganic Chemistry*, 2018, **57**, 14810-14820.
268. X.-W. Chi, Q.-Y. Wu, Q. Hao, J.-H. Lan, C.-Z. Wang, Q. Zhang, Z.-F. Chai and W.-Q. Shi, *Organometallics*, 2018, **37**, 3678-3686.
269. I. D. Prodan, G. E. Scuseria and R. L. Martin, *Physical Review B*, 2007, **76**, 033101.
270. M. P. Kelley, G. J. P. Deblonde, J. Su, C. H. Booth, R. J. Abergel, E. R. Batista and P. Yang, *Inorganic Chemistry*, 2018, **57**, 5352-5363.